ABSTRACT

Title of dissertation: WIND TUNNEL TEST ON SLOWED ROTOR AEROMECHANICS AT HIGH ADVANCE RATIOS

Xing Wang
Doctor of Philosophy, 2020

Dissertation directed by: Professor Inderjit Chopra
Department of Aerospace Engineering

In forward flight, slowing down a rotor alleviates compressibility effects on the advancing side, extending the cruise speed limit and inducing high advance ratio flight regime. To investigate the aerodynamic phenomena at high advance ratios and provide data for the validation of analysis tools, a series of wind tunnel tests were conducted progressively with a 33.5-in radius, 4-bladed Mach-scaled rotor in the Glenn L. Martin wind tunnel.

In the first stage of the research, a wind tunnel test was carried out at high advance ratios with highly similar, non-instrumented blades and on-hub control angle measurements, in order to gain a baseline performance and control dataset with minimum error due to blade structural dissimilarity and pitch angle discrepancy. The tests were conducted at advance ratios of 0.3 to 0.9, and a parametric study on shaft tilt was conducted at 0° and $\pm 4^\circ$ shaft tilt angles. The test data were then compared with those of previous tests and with the predictions of the in-house comprehensive analysis UMARC. The airload results were investigated using com-

prehensive analysis to gain insights on the influences of advance ratio and shaft tilt angle on rotor performance and hub vibratory loads. Results indicate that the thrust benefit from backward shaft tilt is dependent on the change in the inflow condition and the induced angle of attack increment, and the reverse flow region at high advance ratios is the major contributor to changes in shaft torque and horizontal force.

In the second stage of the research, the rotor blades were instrumented with pressure sensors and strain gauges at 30% radius, and pressure data were acquired to calculate the sectional airloads by surface integration up to an advance ratio of 0.8. The test results of blade airloads and structural loads were compared with the predictions of comprehensive analysis (UMARC and PrasadUM) and CFD/CSD coupled analysis (PrasadUM/HAMSTR). The focus was on the data correlation between experimental pressure, airload and structural load data and the CFD/CSD predicted results at various collective and shaft tilt settings. Overall, the data correlation was found satisfactory, and the study provided some insights into the aerodynamic mechanisms that affect the rotor airload and performance, in particular the mechanisms of backward shaft tilt, hub/shaft wake and the formation of dynamic stall in the reverse flow region.

The next stage focused on hingeless rotor with lift offset. Previous wind tunnel tests have shown that an articulated rotor trimmed to zero hub moment generates limited thrust at high advance ratios, because the advancing side needs to be trimmed against the retreating side with significant reverse flow, in which the rotor is ineffective in generating thrust. Therefore, a hingeless rotor that allows the

advancing side to generate more thrust can be rewarding in overall thrust potential. Wind tunnel tests were conducted up to an advance ratio of 0.7 to investigate the behavior of hingeless rotors at high advance ratios with lift offsets. Performance, control angles, hub vibratory loads and blade structural loads were compared with comprehensive analysis predictions from UMARC, plus the wing performance predictions from AVL. The results demonstrate that a hingeless rotor with lift offset is more efficient in generating thrust and exhibits higher lift-to-drag ratio at high advance ratios. The blade structural load level is significantly higher compared to an articulated rotor, especially for 2/rev flap bending moment, which can pose a critical structural constraint on the rotor.

WIND TUNNEL TEST ON ROTOR AEROMECHANICS AT HIGH ADVANCE RATIOS

by

Xing Wang

Dissertation submitted to the Faculty of the Graduate School of the
University of Maryland, College Park in partial fulfillment
of the requirements for the degree of
Doctor of Philosophy
2020

Advisory Committee:
Professor Inderjit Chopra, Chair/Advisor
Professor Anubhav Datta
Professor Anya Jones
Professor James Baeder
Professor Daniel Lathrop, Dean's Representative

© Copyright by
Xing Wang
2020

Acknowledgments

First, I would like to thank my advisor, Dr. Inderjit Chopra for giving me an invaluable opportunity to work on the project. Without his patient guidance and resourceful support, this dissertation would not be possible to be accomplished. It has been my honor to work with him and learn from him. I would also like to thank my committee members, Dr. Anubhav Datta, Dr. Anya Jones, Dr. James Baeder, and Dr. Daniel Lathrop, for reviewing my research. I would like to especially thank to Dr. V.T. Nagaraj for his technical help on the hydraulic system and test planning. This project was supported by the Army/Navy/NASA Vertical Lift Research Center of Excellence (VLRCOE) with Dr. Mahendra Bhagwat as the technical monitor.

Benjamin Berry was my first supervisor since I was an undergraduate student, and my initial understanding of wind tunnel test was from him. Ben provided many fruitful insights about data acquisition and interpretation even after his graduation. Anand Saxena and Vikram Hrishikeshavan guided me on getting started in the rotorcraft lab, and offered me critical help in wind tunnel testing. Anand installed the 150-line slipring on the test stand, and Vikram was a talented pilot in rotor trimming. The third test on articulated rotor was held by Lauren Trollinger, and the nylon fuselage used in the test was designed by Peter Oas. For the hingeless rotor tests, the test stand was modified by Andre Bauknecht to accommodate the plastic modular fuselage and the stub wing, and the UT-69A 6-component balance installed in the wing spar was borrowed from NASA Langley Research Center. Shashank Maurya, Brandyn Phillips, and Elena Shrestha helped me to debug lab electronics

for countless times. I would also like to acknowledge Dr. Jewel Barlow, Andrew Lind, Luke Smith, Lex Chi, Frederick Tsai, James Sutherland-Foggio, Nanwei Zhou, Andrew Grizzle, all the staff of the Glenn L. Martin Wind Tunnel, and all the undergraduate students who participated the tests for their valuable assistance with wind tunnel testing.

I owe my gratitude to Graham Bowen-Davies and Joseph Schmaus, who helped me step-by-step with UMARC and data processing. The discussion with Stacy Sidle and Daniel Escobar on UMARC were also very fruitful. William Staruk and Elizabeth Ward shared their extensive experiences in composite material and blade structural modeling. Ananth Sridharan developed the comprehensive analysis PrasadUM, and guided me through the process of CFD/CSD coupling. Most of the CFD cases with HAMSTR were executed by Yong Su Jung. These inputs in my data correlation studies are greatly appreciated.

Finally, I owe my deepest thanks to my family, my mother Mary Yang, my father Shirong Wang, and my girlfriend Chenfang Wang. Their unconditional support and warm encouragement all the time are the motivation to keep me forward. I would also thank my gamemates, Haoyan "Doctorfaust" Guo, Jerry "Advance" Zhang, and Lihua "Zerphy" Zhang. I doubt whether they speed up the process of my graduation, but they do make the tough time easier to carry on.

Every journey has its inevitable end, but every end is a new beginning.

Table of Contents

List of Tables

List of Figures

List of Abbreviations

AGRC	Alfred Gessow Rotorcraft Center
AVL	Athena Vortex Lattice code
BNC	Bayonet Neill–Concelman connector
CAD	Computer-Aided Design
CAMRAD	Comprehensive Analytical Model of Rotorcraft Aerodynamics and Dynamics
CFD	Computational Fluid Dynamics
CHARM	Comprehensive Hierarchical Aeromechanics Rotorcraft Model
CSD	Computational Structural Dynamics
FET	Finite Elements in Time
FFT	Fast Fourier Transform
HAMSTR	Hamiltonian/Strand flow solver
LVDT	Linear Variable Displacement Transducer
NASA	National Aeronautics and Space Administration
MFW	Maryland Free Wake model
PCB	Printed Circuit Board
PIV	Particle Image Velocimetry
PrasadUM	Parallelized Rotorcraft Analysis for Simulation and Design, University of Maryland
RANS	Reynolds-Averaged Navier–Stokes simulation
RCAS	Rotorcraft Comprehensive Analysis System
RPM	Revolutions Per Minute
RVR	Reverse Velocity Rotor
SMR	Single Main Rotor
TURNS	Transonic Unsteady Rotor Navier-Stokes method
UMARC	University of Maryland Advanced Rotorcraft Code
UAV	Unmanned Aerial Vehicle
UMD	University of Maryland
VI	Virtual Instrument
VLRCOE	Vertical Lift Research Center of Excellence
VTOL	Vertical Take-Off and Landing
WENO	Weighted Essentially Non-Oscillatory scheme

A	Area (ft^2)
a	Acoustic speed (ft/s)
c	Rotor blade chord (ft)
C_D	Drag force, divided by $\rho\pi R^2(\Omega R)^2$
C_H	Horizontal force, divided by $\rho\pi R^2(\Omega R)^2$
C_L	Overall lift force, divided by $\rho\pi R^2(\Omega R)^2$

C_{Mx}	Rotor rolling moment, divided by $\rho\pi R^3(\Omega R)^2$
C_Q	Rotor shaft torque, divided by $\rho\pi R^3(\Omega R)^2$
C_T	Rotor thrust force, divided by $\rho\pi R^2(\Omega R)^2$
$c_c M^2$	Sectional chordwise force, divided by $1/2\rho a^2 c$
$c_{in} M^2$	Sectional in-plane force, divided by $1/2\rho a^2 c$
$c_m M^2$	Sectional pitching moment, divided by $1/2\rho a^2 c^2$
$c_n M^2$	Sectional normal force, divided by $1/2\rho a^2 c$
$c_p M^2$	Pressure coefficient, $(p - p_\infty)/(1/2\rho a^2)$
$c_x M^2$	Sectional X-direction force, divided by $1/2\rho a^2 c$
$c_z M^2$	Sectional vertical force, divided by $1/2\rho a^2 c$
D	Drag force (lb)
EA	Axial stiffness $(lb - ft^2)$
EI_y	Flap bending stiffness $(lb - ft^2)$
EI_z	Lag bending stiffness $(lb - ft^2)$
F	Applied force (lb)
F_{in}	Hub in-plane force (lb)
F_x	Hub horizontal force (lb)
F_y	Hub side force (lb)
F_z	Hub vertical force (lb)
f	Frequency (Hz)
GJ	Torsional stiffness $(lb - ft^2)$
g	Gravitational acceleration (ft/s^2)
H	Horizontal force (lb)
I_β	Flap/lag moment of inertia $(slug - ft^2)$
L	Lift force (lb)
LO	Rotor lift offset, divided by R
LS	Rotor lift share
l	Length (ft)
M	Applied moment $(lb - ft)$
M_{air}	Molar mass of the air (kg/mol)
M_T	Total mass $(slug)$
m	Mass per unit length $(slug/ft)$
N_b	Number of blades
p	Blade surface pressure (psf)
p_{air}	Ambient pressure (psf)
p_∞	Freestream pressure (psf)
Q	Rotor shaft torque $(lb - ft)$
q	Freestream dynamic pressure (psf)
R	Rotor radius (ft)
R_{air}	Gas constant $(J/kg \cdot K)$

T	Thrust force (lb)
T_∞	Ambient temperature (K)
V_∞	Freestream speed (ft/s)
w	Vertical displacement (ft)
α	Angle of attack (deg)
α_s	Shaft tilt angle, backward positive (deg)
β_{1c}	1/rev longitudinal flap angle (deg)
β_{1s}	1/rev lateral flap angle (deg)
Γ	Vortex strength (ft/s)
γ	Lock number
δ	Phase angle (rad)
δ_w	Boundary correction factor
ζ	Damping constant
θ	Blade pitch angle (deg)
θ_0	Collective control angle (deg)
θ_{1c}	Lateral cyclic control angle (deg)
θ_{1s}	Longitudinal cyclic control angle (deg)
μ	Advance ratio, $V_\infty/\Omega R$
ρ	Freestream density ($slug/ft^3$)
σ	Rotor solidity, $N_b c/\pi R$
ϕ	Blade twist angle (deg)
ψ	Azimuth angle (deg)
Ω	Angular velocity (rad/s)
ω_d	Driving frequency (rad)
ω_n	Natural frequency (rad)

Chapter 1: Introduction

This chapter introduces the background of high speed rotorcraft and the design features to expand the flight envelope and improve the cruise performance. Then, the history of high advance ratio rotor research is summarized separately in experimental and computational categories. At last, the scope and contributions of the current research are presented, followed by an outline of the dissertation.

1.1 Background and Motivation

The most unique feature of helicopters and other rotorcraft is the capability to hover and takeoff/land vertically. The capability is critical for missions without runway, and provides an enormous low speed maneuverability for search and rescue, cargo delivery, and reconnaissance missions. However, the cruise speed of a helicopter is limited compared to that of a fixed-wing aircraft due to the compressibility effect. On the advancing side, the tip speed is the summation of cruise speed and rotation speed. With a constant rotation speed, the cruise speed is constrained by the tip speed, otherwise a large wave drag can be induced exceeding the critical Mach number (Fig. 1.1). Today, there is a strong demand for high speed rotorcraft with a 250 - 300 knots cruise speed. Several novel design features have been ap-

plied to expand the flight envelope of rotorcraft, and a tradeoff must be carried out between the hover efficiency and the forward flight performance.

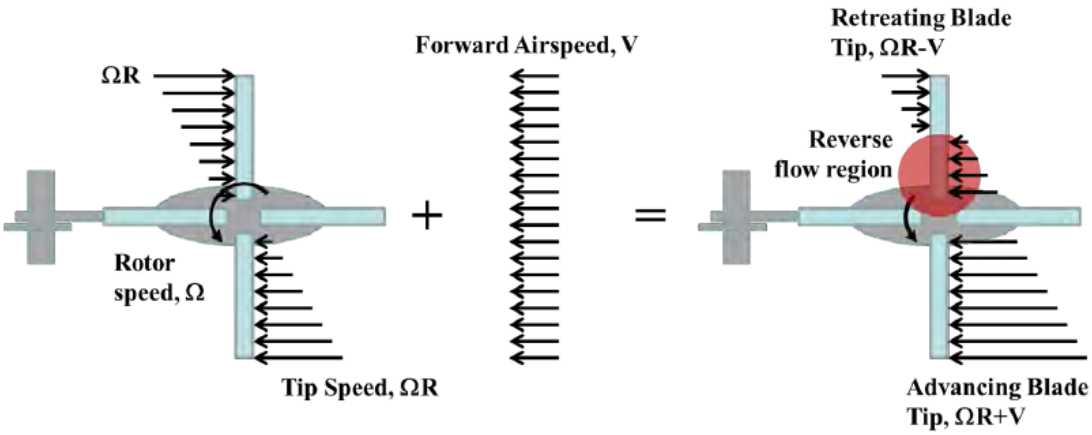

Fig. 1.1: The flight regime of a high speed rotorcraft [1].

A balanced solution between hover and cruise is to slow down the rotor in forward flight. A slowed rotor can alleviate the compressibility effects on the advancing side, thus extending the cruise speed limit. The technique has a wide range of application: it can be adopted for Single Main Rotor (SMR) and coaxial helicopters, even for autogyros. Notable examples of slowed rotor aircraft include the Sikorsky S-97 (coaxial, Fig. 1.2(a)) that was developed from the X2 project, the Eurocopter (now Airbus) X^3 (SMR, Fig. 1.2(b)), the Boeing A160 (SMR UAV, Fig. 1.2(c)), and the CarterCopter CC1 (autogyro, Fig. 1.2(d)). A major issue of the slowed rotor is the high advance ratio flight regime it induced. A large reverse flow region emerges on the retreating side (see Fig. 1.1), where the airflow is from the trailing edge to the leading edge, and the local pitch angle is high due to the trim control. Intense reverse flow dynamic stall occurs in this region, and the blades become inefficient in generating thrust. The behavior of a rotor at high advance ratios is the primary

focus of the current research.

(a) Sikorsky S-97 (b) Eurocopter X^3

(c) Boeing A160 (d) CarterCopter CC1

Fig. 1.2: Rotorcraft with slowed rotor feature.

To compensate the rotor performance degradation at high advance ratios, a straightforward method is to install additional lifting surfaces and/or propellers, which results in a compound rotorcraft. The wing and propeller become more efficient with higher speed, while the main rotor has a reduced performance. Thus, the rotorcraft operates more like a fixed-wing aircraft, which is inherently more effective at high cruise speed. The lift and propulsion compounding can be applied separately, and the lifting surface is not necessarily symmetric, as shown in Fig. 1.3. The compound configuration is commonly used with a slowed rotor: as mentioned above, the Sikorsky S-97 (Fig. 1.2(a)) uses a tail propeller without a wing, and the Eurocopter X^3 (Fig. 1.2(b)) uses twin propellers and symmetric stub wings.

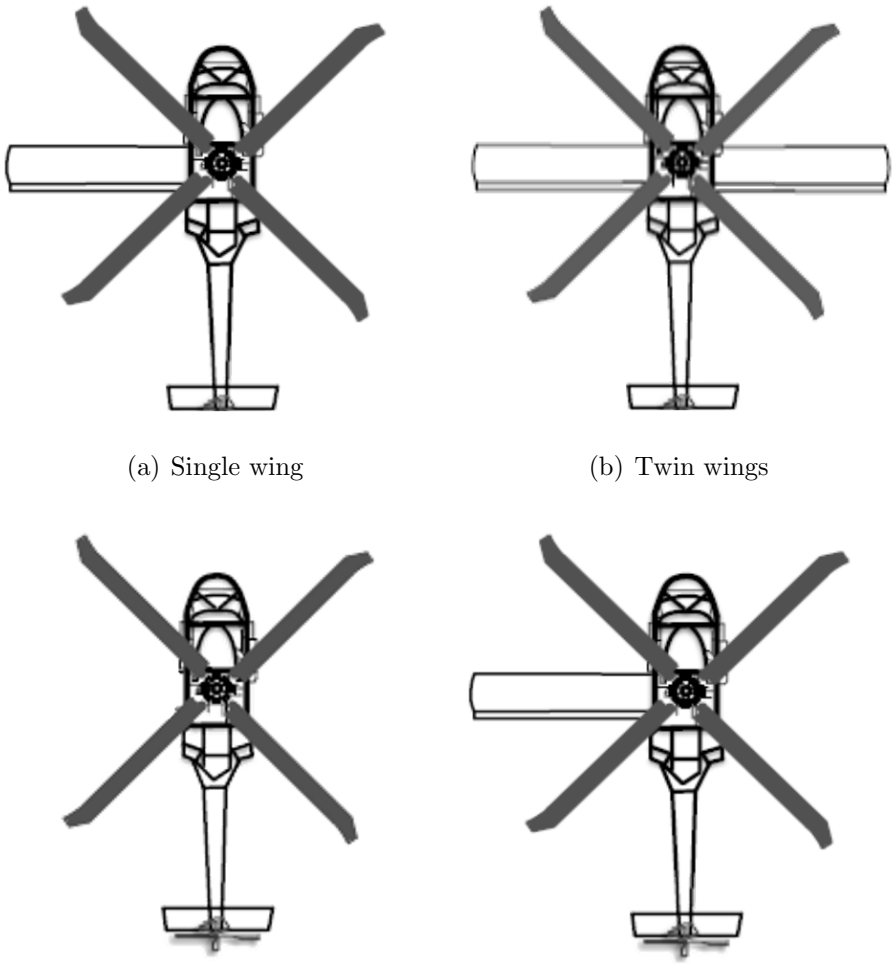

(a) Single wing (b) Twin wings

(c) Tail propeller (d) Wing-propeller hybrid

Fig. 1.3: Different configurations for lift and propulsion compounding [2].

Without additional wing or propeller, the rotor performance can be improved by trimming with lift offset. The technique can be used on a hingeless rotor only: for an articulated rotor, the flap hinges cannot transmit moment, so the advancing side must be balanced with the retreating side with significant reverse flow, resulting in limited thrust on both sides. For a hingeless rotor, the lift distribution on the rotor disk can be shifted by trimming to a non-zero rolling moment, increasing the thrust on the advancing side to make it more effective at high advance ratios (Fig. 1.4(a)).

The concept of lift offset was initially proposed for a coaxial configuration [17, 18], since the two countra-rotating rotors can be offsetted to opposite directions to cancel each other (Fig. 1.4(b)). The Sikorsky S-69 was developed as a technical demonstrator of the technique, and wind tunnel tests [19] and flight tests [20] were conducted. Trimming with lift offset is also possible for a SMR rotorcraft, and an asymmetric wing is required to balance the rolling moment from the single rotor. A UAV has been built and tested with asymmetric winged compound [21], and a recent computational analysis pointed out that the configuration can achieve better performance than a coaxial rotor with lift offset in some cases [2]. More experimental results are required to investigate the performance of the asymmetric configuration with lift offset.

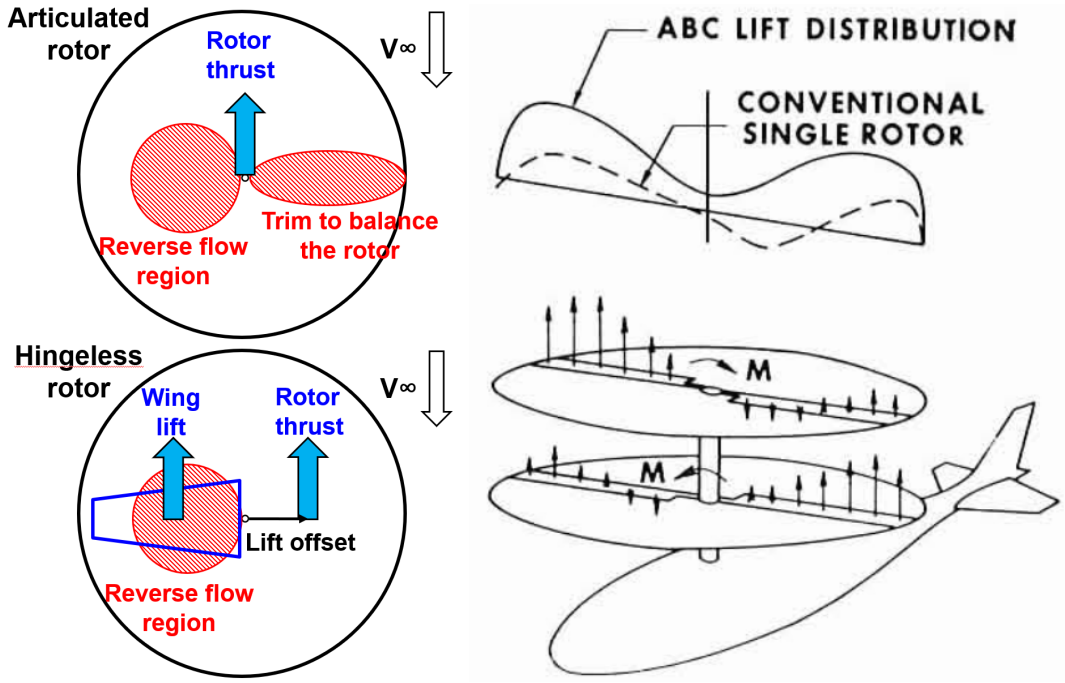

(a) Single rotor [22] (b) Coaxial rotors [17]

Fig. 1.4: A diagrammatic sketch of the mechanics of lift offset.

Other than to slow down the rotor, another high speed solution for VTOL aircraft is to align the rotor with the forward flight direction, which leads to a tiltrotor, tiltwing, or tail sitter design. With any of these configurations, there is no advancing or retreating side anymore, and the compressibility limit is on the vector addition of cruise speed and rotation speed, instead of the simple summation of them. Thus, the cruise speeds of such rotorcraft can be comparable to those of fixed-wing aircraft with propellers. A number of manned rotorcrafts and UAVs have been built with these configurations, such as the Bell V-22 (tiltrotor, Fig. 1.5(a)), the AgustaWestland AW609 (tiltrotor, Fig. 1.5(b)), the Airbus Vahana (tiltwing, Fig. 1.5(c)), and the Bell APT (tailsitter UAV, Fig. 1.5(d)). For these designs, a common disadvantage is that the hover performance is worse than that of a compound helicopter due to the higher disk load. Also, the unstable wing stall may occur during transition for tiltwing, the rotor downwash is hampered by the wing in hover for tiltrotor, and a mechanism to tilt the rotor is required for both configurations, inducing additional weight and mechanical complexity. For a tailsitter, tilting the whole fuselage appears to be a straightforward technique, but it changes the orientation of the payload during transition, so the configuration is more appropriate for UAVs. These configurations are active areas of research in rotorocraft field, but they are not the focus of the current study.

(a) Bell V-22 (b) AgustaWestland AW609

(c) Airbus Vahana (d) Bell APT

Fig. 1.5: Rotorcraft with tiltrotor/tiltwing/tailsitter configuration.

1.2 Summary of Previous Work

The initial research on high advance ratio rotor began in 1930s, reached its climax in 1960s in need of high speed military rotorcraft, and ceased in 1970s due to mechanical complexity, excessive cost and limited missions. The subject became active again in 21st century, made possible by advanced composite material and the breakthrough of computational analysis capability. A review of previous works on high advance ratio rotors is presented in this section, with the researches summarized in experimental and computational categories separately.

1.2.1 Experimental Studies

In 1933, the earliest rotor test at high advance ratios was conducted in the NACA Langley 30 by 60 ft wind tunnel [3]. The test subject was a full-scale Pitcairn PCA-2 autogyro rotor without fuselage (Fig. 1.6(a)). The test objective was to examine the rotor performance (especially drag and lift-to-drag ratio), the downwash distribution and the effect of protuberance fairing. A collective sweep with fixed RPM and tunnel speed was not possible because the rotor was unpowered, and the rotation speed is a function of the collective, the angle of attack of the rotor disk, and the tunnel speed. During the test, the collective was fixed at first, the rotor disk plane was adjusted to match the desired RPM. Tunnel speed sweeps were carried out at three collectives up to an advance ratio of 0.7, and rotor tracking was performed when the collective setting was changed. Results showed that the rotor lift-to-drag ratio reached its peak of 7 at an advance ratio of about 0.35, and the trend was not significantly affected by the collective setting (Fig. 1.6(b)).

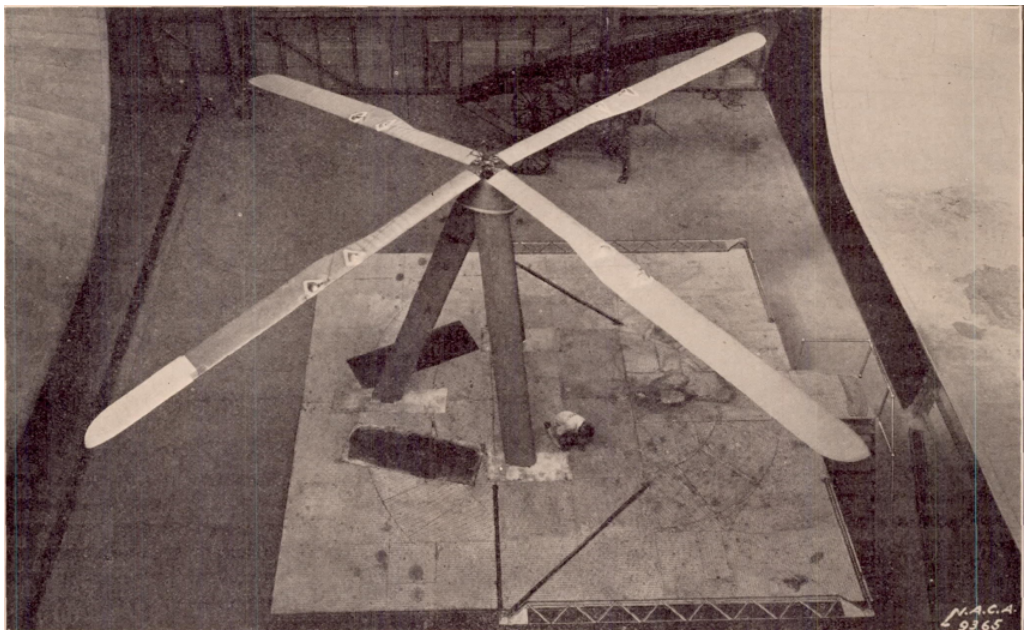

(a) Rotor setup in wind tunnel

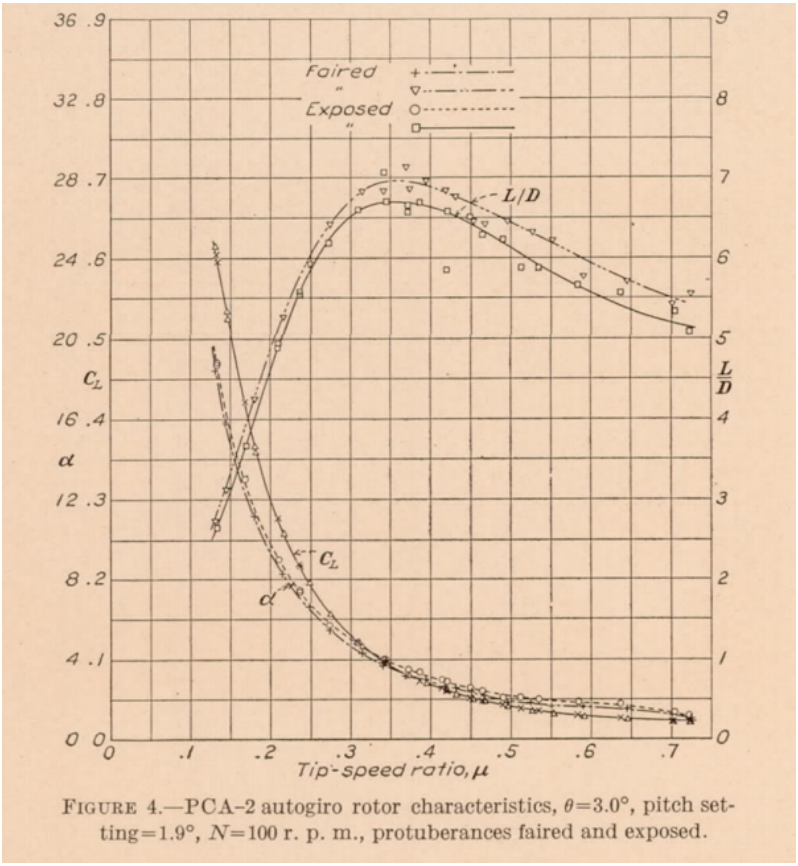

FIGURE 4.—PCA-2 autogiro rotor characteristics, θ=3.0°, pitch setting=1.9°, N=100 r. p. m., protuberances faired and exposed.

(b) High advance ratio performance

Fig. 1.6: The setup of PCA-2 rotor test and key results [3].

In 1955, a 5-ft diameter rotor with 13% flap hinge offset was tested up to an advance of 1.0 [4] (Fig. 1.7). It was the first attempt to acquire blade surface pressure data and airloads (referred to aerodynamic loading in the report). A pressure pickup unit was installed in the hub, which connected to pressure port holes distributed on the blades with internal tubing, measuring the pressure difference between the upper surface and the lower surface. The pressure transducer in the hub could only process the data at a single pair of pressure ports, so a switching mechanism was implemented to activate different pressure ports. The long tubing in the blades posed a problem on the frequency response on the pressure readings, so a dynamic calibration was conducted to correct the measurements. The airload data were presented across the span at various azimuth, and were visualized as contour plots on the rotor disk (Fig. 1.7(b)). Only one collective was studied at each advance ratio (usually 8°, and 4° at highest μ) and no cyclic pitch was applied to trim the rotor. Also, the rotor performance data were not included in the report.

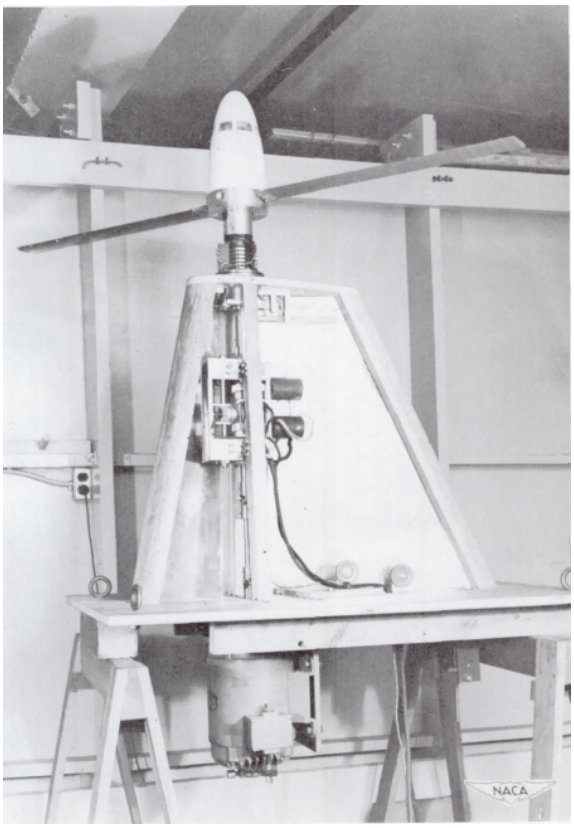

(a) Rotor setup in wind tunnel

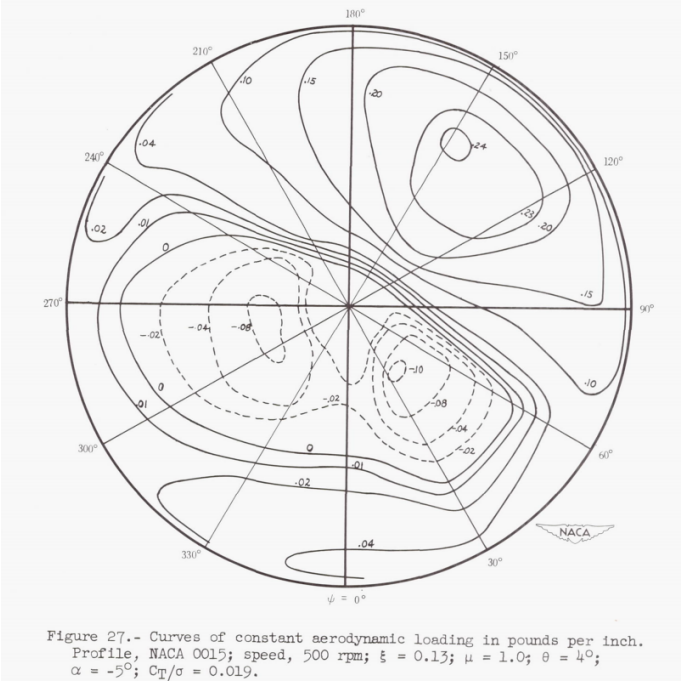

(b) High advance ratio airload contour

Fig. 1.7: The setup of 5-ft rotor test with pressure ports and key results [4].

In 1965, a 15-ft diameter teetering rotor was tested in the NASA Langley 30 by 60 ft wind tunnel, and the test reached 1.45 advance ratio (Fig. 1.8(a)). The model rotor used untwisted, untapered blades with a NACA0012 airfoil [5]. The primary focus of the test was to explore the rotor performance at high advance ratios, and the swashplate control angles and flap angles. The flow direction and separation status on the retreating side were studied with a camera and tufts on the blades. For the first time, collective sweep was conducted at each advance ratio with the rotor trimmed, and the thrust reversal phenomenon was observed at high advance ratios, in which an increment of collective induced a reduction of thrust(Fig. 1.8(b)). In addition, a parametric study was conducted on shaft tilt angle, and an impact of shaft tilt on lift-to-drag ratio was reported. As a drawback, the blade stiffness and mass properties were not included in the report, making the dataset less suitable for a validation study.

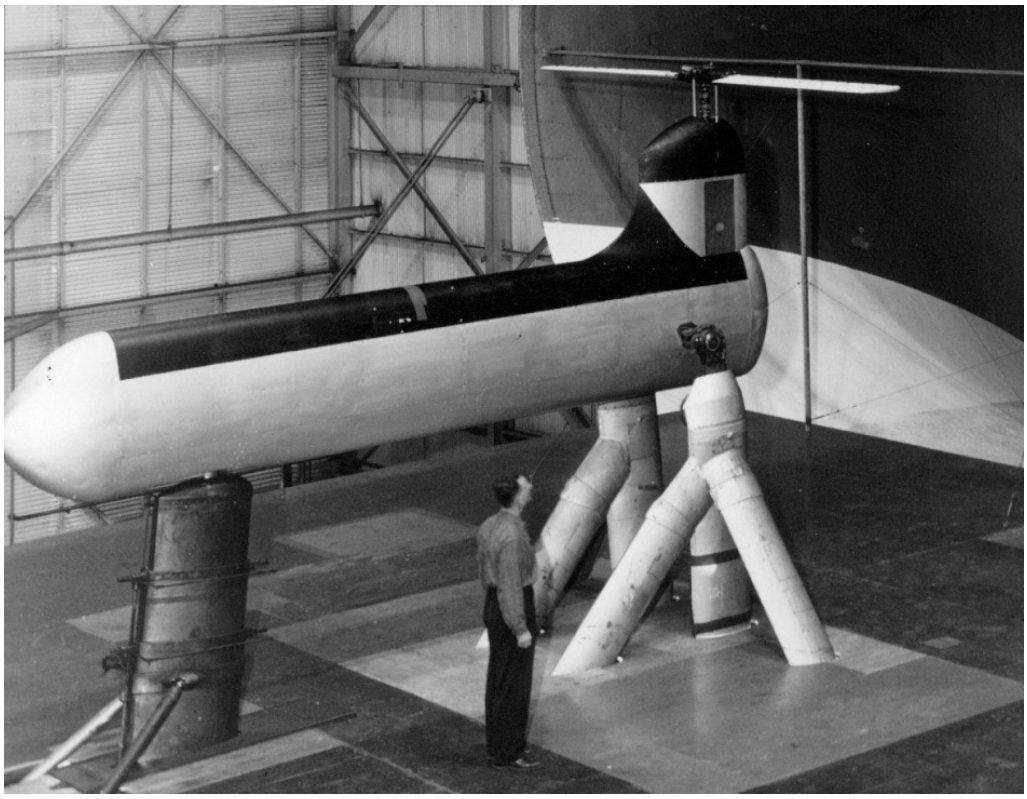

(a) Rotor setup in wind tunnel

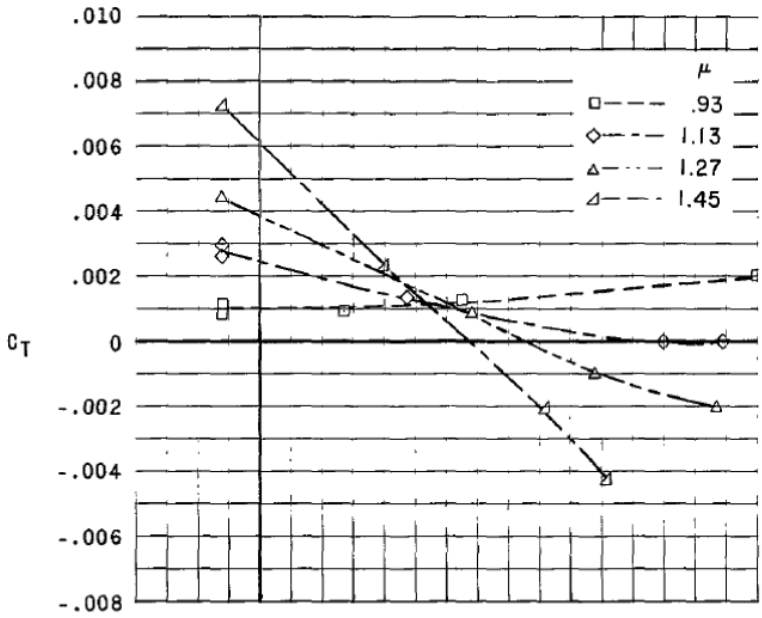

(b) Thrust reversal

Fig. 1.8: The setup of 15-ft rotor test and key results [5].

In 1968 and 1969, a series of wind tunnel tests was conducted in the NASA Ames 40 by 80 ft wind tunnel [23,24]. Several full-scale rotor geometries were tested. Two of them were 56-ft diameter articulated rotors modified from a H-34 rotor (Fig. 1.9(a)): one was untwisted and another with $-8°$ linear twist. The others were modified UH-1B and UH-1D teetering rotors (Fig. 1.9(b)) with different diameters (48 ft, 44 ft and 34 ft), blade twists (from $-1.41°$ to $-10.9°$) and tip taper (untapered or tapered from 80% radius to the tip). All untapered blades used NACA0012 airfoil for the whole span, and the blades with tapered-tip used NACA0012 for the inboard section and NACA21006 at the tip. Blade geometric and mass properties were provided in the reports, but stiffness properties were not included. The primary objective of these tests was to validate the state-of-art analyses at the time, so the rotor performance and control angle measurements were emphasized. Collective sweeps were conducted at various advance ratios: the RPM was fixed and the tunnel speed was adjusted at moderate advance ratios, and the RPM was adjusted to achieve desired advance ratios when the maximum tunnel speed of 190 knots was reached. At each test case, the rotor was trimmed to zero 1/rev flap angle. The maximum advance ratio was 1.05 for the 56-ft H-34 rotor and 1.1 for the 34 ft UH-1 rotor (Figs. 1.9(c) and 1.9(d)), and the maximum tip Mach number reached 1.0. At high advance ratios, increased control sensitivity and reduced stability were observed, and the transient response before achieving steady state became slower. Based on the test data, multiple computational analyses were conducted, and the results are discussed in the next section.

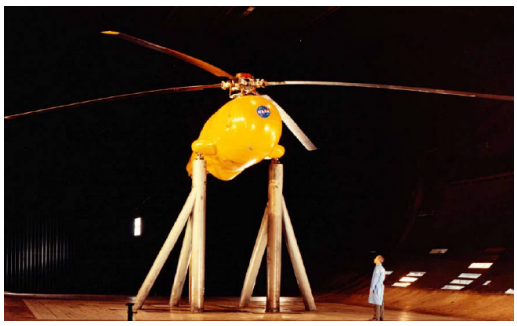

(a) H-34 rotor setup

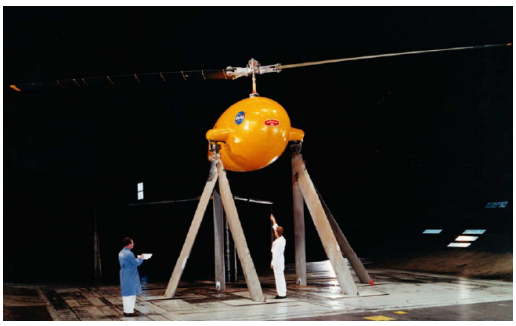

(b) UH-1 unmodified rotor setup

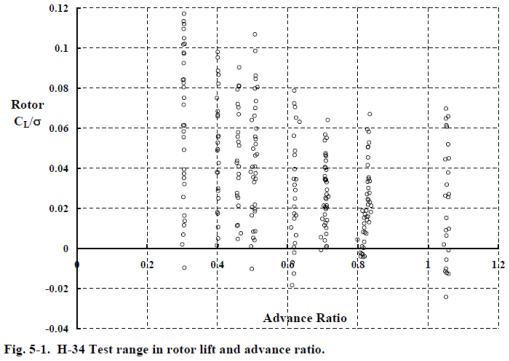

Fig. 5-1. H-34 Test range in rotor lift and advance ratio.

(c) H-34 rotor test envelop

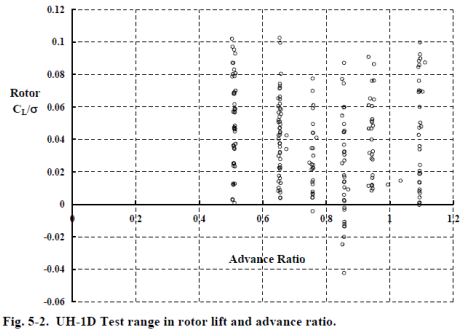

Fig. 5-2. UH-1D Test range in rotor lift and advance ratio.

(d) UH-1 rotor test envelope

Fig. 1.9: The setup of H-34 and UH-1 rotor tests and sample test envelopes [6].

In 1972, an 8-ft diameter articulated rotor was tested in the 12 ft pressurized wind tunnel at NASA Ames Research Center [7]. The rotor was a 1/7th scale model of the Reverse Velocity Rotor (RVR) system, on which several novel features were implemented, including a 2/rev swashplate control to manipulate the lift distribution on the rotor disk (result not shown), and elliptic airfoils to improve thrust generation in the reverse flow region (Fig. 1.10(a)). The test reached a maximum advance ratio of 2.46 at 350 knots tunnel speed, unprecedented in any other rotor test, and a shaft tilt study was performed from 5° forward to 12.5° aft. Rotor performance, control angles, blade root motions and blade flap bending moment at 31%, 51% and 71% radius were measured. Axial loads on the lag dampers and pitch links were

also recorded. The rotor was successfully trimmed to zero longitudinal flap and zero rolling moment, and no dynamic instability was observed during the process. As reported before [5], the thrust reversal occurs at around 0.9 advance ratio and the collective control was ineffective there. A notable finding was that the thrust level and lift-to-drag ratio recovered at an extremely high advance ratio beyond 1.4 (Fig. 1.10(b)), and the collective-thrust control sensitivity was regained (although the correlation became negative).

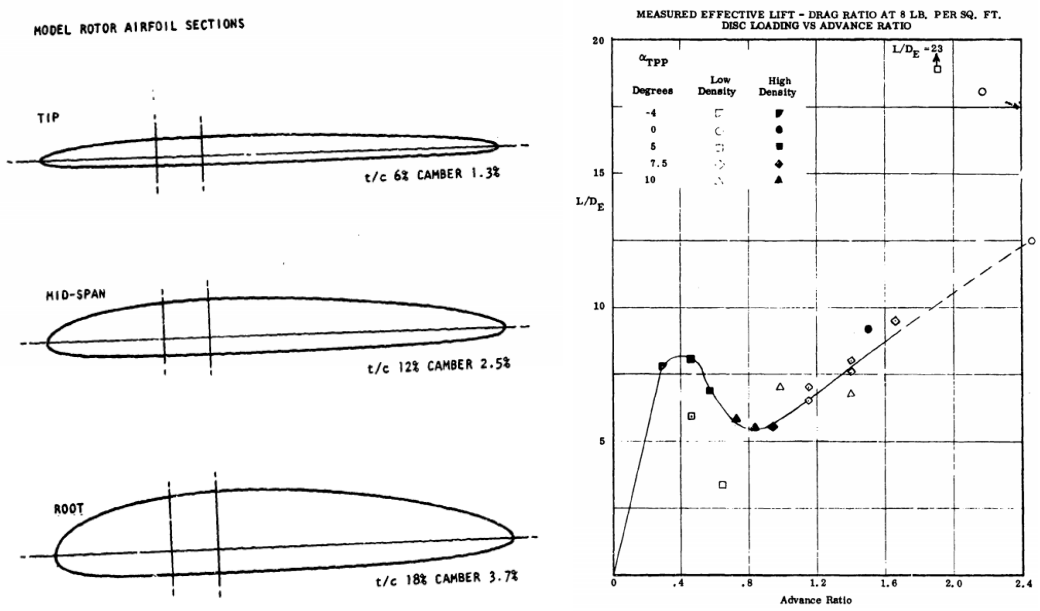

(a) Elliptical airfoils (b) L/D_e up to $\mu = 2.46$

Fig. 1.10: The airfoils in RVR test and key results [7].

In 2009, at least three wind tunnel tests were conducted in the Glenn L. Martin Wind Tunnel with a 4.33-ft articulated rotor [8] (Fig. 1.11(a)). The objective was to study the autorotation of an unpowered rotor, which was of considerable interest for high speed compound rotorcraft such as the Heliplane project sponsored by DARPA [25]. The unpowered rotor test was up to an advance ratio of 2.0, and

test on powered rotor was conducted up to an advance ratio of 1.0. The test was conducted with low collective settings (from 0° to −2°) and rotor was not trimmed: most of the cases were taken with zero cyclic controls, and limited cyclic angles were applied when the advance ratio was above 1.6 to prevent excessive flap motion. Rotor performance and blade root motions were measured, and flow visualization was performed with a camera and tufts on the blades at $\mu = 1.7$. The performance results showed similar trends as the previous PCA-2 autogyro test [3], and expanded the test envelope for high advance ratio autorotation. The tufts visualized complex flow behavior on the retreating side (Fig. 1.11(b)), and revealed radial/yawed flow trends on the advancing side.

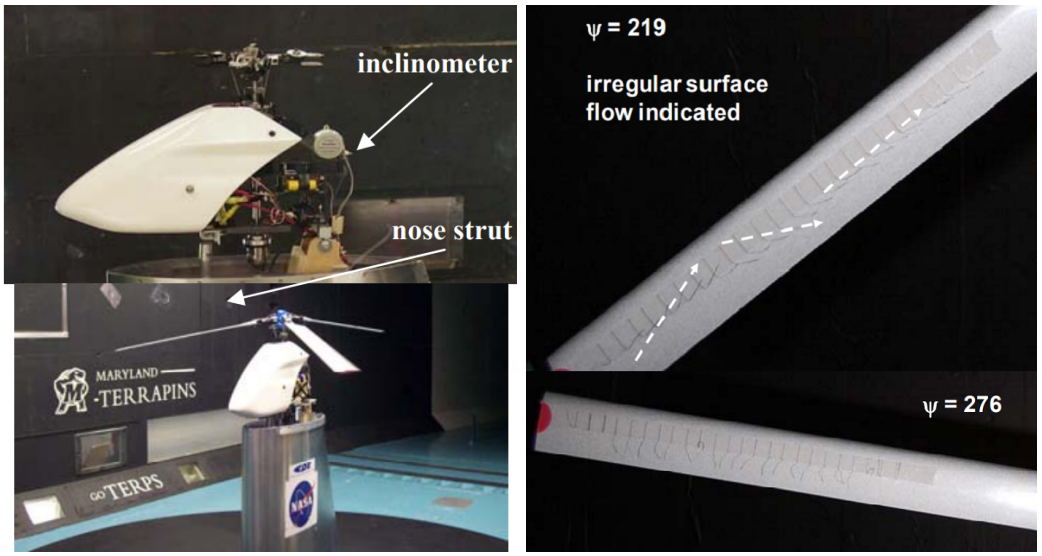

(a) Rotor setup in wind tunnel (b) Rufted blade in revere flow at $\mu = 1.7$

Fig. 1.11: The setup of 2009 autorotation test and key results [8].

In 2010, a full-scale UH-60A rotor was tested in the NASA Ames 40 by 80 ft wind tunnel [26] (Fig. 1.12(a)). The primary objectives were to acquire high quality comprehensive datasets to validate computational analyzing tools, and to

evaluate the differences between the wind tunnel test and flight test data. The test subject was the same rotor used in the 1993 UH-60A flight test with instrumented blades [27]. One blade featured 235 pressure sensors to measure airloads at 9 spanwise stations, and its opposite blade was instrumented with 26 strain gauge cells and accelerometers to measure structural loads and blade motions. Other measurements included steady and vibratory hub loads, shaft torque, control angles, blade displacement (along the whole span with photography), and the flow field was analyzed with Particle Image Velocimetry (PIV). The test was conducted at 100%, 65% and 40% nominal RPM, and a maximum advance ratio of 1.0 was achieved at 40% nominal RPM. Collective sweeps were performed at 0°, 2°, 4° shaft tilt angles, and the rotor was trimmed to minimize 1/rev flap angle.

(a) Wind tunnel test setup

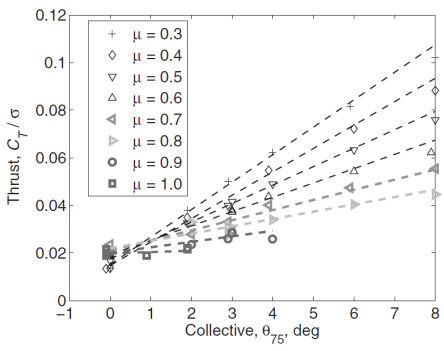

(b) Thrust results up to $\mu = 1.0$

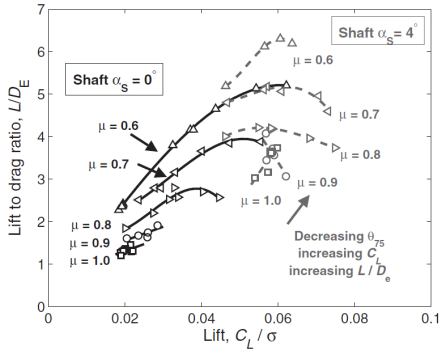

(c) L/D_e results up to $\mu = 1.0$

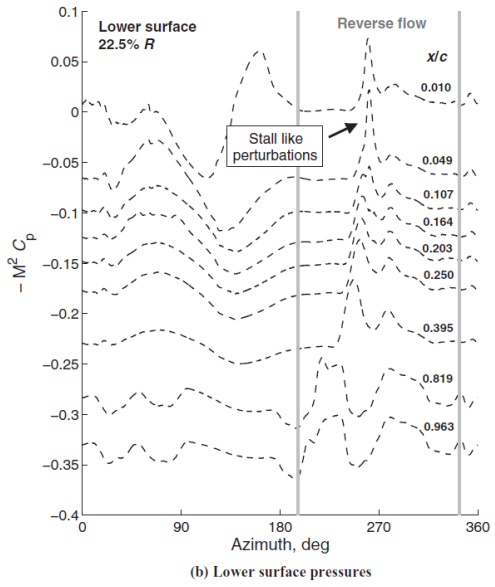

(d) Sample pressure data at $\mu = 0.8$

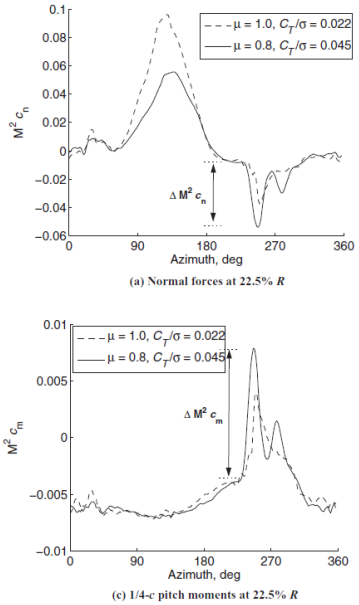

(e) Sample airloads at $\mu = 0.8$

Fig. 1.12: The setup of UH-60A test and key results [9].

The key results in performance, vibratory loads, and blade pressure/airloads were published in a subsequent paper [9]. These results were extensively used for correlation studies. The thrust reversal and the reduction of lift-to-drag ratio were noted, and a backward shaft tilt appeared to be effective to improve the rotor performance at high advance ratios (Fig. 1.12(b) and 1.12(c)). Blade pressure data revealed complex flow pattern on the retreating side at high advance ratios. Reverse flow induced separation from the trailing edge, forming a vortex propagating from trailing edge to leading edge on the lower surface (Fig. 1.12(d)). The pressure data were integrated along the chord to calculate sectional normal force, pitching moment, and chord force (Fig. 1.12(e)). An increment of blade loads was observed at high advance ratios, especially the 4/rev flap bending moment. For the torsional moment, a large impulsive peak emerged on the retreating side at high collective settings, which could be associated with the inboard pitching moment (see Fig. 1.12(e)).

From 2009 to 2015, a series of five wind tunnel tests were conducted in the Glenn L. Martin Wind Tunnel, achieving advance ratios up to 1.61 [1] (Fig. 1.13(b)). The main focuses were to create public-available experimental datasets at high advance ratios with simplified rotor configurations and to understand the fundamental aeromechanic phenomena on edgewise rotors in the unique flight regime. Two rotor geometries were studied, and blade geometry, mass distribution, and stiffness properties were all documented. One rotor had a 5.6-ft diameter, a NACA0012 airfoil, and was untwisted, and the other had a 6.0-ft diameter, a cambered SC1095 airfoil, and a -12° linear twist. Both of them were 4-bladed articulated rotor with no sweep nor taper. Steady and vibratory hub loads, shaft torque, control angles, blade root

motions were measured for all the tests, and later tests featured blade instruments to monitor structural loads and surface pressure.

The first two wind tunnel tests were conducted with twisted blades. The first test investigated the effect of variable RPM on performance and loads and reached an advance ratios of 0.66 [28]. The second test focused on flight conditions for compound helicopters (lower RPM and backward shaft tilt), and achieved advance ratios up to 1.2 [29]. Further wind tunnel tests used the untwisted blades and focused more on blade instruments. The third test was up to an advance ratio of 1.0, and the performance and vibratory loads data were compared with previous test results [30]. The fourth test was the first to incorporate blade embedded pressure sensors on the inboard blade section, but the sensor survivability was low and not much pressure data were obtained. Collective sweeps were performed up to $\mu = 1.04$, and an advance ratio of 1.41 was achieved with zero collective [31]. The last wind tunnel test was the most successful one, reaching a maximum advance ratio of 1.61 [32,33]. Collective sweeps were performed up to $\mu = 1.51$ (Fig. 1.13(b)), and blade surface pressures were successfully acquired to calculate sectional airload with limited sensor failures (Fig. 1.13(c)). As previously reported, the thrust reversal and evidence of reverse chord dynamic stall were observed in these tests. Difficulties in tracking and trimming occurred at high advance ratios, and it was unclear whether the measured 4/rev hub loads was due to the flight regime or the insufficient trim. This study was a direct predecessor of the current research.

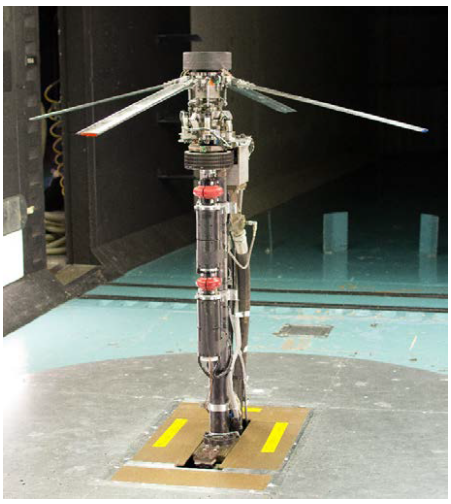

(a) Wind tunnel test setup (5th test)

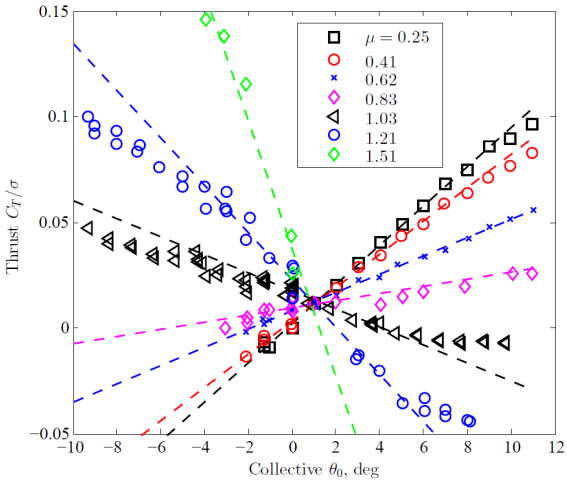

(b) Thrust results up to $\mu = 1.51$

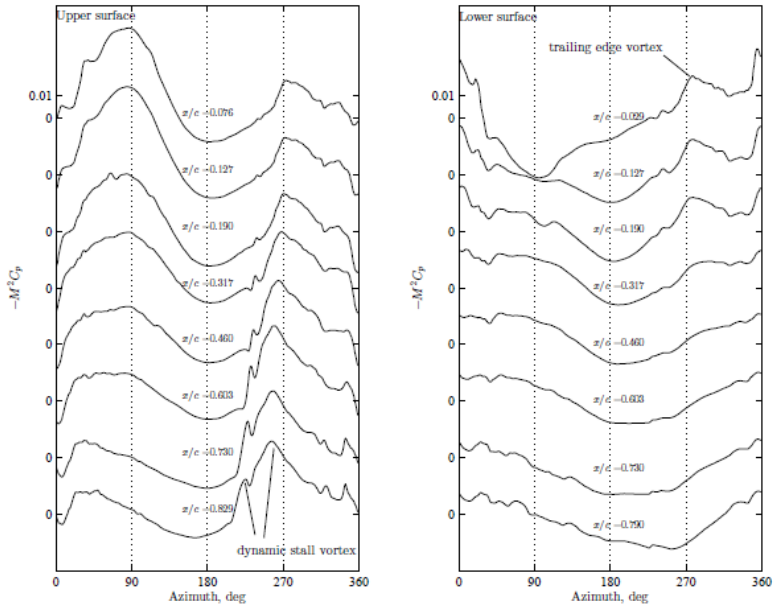

(a) Upper surface

(b) Lower surface

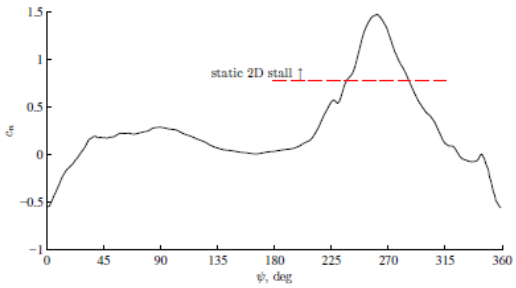

(c) Normal force coefficient

(c) Sample pressure and normal force at $\mu = 1.21$

Fig. 1.13: The setup of previous UMD test and key results [1].

From 2015 to 2019, three wind tunnel tests were conducted with a model AH-64 rotor at 24.5% scale in Boeing V/STOL Wind Tunnel [10], reaching an advance ratio of 0.72. Among these tests, two were isolated rotor tests, and one was carried out with a fuselage and various wing configurations (Fig. 1.14(a)). The majority of cases were taken with shaft angle sweeps at constant lift, and airspeed sweeps were performed for cross plotting and comparisons. During the test, rotor performance and control angles, hub loads, and blade motions were measured. In addition, the fuselage featured pressure taps, mini-tufts and off-body flow measurement. A wide range of lift sharing was explored, and the effects of lift compounding and rotor-wing interference were quantified (Fig. 1.14(b)). However, many figures in the paper were presented without coordinate scale for confidentiality reasons.

(a) Rotor setup in wind tunnel

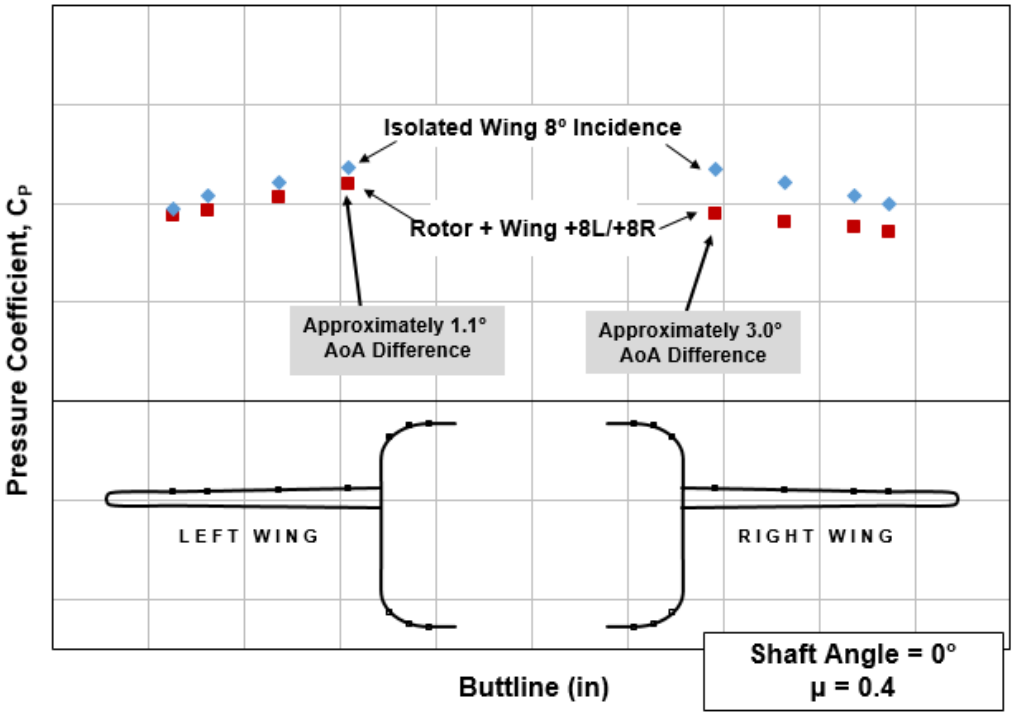

(b) Wing C_p change due to rotor effect

Fig. 1.14: The setup of AH-64 model rotor test and key results [10].

1.2.2 Computational Studies

An extensive correlation study was published [6] in 2008, comparing the results of three full-scale wind tunnel tests with the predictions of computational analyses. The objective was to demonstrate the improved capability of modern computational analyses at high advance ratios, and point out any persistent deficiency. The experimental results for the validation study were from the PCA-2 autogyro test [3], and the H-34 and UH-1 wind tunnel tests [23, 24]. Three comprehensive analyses (CAMRAD II [34], RCAS [35], CHARM [36]) and one Computational Fluid Dynamics (CFD)/Computational Structural Dynamics (CSD) coupled analysis (OVERFLOW/CAMRAD II [37]) were used to generate predictions, and the theoretical model in the PCA-2 test report [3] was used as baseline. The study focused on rotor performance, vibratory loads, and control angles. The results showed overall good thrust correlations and predicted the thrust reversal at high advance ratios. Significant improvements were observed in the lift-to-drag ratio predictions, where the baseline theoretical model made major overestimation. However, the data correlation degraded beyond an advance ratio of 0.62. None of the analyses accurately predict the shaft torque and the horizontal force at high advance ratios, which might be due to the lack of rotor shank aerodynamic modeling. Also, the author cast doubt on the reliability of the test data above 1.05 advance ratio for validation study, partially due to the trim condition.

Comprehensive Analytical Model of Rotorcraft Aerodynamics and Dynamics (CAMRAD) II was one of the most widely used comprehensive analyses for high

advance ratio rotors. In 2009, a correlation study [38] was published on the 15-ft teetering rotor test results [5]. A rigid blade assumption and a prescribed wake model were used in the study. The thrust correlation was generally satisfactory and the thrust reversal was predicted between advance ratios of 0.9 and 1.0, but offset-type errors were present for most of the results, and the data correlation degraded with backward shaft tilt. The in-plane force and shaft torque predictions showed correct trends, but with slope and magnitude errors. It was unclear whether these discrepancies were from the measurement or the simulation. In the same year, another correlation study [39] was published on the H-34 and the UH-1 rotor test results [23, 24]. The analyses implemented non-uniform inflow from a free wake model and unsteady aerodynamics, and the hub/shank drag was tuned. It was suggested that the underestimated power could be due to optimistic stall characteristics.

After the UH-60A high advance ratio test [26], a preliminary correlation study was conducted with CAMRAD II on 2012 [40]. The study used a simplified rotor model and focused on rotor performance predictions with zero shaft tilt. Correlation of trends was generally satisfactory up to an advance ratio of 0.7, but the magnitudes were not as well predicted and deteriorated at higher advance ratios. A more detailed analysis on UH-60A results was conducted later that year, with dual peak wake, yawed flow [41, 42] and hub/shank drag models included [11]. In addition to rotor performance, sectional airloads and blade loads were also predicted. The analysis showed an accurate prediction of thrust (Fig. 1.15(a)), and the total power prediction was improved with tuned shank drag (Fig. 1.15(b)). Only airloads at ourboard section (92% radius) and structural loads at midspan (50% radius) were shown in

the paper. The normal force prediction was satisfactory (Fig. 1.16(a)), while the pitching moment and flap bending moment were underpredicted (Figs. 1.16(b) and 1.16(c)), and the prediction of torsional moment lacked some high harmonic details (Fig. 1.16(d)).

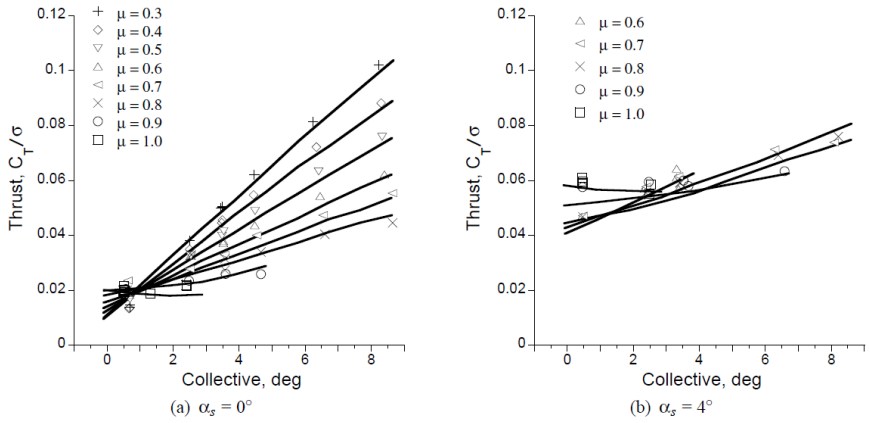

(a) Thrust at different shaft tilt

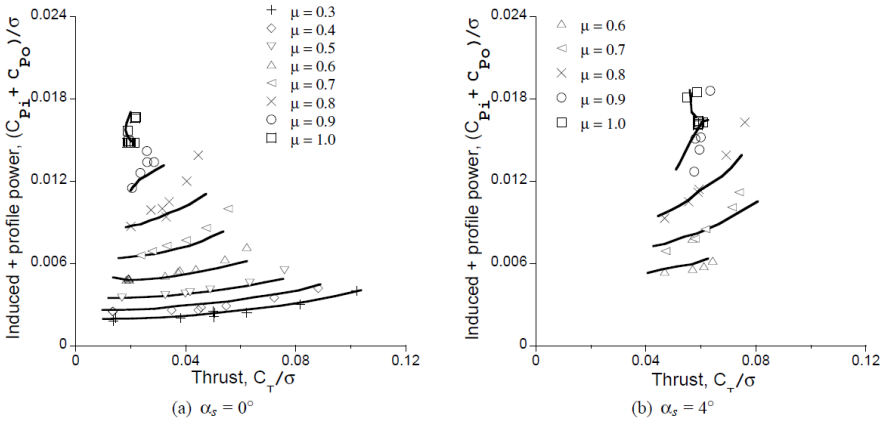

(b) C_P vs. C_T at different shaft tilt

Fig. 1.15: Key performance results of CAMRAD II correlation study on UH-60A [11].

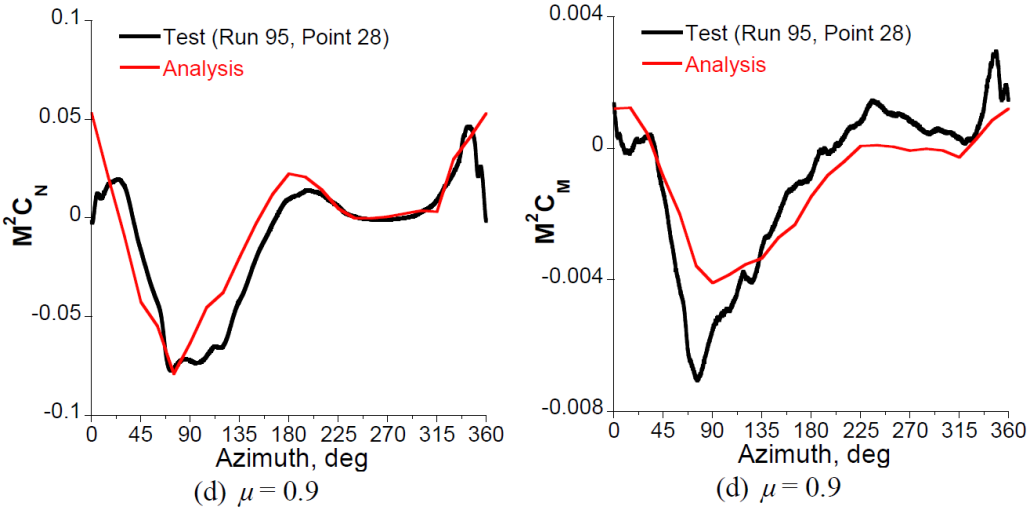

(a) Outboard normal force

(b) Outboard pitching moment

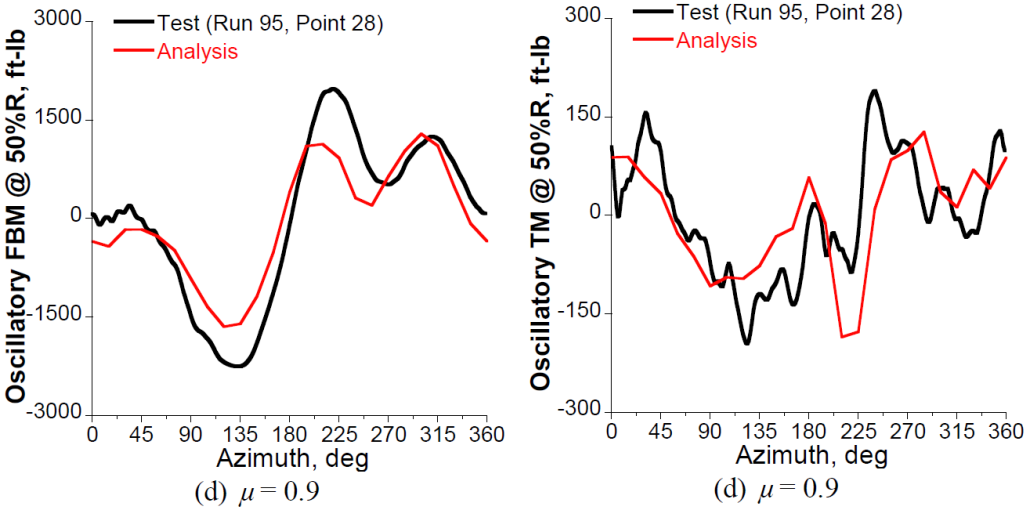

(c) Midspan flap moment

(d) Midspan torsional moment

Fig. 1.16: Key structural load/airload results of CAMRAD II correlation study on UH-60A [11].

From 2004 to 2012, correlation studies [12, 43, 44] were conducted with Rotorcraft Comprehensive Analysis System (RCAS) to investigate the data of the H-34, UH-1, and UH-60A wind tunnel tests [23, 24, 26]. These analyses focused on rotor performances, especially the induced power at high advance ratios. The preliminary analyses on H-34 and UH-1 results used a rigid blade assumption, and an

elastic blade model was included for later analyses on UH-60A results. Peters-He inflow model [45] was used for all the analyses. An analytical induced power model was developed from linear aerodynamic theory, using sectional airloads and induced velocities integrated along the span and azimuth to obtain the induced power. Through this exercise, one could compare the efficiency of three modes of controlling rotor thrust: collective pitch, disk angle of attack (shaft tilt), and blade twist rate (Fig. 1.17(a)). The effective lift-to-drag ratios were calculated by adding a simple model for profile power, and the angle of attack mode seemed to be more efficient at the critical advance ratio, where the thrust reversal occurs (Fig. 1.17(b)). It was also hypothesized that the critical advance ratio was sensitive to root cutout, because the inboard blade section in reverse flow generated negative thrust.

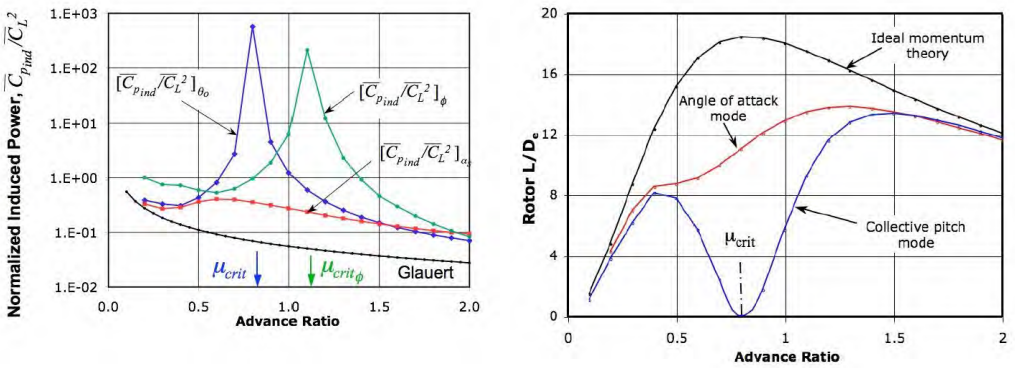

(a) Effects of different control modes on induced power

(b) L/D_e trends for a hypothetical rotor

Fig. 1.17: Key results of RCAS correlation study [12].

From 2013 to 2015, a series of correlation studies [13] were conducted progressively with an in-house comprehensive analysis, UMARC. The analysis is also used in the current research, and a detailed description can be found in chapter 4. The experimental results of the UH-60A test [26] and previous UMD tests [30, 31]

data were used for the validation study. The first stage of UH-60A rotor analysis emphasized the performance and load predictions, and various trailer types were attempted [46, 47]. The thrust slopes were correctly represented up to an advance ratio of 0.7, but offset-type errors were present, and the thrust reversal occurred earlier in the predictions than in the test results (Fig. 1.18(a)). Including a drag model for the blade shank and the effect of fuselage-induced upwash significantly improved the horizontal force predictions (Fig. 1.18(b)). The sectional normal force was accurately predicted in both magnitude and phase, while the pitching moment was poorly correlated. The flap moment prediction was accurate at some spanwise stations but generally underestimated the loads, and the torsional moment high harmonics were not captured. The next phase of UH-60A rotor analysis focused more on the reverse flow dynamic stall [48], and a modified Leishman-Beddoes dynamic stall model [49] was implemented in the UMARC. At moderate advance ratios, the dynamic stall was accurately represented and the airload correlation was improved (Fig. 1.18(c)). At 1.0 advance ratio, multiple shedding vortices were predicted, which also occurred in the test data but with phase offset. Yawed flow correction was applied to delay the reverse flow stall, improving thrust correlation at high advance ratios.

For the UMD test [46, 50], the thrust correlation was satisfactory up to an advance ratio of 0.83, but the thrust reversal was predicted only at low collectives. The author noted that the phenomenon was sensitive to reverse flow stall angles, root cutout, nose-down blade twist, and yawed flow corrections. Rotor horizontal force and shaft torque predictions were accurate but deteriorated at high advance ratios

because of the underpredicted reverse flow drag. 4/rev vertical hub load increased rapidly with advance ratio because of the proximity of second flap to 4/rev, and the in-plane vibratory loads were not well predicted. It was also shown that a fuselage model might be important for hub load prediction. Airloads correlation showed all the key features of the normal force. Wake interactions were predicted to be sharper than in the test data (Fig. 1.18(d)).

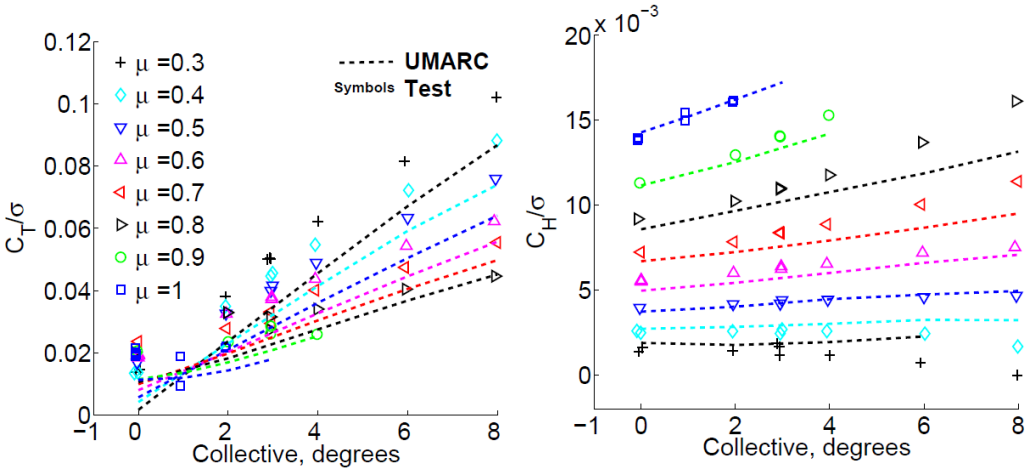

(a) UH-60A thrust

(b) UH-60A horizontal force

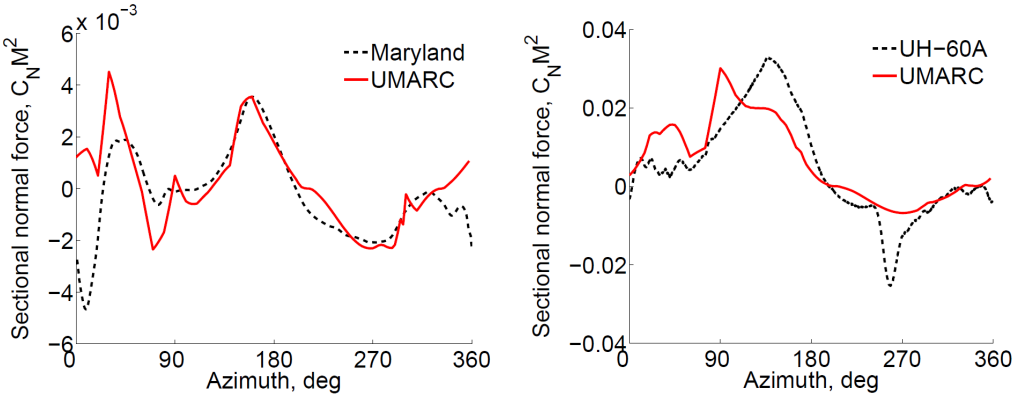

(a) Maryland, r/R = 30%, $\mu = 0.62$, $\theta_0 = 6.0°$

(b) UH-60A, r/R = 22.5%, $\mu = 0.60$, $\theta_0 = 7.8°$

(c) UH-60A inboard normal force

(d) UMD rotor inboard normal force

Fig. 1.18: Key results of UMARC correlation study [13].

In 2008 and 2010, researches on a hypothetical autorotating rotor were con-

ducted with the comprehensive analysis FLIGHTLAB [51, 52]. Compared to other mentioned analyses, these researches emphasized more on rotor trim and control in autorotation. Rotor control strategies were developed using variable shaft incidence to achieve rotor speed control, and using cyclic control to reduce hub moment. An isolated rotor model was analyzed first to establish a trim condition, then a coupled rotor-airframe model was used to extract a linear model by a perturbation method to predict the longitudinal and rotor-speed modes. Result showed that the rotor could be trimmed for zero hub-moments and zero-torque over a range of angles of shaft incidence (shaft tilt angle) to a freestream speed, but the control sensitivities could be very nonlinear. It was also shown that adjusting the shaft incidence angle was an effective way to control the thrust, and the hub moment trim results in a thrust reversal at an advance ratio of 1.0.

Since 2012, CFD/CSD coupled analyses were frequently used for correlation studies at high advance ratios, allowing flow field visualization and blade pressure comparison. A series of studies [14, 53] were conducted with Helios/RCAS [54] and OVERFLOW/CAMRAD II to compare with the UH-60A test results [26]. The objectives were to validate the analyses with experimental data and to complement test measurements and expand fundamental understanding of high advance ratio physics. The prediction of performance captured the overall trends but the terms with hub drag continued to be underpredicted. The airload results showed excellent correlation with normal force, but the pitching moment was not accurately predicted (Fig. 1.19(a)). The study was the first to visualize the flow field, showing complex interactions of vortices released from the tip, inboard stations, leading and trailing

edge and from the blade root (Fig. 1.19(b)). The CFD analysis also predicted dynamic stall on the reverse flow airfoil. In further Helios/RCAS correlation study, a model of the blade shank and root fixtures was included [55]. The results showed that the modeling of the shank region was critical for realistic drag prediction. The CFD/CSD analysis was more accurate than the baseline comprehensive analyses in drag and torque predictions.

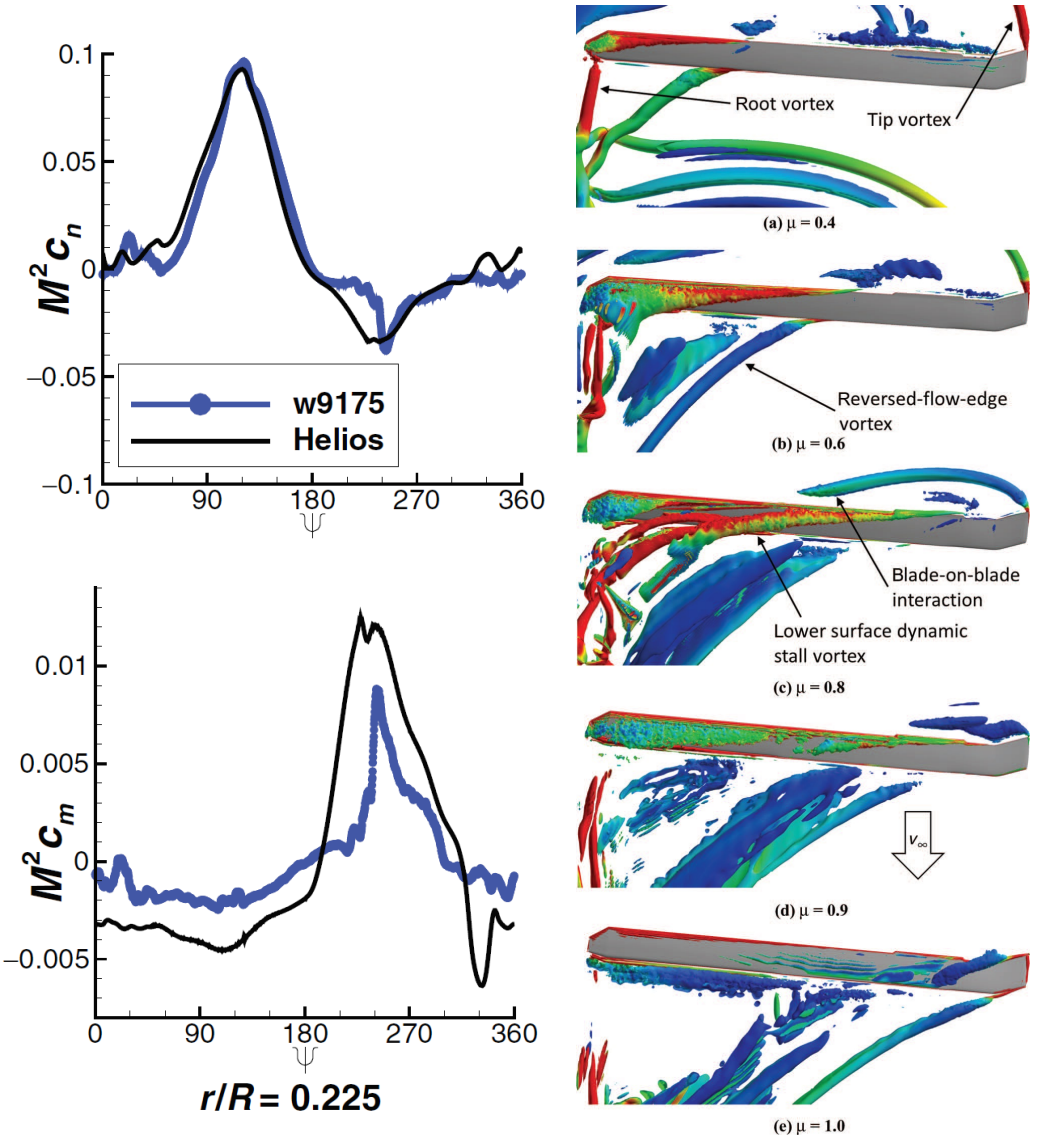

(a) UH-60A inboard airloads at $\mu = 1.0$ (b) Retreating side wake visualization

Fig. 1.19: Key results of Helios/RCAS correlation study on UH-60A test [14].

CFD analyses were conducted in several institutes with various analyzing tools. In 2014, a CFD/CSD coupled study was conducted with OVERFLOW/Dymore [56]. The 2011 autorotation test in the Glenn L. Martin Wind Tunnel [8] was used as a baseline in the correlation study, and both autorotation and powered modes were studied. Significant radial vortex interaction was observed at about 1.0 advance ratio, accompanied by high vibratory loads and increased trim sensitivity. In the same year, the UH-60A test rotor was modeled with a Hybrid Navier-Stokes-Free Wake methodology coupled with multibody dynamics [57]. Rotor performance, blade structural loads and airloads were presented, and the load distribution on the rotor disk was investigated. It was suggested that the rotor behaved like a low aspect ratio wing with highly non-uniform inflow, high induced drag and power at high advance ratios. In 2015 and 2016, two correlation studies were published, using rFlow3D to compare with the test results of the UH-60A wind tunnel test and the UMD test series [58, 59]. The analyses were pure CFD with prescribed blade motions, and the primary objective was to validate the capability of the CFD routine for future compound rotorcraft study at high advance ratios.

1.2.3 Summary of Previous Studies

Based on previous publications on the wind tunnel tests and computational analyses, some general conclusions can be made:

1. Model-scale rotor tests were conducted up to an advance ratio of 2.5, and full-scale tests were up to 1.1. Among the tests, the most notable one was the UH-60A rotor test in 2010, which provided comprehensive datasets of blade

structural loads and airloads. Early model tests were conducted at very high advance ratios, but the sensor sets were limited. Few wind tunnel tests featured blade surface pressure measurement, and tests with compound configuration were lacking.

2. Thrust reversal was observed at about 0.9 - 1.0 advance ratio, in which an increment of collective resulted in a reduction of thrust. At high advance ratios, intense reverse flow dynamic stall was presented on the retreating side, inducing high vibratory loads. Backward shaft tilt appeared to benefit rotor thrust and lift-to-drag ratio, and the impact was increasing with higher advance ratio. Also, difficulties in rotor tracking and trimming occurred at high advance ratios, reducing the reliability of experimental data at these extreme flight regimes.

3. Various comprehensive analyses were conducted for correlation studies, primarily using the full-scale tests. The thrust was the most accurately predicted performance component, and the thrust reversal was predicted by most of the analyses. Rotor shank drag modeling was critical for horizontal force and shaft power predictions, and needed to be tuned for better correlation. Generally, the performance predictions were more accurate at low and moderate advance ratios, and the correlation degraded rapidly beyond an advance ratio of 0.7. The structural loads and airloads were less accurately represented.

4. CFD analyses were also applied for correlation studies, usually coupled with comprehensive analyses for structural modeling. These analyses allowed flow

field visualization and direct comparison with surface pressure data. Also, a model of the blade shank and root fixtures could be included to model the aerodynamics without arbitrary tuning. Generally, the CFD/CSD analyses were more accurate than comprehensive analyses using lifting line theory, especially for the sectional airload prediction. The flow field visualization feature was helpful in inspecting dynamic stall vortex progression and vortex interaction.

1.3 Scope of Present Research

The current research focuses on two main objectives: to acquire reliable experimental datasets at high advance ratios with carefully-documented rotor properties, and to explore and understand the unique aeromechanic phenomena at high advance ratio flight regimes, including the dynamic stall in the reverse flow region, and the benefits from backward shaft tilt and lift offset. Both wind tunnel tests and data correlation studies were conducted to achieve these objectives.

In the experimental aspect of the research, a total of six wind tunnel tests were conducted progressively. All the tests were conducted with a 4-bladed rotors with a 33.5-in radius. The blades were constructed with carbon fiber and foam in a simple geometry (untapered and untwisted with a NACA0012 airfoil) to generate public-available datasets for validating studies. The nominal RPM was to match the tip Mach number of a full-scale helicopter, and the rotor was slowed to reach high advance ratios in the wind tunnel. The default measuring instruments included a 5-component hub balance, a shaft torque cell, swashplace displacement measure-

ments, optic/magnetic shaft encoders, a 3-component accelerometer, pitch/flap Hall sensors, and pitch link gauges. The tests were conducted with various fuselage configurations, and dynamic calibration were performed for each setup to correct the hub vibratory loads. Some wind tunnel tests were jointed with PIV studies, which results are presented in separate publications [60–62].

The first three wind tunnel tests were conducted with articulated rotors, with coincident flap and lag hinges at 16.5% radius. Pressure sensors and strain gauges were embedded under the blade skin in the first articulated rotor test. The test reached a maximum advance ratio of 1.15 and collective sweeps were carried out up to an advance ratio of 0.8. However, limited pressure data were obtained due to the failures of pressure sensors and a slipring [63]. The second articulated rotor test implemented pressure sensors and strain gauges with 3D-printed sensor mounts. The test was conducted up to an advance ratio of 0.8, and enough surface pressure data were acquired to calculate the sectional airloads through integration [64–66]. The third articulated rotor test featured non-instrumented blades with high structural similarity, and the on-hub pitch and flap angles were analyzed to quantify the error level. Baseline performance and hub load datasets were obtained up to an advance ratio of 0.9, and a shaft tilt study was conducted at $\pm 4^\circ$ [67, 68].

For later wind tunnel tests, the test stand was modified to accommodate a hingeless rotor. The blade grips were replaced by rigid steel blocks to remove the flap and lag degrees of freedom. The first hingeless rotor test was conducted without lift offset up to an advance ratio of 0.7. The main objectives of the test were to validate the structural integrity of the setup, and to test the trim method based on

the hub balance [69]. For further tests on hingeless rotors, a stub wing was installed on the retreating side, and the rotor was operated with lift offset, which enableds the rotor to generate more thrust on the advancing side. The maximum advance ratio was 0.7 among the tests with lift offset, and various wing angles of incidence, shaft tilt angles, and blade structural properties were tested [22].

In the data correlation aspect of the research, the test data were compared with the results of previous wind tunnel tests, comprehensive analyses and CFD/CSD coupled analysis. The high advance ratio UH-60A wind tunnel test in NASA Ames [9] and the previous wind tunnel tests in UMD [1, 32, 33] were primary data sources for the comparison. Two comprehensive analyses were used in the current study: UMARC generated most performance and load predictions with batch processing, while PrasadUM provided a ready-to-use interface for CFD coupling. Both analysis tools used a structural model based on the finite element analysis on an Euler-Bernoulli beam, and an aerodynamic model based on the lifting-line theory in conjunction with 2D airfoil look-up tables [70, 71]. In addition to the rotor analysis, a vortex lattice model AVL was used to represent the wing in hingeless rotor tests, modeling the influence of rotor wake on the wing by a downwash. The CFD analysis was performed with HAMSTR, an in-house Hamiltonian/Strand flow solver, and delta-coupling process was used for airload correction.

1.4 Contribution of Present Research

The current work contributes to refine the experimental datasets of an articulated rotor, to investigate the mechanics of the reverse flow dynamic stall by surface pressure measurements and CFD/CSD analysis, and to explore the performance benefits from a hingeless rotor with lift offset. Some key contributions are listed below:

1. Refined performance and hub load datasets were obtained in an articulated rotor test, which features non-instrumented blades with high similarity. The test was up to an advance ratio of 0.9, and a shaft tilt study was conducted at $\pm 4^{\circ}$. Data correlation study was conducted with comprehensive analysis to gain insights on the influences of advance ratio and shaft tilt angle. Results reveal that the thrust benefit from backward shaft tilt is dependent on the change in the inflow condition and the induced angle of attack increment.

2. In another articulated rotor test, pressure data at 30% radius were acquired to calculate the sectional airloads by surface integration. The experimental results of surface pressure data and sectional airloads were compared with the predictions of CFD/CSD analysis. The study provide some insights into the aerodynamic mechanisms that affect the rotor airload and performance, in particular the effect of hub/shaft wake and the formation of dynamic stall in the reverse flow region.

3. The test stand was modified to accommodate a hingeless rotor, and a wind

tunnel test was conducted without lift offset to validate the structural integrity of the setup, and the trim method using the hub balance readings only. For the hingeless rotor, the performance trends are found similar to those of an articulated rotor, but the blade structural loads (especially the 2/rev flap bending moment) are significantly higher, which poses a major structural constraint on hingeless rotor tests. Also, the in-plane hub load becomes predominant for a hingeless rotor.

4. In further tests, the hingeless rotor was tested with a compound configuration, in which a wing was installed on the retreating side. The rotor was trimmed to balace the rolling moment from the wing, inducing a lift offset. The results show that the rotor thrust, the rotor effective lift-to-drag ratio and the overall lift-to-drag ratio (rotor and wing) are significantly increased due to lift offset and lift compounding, while the shaft torque and the horizontal force are insensitive to the wing configuration. The trim with lift offset also induces 1/rev flap bending moment, further increasing the blade load level.

1.5 Overview of Dissertation

Chapter 1 introduces the background and motivations of investigating high advance ratio flight regimes. A literature review provides a state-of-art overview on high advance ratio research, including the previous wind tunnel tests and computational analyses. The scope and contribution of the current study are highlighted at the end of chapter.

Chapter 2 to 4 are about the methodology of the wind tunnel tests and the computational analyses. Chapter 2 focuses on the fabrication of non-instrumented and sensor-embedded blades. The static tests to characterize blade structural properties are also discussed. Chapter 3 introduces the instruments on the test stand and their calibration, as well as the procedures of hover test and wind tunnel test. Chapter 4 describes the comprehensive analyses UMARC and PrasadUM, the CFD analysis HAMSTR and its coupling method with the structural model, and the vortex lattice model AVL for wing analysis.

Chapter 5 and 6 present the wind tunnel test results, along with the computational predictions. The results of articulated rotor tests are shown in chapter 5, while those of hingeless rotor tests are discussed in chapter 6. The refined performance and hub load data from a high similarity blade set, the blade pressure and integrated airload data from blade-embedded pressure sensors, and the performance benefits of hingeless rotors from lift offset are the primary emphases in the result chapters.

Chapter 7 summarizes the current work, draws key conclusions, and recommends works for future research.

Chapter 2: Blade Fabrication and Evaluation

The blades used in the six wind tunnel tests share the same baseline design, yet different blade sets have unique characteristics to accommodate various test objectives. All of them are untwisted, untapered blades with a NACA0012 symmetric airfoil. The blade length is 28 in, and the chord length is 3.15 in (3 in with airfoil shape and 0.15 in trailing edge tap). The blade is composed of a foam core, a rectangular spar placed at 25% chord, counterweight pieces in the leading edge, and a carbon fiber skin. The technique of blade fabrication was developed in a previous research project [1], which used an aluminum two-part mold to shape the blade. The key blade components and a schematic diagram of the baseline design are shown in Fig. 2.1. A set of baseline non-instrumented blades was built for the third articulated rotor test to reduce blade dissimilarities and gain reliable performance and hub load datasets. The same set of blades was used again for the first hingeless rotor test. Non-instrumented blades were also used in the second and third hingeless rotor tests, but their constructions were slightly different to adjust the structural properties. Pressure sensors and strain gauges were embedded in the blades for the first and second articulated rotor tests, with two distinct fabrication methods.

Prior to hover test, the blades were subject to extensive tests to characterize

their structural properties. Blade stiffness and mass distribution were measured on bench top, and if a blade features embedded sensors, calibration of theses sensors were performed. Then, the blades were assembled with the blade grips for frequency tests. The rotor fan plot could be generated based on these results.

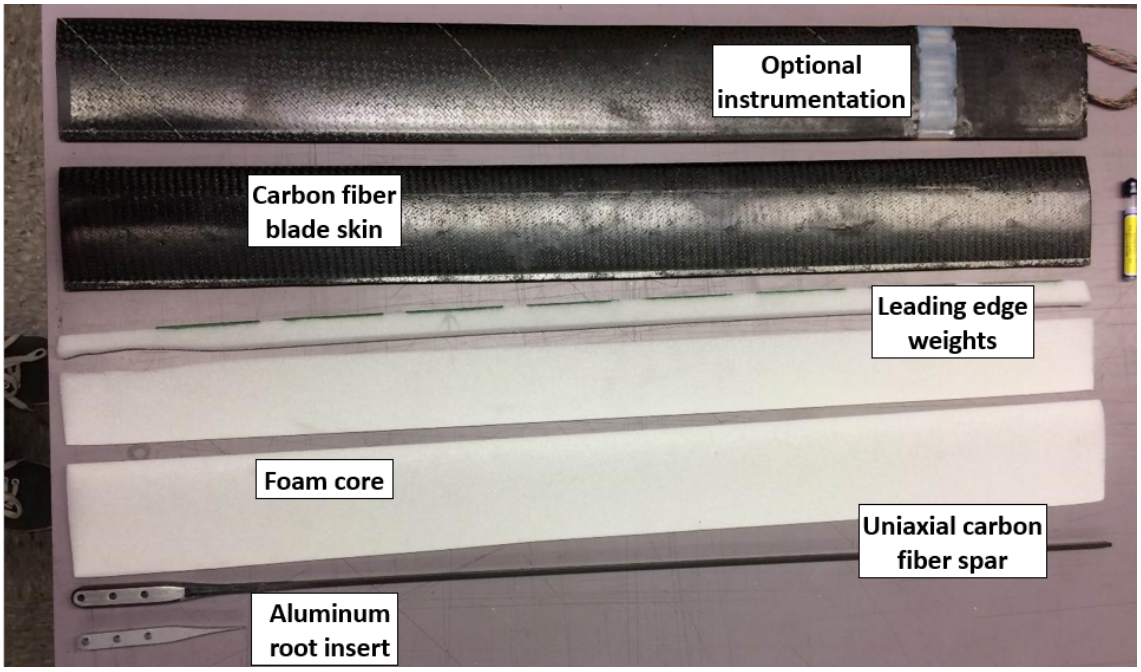

(a) Key components

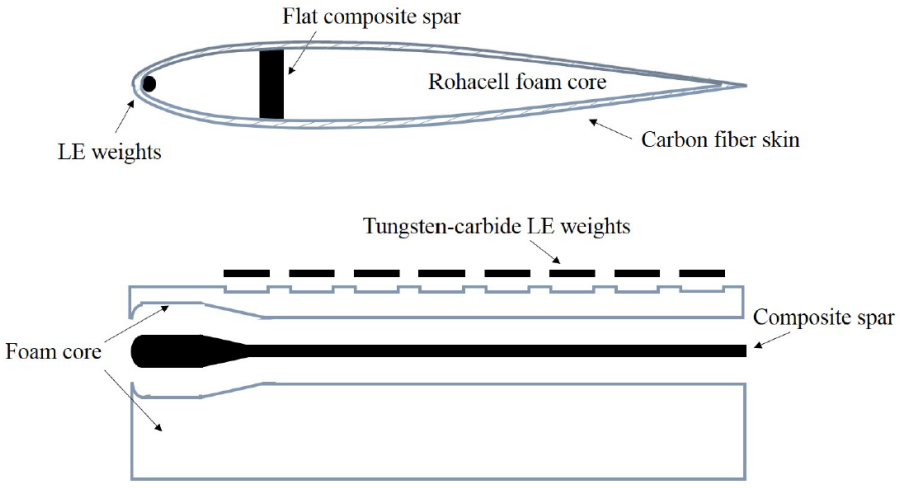

(b) Schematic diagram

Fig. 2.1: Structural components of a baseline test blade [15].

2.1 Non-Instrumented Blade Fabrication

For a non-instrumented blade, there are three key components: an uniaxial carbon fiber spar that bears axial and flap bending loads, a foam core that maintains the airfoil shape, and a $\pm 45°$ plain weave carbon fiber skin that provides torsional stiffness. In this section, the fabricating procedures of the three components are discussed in detail.

2.1.1 Spar Building

The first step of blade fabrication is building the spar (Fig. 2.2), which is made of an aluminum root insert piece and uniaxial carbon fiber strips. The spar provides attaching points for blade installation, and bears most of the axial and flap bending loads during the test.

1. Machine the root insert with CNC mill (Fig. 2.2(a)). The root insert provides attaching points to be bolted with the blade grip, and its teardrop shape prevents the uniaxial carbon fiber from splitting at the tip. The machining process involves drill bit and end mill, so it is crucial to keep the alignment consistent. First install the drill bit, phase down the aluminum slab to the correct thickness (0.32 in for the current design), zero the mill in X- and Y-directions, and mark the spots for the three through holes. Then switch to the end mill, touch the slab surface and zero Z-direction to cut the outer profile of the insert with G-code. Remove the insert from the slab, and finish the through holes.

2. Cut strips of uniaxial prepreg carbon fiber (IM8/Patz or IM6/3501-6). The original spar mold for baseline blades requires 8 strips of carbon fiber, while the new mold for stiffened blades requires 20 strips. The width of a strip should be slightly narrower than the mold slot (0.325 in width), and the length should be longer than two times of the blade length (0.32×58 in is an appropriate dimension for the current design). It is difficult to fit the strips into the mold if they are slightly wider, so a metal template is highly recommended for the cutting process. Always wear rubber gloves when handling prepreg carbon fiber and film adhesive to avoid greasing the material.

3. Clean the spar mold with acetone to remove any fiber or epoxy scrap, then spray mold release agent (Loctite Frekote) on the mold slots, coating the mold at least twice. If multiple blades are made in a batch, coat twice for the first blade and coat once from the second one.

4. Wrap film adhesive (Cytec FM300 or Loctite EA7000) on the side of the root insert. The adhesive improves the bonding strength between carbon fiber and other materials (metal or foam). Make an overlap at the tip of the root insert: the spot is vulnerable to axial blade load and tend to delaminate.

5. Wrap the carbon fiber strips on the root insert. First lay a strip in the mold slot to align it (do not remove the release liner yet), then fit the root insert in. Press the strip on the rear of the insert tightly and wrap it around to bond to itself in the mold slot. Use a roller on the release liner to help attaching and to remove any uneven spot or wrinkle. Pay extra attention to the rear

end, because the spot cannot be pressurized by the mold and all the pressure is from the tension along the carbon fiber. If the prepreg carbon fiber is not sticky enough to attach, use heat gun to warm it a little bit. Once the first strip is finished, lay the next strip in the mold, remove the release liner from the first strip and fit the strip-insert piece in, and repeat the process. After all the strips are finished, cut off some material from the spar tip so that the carbon fiber does not fill the whole mold slot, otherwise the spar will buckle after curing.

6. Close the spar mold. Use a large vice in the middle first to keep the two mold pieces parallel, and tighten the mold with 4-6 additional C-clamps. Then place the mold cap on the root insert and fix it with small C-clamps. Tight thoroughly to the two mold pieces, but do not apply too much force on the cap, otherwise it will be pressed into the spar structure, forming a weak spot at the tip of the root insert.

7. Cure the spar mold in the convection oven (Thermo Scientific Freas 645) at $350°F$ ($177°C$) for 150 min. When finished, use scissor, knife and sandpaper to remove excessive material and clean up the spar, and use dremel to cut the spar to the correct length (≤ 28 in to fit into the blade mold). Wear mask and thick gloves to protect against carbon fiber dust and sharp spikes at the edge of the spar.

8. Reinforce the spar at the weak spot to prevent delamination. Cut a piece of 1.5 in wide uniaxial carbon fiber and wrap it perpendicularly around the spar

at the tip of the root insert. Place the spar into the mold, repeat the curing process, and clean the blade again. Record the final weight of the spar 2.2(b).

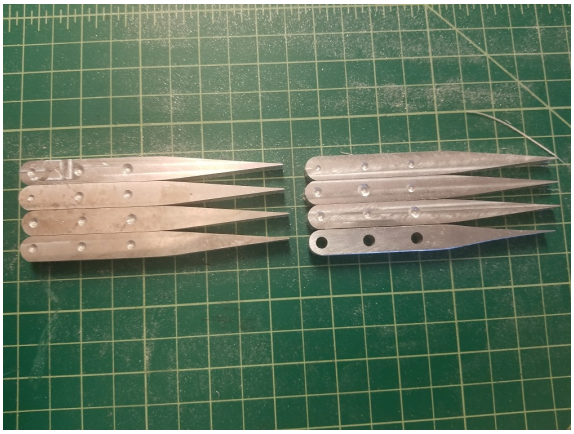

(a) Aluminum root insert

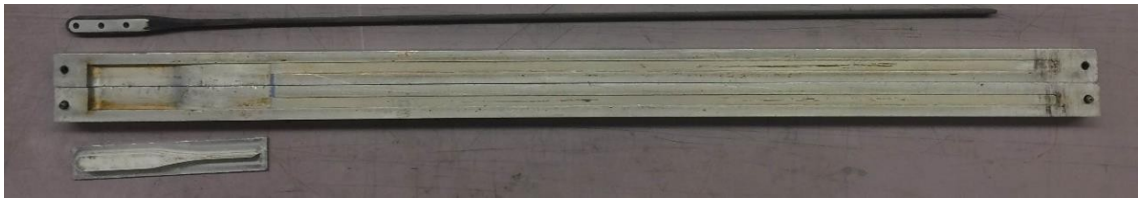

(b) Finished spar with the original mold

Fig. 2.2: Blade spar fabrication [15].

2.1.2 Core Fabrication

The next step is preparing the blade core, which maintains the shape of airfoil and provides some lag bending stiffness. The spar is hold in position with the foam pieces, and the leading edge weights are installed. Some pictures in the process are shown in Fig. 2.3.

1. Cut the foam piece to the size of the blade mold (3.15 × 28 in for the current design). 0.5 in thick Rohacell 31 foam sheet is frequently used because no additional processing is required. If using foam with higher density, the sheet

needs to be phased down or else the mold can be hard to close. One cut on the long edges must be straight and perpendicular to the sheet for the leading edge finishing, and the other cuts and dimensions do not need to be perfect because the piece will be trimmed afterward.

2. Set the foam piece in the mold (Fig. 2.3(a)) and close it. Press the foam piece towards the leading edge of the mold slot, lay the upper mold part on top of the foam and place the bolts to keep the two parts parallel. Look into the mold from the side to check if the foam is still on the leading edge side. If not, lift the upper mold part gently and press the foam again. It is absolutely important to make sure the foam piece is all the way to the leading edge, otherwise the leading edge geometry will not be precise and the piece needs to be discarded. After aligning the foam piece, tighten the bolts with impact wrench to close the mold. Always tighten the trailing edge first, because the foam need to be compressed more on that side. Then, tighten the bolts uniformly in an alternate pattern to avoid twisting the mold too much or applying too much torque on one bolt. Keep tightening until the mold is completely closed.

3. Heat up the wing mold in the convection oven at $350°F$ ($177°C$) for 90 min. This step is to release the strain in the foam core, otherwise it will bend in chordwise direction after the mold is open. When finished (Fig. 2.3(b)), trim off the tap material on the trailing edge with scissor or knife, only maintaining the airfoil shape (about 3 in chord). Sand the leading edge carefully, remove any ridge and make it straight and smooth: later steps require aligning against

the leading edge.

4. Cut the foam piece into two pieces at quarter chord for spar placement. First apply double-sided tape on the CNC mill table, align the foam piece with the leading edge and attach the tape, then push some wedge material from the trailing edge to stabilize the foam piece. Select end mill based on the spar thickness: 1/8 in diameter end mill can be used for the original spar, and 1/4 in diameter can be used for the new stiffened spar. Approach the leading edge with the end mill, stop and zero in chordwise direction when in contact. Then move the end mill to quarter chord and start the cut. Drawing a line along the cut beforehand is recommended so that one can stop immediately if something is wrong. After finishing the through slot (Fig. 2.3(c)), cut more space for the root insert part of the spar (lay the spar on the foam to draw a profile to help cutting).

5. Cut slots for counterweight pieces on the leading edge foam with a CNC mill. To choose appropriate material and dimension for the weights, assign the component mass in the blade Computer-Aided Design (CAD) model to adjust the center of gravity to quarter chord. In the current design, eight 2.5 in length, 9/64 in diameter tungsten carbide rods are used. Attach the leading edge foam on the CNC mill table upright with double-sided tape, zero Z-direction at the leading edge and cut the even-distributed slots with a slightly larger ball end mill (5/32 in for this design). The milling depth should be equal to the end mill diameter so that the weights can sit snuggly in the slots.

6. Install the leading edge weights (Fig. 2.3(d)). Wrap the weights with film adhesive (cover all the surface including the ends and no overlap is required), then insert them in the leading edge foam. If it is hard to press the weight into the foam, open the slot more with knife and vacuum it thoroughly. One may also bind the weights into the slots with film adhesive but it is optional. Weight the two foam pieces and record the weights (note that the leading edge piece is fragile with the weights installed, so hold it with both hands).

7. Wrap the two foam pieces and the spar with film adhesive (Fig. 2.3(e)). If multiple blades are being made, pair the components according to the weights so that each combination has roughly the same gross weight. For the two foam pieces, start from the cut surface and overlap there because the flat surface is easy to attach. For the spar, start from the carbon fiber beam and wrap the root insert section with a separate piece of film adhesive. If one is not able to continue the work immediately, the parts should be kept in refrigerator.

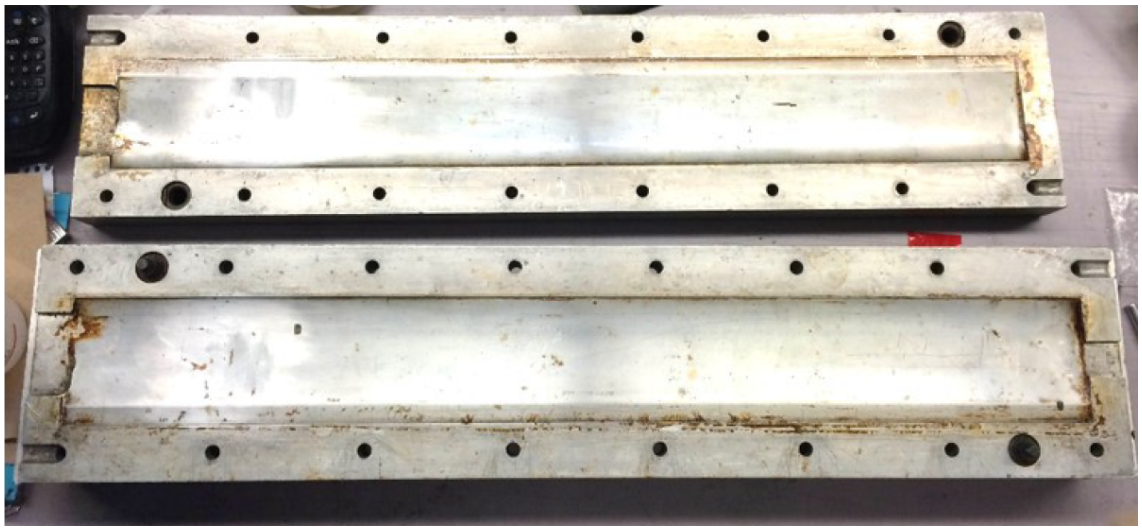

(a) Aluminum blade mold

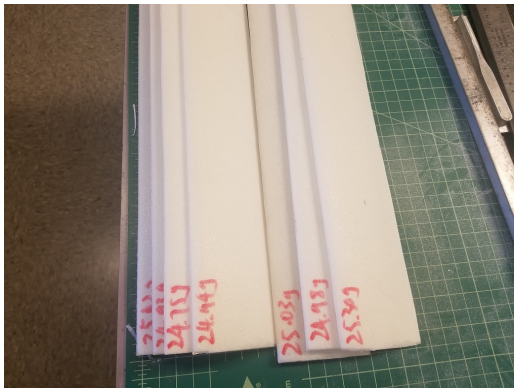

(b) Foam core shaped by the mold

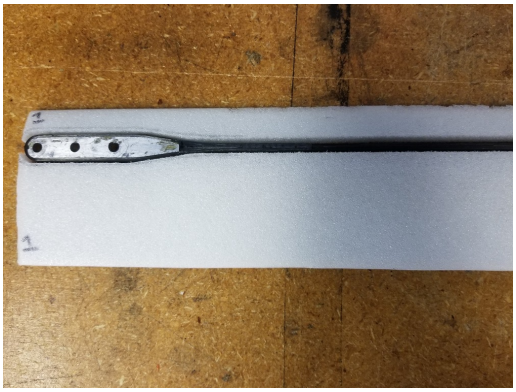

(c) Cut through slot for the spar

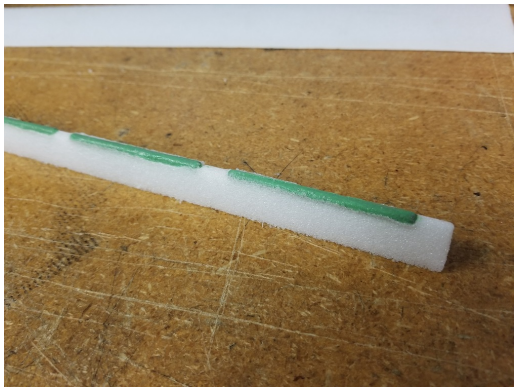

(d) Install leading edge weights

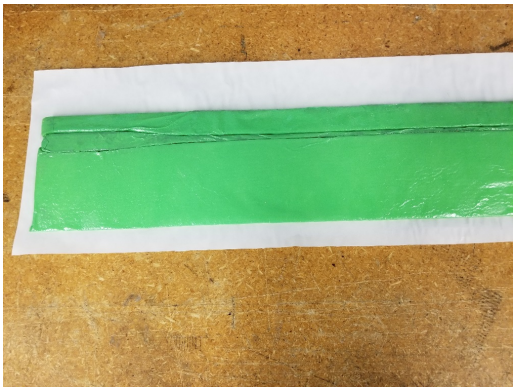

(e) Wrap with film adhesive

Fig. 2.3: Blade core preparation [15].

2.1.3 Skin Bonding

The final stage of blade fabrication is blade skin attachment. The ±45° plain weave carbon fiber skin holds the blade components together, and provides a major proportion of torsional stiffness for the blade. The intermediate steps are shown in Fig. 2.4.

1. Clean the workspace and the blade mold. In general, keeping the environment dust free is required for processing prepreg carbon fiber and film adhesive, and it is particularly important for a release foil, which is prone to static cling. Clean the mold with acetone to remove any fiber or epoxy scrap (mold release agent is not necessary because a release foil will be used).

2. Cut the carbon fiber skin (IM7/8552 or IM8/8552) and the release foil (Airtech Wrightlon 5200). Cut an oversized piece of plain weave prepreg sheet with ±45° fiber orientation. The orientation need to be accurate for torsional stiffness consistency, while the dimension is not as important (8 × 28.5 in is good for the current design). In a previous research [1], a layer of fiberglass was applied outside the carbon fiber skin to improve the surface finish. The fiberglass layer is optional, cut to the same size as the carbon fiber skin if needed. Then, cut a piece of release foil that is sufficient to cover the carbon fiber skin with some excess width. Lay the carbon fiber skin on the table and cover it with the release foil (lay the fiberglass layer in between if applicable), and go over with roller to remove any bubble or wrinkle.

3. Assemble the blade (Fig. 2.4(a)). First, align the two foam pieces and the spar from the root end and splice them together. Make sure no gap between these components. Then, lay the skin on the lower mold part, and keep it parallel with the mold slot (or else the blade loses torsional stiffness). Then, lay the core assembly onto the skin carefully. Always start from the leading edge at the root (the side with larger slot for passing wires is the root of the mold), then let the whole leading edge bond to the skin, and lay down the trailing edge at last. This needs to be finished at once because the core assembly and the prepreg skin are so sticky and are not possible to separate after attached. Next, wrap the skin tightly around the leading edge and bond to itself at the trailing edge.

4. Trim off excessive material from the trailing edge and sides (keep enough extra on the trailing edge so that the chord is at least 3.15 in), then close the mold as described in foam core preparation section. The mold should be much easier to close because it is already in airfoil shape, yet the leading edge alignment is still crucial.

5. Cure the blade mold in the convection oven at $350°F$ $(177°C)$ for 150 min. When unmolded (Fig. 2.4(b)), sand off the ridge at the leading edge to make the geometry smooth. Locate the the root insert holes and pierce the carbon fiber skin with punch, then open them up with knife.

6. Trim the blade to desired span and chord lengths with a CNC mill. Align and attach the blade onto the mill table, as described in foam core preparation

section. Then, cut the blade tip and trailing edge with an end mill. The chord length is self-explanatory because the leading edge always provides a reliable zeroing spot, while the geometry at the blade root can be undefined, so use the first spar hole as a clear reference. If multiple blades are made, fix them together with bolts to check their dimension consistency after cutting.

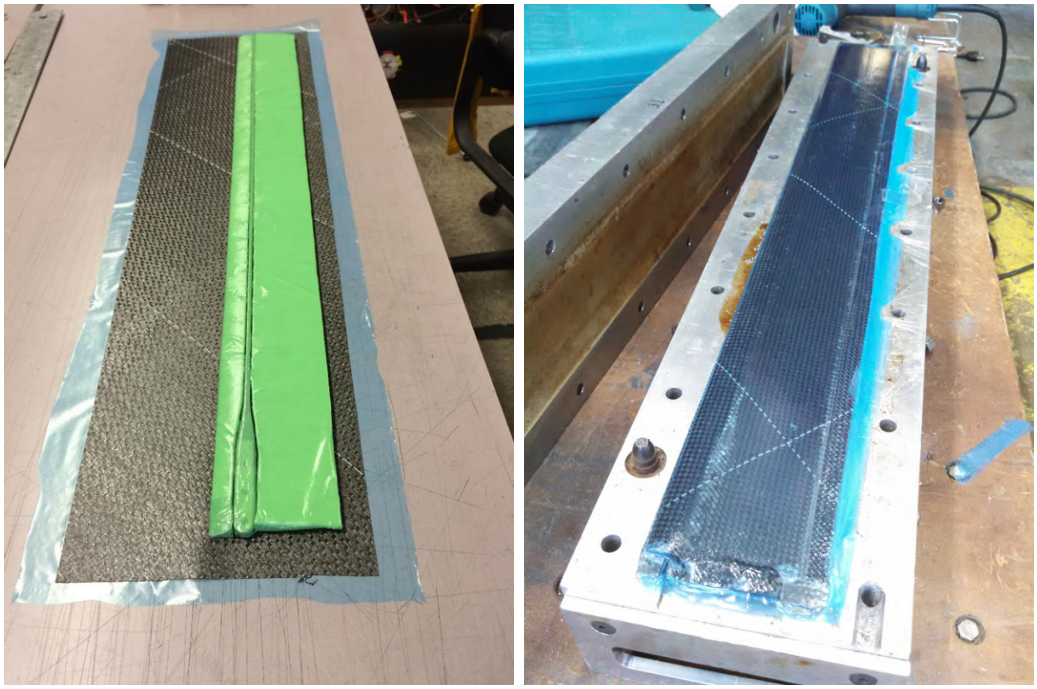

(a) Blade components before assembling (b) Unmolded blade with release foil

Fig. 2.4: Blade skin attachment [1, 15].

2.2 Instrumented Blade Fabrication

Except for the third articulated rotor test that emphasized blade similarity, all other wind tunnel tests featured blade sensors. Strain gauges are the most common blade sensors for monitoring sectional structural loads (Fig. 2.5). Usually, full bridges are used for temperature compensation: two pairs of side-by-side parallel

gauge cells for flap bending load (Fig. 2.5(a) and 2.5(b)), two pairs near the leading and trailing edges are for lag bending load (Fig. 2.5(a)), and two pairs with ±45° pattern for torsional load (Fig. 2.5(b)). These gauges are robust and compact in size, so they can be applied on the outer skin and wired up with enameled wires without affecting the airfoil geometry too much. If the blade structural integrity is a major concern (for example, a hingeless rotor test with high load level), it is recommended to bond the gauges on the outer surface of the blade without embedding, and secure the gauges and wires with a layer of epoxy coating.

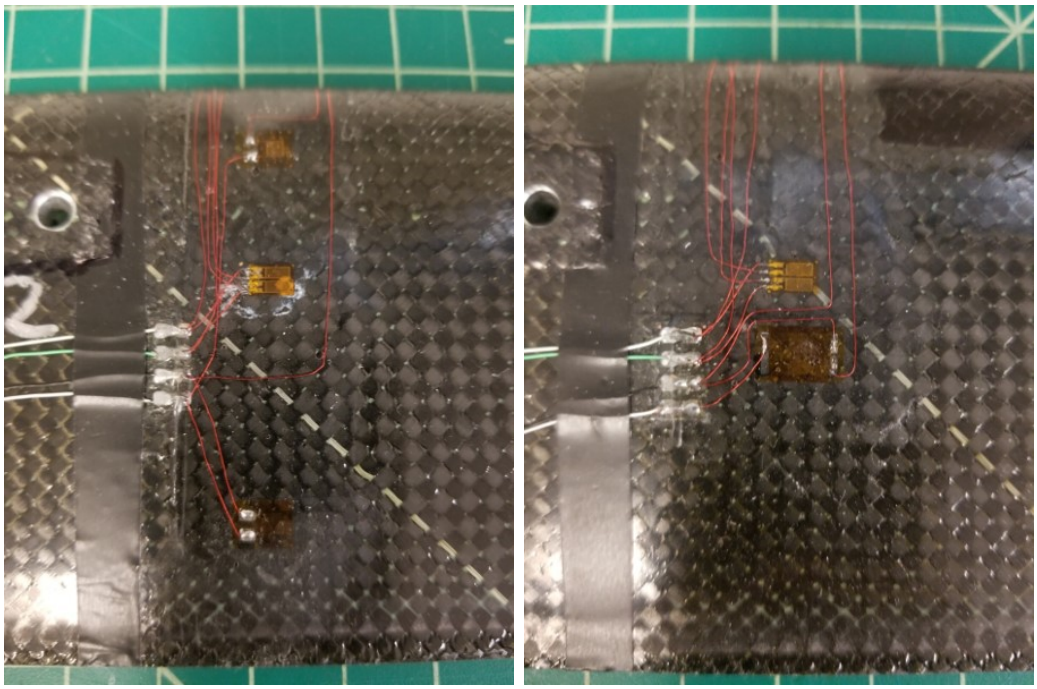

(a) Flap bending and lag bending (b) Flap bending and torsional

Fig. 2.5: Surface bonded strain gauge configurations.

Pressure sensors are used for capturing blade surface pressure data, which can be integrated into sectional airloads. In the first and second articulated rotor tests, full bridge miniature silicon piezoresistive sensors were implemented (Meggitt

Endevco 40931 Fig. 2.6). The Endevco sensor has similar basic functionality as the widely used Kulite LE-062 sensor, while the cost is only about 1/6 and the lead-in time is much shorter [1]. A bench top test showed that the Endevco sensor has comparable accuracy and frequency response as the Kulite sensor up to 250 Hz, although external compensation is required for temperature effect [72]. The sensors were initially supplied in die form with surface mounting pads (Fig. 2.6(a)). Then, they were shipped to Zentech Manufacturing to be mounted on custom designed Printed Circuit Boards (PCB) for wiring spots (Fig 2.6(b)). Unlike a strain gauge, the pressure sensor (plus the PCB) has a considerable thickness and the sensor chip is prone to shear off from the wiring PCB. Therefore, the pressure sensors need to be embedded in the blade, either directly under the carbon fiber skin, or within a 3D-printed mount.

(a) Sensor chip (mounting side up) (b) Sensor mounted on wiring PCB

Fig. 2.6: Endevco 40931 pressure sensor [1].

2.2.1 Sensor Under Blade Skin

The Endevco pressure sensor has a temperature limit of $212°F$ $(100°C)$, so it cannot survive the curing process for the prepreg carbon fiber. To embed the

sensors under blade skin, the blade core and the skin should be cured separately at first, and bond together with epoxy afterwards. The technique was used for the first articulated rotor test, and the specific steps are described as follows (see Fig. 2.7):

1. Prepare the spar and the blade core. The components are similar to those for a non-instrumented blade, so follow spar building steps 1-8 and core building steps 1-7 in general. In core building step 5, redistribute the slots for leading edge weights to keep them away from the sensor section (consider using counterweights with different dimension).

2. Cure the blade core. Follow skin bonding steps 1-6 in general, while in step 2, do not apply a carbon fiber skin. Use a prepreg fiberglass layer (Fibre Glast 7781 E-glass) instead to hold the blade components together. After curing, trim the blade core like a foam piece: remove the tab at the trailing edge, only keep the airfoil shape (follow core building step 3 instead of skin bonding step 6).

3. Use the blade core as a template to cure the blade skin. Follow skin bonding steps 1-6 again, while in step 2, use two layers of release foil to sandwich the carbon fiber skin. Cut oversized release foil pieces to prevent the skin from attaching to either the core or the mold. After curing, separate the carbon fiber skin from the blade core (Fig. 2.7(a)) and trim the skin to desired span and chord lengths. Also, clean the inner side of the skin with sandpaper and acetone.

4. Install pressure sensors/strain gauges to blade core/skin. Micro-Measurements

FTT-436 4-conductor wire is use to connect the sensors. The wire is extremely thin (36 AWG, 0.01 in diameter), and its multi-strand structure provide some resistance to blade deformation. For pressure sensor installation, solder the wires on the mounting PCB first. Then, cut sensor slots on the blade core with a CNC mill. Attach the blade core on the mill table with double-sided tape, then adjust the angle via the wedge block on the trailing edge to make the sensor slot tangent to the airfoil shape. Insert the sensors into the slots, and secure them with silicon gel. Also apply silicon gel at the boundary of the sensor section to keep out epoxy in the skin bonding step, and around each individual sensor ports to improve isolation (Fig. 2.7(b)). Meanwhile, puncture the blade skin at the sensor ports (a 3D-printed template can be helpful for locating the spots [1]). For strain gauge attachment, bond the gauges to the inner surface of the skin, then solder the wires (Fig. 2.7(c)). Do not pass wire to the other side through the leading or trailing edge, otherwise the wire will be pinched off in the mold. Instead, pass the wires to the root end and form bridge circuits outside the blade. Label all the wires before proceeding.

5. Bond the carbon fiber skin to the blade core in the mold at room temperature. Mix epoxy (West System 105/206) then brush on the inner side of the skin as uniform as possible. For pressure sensors, keep epoxy at least 1 in from the sensor section; for strain gauge, cover them with epoxy to improve strain transfer. After applying epoxy, align the skin in the spanwise direction and

straighten out the wires to the blade root, then press the core inside the skin carefully without any spanwise sliding (this is particularly important for a blade with pressure sensors, since sensors would not read correctly if misaligned with port holes on the skin). Wrap the assembly with release foil and load it into the mold (pass the wires through the slot on the root end). Then close the mold gently, do not apply too much clamping pressure to avoid damaging the sensors. Cure at room temperature for 24 hrs.

6. Post-proceed with the cured blade. Trim the blade, drill root insert holes, and remove excessive epoxy carefully. Pay extra attention when handling epoxy stick to the wires, since breaking a sensor wire is equivalent to losing a sensor. After all finished, check sensor resistances with multimeter and consider replacing the sensor if any abnormal reading occurs. Protect the pressure sensor ports with tape or a 3D-printed sheath.

The major advantages of the sensor mounting technique are relatively consistent structural properties along the span, improved blade surface finish (carbon fiber skin soaked with additional epoxy), and near-perfect airfoil geometry in the sensor section (the skin shape is uninterrupted). The disadvantages include mass inconsistency due to arbitrary epoxy coating, imperfect sensor placement due to manual handling, tendency to lose sensor when closing the mold for skin bonding, and difficult sensor replacement. To replace a pressure sensor, cut off the malfunctioned sensor with a CNC mill and insert a new one in the slot, then fix it with epoxy from below and secure it with epoxy and tape on top (see Fig. 2.7(d) at the

trailing edge). Do not try to remove a malfunctioned strain gauge; attach a new one on the outer skin instead. Blades fabricated with this method are significantly heavier than non-instrumented blades, resulting in lower Lock number.

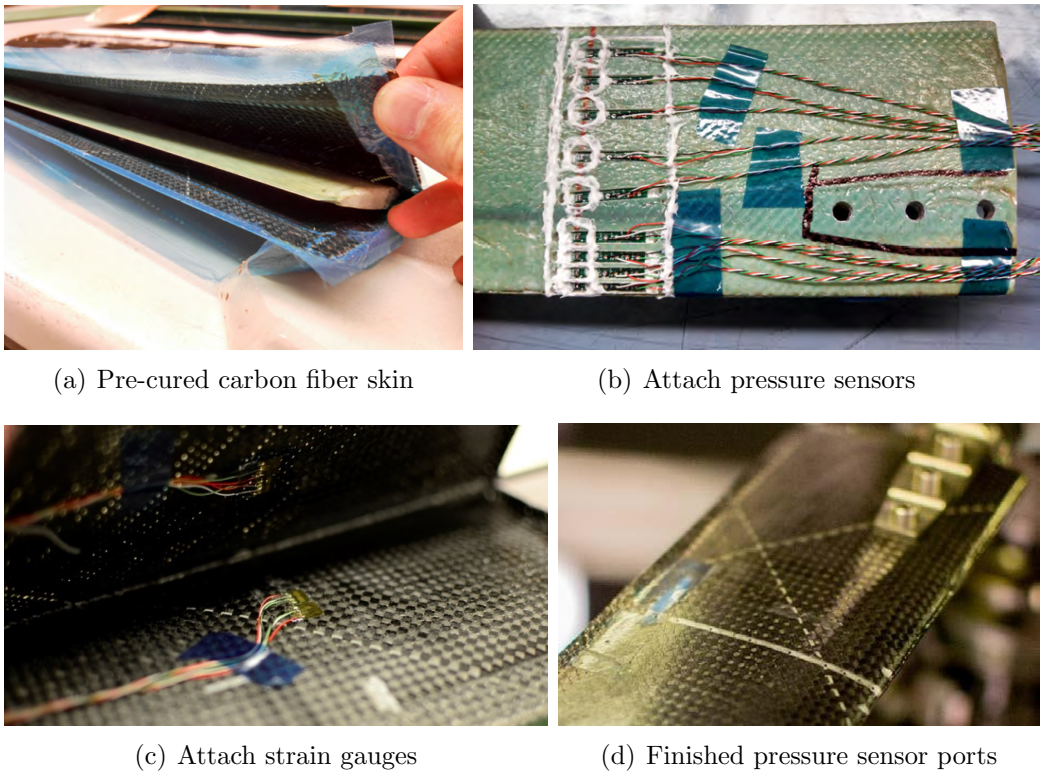

(a) Pre-cured carbon fiber skin (b) Attach pressure sensors

(c) Attach strain gauges (d) Finished pressure sensor ports

Fig. 2.7: Sensor installation under blade skin.

2.2.2 Sensor With 3D-Printed Pieces

Another sensor integration method is to place sensors above the carbon fiber skin. In the sensor section, the carbon fiber skin is further compressed with shims, and 3D-printed pieces are used to mount pressure sensor or enclose strain gauges (Fig. 2.8). The technique was used for the second articulated rotor test, in which enough pressure sensors survived to provide data for sectional airload integration.

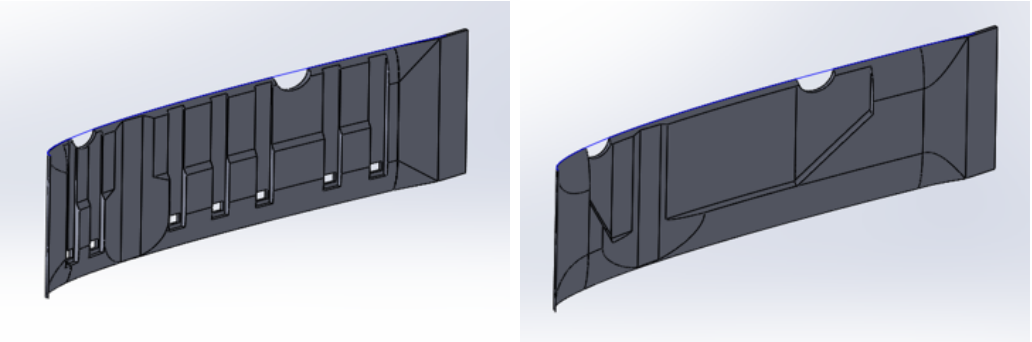

(a) For pressure sensor (b) For strain gauge

Fig. 2.8: CAD models of sensor mounts for 3D-printing.

1. Design and 3D-print the mounting pieces. The dimensions depend on the pressure sensor: the width should be slightly longer than the wiring PCB, and the thickness should be the sum of PCB and sensor chip thicknesses to ensure that the sensor chip is in plane with the blade surface after mounting. The edges of the mounting piece are smooth to fit the shimmed dent on the carbon fiber skin, and spaces for spar and wires are reserved (Fig. 2.8(a)). For structural consistency, similar geometry is used for strain gauge mounting piece, which features a pocket to enclose the gauges on the bottom side (Fig. 2.8(b)). The miniature features requires high resolution process, especially at the sensor ports. So, a photopolymer jetting printer (Objet Eden 350) is used to build the parts.

2. Prepare the spar and the blade core. Again, follow spar building steps 1-8 and core building steps 1-7 in general. In core building step 1, cut slots on the foam piece to embed wires. Use 1/8 in diameter end mill to cut slots with 1/8 in depth on leading and trailing edges, both sides of the core. Pass the wires

through (Micro-Measurements FTT-436 is still the best option), lay at least one spare wire in each slot, and keep enough lead length for sensor attachment. Then, cut $1/8 \times 1/8$ strips in from a scratch foam to insert into the wire slots, and compress until flat. Separate the lead wires and secure them with tape towards the root end. In core building step 5, redistribute the counterweight slots away from the sensor section.

3. Assemble the blade with shims to make dents in sensor section. Follow skin bonding steps with steps 2 and 3 modified. This time, do not attach the carbon fiber layer with the release foil at first. Adjust the interwoven fiber to pass the lead wires through the skin, then wrap the fiber to the blade core. Separate the lead wires and tape them towards the root end (also put some tape under the wires to insulate epoxy from the prepreg). Then, wrap the release foil and remove any bubble or wrinkle with roller. Prepare some soft brass shims with the width of the mounting piece and the length from the spar aft to about 85% chord (do not make them all the way to the trailing edge to prevent mold damaging). Lay shims until the thickness is similar to the mounting piece, then fix them right aft the spar with tape, and do exactly the same on the other side of the blade. Do not try to attach shims near the leading edge: they will shove the whole blade backward and affect leading edge geometry. Then close the mold and cure as a non-instrumented blade, and perform the regular trim. Cut off the carbon fiber skin near the leading edge and make enough space for the mounting piece: start the cut with end mill and finish with knife

and sand paper, and check the fitness frequently by laying a mounting piece on top to avoid cutting too much material off. A finished sample section with dents is shown in Fig. 2.9(a).

4. Reinforce the sensor section with additional carbon fiber. In the sensor section, the $\pm 45^\circ$ carbon fiber skin is cut on the leading edge and compressed on the trailing edge, which induces a significant torsional stiffness loss. To compensate the loss, the sensor section is reinforced with an additional layer of $\pm 45^\circ$ carbon fiber. Because the geometry is complicated, the reinforcement is applied with normal carbon fiber and a vacuum bag, instead of prepreg carbon fiber and a mold. Cut carbon fiber to wrap the sensor section with at least 1 in margin on each side, pass the lead wires through the fiber (follow the last step to secure them), then apply epoxy (West System 105/206) on the top uniformly. Next, make a vacuum bag with teflon foil and Tacky Tape, drain the air with a vacuum pump and cure for 24 hrs. Remove excessive epoxy carefully afterwards (pay attention to the wires).

5. Implement pressure sensors or strain gauges. For pressure sensors, first attach them to the 3D-printed piece with epoxy, and apply silicon gel on the side for insulation (Fig. 2.9(b)). Then, support it upright on the blade, and solder the wires from the bottom carefully (Fig. 2.9(c), this is a challenging process, using a good soldering iron tip with flux is recommended. For strain gauges, attach them on the reinforced dents directly (Fig. 2.9(d)), and connect them as surface-bond gauges (Fig. 2.9(e)). Also, form bridge circuits for strain gauges

at the blade root.

6. Attach the mounting pieces to the blade. Apply epoxy on the spar, the edges of the mounting piece, the back of the pressure sensors, and on top of the strain gauges, and fit the piece to the blade dent. Pay extra attention on the pressure sensor ports to avoid epoxy stain. When finished, fill epoxy in any gap and smooth out the geometry of the leading and trailing edges, and use teflon tape to flat out the epoxy drop and maintain the shape. Protect the pressure sensor ports with a 3D-printed sheath. The finished sensor sections are shown in Fig. 2.9(f).

The technique with 3D-printed mounting pieces is more robust yet less delicate than the other technique. The technique guarantees high sensor survivability and allows simple sensor replacement if needed. Also, it involves minimal manual handling (epoxy applying, sensor slot cutting) so the mass consistency and sensor placement accuracy are improved. However, the reinforced sensor section also induces some problems. With an additional layer of carbon fiber and extra epoxy, the section is 10% to 12% thicker than the normal section, and the structural properties variance becomes larger between the sensor section and the normal section (see Table X). The blade surface finish is comparable with a non-instrumented blade.

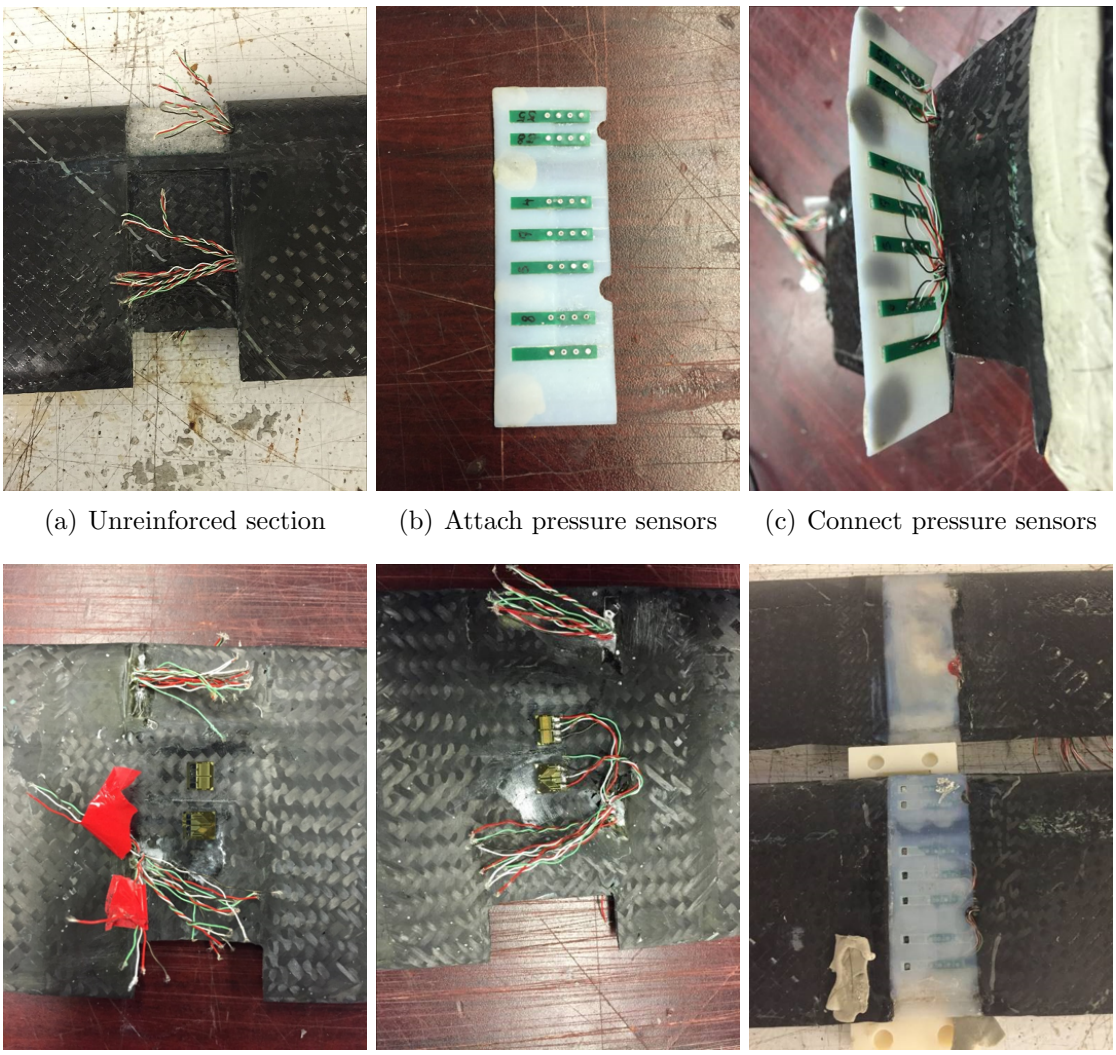

(a) Unreinforced section (b) Attach pressure sensors (c) Connect pressure sensors

(d) Attach strain gauges (e) Connect strain gauges (f) Finished sensor sections

Fig. 2.9: Sensor installation with 3D-printed pieces.

2.3 Blade Property Evaluation

For finished blades, bench top tests should be performed before the hover test. Blade stiffness parameters were measured by static displacement tests and rap tests (the strain gauges are calibrated at the same time). The blades were subject to spanwise and chordwise balancing, and the flap/lag moments of inertia were characterized by pendulum tests. The blade grip properties were analyzed

with a CAD model, and rap tests were performed for the blade-grip assembly. With these structural properties measured, the rotor fan plot could be generated by a comprehensive analysis. Other blade tests included pressure sensor calibration and tensile load test for the spar.

2.3.1 Blade Stiffness

The blade was relatively soft for flap and twist deformations, so the stiffness could be determined by static displacement tests (Fig. 2.10 and 2.11). Airfoil-shaped clamp blocks were applied to the tip and root of the blade. Then, the blade was cantilevered with the clamp at the root, and weights were applied on the clamp at the tip (Fig.2.10). A height gauge was used to monitor the vertical displacement, and the measurements were made at the fore and aft edges of the blade tip clamp and averaged to reject the error from twist deformation. The process was repeated with various loads at the tip clamp to get multiple data points. During the time, the flap bending gauges were connected for calibration. Treat the blade as an Euler-Bernoulli beam to calculate the stiffness, and use appropriate force arm for flap gauge calibration:

$$\Delta w = \frac{F l_{beam}^3}{3 E I_y} \tag{2.1}$$

$$M_{flap} = F l_{gauge} \tag{2.2}$$

where Δw is the tip vertical displacement, l_{beam} is the length of the cantilever

beam (from the cantilever beam root to the tip load position, measured at the tip clamp midpoint), l_{gauge} is the spanwise length from the strain gauge to the tip load, F is the applied tip load, EI_y is the flap bending stiffness, and M_{flap} is the flap bending moment. For strain gauge calibration, only the slope is important, and the offset can be tared out during the test. If the blade properties between the normal blade section and the sensor section are significantly different, apply the root clamp outboard to characterize the normal section first, then clamp inboard right next to the sensor section and assume the blade as a jointed Euler-Bernoulli beam to calculate the stiffness of the sensor section (the subscript normal indicates the normal blade section, and sensor indicates that of sensor section):

$$\Delta w = \frac{Fl_{normal}^3}{3EI_{ynormal}} + \frac{Fl_{sensor}^3}{3EI_{ysensor}} + \frac{Fl_{sensor}^2 l_{normal}}{2EI_{ysensor}} \tag{2.3}$$

Fig. 2.10: Blade flap bending stiffness static test setup.

For torsional stiffness measurement, A rigid carbon fiber bar was attached to the tip clamp in chordwise direction to apply the torque (Fig. 2.11). Various weights were attached to the bar at the the leading edge and trailing edge ends, and the vertical displacements at the two ends were measured by the height gauge to calculate the twist angle. Also, torsional strain gauges were connected for calibration. Treat the blade as a torsional rod to derive the stiffness, and calculate the torsional moment for gauge calibration:

$$\Delta\phi = atan(\frac{\Delta w_{TE} - \Delta w_{LE}}{l_{LE} + l_{TE}}) = \begin{cases} -\frac{Fl_{LE}l_{beam}}{GJ}, & \text{for leading edge load} \\ \frac{Fl_{TE}l_{beam}}{GJ}, & \text{for trailing edge load} \end{cases} \tag{2.4}$$

$$M_{torsion} = \begin{cases} -Fl_{LE}, & \text{for leading edge load} \\ Fl_{TE}, & \text{for trailing edge load} \end{cases} \tag{2.5}$$

where $\Delta\phi$ is the tip twist angle, Δw_{TE} and Δw_{LE} are the vertical displacements of the torsional bar at the leading edge and trailing edge ends, l_{TE} and l_{LE} are the chordwise distances from the blade structural center to the torsional bar ends, GJ is the torsional stiffness, and M_{lag} is the lag bending moment. Note that the blade structural center may not be at quarter chord: find the exact position by adjusting l_{TE} and l_{LE} to match the stiffness results from leading edge and trailing edge loads. The blade was considered as a jointed torsional rod to measure sensor section property individually, following the same procedure as flap bending stiffness

measurement:

$$\Delta\phi = atan(\frac{\Delta w_{TE} - \Delta w_{LE}}{l_{LE} + l_{TE}}) = \begin{cases} -\frac{Fl_{LE}l_{normal}}{GJ} - \frac{Fl_{LE}l_{sensor}}{GJ}, & \text{for leading edge load} \\ \frac{Fl_{TE}l_{normal}}{GJ} + \frac{Fl_{TE}l_{sensor}}{GJ}, & \text{for trailing edge load} \end{cases} \tag{2.6}$$

Fig. 2.11: Blade torsional stiffness static test setup.

The blade was significantly more rigid in lag bending than in flap bending, making it infeasible to measure on tip displacement directly. Therefore, a rap test was carried out to determine the lag bending stiffness from frequency. The strain gauges in lag direction were used for frequency measurement (for non-instrumented blade, apply surface-bond lag gauges after wind tunnel test, or use a magnet-Hall sensor combination). Connect the lag gauges and cantilever the blade only at the

root, tap the blade tip at the leading edge and record the data. Then, a Fast Fourier Transform (FFT) analysis was carried out to identify the primary lag frequency, and the stiffness could be calculated. The calibration process of lag gauges was similar to that of flap gauges, the tip clamp was attached to apply weights in lag direction:

$$f = \frac{K}{2\pi}\sqrt{\frac{EI_z}{ml_{beam}^4}} \tag{2.7}$$

$$M_{lag} = Fl_{gauge} \tag{2.8}$$

where f is the measured primary lag frequency, m is the blade mass per unit length, EI_x is the lag bending stiffness, and K is 3.52 for the first bending mode [73]. Note that the length for stiffness measurement is up to the blade tip (the tip clamp should not be used), and the length for gauge calibration ends at the midpoint of the tip clamp. For lag bending stiffness, all blades were considered as uniform beams and no specific parameter was assigned for sensor section.

2.3.2 Blade Mass Distribution

For non-instrumented blades and blades with only surface-bond strain gauges, the mass distribution was usually considered as uniform. The weights of the aluminum root insert and the bolts were counted into the blade grip mass. For blades with embedded sensors (especially for the ones with 3D-printed mounts), the blade mass was divided into different components to assign the distribution properly. An example weight breakdown is shown in Fig. 2.12, where the elements are for the

structural mesh in comprehensive analysis.

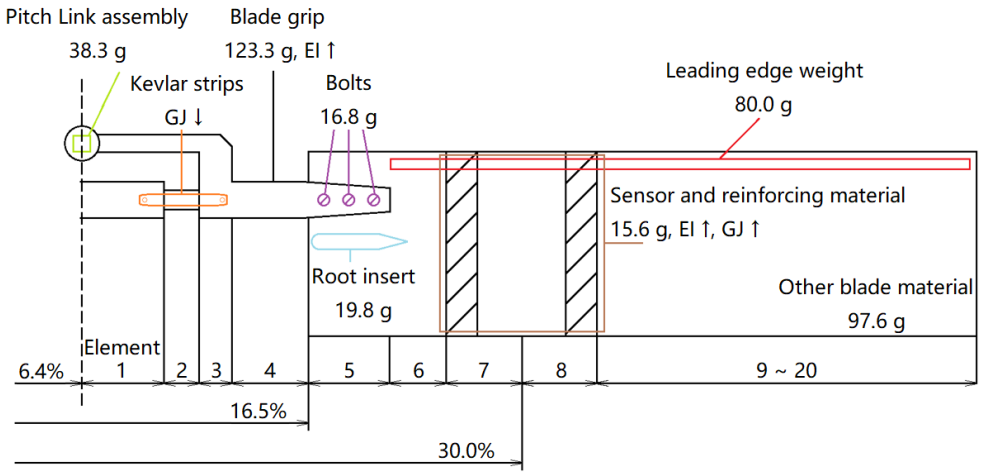

Fig. 2.12: The weight breakdown and structural mesh of a blade with embedded sensors.

The blades were subject to spanwise balancing and chordwise balancing (Fig. 2.13). If the rotor center of mass is misaligned with the center of rotation, a 1/rev hub load occurs due to centrifugal force, which is proportional to the square of the rotor RPM. To avoid the load and alleviate hub vibration, the blades were balanced in pairs on a needle-edged pivot in a seesaw manner (Fig. 2.13(a)). To achieve a balance, a small piece of aluminum tape was attached to the tip of lighter blade to adjust the center of mass. If that is not sufficient, epoxy is injected into the foam core near the blade tip. Meanwhile, the chordwise center of mass should be slightly ahead of the aerodynamic center (quarter chord) to prevent aeroelastic instabilities. To ensure that, each blade was balanced on a smooth metal bar to measure the chordwise position of mass center (Fig. 2.13(b)). At least one spare blade was built, in case of a blade failed to balance with others or had an unacceptable mass center. If more than four blades were qualified, the four with the most similar structural

properties were selected. Reflecting tapes of different color were attached to the blade tip with epoxy to identify each blade during the tracking process (discussed in chapter 3). The structural properties of the blades in all six wind tunnel tests are summarized in Table 2.1. Note that the third articulated test and the first hingeless test shared the same set of blades, and similar structural properties were used as the normal section properties for the second articulated test in analyses.

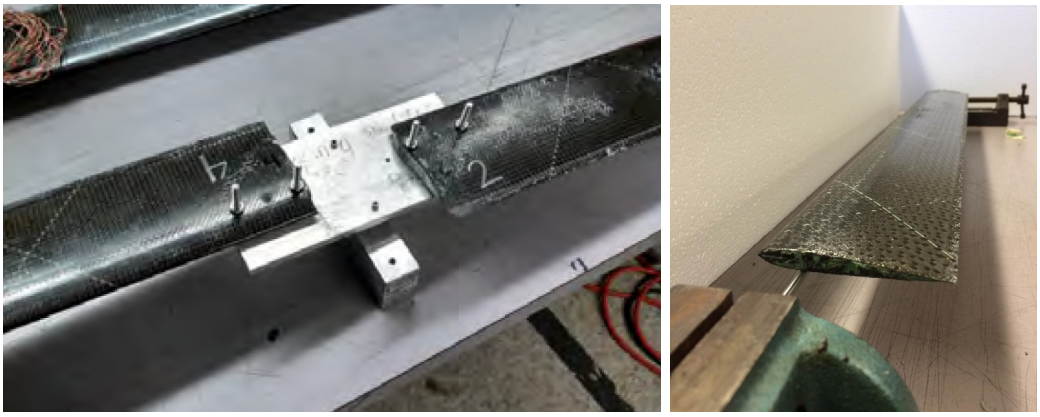

(a) Spanwise balancing (b) Chordwise balancing

Fig. 2.13: Blade mass balancing setup [1, 15].

Tab. 2.1: Blade structural properties of six wind tunnel tests.

Test	1st articulated	2nd articulated	3rd articulated
Lock number γ	4.04	4.83	5.24
Mass per span m (lb/ft)	0.238	0.187 (normal) 0.322 (sensor)	0.187
Flap bending stiffness EI_y $(lb-ft^2)$	87.1	76.8 (normal) 115.3 (sensor)	76.8
Lag bending stiffness EI_z $(lb-ft^2)$	1247	2174	2174
Torsional stiffness GJ $(lb-ft^2)$	87.1	60.0 (normal) 89.9 (sensor)	60.0
Test	1st hingeless	2nd hingeless	3rd hingeless
Lock number γ	5.24	4.26	4.74
Mass per span m (lb/ft)	0.187	0.216	0.200
Flap bending stiffness EI_y $(lb-ft^2)$	76.8	103.6	69.3
Lag bending stiffness EI_z $(lb-ft^2)$	2174	2302	1458
Torsional stiffness GJ $(lb-ft^2)$	60.0	64.2	71.5

2.3.3 Properties of the Blade-Grip Assembly

The structural properties of the blade grip had a considerable impact on the frequency response of a rotor, especially for a hingeless rotor. However, the geometry was too complicated to be assumed as a beam for static tests. So, the structural analysis was first performed with a CAD model, and the mass distribution and stiffness parameters were assigned for the comprehensive analysis to calculate non-rotating frequencies, then the frequency results were validated by rap tests on the blade-grip assembly. Fig. 2.14 shows a sample CAD model of the articulated rotor grip, which is divided into four sections. The mass distribution in each section was calculated according to the volume (the grip was made of uniform steel), and the

flap and lag bending stiffness were calculated with finite element analysis. Because of the pitch bearings, the blade grip structure did not provide torsional stiffness, and the torsional stiffness of the whole grip section was determined by the pitch link, which could be calculated by:

$$GJ = \frac{EA_{PL} l_{grip} l_{PLoffset}}{l_{PL}} \tag{2.9}$$

where EA_{PL} is the axial stiffness of the pitch link, l_{grip} is the length of the blade grip, $l_{PLoffset}$ is the pitch link offset from the quarter chord, and l_{PL} is the length of the pitch link. The structural properties of the blade-grip assembly for the third articulated rotor test are summarized in Table 2.2.

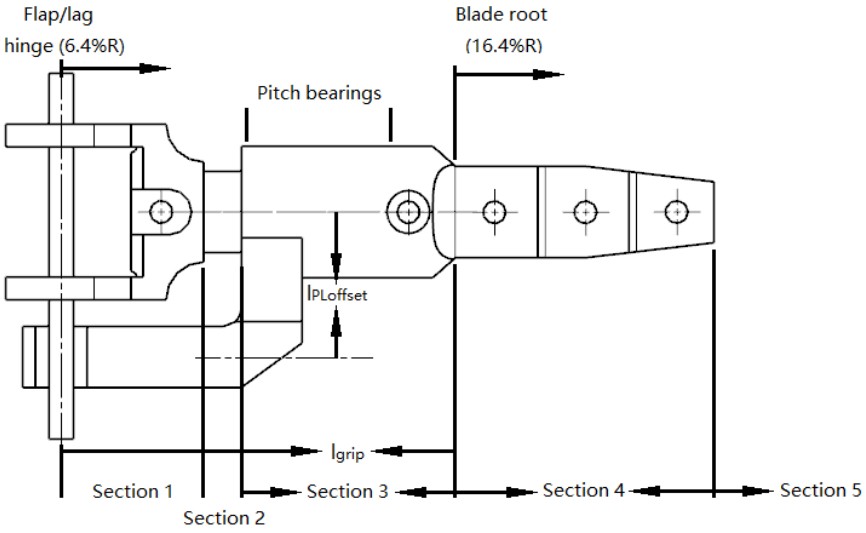

Fig. 2.14: A diagrammatic sketch of the blade grip for articulate rotor.

Tab. 2.2: Properties of blade-grip assembly, 3rd articulated test (spanwise averaged).

Section	1	2	3	4	5
Starting point	6.4%R	10.0%R	11.0%R	16.4%R	22.8%R
EI_y $(lb-ft^2)$	215.1	875.9	5713	129.4	72.78
EI_z $(lb-ft^2)$	6209	878.4	6500	3673	2064
GJ $(lb-ft^2)$	10461	10461	10461	10461	57.06

To correlate the structural parameters with the analysis, rap tests were conducted for the blade-grip assembly. For a hingeless blade grip, the test can be carried out directly on the rotor hub, while for an articulated blade grip, the flap and lag hinges should be blocked such that the blade is in a hingeless mode. The flap and lag frequencies recorded by the strain gauges (for a non-instrumented blade, attach gauges on blade surface after wind tunnel test) were then compared with the predictions of the comprehensive analysis with a hingeless model. After matching the results from the CAD model and the rap tests, the fan plot could be calculated in the comprehensive analysis based on these values (Fig. 2.15).

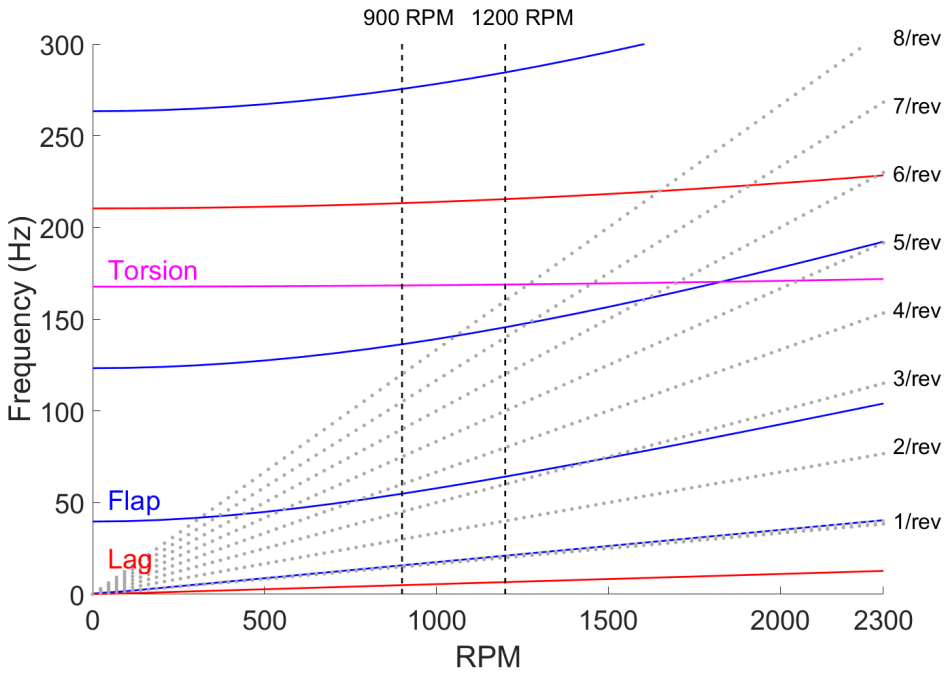

(a) Articulated rotor (3rd test)

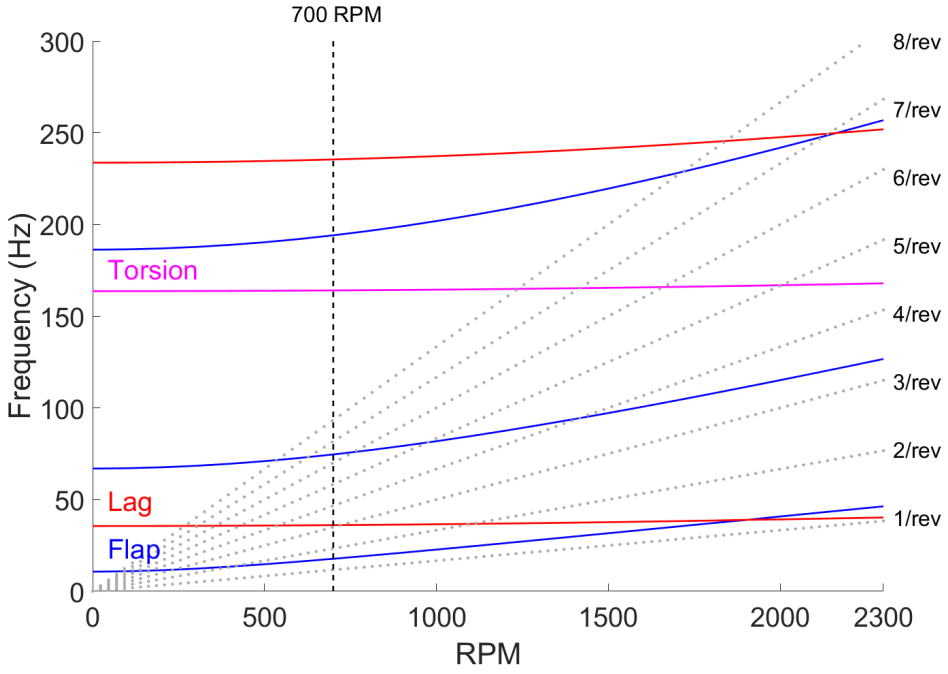

(b) Hingeless rotor (3rd test)

Fig. 2.15: Sample slowed rotor fan plots.

2.3.4 Other Blade Tests

The blade-embedded pressure sensors were calibrated after installation to check the functionality. The calibration was conducted with a vacuum bag. A 3D printed sleeve covered the sensor section to prevent the bag from contacting the sensor ports, and to ensure uniform pressure distribution to all sensors [1]. Then, a teflon bag was sealed around the section with Tacky Tape, except for two port holes for a pre-calibrated pressure transducer (Mensor CPT6100) and a vacuum pump. The pump was manually operated to lower the pressure in the bag by 1 psi (about 4 times of the measuring range during the wind tunnel tests), while the signals of the blade sensors and the reference transducer were recorded continuously. Note the Mensor transducer has a low sampling rate (50 Hz), so the pressure adjustment should be slow to maintain a quasi-steady condition in the vacuum bag (if a Kulite sensor is available, seal one in the vacuum bag for dynamic pressure reference). Similar to the strain gauge calibration, only the slopes were kept from the pressure sensor calibration. In the wind tunnel, an on-site pressure sensor calibration is recommended prior to data acquisition, and the setup is shown in Fig. 2.16.

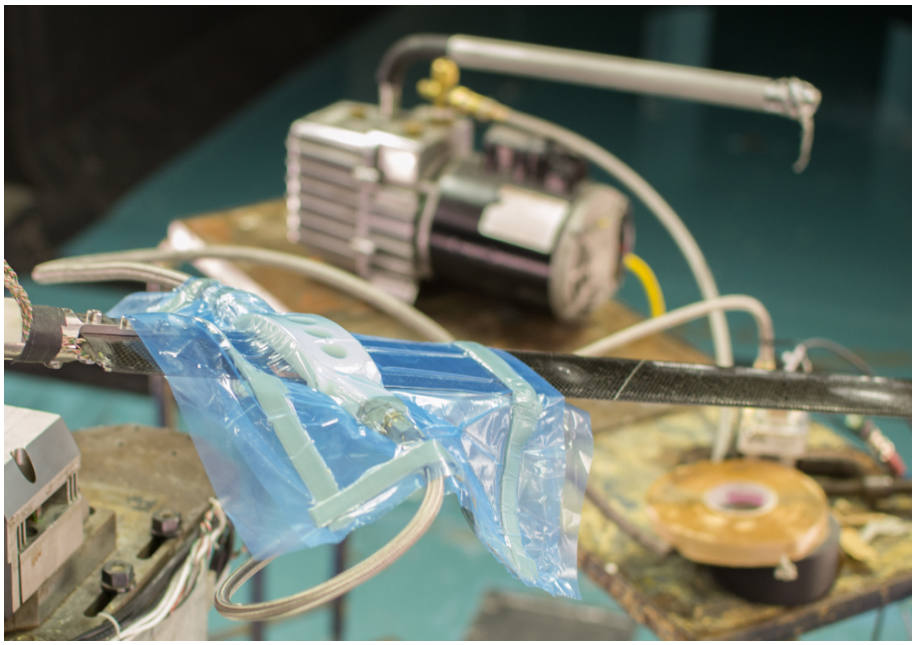

Fig. 2.16: Blade-embedded pressure sensor calibration setup.

The third articulated rotor test emphasized blade property characterization, so the flap/lag moment of inertia was measured by a pendulum test (Fig.2.17). A 3D-printed grip held the blade on a horizontal shaft with the correct root cutoff distance, allowing it to oscillate in lag direction (the rotor had coincident flap and lag hinges, so the flap and lag moments of inertia should be approximately equal). A magnet was attached on the blade grip with epoxy, and a Hall sensor on the shaft read a peak when the blade passed through the vertical position. Thus, the period of motion was obtained, and the moment of inertia I_β could be calculated with the total mass M_T, the center of mass location l_{CG} (derived from the mass distribution), the oscillation frequency f, and the gravitational acceleration g:

$$I_\beta = MTgl_{CG}(\frac{1}{2\pi f})^2 \tag{2.10}$$

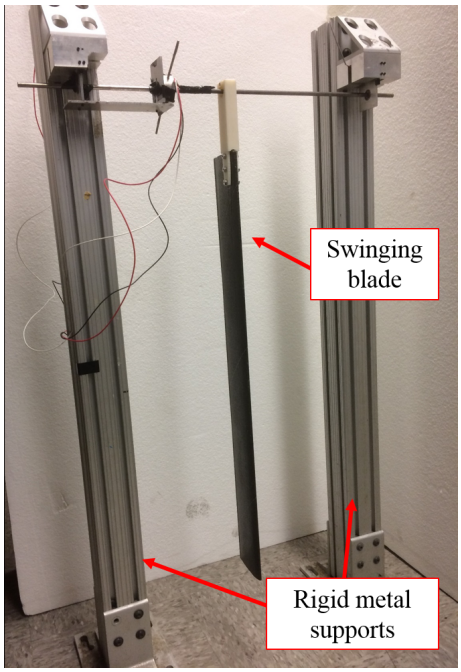

Fig. 2.17: Blade pendulum test setup for flap/lag moment of inertia [15].

In a previous research [16], a tension test was performed on the spar, which was critical for withstanding the centrifugal loads. A spare spar was tested in the material testing machine under tensile loading, and the test setup and results are presented in Fig. 2.18. The initial failure at the cross-strap near the root insert tip occurred at about 4150 lb axial load, and a complete failure was observed at about 4250 lb axial load [16]. The results demonstrated that the spar strength to bear centrifugal loads is well above the loading condition during hover and wind tunnel tests. The tension test was not repeated in the current study because the spar fabrication method did not change, and the rotor was operated with reduced RPM.

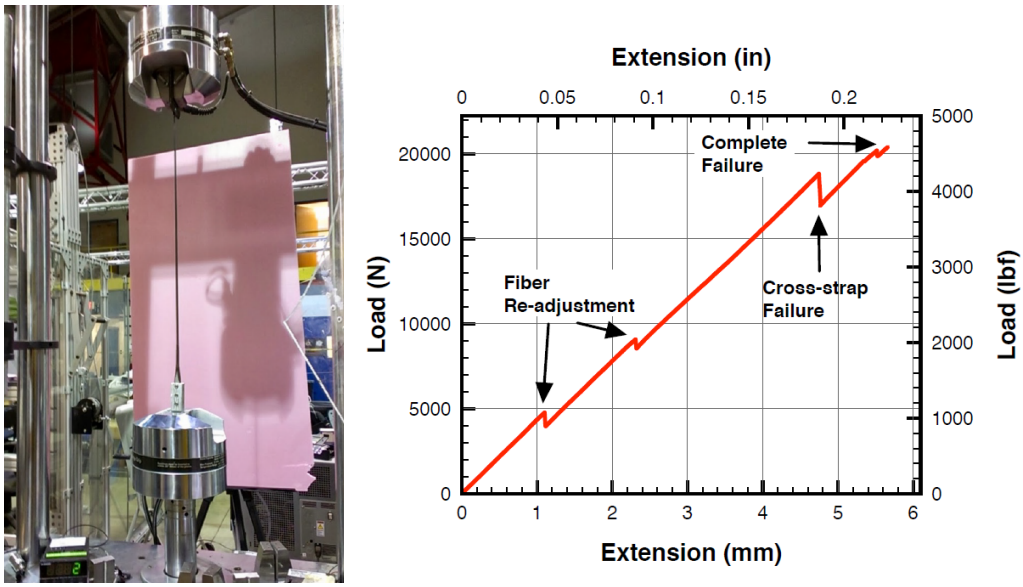

(a) Test setup

(b) Test results

Fig. 2.18: Spar tension test setup and results [16].

Chapter 3: Rotor Test Methodology

The primary research methodology of the current research is wind tunnel testing: six tests were conducted in total. In this chapter, the instruments used in the tests are introduced (including sensor calibration methods), the procedures of hover tests and wind tunnel tests are described, and the test matrices and emphases of the six wind tunnel tests are discussed.

3.1 Test Instruments

The model rotor test rig at the Alfred Gessow Rotorcraft Center (AGRC) was used for the wind tunnel test series. For the current study, the rotor diameter was 33.5 in and the nominal RPM was 2300. Coincident flap and lag hinges at 6.5% radius were used for articulated rotors, while the blade grips were replaced by rigid block pieces for hingeless rotors, eliminating the flap and lag degrees of motion. Blade feathering was enabled with pitch bearings and Kevlar tension-torsion bars. The rotor was driven by a 75 hp hydraulic pump through a belt-pulley system. The test stand can be mounted on a 6 ft pole at AGRC for hover tests or be transferred to the Glenn L. Martin Wind Tunnel for wind tunnel tests (Fig. 3.1).

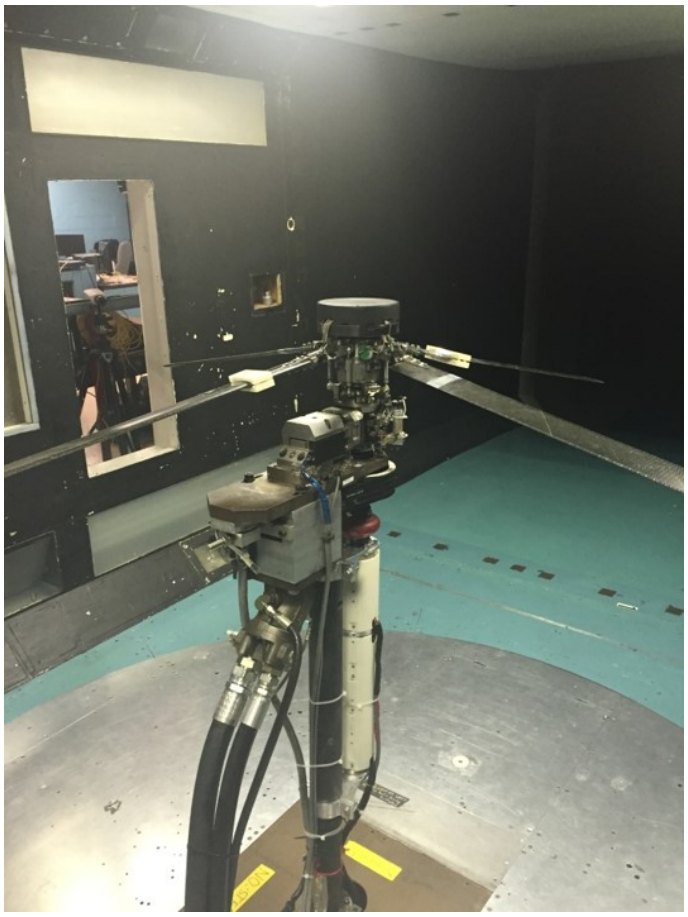

Fig. 3.1: Test stand in Glenn L. Martin Wind Tunnel (2nd articulated rotor test).

A hub balance was used to monitor the rotor performance and the hub vibratory loads (Fig. 3.2(a)). It was initially a 6-component balance that measures forces and moments in three directions, and the strain gauge for yaw moment was damaged, so the rotor torque was measured by a gauge cell on the shaft instead (Fig. 3.2(b)). Also, a 3-component accelerometer (Analog Devices ADXL326) monitored the vibration at the hub. The hub balance was in the fixed-frame, and all the loads transmitted through the hub and the swashplate were measured. The gauge cells were pre-calibrated about its geometric center, but the hub center was above and in front of the geometric center of the balance, inducing additional coupled

terms: the axial and vertical forces were coupled with the pitch moment reading, and the side force was coupled with the roll moment reading. Therefore, a static calibration was required, as shown in Fig. 3.2(c). A test frame was constructed to apply forces and moments in any direction with a pulley system, and the upper hub was replaced by an aluminum slab for attaching points. A load cell was implemented between the hub and the pulley to measure the applied load directly, isolating the frictional loss from the pulley (see Fig. 3.2(d)). Then, loads were applied up to 50 lb, and rolling and pitching moments were applied using a 5.5 in offset. In each load condition, the readings of all gauge cells were recorded. The load conditions and balance readings were summarized in matrices $[H]$ and $[R]$ respectively, and a first order $[R] = [C][H]$ type model was used to calculate the calibration coefficient matrix with multi-variable regression method [74].

The torque gauge cell on the rotor was calibrated with similar setup (coupling terms were neglected). The torque was applied with two opposite forces with offsets, and the driving pulley was blocked to prevent rotation during the calibration. According to a previous research, the uncertainty of the calibration slope was estimated to be 1.5% [1]. The accelerometer had been pre-calibrated so no lab calibration was required, and the functionality could be checked by observing its response to gravitational acceleration.

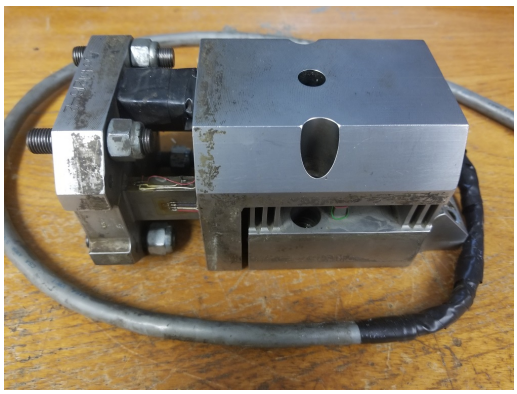

(a) Hub balance

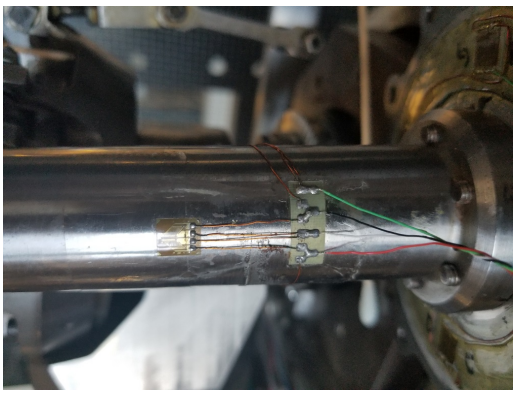

(b) Shaft torque cell

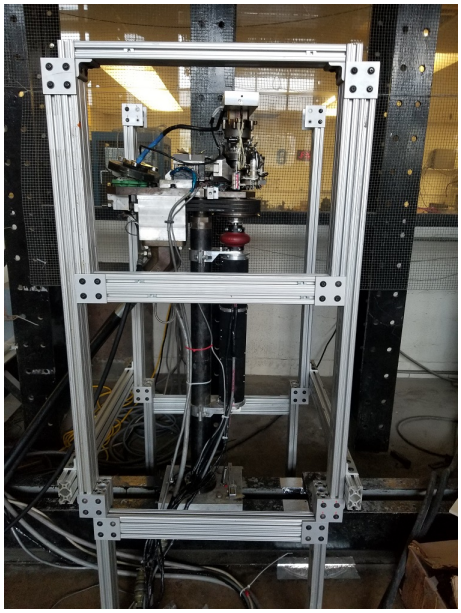

(c) Calibration frame

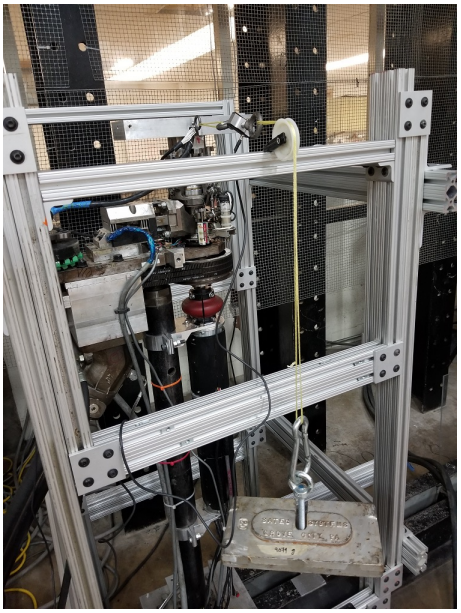

(d) Calibration setup (side force)

Fig. 3.2: Hub balance, shaft torque cell, and calibration setup.

The collective and cyclic control angles were set by three gearmotors (Globe Motors 43A108). One motor moves the swashplate up and down to control the collective (Fig. 3.3(a)), and the other two tilt the swashplate to adjust the two cyclics (Fig. 3.3(b)). The motors provided no displacement measurement, so the swashplate displacements were monitored by three Linear Variable Displacement Transducers (LVDT, Maurey Instrument M1326, see Fig. 3.3(c)).

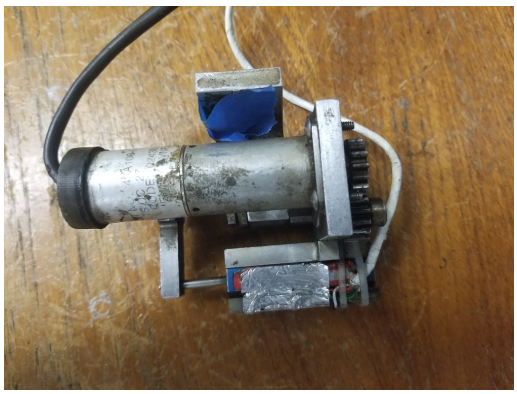

(a) Collective control assembly

(b) Cyclic control assembly

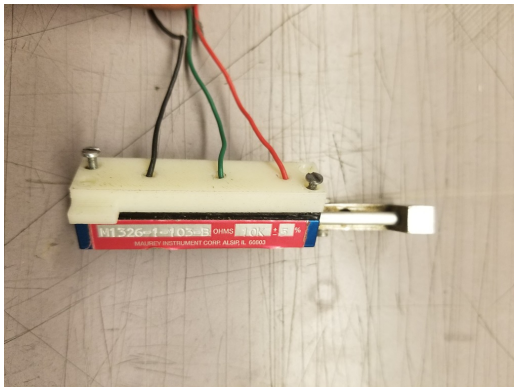

(c) LVDT for swashplate displacement measurement

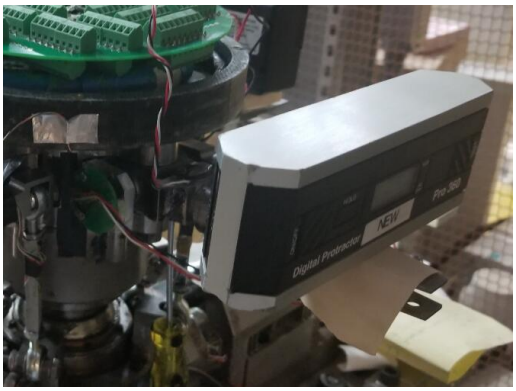

(d) Control angle calibration setup

Fig. 3.3: Swashplate control mechanism and calibration setup.

The voltages from the LVDTs were not calibrated against the swashplate displacements. Instead, the control angles were derived from the voltages directly. The calibration was conducted after the rotor hub had been fully assembled. First, the pitch link length of the first blade was fixed, and an inclinometer was attached on the grip chordwisely: the control angle measurements were based on it. If using the articulated blade grip, block the flap hinge to make the grip at approximately zero flap (see Fig. 3.3(d)). Then, the ranges of control angles were determined by adjusting the motors carefully while monitoring the angle change with the inclinometer (do this at any azimuth for collective, at 0° for lateral cyclic and at 90° for

longitudinal cyclic). The collective angle range should be around 16° (the absolute limits depend on the pitch link length, −4° to 12° are acceptable limits), and these limits of the two cyclics should be around ±12°. Record the corresponding LVDT voltages at the limits, and perform a linear interpolation to get 5-10 intermediate voltages, then randomly combine these voltages into 5-10 test conditions. For each case, adjust the motors to reproduce the LVDT voltages (does not need to be exact, but record the measured voltages for calibration), then read the pitch angle from the inclinometer at 0°, 90°, 180°, and 270° azimuth to calculate the corresponding control angles:

$$\theta_0 = \frac{\theta_{0^\circ} + \theta_{90^\circ} + \theta_{180^\circ} + \theta_{270^\circ}}{4} \tag{3.1}$$

$$\theta_{1c} = \frac{\theta_{0^\circ} - \theta_{180^\circ}}{2} \tag{3.2}$$

$$\theta_{1s} = \frac{\theta_{90^\circ} - \theta_{270^\circ}}{2} \tag{3.3}$$

Two optic sensors (Photologic OPB980) and a magnetic shaft encoder (US Digital MAE3) were used to track the rotor RPM and azimuth angle. The optic sensors recorded the rotor RPM at 1/rev and 60/rev: each read a toothed disk on the rotor shaft, returning a peak when a gap on the disk passed the sensor (Fig. 3.4(a)). The shaft encoder was attached near the bottom of the slipring with 3D-printed parts (Fig. 3.4(b)). It is an absolute rotary encoder that reads the orientation of

a magnet on the slipring and returns a voltage linear to the azimuth angle. As a calibration, the azimuth offset of the 1/rev optic sensor should be measured to calculate the azimuth from 1/rev and 60/rev signals. Also, the shaft encoder should be installed such that the zero position is at zero rotor azimuth, so that the azimuth can be linearly converted from the voltage reading.

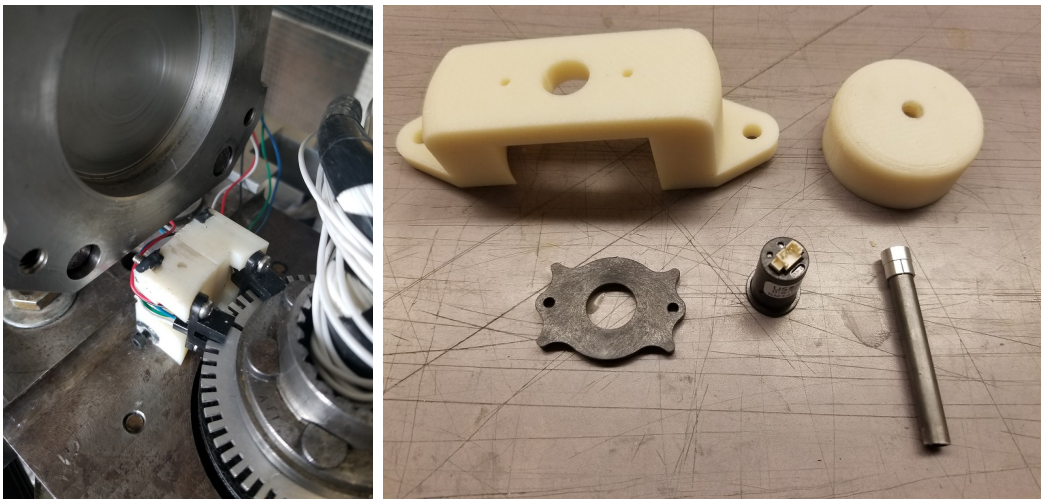

(a) Optic sensors (b) Magnetic shaft encoder parts

Fig. 3.4: Optic sensors and magnetic shaft encoder.

In the rotational frame, Hall effect sensors were implemented at the pitch bearings to monitor the root pitch of each blade directly. As a supplement to the swashplate measurement, the on-hub measurement of the control angles helped rule out the performance data scatter due to swashplate linkage looseness. For articulated blade grips, similar Hall sensors were installed at the blade flap hinges to measure the flap angles at the blade roots, which were used to trim the rotor during wind tunnel tests. Also, strain gauges were applied on pitch links to measure the pitch link axial loads. The rotational frame sensor configuration is shown in Fig. 3.5(a). For the Hall calibration, a L-shaped metal piece was bolted onto the

grip with the blade, where two inclinometers could be attached in spanwise and chordwise directions with double-sided tape (Fig. 3.5(b)). To calibrate the pitch sensor, block the flap hinge so that the flap angle is about zero, then adjust the collective and cyclic to read the sensor voltages at various local pitch. To calibrate a flap sensor, adjust the control angles so that the local pitch is about zero, then block the flap hinge at various locations to read the sensor voltage. Note that the calibration curve of a pitch sensor is non-linear and requires a 2nd or 3rd order polynomial fit, because it is not possible to install the Hall sensor and the magnet at the pitching axis. To calibrate a pitch link gauge, apply various hanging loads to read the gauge voltages.

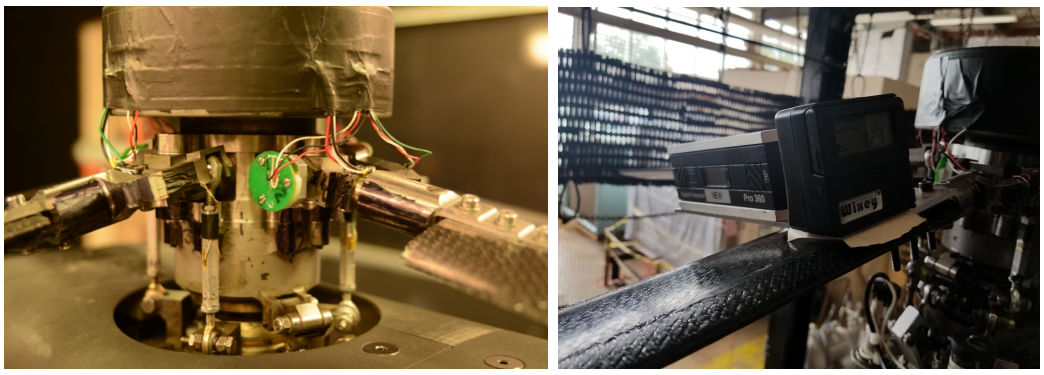

(a) Rotational frame sensor configuration (b) Hall sensor calibration setup

Fig. 3.5: Rotational frame sensors and calibration setup.

The first two articulated rotor tests were conducted without fuselage or wing. In the third articulated rotor test, a 3D-printed nylon fuselage was mounted as a fairing to shield the irregular shape of the test stand instruments (Fig. 3.6(a)), making it a standard aerodynamic geometry for CFD analyses. The fuselage lacked mounting points for wings and was hard to modify, so a modular fuselage based on

a modified ROBIN fuselage [75] was implemented for the three hingeless subsequent rotor tests (Fig. 3.6(b)). The fuselage was 3D-printed with ABS plastics, and was scaled to match the rotor radius: the total height was increased by 10%, the total width was increased by 20%, and the tail length was reduced by 9%. It was attached to the test stand with a steel frame, which also provided six mounting points for a wing on each side.

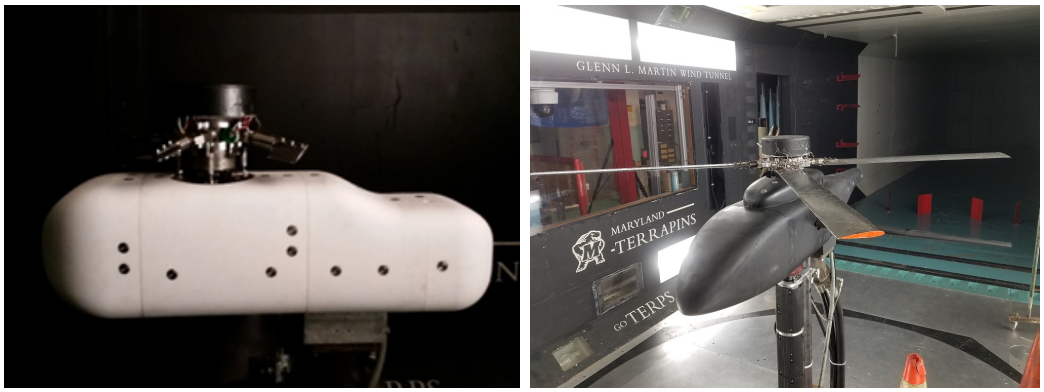

(a) Old fuselage (b) New fuselage with a wing

Fig. 3.6: Two fuselages for different wind tunnel tests.

In the last two hingeless rotor tests, a stub wing was added on the retreating side of the fuselage for the test cases with lift offset stats (Fig. 3.7(a)). The wing had a span of 23.4 in (70% radius), an aspect ratio of 5.0 and a taper ratio of 0.5. The airfoil was NACA0015 on the outboard section and NACA0020 on the inboard section to install a balance in the root of the steel spar. The wing was installed 8.0 in below the rotor hub (24% radius), and the angle of incidence was adjustable (studied at 4° and 8° in the current research). The UT-69A 6-component balance (borrowed from NASA Langley, Fig. 3.7(b)) was used to measure the wing lift, drag and rolling moment. It was a delicate pre-calibrated instrument.

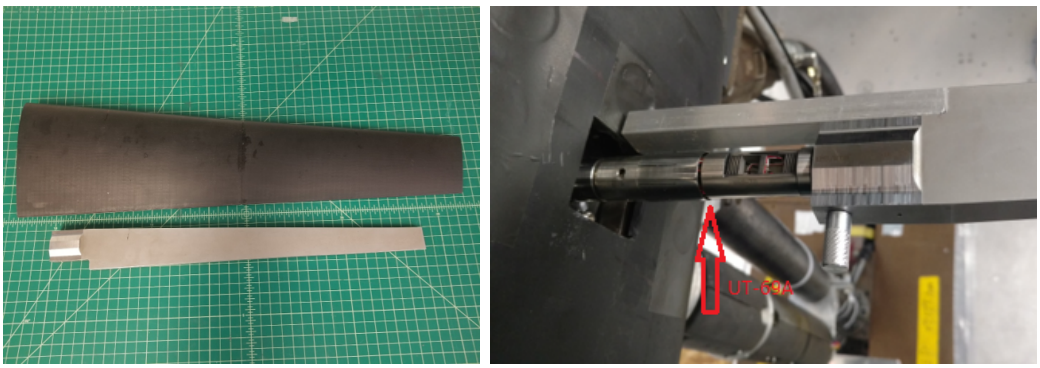

(a) 3D-printed wing and steel spar (b) UT-69A balance in the spar

Fig. 3.7: Stub wing and balance for hingeless rotor tests.

The rotating frame sensors were wired onto a PCB board in the hub cap, and the signals were routed to the stationary frame through one or multiple sliprings. The sliprings were designed and fabricated by Fabricast. In the first articulated test, two 64-line sliprings were jointed in tandem. However, the tandem configuration was challenging to align, resulting in abnormal loads and damaging the lower slipring. A custom-made 150-line slipring was used for later tests (Fig. 3.8(a)). The data acquisition system were built with National Instruments components. The signals of strain gauges and pressure sensors were processed by SCXI-1520 modules, and the voltages of other sensors were processed by a SCXI-1102C module. The modules were installed on a SCXI-1001 chassis, and the data collection was conducted with a USB-6255 I/O device at 16-bit resolution and a sampling rate of 5000 Hz. A LabVIEW Virtual Instrument (VI) panel was used for data logging and monitoring sensor readings in real time. The data acquisition system was placed on a control station, along with a control box for the hydraulic driving system and control sticks for swashplate angle control (Fig. 3.8(b)).

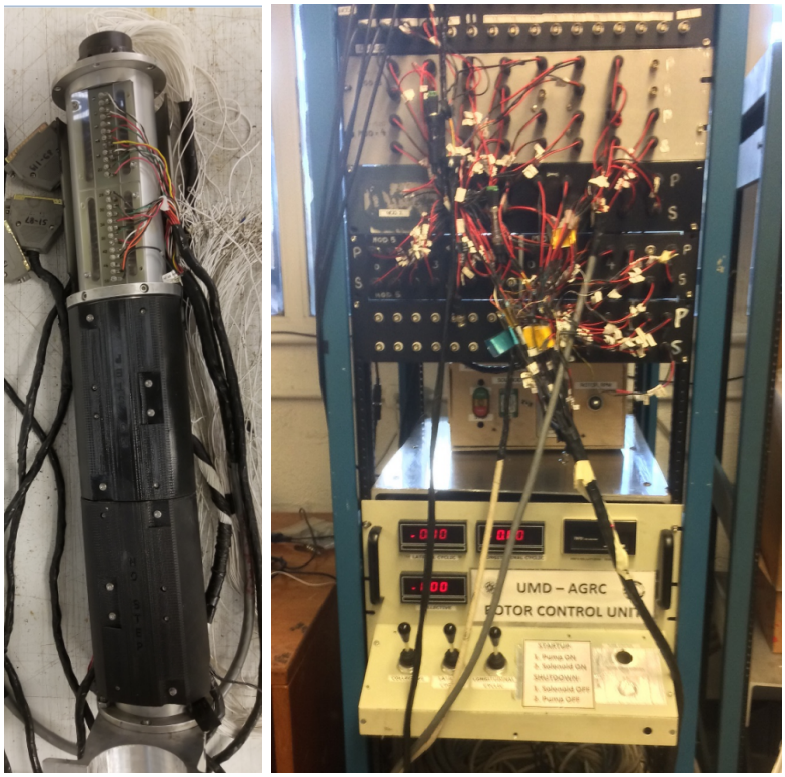

(a) 150-line slipring (b) Control station

Fig. 3.8: Hardwares for data acquisition [15].

3.2 Hover Test

Prior to a wind tunnel entry, a hover test is required to verify the functionality of the hydraulic driving system, the data acquisition system, and the test stand instruments. The hover tests were conducted on the AGRC hover tower, which is a 6 ft height rigid pole with an adapter to mount the test stand. The rotor was about 12 ft above the ground on the hover tower (430% of the rotor radius), reducing the ground effect to a neglectable level. The test procedure is as follows:

1. Connect the wires from the hub sensors to the data acquisition system. With a multimeter, check the slipring connectivity from the hub PCB board to the

cable connectors. Next, connect the hub sensors to the PCB board (torque cell, pitch/flap Hall sensors, pitch link gauges), and connect the data cables to the control station (2-3 cables for slipring, 1 for hub balance, 1 for control mechanism, 1 for miscellaneous stationary sensors). Check the sensor signals on the LabVIEW VI and test the swashplate control responses, then calibrate the hub sensors as described in the test instruments section.

2. Connect the hydraulic motor and perform a test spin. Three hydraulic hoses (inlet, outlet and speed control) and two cooling water hoses (inlet and outlet) need to be connected, along with the cables/wires for power supply, control switch and solenoid. Also, a thermocouple wireless transmitter to monitor the oil temperature is to be checked. Use a bucket to prevent oil spillage, and another clean bucket or box to keep the hose caps, otherwise the dust on the caps can spoil the hydraulic oil and damage the hydraulic motor. Before power-on, tighten everything on the test stand, and check the hydraulic oil level and the status of the two oil filters. Run the cooling water and test spin at a low RPM (< 500) to identify any abnormal noise (locate the source on the hub, the slipring, the belt-pulley system, or the hydraulic system), rotating part heating up (indicating a jam or misalignment), or oil/water leakage.

3. Transfer the test stand onto the hover tower with the high bay crane. Secure the data cables and hydraulic lines with zip ties, then wrap a Kevlar strap on the test stand pole on each side to apply the hook (pay attention not to damage the belt and the blade grips). At least three personnel are required to

move the stand: one operates the crane, one stabilizes the stand and secures the wires, and one aligns the stand on the hover tower and fasten the bolts.

4. Install the test blades. After all are bolted on the grips, leave the blade 1 unchanged, and adjust the pitch link lengths of blade 2-4 until their local pitch angles are about same as that of blade 1 (the pitch link is held by normal thread on the top and left-handed thread on the bottom, so the length can be adjusted by screwing. Lock the position with lock nuts after adjusting). Connect the blade sensors if applicable (a sensor chart can be helpful to keep track of the channels). Check the sensor responses on the LabVIEW VI, then close the hub cap, and secure the blade sensor wires on the side of the hub cap with aluminum tape (leave some extra length to allow flap and lag motions).

5. Test spin to adjust the zero points for cyclic controls, and balance the rotor. Set the collective to a moderate level (like 4°) and the cyclics to zero, then turn on the hydraulic machine to set a test RPM. Adjust the cyclics to minimize the fluctuation in pitch Hall sensor signals, and make the current cyclic settings as zero by applying offsets to the initial calibration results. Save a data point to check the magnitude and phase of 1/rev in-plane hub load, which is due to hub mass imbalance. Attach a counterweight on the hub to balance the rotor (if less than 10 g is needed, attach it on the side of the hub cap with aluminum tape, otherwise epoxy it in inside the hub cap).

6. Perform rotor tracking at hover. Turn on the RPM and illuminate the blade tip using a strobe light (Checkline LS-5-12000) in the rotor plane, with a

4/rev frequency. Record the tip path pattern by observing the reflecting tape on each blade tip, then shut down the RPM. For blades 2-4, if the tip path of the blade is higher than that of the blade 1, shorten the pitch link; otherwise extend the pitch link. Turn on the RPM and repeat with smaller pitch link adjusting steps, until the tip paths of blades 2-4 perfectly align with that of blade 1.

7. Perform collective sweep to acquire data. First take a static zero data point, then set the lowest test RPM. Adjust the collective control by 1° or 2° steps to save data points, then move to the next RPM and repeat the process. Stay away from 500-550 RPM to avoid test stand resonance, and save data as quick as possible around zero collective where the vortex ring state occurs, which is indicated by loud whizzing noise. When finished, shut down the RPM and save another zero point to check if the sensor readings are consistent before and after the test.

Sample hover test results are shown in Fig. 3.9. The emphases were repeatability and consistency: the data point at a specific collective should be repeatable and consistent with previous hover data. If the the thrust versus torque plot is erroneous, identify which component (thrust or torque) causes the problem and check the corresponding instrument for any mechanical sloppiness or poor connection. If the thrust versus torque plot is satisfactory but the collective-related results are scattered, the problem is likely to come from the control angle measurement: regenerate the plots with pitch Hall sensor results to isolate the problem.

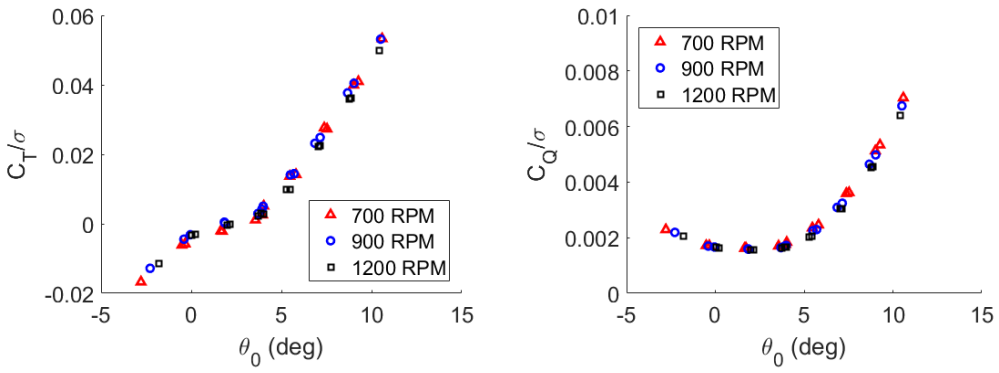

(a) Thrust vs collective

(b) Shaft torque vs collective

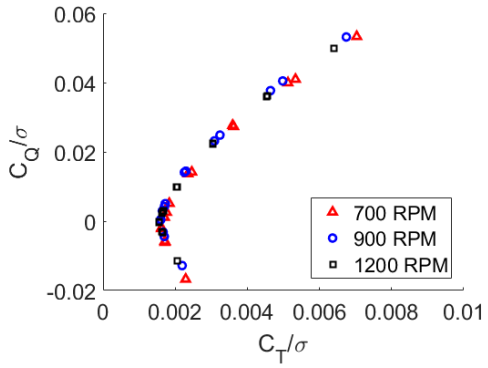

(c) Thrust vs shaft torque

Fig. 3.9: Sample hover test results (before 1st hingeless rotor test).

3.3 Wind Tunnel Test

The wind tunnel tests were carried out in the Glenn L. Martin Wind Tunnel, a closed-return wind tunnel with a cross section of 7.75 by 11.04 ft. The maximum tunnel speed is 230 knots (approximately 0.3 Mach), while the speed is usually limited to 200 knots with a test model. The freestream turbulence intensity is 0.21% from a hot wire measurement [76]. A total of six wind tunnel tests were conducted: three on articulated rotors, and three on hingeless rotors. Their test matrices and configurations are summarized in Table 3.1.

Tab. 3.1: Test matrices and configurations of the six wind tunnel tests.

Test	RPM	Advance ratio	Shaft tilt	Fuselage	Blade instrumentation
1st articulated rotor test (2015)	900	0.3-0.8 ($\theta_0 = -4° - 12°$) 0.8-1.15 (at $\theta_0 = 4°$)	0°	None	Blade 1: 17 pressure sensors at 30% radius Blade 3: 17 pressure sensors at 86% radius Blade 2: flap/torsion gauges at 30%, 40%, 50%, 60%, 70%, 86% radius (embedded under blade skin)
2nd articulated rotor test (2016)	700, 900	0.3-0.8 ($\theta_0 = -3° - 11°$)	0°, ±2°	None	Blades 1, 3: 14 pressure sensors Blades 2, 4: flap/torsion gauges (with 3D-printed mount at 30% radius)
3rd articulated rotor test (2017)	900, 1200	0.3-0.9 ($\theta_0 = -2° - 12°$)	0°, ±4°	Old fuselage	Non-instrumented blades with similar structural properties
1st hingeless rotor test (2018)	700, 1200	0.3-0.7 ($\theta_0 = -2° - 12°$)	0°, ±2°	New fuselage, no wing	Blades 1, 3: flap/lag gauges Blades 2, 4: flap/torsion gauges (surface-bond at 25% radius)
2nd hingeless rotor test (2018)	700, 1200	0.3-0.5 ($\theta_0 = -2° - 12°$)	0°, 4°	New fuselage, wing at 4° angle of incidence	Blades 1, 3: flap/lag gauges Blades 2, 4: flap/torsion gauges (surface-bond at 25% radius)
3rd hingeless rotor test (2019)	700	0.3-0.7 ($\theta_0 = -2° - 12°$)	0°, ±4°	New fuselage, wing at 4°, 8° angle of incidence	Blades 1, 3: flap/lag gauges Blades 2, 4: flap/torsion gauges (surface-bond at 25% radius)

3.3.1 On Site Preparation

The test instruments were transferred to the wind tunnel using a cart. During transportation, the test stand should be fixed on a metal slab and secured with splints. Upon arrival, the test stand was installed in the test section with a specific mounting structure, which allows a $\pm 4.5^\circ$ shaft angle adjustment. The hydraulic machine was moved to the basement with a crane to get access to power supply and cooling water, while the control station and the computer for data acquisition were in the control room. First, connect the hub balance cable and construct the test frame to set up a dynamic calibration (Fig. 3.10(a)), from which transfer functions can be gained to correct the vibratory hub load readings. The upper hub was replaced by an aluminum slab to represent the mass of all removed parts, and a shaker was rigidly attached to the slab, in tandem with a high frequency response load cell (Fig.3.10(b)). The dynamic calibration was 1-dimensional: only one hub balance degree of freedom corresponded to the load cell at a time. All the couplings were neglected, which was due to the limitation that only one external load cell was available to measure the applied load. A frequency sweep was performed with the shaker, and a transfer function between the actual load from the load cell and the measured load from the hub balance was obtained. The dynamic calibration was performed in multiple wind tunnel tests for configurations without fuselage, and with the old and new fuselages.

(a) Overall setup (b) Shaker attachment (side force)

Fig. 3.10: Dynamic calibration setup (3rd articulated rotor test).

The results of the dynamic calibration are presented in Fig. 3.11. Multiple resonance peaks are present for the two in-plane loads, accompanied with abrupt phase changes. Different fuselage configurations have a significant impact on these resonance frequencies, even inducing new resonance peaks. Because of the supporting pole, the vertical load is less sensitive to the frequency sweep or the fuselage configurations: both the gain and the phase changes are mild compared to the two in-plane loads. The rotor speeds that the 4/rev coincide with any resonance peak should be avoided if possible during the wind tunnel test. In the following result chapters, all the hub vibratory load data are corrected with the transfer functions obtained from the dynamic calibration.

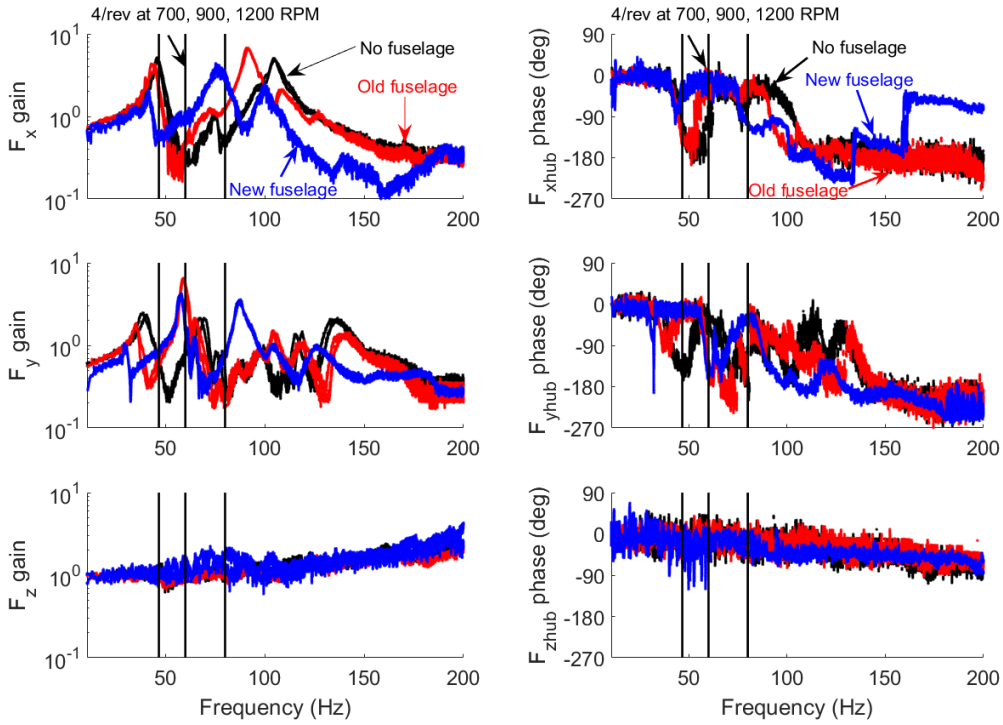

(a) Gain plot (b) Phase plot

Fig. 3.11: Transfer functions from dynamic calibration.

After dynamic calibration, the test setup was assembled by following hover test steps 1-4 (if a PIV study is planned simultaneously, the instruments should be set up in this stage). Then, secure all the cables and wires with zip ties and aluminum tape, and check all the bolts and nuts to make sure nothing is loose. Also, the status of the sensors should be revisited. For the most critical control mechanism and the most fragile pressure sensors, an on site calibration is highly recommended. For other sensors, a few data points are to be checked at first, and if these points match well with the lab calibration results, a complete re-calibration can be omitted. The calibration requirements are summarized in Table 3.2. In addition, the ambient pressure p_{air}, ambient temperature T_∞, and freestream dynamic pressure q data are

supplied by the wind tunnel instruments through BNC cables. Along with the gas constant R_{air} and the molar mass of the air M_{air}, a referential tunnel speed V_∞ can be derived from these data:

$$V_\infty = \sqrt{\frac{2qR_{air}T_\infty}{p_{air}M_{air}}} \tag{3.4}$$

Tab. 3.2: Type of calibration required for the sensors.

Sensor	Pre-calibration	Lab calibration	On site calibration
Hub balance	Yes	Yes	No
Shaft torque cell	No	Yes	No
Swashplate control/LVDTs	No	Yes	Yes
Shaft encoders	No	Yes	Check
Hub accelerometer	Yes	No	No
Pitch/flap Hall sensors	No	Yes	Check
Pitch link strain gauges	No	Yes	No
Blade strain gauges	No	Yes	Check
Blade pressure sensor	No	Yes	Yes
Wing balance	Yes	No	No

Because of the fragility of the wing balance, the stub wing for hingeless rotor tests should be installed after all other preparations are finished. First, the data cable was passed through a connecting nut, an adapting base for angle adjustment, and the side plate of the test stand with wing attaching points, while the balance remained in its container (Fig. 3.12(a)). Since then, the balance signal should be connected to the data acquisition computer, and its signal should always be monitored to avoid overloading. The data acquisition system should not only record the six signal channels, but also the actual excitation voltage for a scale correction. Then, the adapting base was clamped down with a vice to align with the nut and

the balance, and the nut was tighten with a spanner wrench. Then, the assembly was bolted to the side plate of the test stand (Fig. 3.12(b)). With slot holes, the adapting base allowed some pitching motion with respect to the stand, so an inclinometer was used to set the desired wing angle of incident on the top edge of the adapter, then the plastic fuselage panel was closed. The next step is wing spar installation. Carefully slide the spar on top of the balance, and check the alignment by a hand-held alignment pin (Fig. 3.12(c)). If the alignment pin does not fit in, pull the spar out and align it again: never try to twist the spar on the balance because of the extremely low load limit. When the alignment is secured, set the brass pin in place with a slide hammer (use a cushion on the other side to cancel the net side force on the balance). As the final step, grease the spar to reduce the friction and slide the two plastic wing sections on (Fig. 3.12(d)), and lock them with bolts at the spar tip.

(a) Wing balance with mounting parts

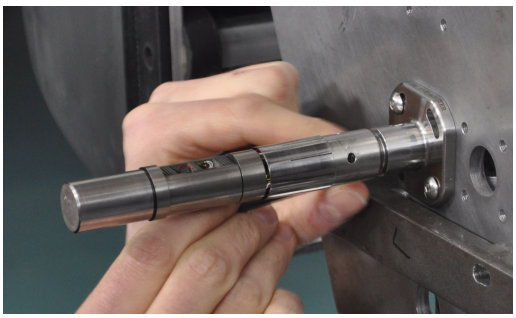

(b) Attach to test stand

(c) Align wing spar

(d) Assemble wing sections

Fig. 3.12: Stub wing installation.

3.3.2 Test Procedure

A wind tunnel test is composed of three main steps: tracking the rotor, performing collective sweep to save data, and acquiring tare cases. At least four personnel are required for the wind tunnel test. One operates the control station to adjust the control angles and RPM; one monitors the LabVIEW VI to save the data; one keep a data log to record key parameters on a separate computer, and one keeps watching the rotor and performs rotor tracking. The test setup is shown in Fig 3.13., and the procedure is as follows:

(a) Test stand in wind tunnel (b) Perform collective sweep

Fig. 3.13: Wind tunnel test setup (3rd articulated rotor test).

1. Test spin the rotor with zero tunnel speed. Set the collective to 4° and the cyclics to zero, then turn on the hydraulic machine to test each planned RPM. Monitor any abnormal vibration by visual inspection and through the accelerometer. Perform cyclic control zeroing, rotor balancing and hover-state tracking again as needed, by following hover test steps 5-6. If time permits, perform collective sweeps for a full hover test (the wind tunnel floor and ceiling need to be removed to allow unrestricted inflow).

2. Track the rotor with wind tunnel speed. Reset the control angles (collective to 4° and the cyclics to zero) and raise the RPM to a planned level, then increase the tunnel speed to a moderate advance ratio (the first target can be $\mu = 0.3$). Adjust the two cyclic angles to trim the rotor: for an articulated rotor, the trim target is to minimize 1/rev flap angle (monitored by the Hall sensors), while for a hingeless rotor, the target is to zero mean rolling and pitching hub moments (monitored by the hub balance), or to balance the rolling moment induced by the wing. Once the rotor is properly trimmed, turn off the wind

tunnel lights and illuminate the blade tip using a strobe light with a 4/rev frequency (Fig. 3.14(a)), and record the tip path pattern of blades 2-4 with respect to blade 1 over one revolution. Note that the pattern can vary at different azimuths, so observations must be made at various positions. In the control room, the windows allow observations at $\psi = 225°$ and 315°, and a camera can be installed on the other side to enable observation at $\psi = 90°$ (each location provides a field of view of about 90°). After recording the pattern, shut shown the tunnel speed first, and turn off the rotor RPM when the tunnel speed is below 10 knots. Adjust the pitch links of blades 2-4 as described in hover test step 7 and repeat the process, until the mean tip path heights of all four blades are in the same level approximately.

3. Perform tracking at all planned advance ratios. Turn on the rotor RPM first and increase the tunnel speed by steps (the first target can be $\mu = 0.3$, then $\mu = 0.5$, use a step of 0.1 after that). At each advance ratio, trim the rotor and repeat the last step to perform tracking. At lower advance ratios ($\mu \leq 0.5$), the tip path plane is rather flat, and the mean tip path level is self-explanatory. At higher advance ratios, large 1/rev or 2/rev differences may occur between blade 1 and other blades, one may need to find the intersecting points between blade 1 and other blades to identify which way to adjust the pitch link length. Also, smaller adjustment steps are recommended at high advance ratios. Generally the tip path plane is more sensitive to pitch link length at higher advance ratios, but it is possible that a rotor tracked at higher advance ratio appears

less tracked at lower advance ratios (mostly due to blade dissimilarity). In such situation, a tradeoff should be made and the maximum advance ratio for collective sweep should be limited.

4. Acquire data in collective sweeps with wind tunnel speed. Reset the control angles, apply the tare button on the VI and take a stationary zero case, then raise the RPM to take a rotational zero case. Next, apply the tunnel speed and trim the rotor. Save a data point for at least for 5 seconds when the trim condition is achieved, and record the key parameters (control angles, thrust, and shaft torque) in the log file. After finishing one test condition, increase the collective to the next test condition by a step of 1° or 2°. Repeat the trimming and data saving process at each test condition until the upper limit of the collective, and proceed reversely towards the lower limit, then move towards the initial collective to finish the sweep. The sweep is conducted in a double passing manner to check the trim repeatability. At critical collectives (the upper and lower limits and the initial collective), also check the rotor tracking as described in step 2, and record the observations in the log file. At high collectives, pay attention to the RPM and the hydraulic oil temperature; at low collectives, pay attention to the vortex ring state (indicated by loud whizzing noise). If any mechanical problem happens (abnormal noise, vibration, loss of swashplate angle or RPM control), immediately reset the collective and shut down the wind tunnel speed while maintain rotor trimming if possible, and turn off the rotor RPM only when the tunnel speed is low. After the collective

sweep is finished, bring down the tunnel speed while trimming the rotor, and save another rotational zero when the tunnel speed is below 10 knots, then turn off the RPM to save another stationary zero.

5. Perform collective sweeps to acquire data at all planned advance ratios. Repeat the last step at various rotor speeds, advance ratios, shaft tilt angles and wing configurations. Test conditions with lowest advance ratio at zero shaft tilt should be tested first, and the test envelope is gradually expand to higher advance ratios. For shaft tilt study, the test conditions at high advance ratios with backward tilt have higher priority. Ideally, the rotor should be stopped once after each collective sweep to check the test stand status and to take new zero points. In practice, 2-3 sweeps are usually conducted in a single run to save wind tunnel time. There are several issues that may limit the maximum collective and advance ratio. The rotor tracking tends to deteriorate with advance ratio: the tip path difference becomes pronounced (larger than 3 blade thicknesses) when the advance ratio is too high, causing high data scatter and less repeatable results. At high advance ratios, the longitudinal cyclic can be saturated at a high collective, making it not possible to trim the rotor. For a hingeless rotor, the intense flap bending moment poses another limitation. The VI is programmed to separate the mean and dynamic components of the load to check whether the load is safe by Goodman relation [77], where the ultimate strength is determined by the $\pm 45^{\circ}$ carbon fiber skin, the fatigue limit is assumed as 50% of the ultimate strength, and a safety factor of 1.5 is used.

Consider lower the advance ratio or collective when any of these limitation occurs.

6. Take tare cases without blades. Open the hub cap to disconnect all blade sensor wires, dismount the blades and mount the short stub blades (Fig. 3.14(b)). If the stub wing is applied, dismount it with extreme caution while monitoring its signal on the VI, and disconnect the data cable only when the balance is restored in the container. Then, close the hub cap and wrap it again with aluminum tape, and reset the control angles. Apply the tare button on the VI, then take a stationary zero case. Raise the RPM to a tested value to take a rotational zero case, then apply the tunnel speed for a tested advance ratio. No trimming or collective sweep is required for the tare cases. Vary the RPM and tunnel speed to save a tare case at target RPM and advance ratio. Once finished, shut down the tunnel speed, and save another rotational zero when the tunnel speed is below 10 knots, then bring down the RPM and save another stationary zero. Adjust the shaft tilt angle and repeat the process, until a tare case is obtained for each combination of rotor RPM, advance ratio and shaft tilt angle.

(a) Check tip path plane for tracking (b) Mount stub blades for taring

Fig. 3.14: Rotor tracking and taring [15].

3.3.3 Data Processing

The raw data from a wind tunnel test were first processed by a Butterworth filter [78] to remove high frequency harmonics beyond 20/rev. Then the time-aligned data were rearranged into azimuth-aligned: for a time-aligned data file, each sample within was assigned with an azimuth, which could be calculated from the magnetic shaft encoder directly, or derived from the 1/rev peak location of the optic sensor plus a time offset. One revolution of the rotor was divided into 360 segments of 1° azimuth, and all samples were sorted into the segments, then averaged in each segment to obtain a 360-element azimuth-aligned data file. In addition, the data from blade specific sensors (pitch/flap Hall sensors, pitch link gauges, blade instruments) were phase adjusted to match with the blade 1 data.

Sensors that had non-zero stationary readings (control mechanism, pitch/flap Hall sensors) did not require taring or zeroing, so the test data acquired in the collective sweep needed no further correction. The blade instruments and the wing balance required zeroing but no taring: the stationary zero (taken right before and

after the collective sweep) needed to be subtracted from the test data. The test data was azimuthal, and the stationary zero data could be averaged before the subtraction. The hub balance required both zeroing and taring. The test data (azimuthal) was subtracted by the test zero cases (averaged), and the tare data (azimuthal) was subtracted by the tare zero cases (averaged), then the zeroed test data (azimuthal) was subtracted by the zeroed tard data (azimuthal). The hub balance data were then corrected by the transfer functions gained from the dynamic calibration: The azimuthal data were discretized into harmonics. Each mode was corrected with the gain and phase shift from the dynamic calibration, then was assembled back into azimuthal domain.

The wall induced effect of the wind tunnel was modeled by a modified version of Glauert correction [79] for rotorcraft [80]. The average induced downwash $\Delta\alpha$ could be calculated by:

$$\Delta\alpha = \frac{2\delta_w C_T \pi R^2}{\mu^2 A_{TS}} \tag{3.5}$$

where δ_w is the boundary correction factor (dependent mostly on test section geometry, $\delta_w = 0.12$ for the current test [81]), C_T is the coefficient of rotor thrust, R is the rotor radius, μ is the advance ratio and A_{TS} is the test section area of the wind tunnel. According to the model, the effect of wind tunnel wall diminishes with advance ratio: the induced downwash is less than 0.1° at an advance ratio of 0.7.

Chapter 4: Data Correlation Study Methodology

Data correlation studies were conducted with previous test datasets, comprehensive analyses and CFD/CSD coupled analysis. The pressure data from earlier in-house wind tunnel tests [1] and the UH-60A wind tunnel test at NASA Ames [9] were compared to the current results. The comprehensive analysis UMARC focused on rotor performance, control angles and hub vibratory loads, while another comprehensive analysis PrasadUM was used as the structural model in the CFD/CSD analysis. The CFD/CSD analysis was performed with HAMSTR/PrasadUM, which emphasized blade pressure data, sectional airloads and structural loads. For the hingless rotor tests with a stub wing, the wing was analyzed with a vortex lattice model by AVL.

4.1 Comprehensive Analysis: UMARC

The University of Maryland Advanced Rotorcraft Code (UMARC) was used to provide analytical predictions of rotor performance, control angles and hub vibratory loads [70]. The analysis also generated fan plots with assigned rotor structural properties (see Chapter 2). A detailed description of the comprehensive analysis can be found in [82]. Previously, this comprehensive analysis has been validated

extensively against UH-60A wind tunnel test data [46], as well as against the in-house high advance ratio wind tunnel test data [13, 50, 63].

The blade structure dynamics was modeled as nonlinear, isotropic Euler-Bernoulli beam retaining second order terms. Finite element methods in space and time were used to discretize the blade structure and azimuthal time history respectively. In the current study, 20 elements were used in the spatial domain, each with 15 degrees of freedom to represent coupled axial, flap, lag, and torsional motions (4 for flap, 4 for lag, 3 for torsion and 4 for extension) [83]. In the time domain, 12 elements were spliced in a loop, each with 5th order polynomial representation. The equations of motion were solved by a variational approach, retaining 10 coupled modes [84].

The rotor aerodynamics was based on a quasi-steady lifting-line theory in conjunction with 2D airfoil look-up tables. The lift, drag, and pitching moment coefficients were from the test results of a wind tunnel test at NASA Langley [85]. The far wake was modeled by Maryland Free Wake (MFW), a subroutine developed from the Bagai-Leishman free wake model [86]. The wake was represented by a single trailer that sheds off the blade tip (blade deformation included) with a vortex strength of 70% maximum circulation strength along the blade span, with two turns of wake tracking and 15° of azimuthal discretization. The comprehensive analysis was also capable to include dual tip trailers, multiple trailers along the span and root trailer [13], although the current study only implemented single tip trailer. The near wake was modeled with the Weissinger-L representation [87], which trailed 30° azimuth in-plane with the rotor. A sweep mechanism was implemented to allow the

nearwake to move with the local flow velocity (precede the blade in the reverse flow region), improving on the inboard sections [84]. Sample wake geometries at $\mu = 0.5$ are shown in Fig. 4.1. The Leishman-Beddoes attached unsteady model [88] and dynamic stall model [49] were also implemented. The analysis did not account for fuselage, wing or root shank aerodynamics.

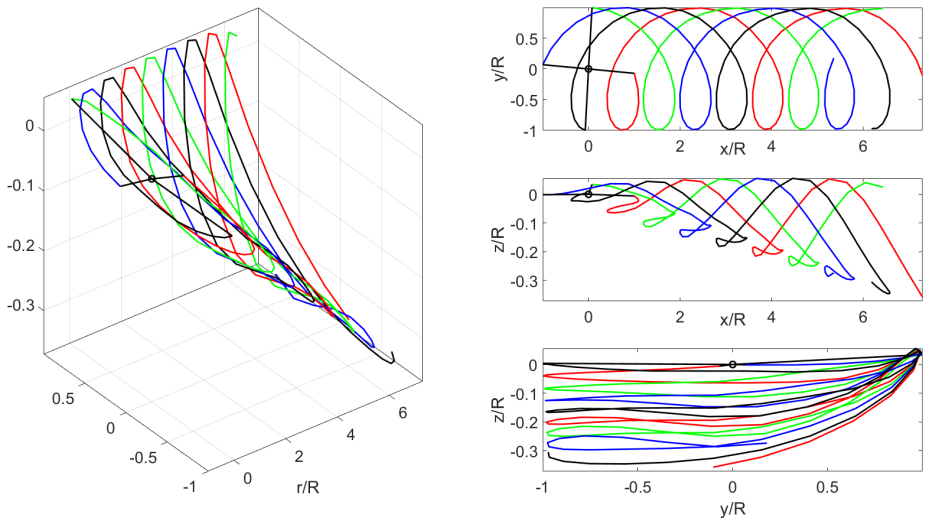

(a) Freewake

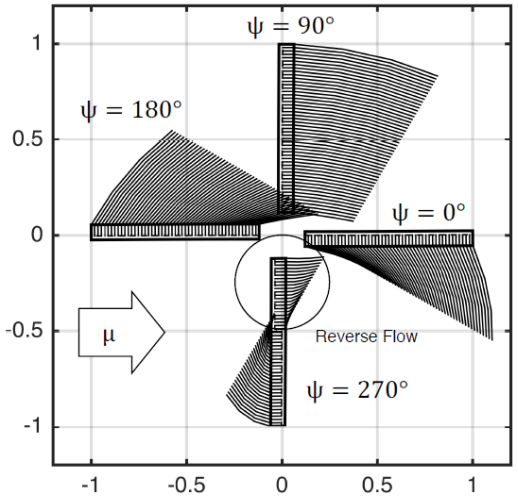

(b) Nearwake

Fig. 4.1: Sample freewake and nearwake geometries at $\mu = 0.5$, $\theta_0 = 8°$.

4.1.1 Trim Methodology

The trim algorithm of UMARC was based on Newton's method. The selected state variables (force and moment residuals) were calculated iteratively to acquire the blade deflections and control angles. In the default wind tunnel trim setup, a target thrust level were given, and the collective and the two cyclic angles were iterated to match the thrust and minimize the 1/rev flap angles. With the procedure, the thrust versus collective slope became flat at high advance ratios, resulting in collective mismatch [63].

A comparison of trim approaches was carried out: the full-prescribed trim set the collective and cyclic controls to calculate rotor response, only iterating on inflow rate; the semi-prescribed trim set the collective, and adjusted the two cyclic angles to minimize 1/rev flap angles; and the full-trim (default) only set a target thrust level, and trimmed to the target thrust and to zero 1/rev flap angles by adjusting the collective and the two cyclic angles. The results of the three trim setups are shown in Fig. 4.2. It can be observed that the full-prescribed method results in offset at zero collective and has poor correlation with the slope, while the full-trim method predicts very low collectives for a given thrust and the control variables deviate from the test data, and the method does not converge for negative thrust assigned. Therefore, the semi-prescribed method was chosen for all the articulated rotor analyses.

The semi-prescribed trim was also applied for hingeless rotor analyses, while the trim target became hub rolling and pitching moments instead of 1/rev flap

angles. For a hingeless rotor without lift offset, the trim target is to zero the two hub moment components. With lift offset, the moment induced by the wing is prescribed as the rolling moment target. For a hingless rotor, the trim with no wing and zero hub moments is referred as normal trim in the following chapters, and the trim with a wing-induced lift offset is referred as wing trim.

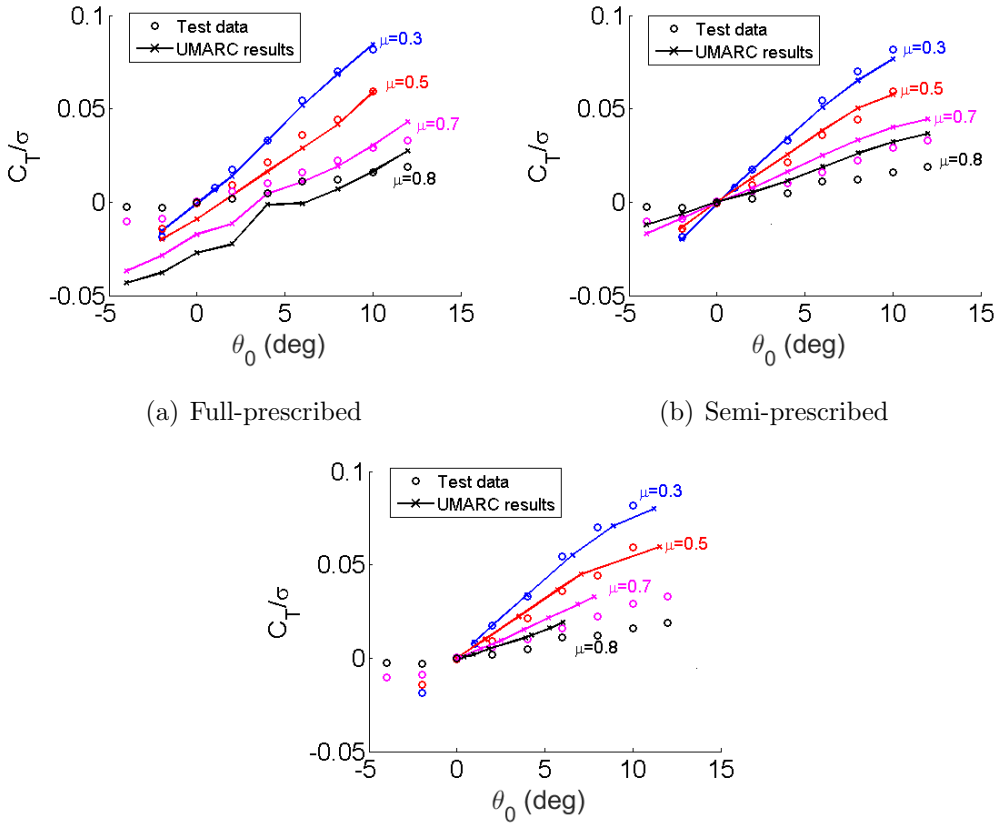

(a) Full-prescribed

(b) Semi-prescribed

(c) Full-trim

Fig. 4.2: Comparison of UMARC trim approaches.

4.2 Comprehensive Analysis: PrasadUM

Another comprehensive analysis, Parallelized Rotorcraft Analysis for Simulation and Design, University of Maryland (PrasadUM) was used in the current study,

mainly as the structural dynamics model for CFD/CSD coupling. It was chosen for the CFD/CSD coupled study because its data interface with HAMSTR was ready to use, while UMARC was only coupled with TURNS during the time [82, 89, 90].

PrasadUM was developed from the legacy code Heli-UM and inherited some common themes [91]. Similar to UMARC, PrasadUM used Euler-Bernoulli beam theory (with no ordering assumption) as the structural model and lifting-line theory with 2D airfoil look-up tables as the aerodynamic model [71]. It also used MFW as far wake model and the Weissinger-L representation as near wake model. The input files of PrasadUM were directly converted from the UMARC input files, so the number and division of structural elements and azimuthal elements were identical, and both analyses used 10 structural modes.

There are two major differences between UMARC and PrasadUM. First, PrasadUM uses harmonic balance to obtain simultaneous rotor-vehicle trim, making it capable for time marching simulation (maneuver), while UMARC uses Finite Element in Time (FET) so it only simulates periodical rotor behavior (steady trim). Second, PrasadUM uses a semi-implicit (partially numerical) formulation of the beam equations to avoid duplication in programming, while terms like acceleration and Coriolis force appear explicitly in the equations of motion in UMARC. PrasadUM also features CPU/GPU parallelization to accelerate the computations [71], and a wing model with finite wing theory [92]. The key similarities and differences between UMARC and PrasadUM are briefly summarized in Table 4.1.

Tab. 4.1: Similarities and differences between UMARC and PrasadUM.

Comprehensive Analysis	UMARC	PrasadUM
Structural model	Euler-Bernoulli beam	
Aerodynamic model	2D airfoil look-up tables	
Solving scheme	FET, (periodic)	Harmonic balance (with time marching)
Far wake model	MFW (Bagai-Leishman)	
Near wake model	Weissinger-L (with sweep mechanism)	Weissinger-L (rigid)
Unsteady aerodynamics	Leishman-Beddoes unsteady and dynamic stall	N/A
Wing aerodynamics	N/A	Finite wing theory
CFD/CSD coupling	TURNS	HAMSTR
Programming language	Fortran	
Computing unit	CPU	CPU/GPU (OpenMP+CUDA-Fortran)

4.3 CFD Analysis: HAMSTR

The next level of data correlation study involved CFD analysis. The study was performed with the in-house Hamiltonian/Strand flow solver (HAMSTR). It is a compressible finite volume Reynolds-averaged Navier-Stokes code with a Spalart-Allmaras turbulence model [93]. The inviscid fluxes were computed using 5th order Weighted Essentially Non-Oscillatory (WENO) scheme and the viscous fluxes were computed using 2nd order central differencing. The solver used 2nd order backward time stepping method.

In the mesh domain, each rectangular blade was modeled with blunt tip to represent the experimental blade accurately. The domains of blades and hub/shaft were discretized based on mixed triangular-quadrilateral surface elements (Fig. 4.3). For each blade surface, the structured mesh comprised of 200 points in the chordwise

direction and 101 points in the spanwise direction. A total of 21,928 quadrilaterals were used including the blade tip region. The blade mesh was extruded in the wall-normal direction for the volume mesh using 47 strand layers where the initial wall normal spacing was 5×10^{-5} of chord length ($y^+ = 0.7$). The blade-grid dimensions were similar to the dimensions of a refined mesh [94], where a grid independence study was conducted using RANS simulation for high-speed UH-60A rotor airload correlation study. For the hub/shaft volume mesh, a total of 510,488 hexahedra were used with the same wall normal spacing as the blade mesh, which consisted of 11,602 quadrilaterals on the surface.

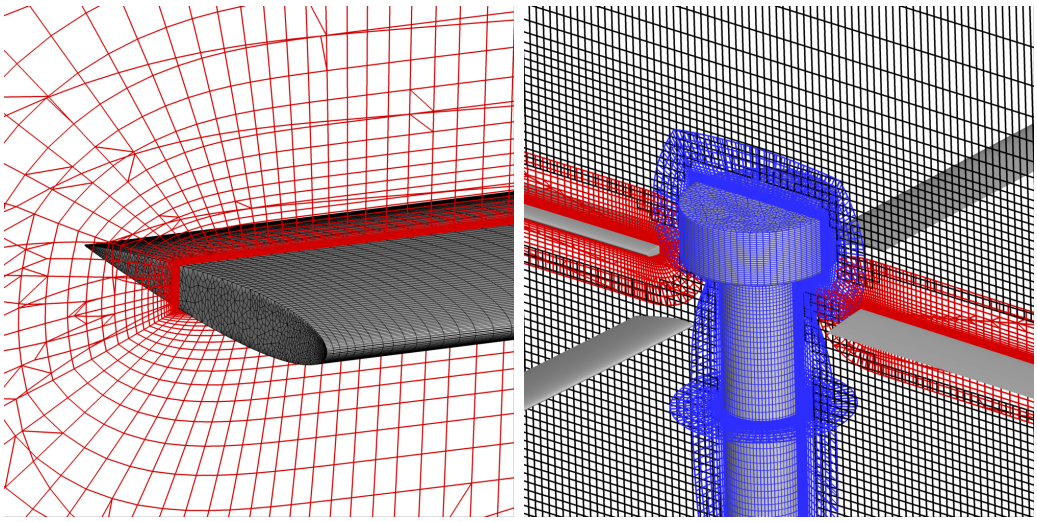

(a) Mesh at the blade tip (b) Model for the hub/shaft

Fig. 4.3: Mesh system of the CFD study, blade tip and hub/shaft model.

The near-body domains of rotor blades and hub/shaft were embedded in the off-body Cartesian domain where the constant grid spacing of 10% chord length was used around the rotor. The current wake-grid spacing was selected to match an efficient grid spacing of typical rotor simulation using RANS [95]. In the overlap

region, a similar grid spacing with off-body domain was used for the near-body domains. A total of 4.6 million and 4.4 million elements were used in the near-body and off-body domains, respectively. As the blade domains rotating in the stationary background domain, the connectivity at overset boundaries was re-calculated at each time step. For the current simulations, a 1° time step size with 15 dual-time-steps was used. This provided acceptable sub-iteration residual drops of a minimum one-order magnitude between time steps for all domains as well as the minimized computational cost for the reconnection at overset boundaries.

4.3.1 Coupling Methodology

The initial stage of CFD analysis was prescribed-motion CFD, in which the blades were treated as rigid bodies and the flap and pitch angle azimuthal histories were prescribed using the wind tunnel test data (from the Hall sensors at the blade roots). The rotor hub and shaft solid body were not implemented in this stage. The prescribed-motion CFD analysis was an intermediate step between comprehensive analysis and CFD/CSD coupled study. The study focused on a representative high advance ratio, high collective case (700 RPM, $\mu = 0.8$, $\theta_0 = 11°$), and emphasized surface pressure and airload predictions.

The following stage was coupled CFD/CSD analysis with the hub/shaft assembly. HAMSTR was used for the CFD part, and PrasadUM was used for the CSD part. A dynamically deforming mesh technique was used in the CFD part to consider blade deflections, which was based on algebraic method [96]. Delta-coupling process was used for airload correction [94], and a diagrammatic flow chart

is shown in Fig. 4.4. The cyclic control angles were used as indicators of convergence, and the iteration usually converge in 4-5 steps (see Fig. 4.5). The CFD analysis was more computationally expensive than the comprehensive analysis, so four representative cases at two collective settings ($\theta_0 = 3°$ and $11°$) and two shaft tilt settings ($\alpha_s = 0°$ and $2°$) were studied at 700 RPM, $\mu = 0.8$. The data correlation study with CFD/CSD analysis was primarily focused on surface pressure and airload data, while rotor performance and control, and blade structural load data were also analyzed.

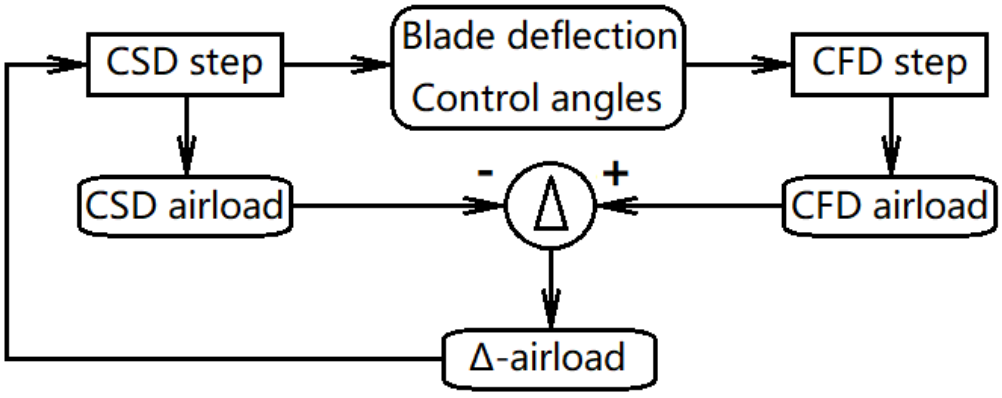

Fig. 4.4: A simplified flow chart of the CFD/CSD coupled analysis.

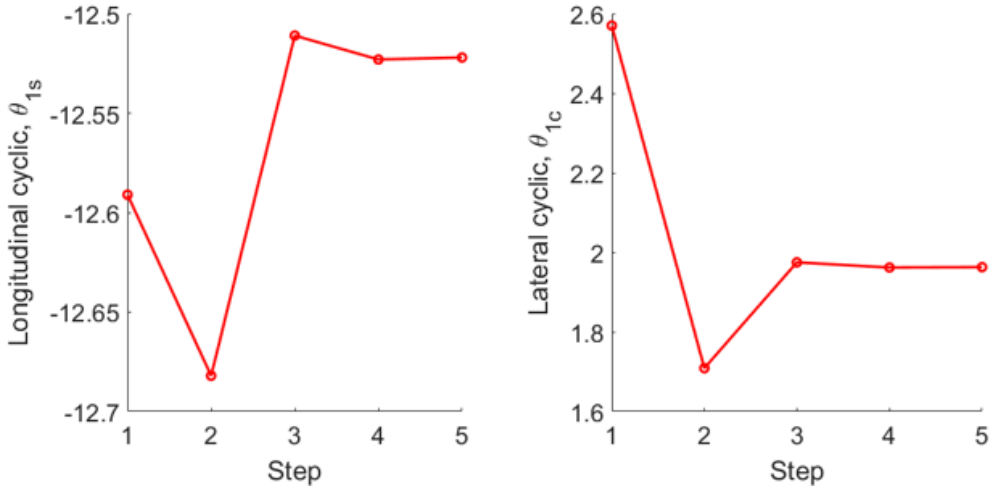

(a) θ_{1s} (b) θ_{1c}

Fig. 4.5: Convergence history of cyclic angles at 700 RPM, $\mu = 0.8$, $\theta_0 = 11°$.

4.4 Wing Analysis: AVL

To set up a data correlation study for a hingless rotor with lift offset, evaluating the force on the wing is critical in predicting the overall performance. The prediction of wing performance was conducted with the Athena Vortex Lattice code (AVL), plus the free wake output from the UMARC rotor prediction. AVL is a program for aerodynamic and flight-dynamic analyses developed by the Massachusetts Institute of Technology. It is suitable for arbitrary wing planform, airfoil and flight state by employing an extended vortex lattice model [92] for the lifting surfaces, together with a slender-body model for fuselages and nacelles [97]. A correction on angle of attack was applied to model the effect of rotor-induced downwash on the wing. First, the wing planform was built as a 12×8 vortex lattice system, and appropriate airfoil were specified in AVL. Then, simulations were conducted at various angles

of attack to determine the lift and drag with respect to angle of attack. Next, the wake geometry and vortex strength outputs from UMARC were used to integrate the rotor-induced velocity along the wake at a specific spanwise location and azimuth with the Biot-Savart law:

$$\vec{v}_{induced}(b,\psi) = \int \frac{\Gamma d\vec{l} \times \vec{r}}{4\pi|\vec{r}|^3} \tag{4.1}$$

where $\vec{v}_{induced}$ is the rotor-induced velocity on the wing, b is the spanwise location on the wing, ψ is the rotor azimuth, Γ is the vortex strength, $\vec{l}$ is the vector along the axis of the infinitesimally small vortex segment, and $\vec{r}$ is the vector from the vortex element to the wing location. For each spanwise location on the wing, the vertical components of all four blade tip vortices were sum up, then averaged over the wing span and azimuth:

$$v_{induced-mean} = \sum_{n=1}^{N_b} \int \int v_{induced-z}(b,\psi) dbd\psi \tag{4.2}$$

Then, the averaged vertical velocity component was combined with the freestream speed to obtain the rotor-induced angle of attack reduction on the wing:

$$\alpha_{induced-mean} = atan(\frac{v_{induced-mean}}{V_\infty}) \tag{4.3}$$

Finally, the angle of attack correction was applied to the AVL results to determine the lift and drag values under the rotor downwash, which were in turn used to estimate the wing performance. Sample rotor-induced downwash of a single blade

and sum of all blades are shown in Fig. 4.6.

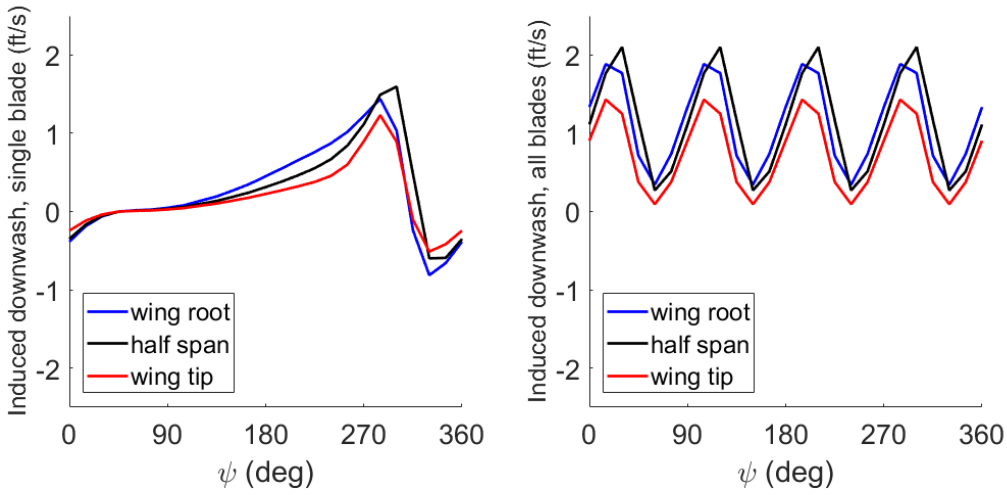

(a) Effect of a single blade

(b) Sum of all blades

Fig. 4.6: Rotor-induced downwash on wing at 700 RPM, $\mu = 0.5$, $\theta_0 = 8°$.

Chapter 5: Articulated Rotor Results

The results of three wind tunnel tests on articulated rotors are discussed in this chapter. The third test featured non-instrumented blades with high blade similarity to obtain a baseline performance dataset. The test was conducted at 900 and 1200 RPM and reached the highest advance ratio ($\mu = 0.9$) among the six wind tunnel tests. The results of rotor performance, pitch controls, and hub vibratory loads are mostly from the third test, except in the CFD comparison section the results are from the second test. The test data are presented with the predictions from comprehensive analysis (UMARC).

In the second test, blade-embedded pressure sensors and strain gauges were implemented, and the primary focus of the test was integrated airloads at 30% radius. The test was conducted at 700 and 1200 RPM, up to an advance ratio of 0.8. The results of surface pressure, airloads and blade structural loads are from this test. Data correlation studies were performed with CFD/CSD coupled analysis (HAMSTR/PrasadUM) in addition to comprehensive analysis (UMARC and PrasadUM).

5.1 Performance and Control

The force and moment on the rotor hub were monitored by the 5-component hub balance, and the three control angles were derived by the swashplate displacement from LVDTs. In each test case, the data were acquired for 5 seconds at a sampling rate of 5000 per second. The raw test data were then averaged and compared with the prediction of comprehensive analysis. The comprehensive analysis also provided the airload data that are challenging to measure directly across the rotor disk (although it is possible to measure at a specific spanwise location, see pressure and airload section). At each blade element, normal force $c_n M^2$ and chordwise force $c_c M^2$ were calculated via analysis. Combined with local pitch angle θ_{local}, the sectional force results can be rewritten into vertical force $c_z M^2$ and in-plane force $c_{in} M^2$, which correspond to rotor thrust and shaft torque. On the rotor disk, the X-component of $c_{in} M^2$ can be separated out as $c_x M^2$, which corresponds to rotor horizontal force. The geometric representations of above parameters are shown in Fig. 5.1, and the calculations are shown in the following equations:

$$c_z M^2 = c_c M^2 sin\theta_{local} + c_n M^2 cos\theta_{local} \tag{5.1}$$

$$c_{in} M^2 = c_c M^2 cos\theta_{local} - c_{in} M^2 sin\theta_{local} \tag{5.2}$$

$$c_x M^2 = -c_{in} M^2 sin\psi \tag{5.3}$$

These airload parameters are discussed as intermediate indicators of rotor behavior: if the test results show a trend in performance or hub vibratory load and the predicted results agree with the trend, then the corresponding parameter can be investigated to isolate the key areas of interest on the rotor disk, and investigate the mechanism behind the trend.

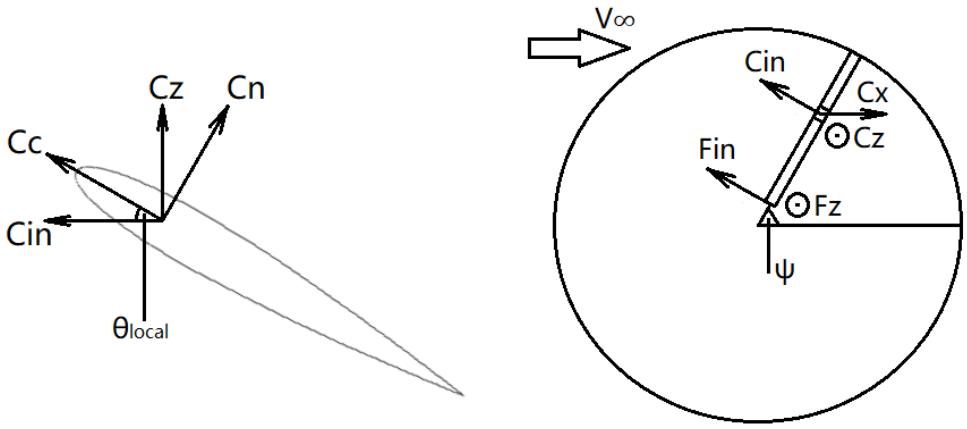

(a) Blade element (b) Rotor disk

Fig. 5.1: A diagram of intermediate parameters to study rotor performance.

5.1.1 Thrust

The thrust versus collective results at various advance ratios and shaft tilt angles are shown in Fig. 5.2. In Fig. 5.2(a), collective sweeps at 900 RPM and 1200 RPM are presented together at zero shaft tilt angle. In Fig. 5.2(b), 900 RPM data are shown with three different shaft tilt angles at $\mu = 0.7$. Solid lines indicate predictions from comprehensive analysis, while symbols represent test data. Multiple points at certain collectives are the results of repeated measurements during the collective sweeps. Similar test cases are presented for horizontal force, shaft torque and lift-to-

drag ratio respectively. The thrust versus collective trend is quite linear, especially at low collectives. The lifting slope decreases with increasing advance ratio, because the rotor needs to balance the loss of lift in the reverse flow region, making it less effective in producing lift even on the advancing side. At $\mu = 0.7$, the rotor loses about 66% of thrust compared to at $\mu = 0.3$ (at $\theta_0 = 8°$, C_T/σ is 0.025 compared to 0.073). At $\mu = 0.9$, the rotor generates almost no net thrust ($C_T/\sigma < 0.01$) regardless of collective setting, indicating the onset of thrust reversal with higher advance ratios (Fig. 5.2(a)). The predicted results are satisfactory at moderate collectives and advance ratios. The comprehensive analysis tends to predict an earlier stall ($\theta_0 \geq 8°$,) than the test results, and data correlation degrades at high advance ratios ($\mu \geq 0.7$), in which the unsteady phenomenon prevails. In the shaft tilt study, the rotor produces more thrust when tilting backward and less thrust when tilting forward (Fig. 5.2(b)). The thrust increment due to backward shaft tilt angle does not change much with different collective setting. At $\theta_0 = 8°$ and 4° backward shaft tilt, the thrust level is doubled compared to zero shaft tilt case (C_T/σ is 0.050 compared to 0.025). This trend is also predicted by the comprehensive analysis.

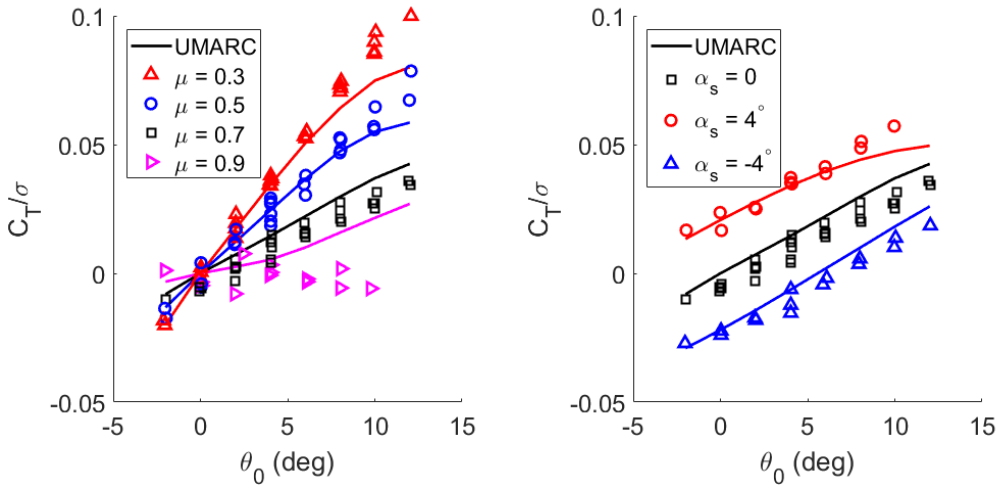

(a) Different μ at zero shaft tilt

(b) Different shaft tilts at $\mu = 0.7$

Fig. 5.2: Articulated rotor thrust vs. collective.

To understand the effect of shaft tilt angle on rotor thrust, the vertical airload $c_z M^2$ with and without shaft tilt across the rotor disk are shown in Figs. 5.3(a) and 5.3(b), and the difference of $c_z M^2$ between them is shown in Fig. 5.3(c) (the case with backward shaft tilt minus the case with zero tilt). The results shown are 900 RPM, $\mu = 0.7$, $\theta_0 = 8°$ at 0° and 4° backward shaft tilt angles. Red on the contour plots indicates positive vertical force, and blue indicates negative vertical force due to reverse flow (on the retreating side) and trimming (on the advancing side). The vertical force increases in the fore and aft area with backward shaft tilt, and decreases in the reverse flow region and the outboard section of advancing side. The change in the inflow condition can provide a simplified explanation for this behavior. With backward shaft tilt, a rotor acts like it is cruising forward while descending at a rate of $V_\infty sin\alpha_s$. The change of the inflow condition leads to increased angle of attack all over the rotor disk, raising $c_z M^2$ on most of the disk

area. However, the increased angle of attack induces more negative vertical force in the reverse flow area, and the stall region near the reverse flow area is insensitive to angle of attack change. Therefore, the advancing side must be trimmed to lower the vertical force such that the rotor is balanced. The overall improvement in thrust is explained by summing $c_z M^2$ across the rotor disk.

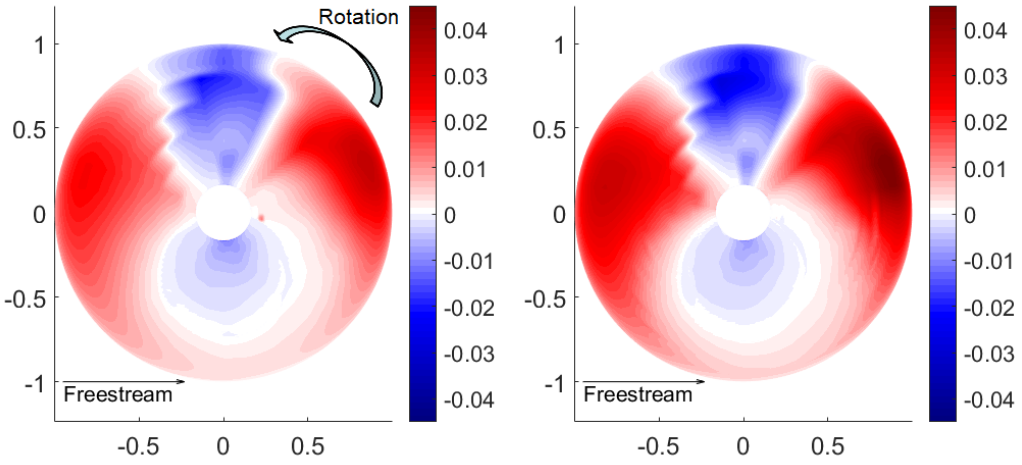

(a) Zero shaft tilt

(b) 4° backward shaft tilt

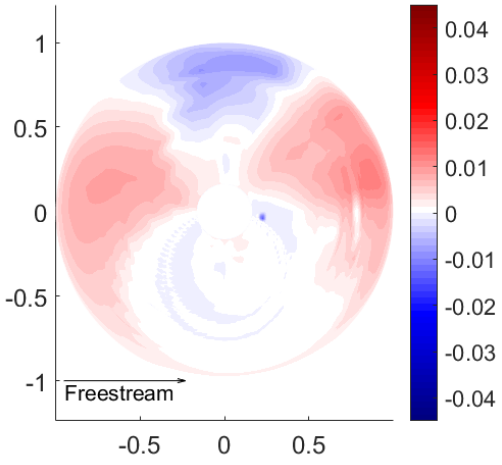

(c) $\delta c_z M^2$ due to 4° backward tilt

Fig. 5.3: Vertical airload distribution $c_z M^2$ at $\mu = 0.7$, $\theta_0 = 8°$.

5.1.2 Horizontal Force

The rotor horizontal force results for various advance ratios and shaft tilt angles are shown in Fig. 5.4. The drag due to fuselage and blade shanks were removed using the tare data. The high scatter level is due to the small magnitude (< 5 lb maximum) of the measured quantity. Figure 5.4(a) shows that the horizontal force decreases with collective at lower advance ratios and increases with collective at higher advance ratios. At low advance ratios, the horizontal force points upstream of the freestream direction at high collective, while at high advance ratios, the force is downstream, and the magnitude becomes more sensitive to advance ratio. The trends are predicted qualitatively by the comprehensive analysis, but discrepancies increase at high collective settings ($\theta_0 \geq 8°$) and high advance ratios ($\mu \geq 0.7$). The shaft tilt study results are shown in Fig. 5.4(b). The test data show that horizontal force increases slightly with forward shaft tilt and decreases with backward shaft tilt, and the patterns are observed in the predictions. The changes in horizontal force are small compared to the discrepancies between test data and predicted results.

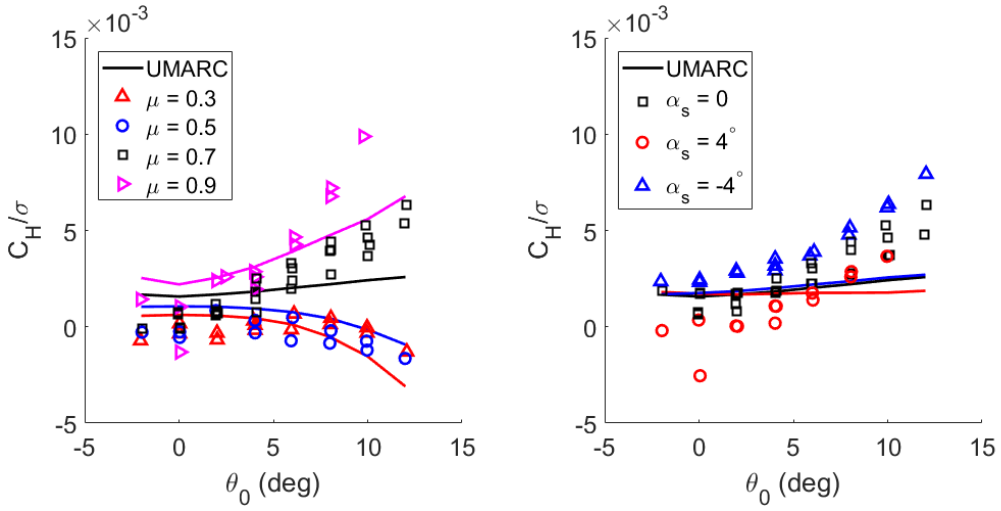

(a) Different μ at zero shaft tilt

(b) Different shaft tilts at $\mu = 0.7$

Fig. 5.4: Articulated rotor horizontal force vs. collective.

To understand why the horizontal force reacts differently with respect to collective at different advance ratios, the airloads in the X-direction $c_x M^2$ across the rotor disk for two collective settings ($\theta_0 = 4°, 8°$) and two advance ratios ($\mu = 0.3, 0.7$) are shown in Figs. 5.5(a) to 5.5(d), and the differences in $c_x M^2$ due to collective changes at each advance ratio are shown in Figs. 5.5(e) and 5.5(f) (high θ_0 minus low θ_0). All the cases are at 900 RPM with zero shaft tilt. Red on the contour plots indicates downstream force (drag), and blue indicates upstream force (propulsive). At $\mu = 0.3$, the X-direction force is downstream on the advancing side and is mostly upstream on the retreating side because of the weak reverse flow. As collective increases from 4° to 8°, both local pitch and angle of attack increase. On the retreating side, the local pitch is higher due to the trim condition (see cyclic control results), so the $c_n M^2 sin\theta_{local}$ term is predominant for in-plane airload. Therefore, the in-plane force is more toward the trailing edge and the X-direction force becomes

more upstream. On the contrary, the local pitch and pitch increment are low due to the trim condition, especially in the fore section. When the local pitch is sufficiently low, the $c_c M^2 cos\theta_{local}$ term for in-plane airload dominates. Then, the in-plane force is more toward the leading edge and the X-direction force becomes more upstream in the low pitch area of the advancing side. Summing $c_x M^2$ together, the overall horizontal force is more upstream at $\mu = 0.3$. The major difference at $\mu = 0.7$ is that the reverse flow becomes much stronger, and the in-plane airload is always toward the leading edge in this area, pushing the rotor downstream. As collective increases from 4° to 8°, the downstream force increases significantly, because of the large increment in local pitch due to collective change and trim condition. On the advancing side, the local pitch and angle of attack are negative near $\psi = 90°$, and they become more negative with the increment of collective due to the trim condition, inducing more downstream force. Summing $c_x M^2$ together, the horizontal force is slightly increased downstream at $\mu = 0.7$. One can expect that the horizontal force becomes more downstream with increased collective at higher advance ratios.

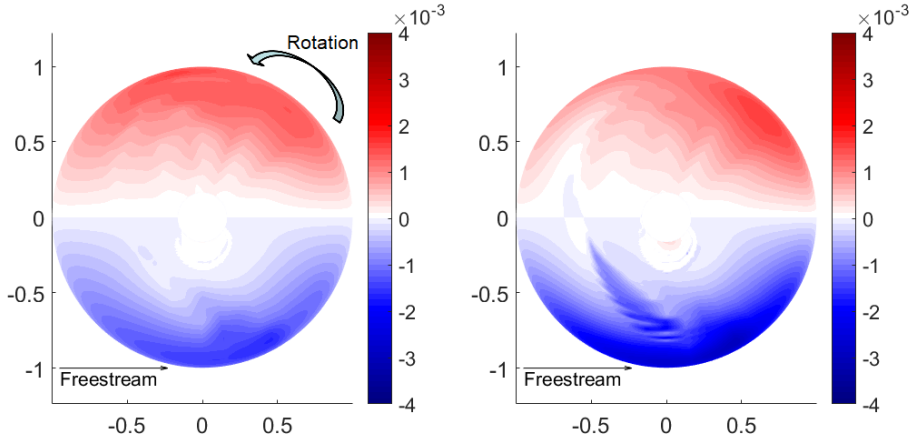

(a) $\mu = 0.3, \theta_0 = 4°$ (b) $\mu = 0.3, \theta_0 = 8°$

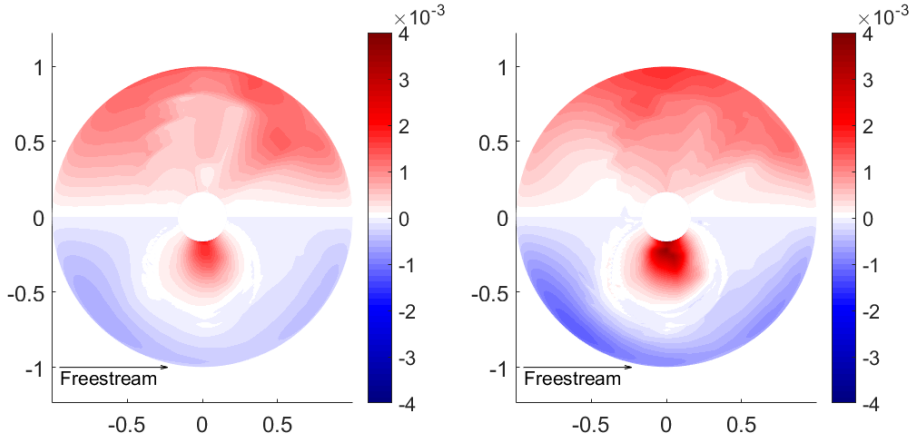

(c) $\mu = 0.7, \theta_0 = 4°$ (d) $\mu = 0.7, \theta_0 = 8°$

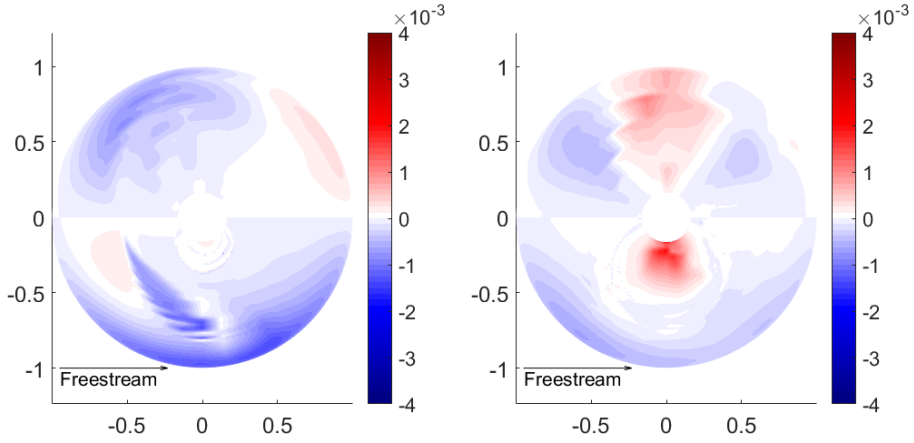

(e) $\delta c_x M^2$ due to θ_0 change at $\mu = 0.3$ (f) $\delta c_x M^2$ due to θ_0 change at $\mu = 0.7$

Fig. 5.5: X-direction airload distribution $c_x M^2$ at zero shaft tilt.

5.1.3 Shaft Torque

The shaft torque results for various advance ratios and shaft tilt angles are shown in Fig. 5.6. Figure 5.6(a) shows that the shaft torque increases with collective at lower advance ratios, though the increment becomes smaller with higher advance ratio. With $\theta_0 = 8°$, the rotor requires 27% less shaft torque at $\mu = 0.7$ compared to at $\mu = 0.3$ (C_Q/σ is 0.0027 compared to 0.0037). At $\mu = 0.9$, the shaft torque becomes insensitive to collective change. Figure 5.6(b) shows the trend of torque with different shaft tilt angles. With shaft tilt either backward or forward and low collective settings, the shaft torque is reduced compared to that of zero shaft tilt, but the torque with shaft tilt rises faster with increasing collective, catching up with that of zero shaft tilt at higher collectives. The shaft torque of 4° backward tilt setup surpasses that of zero shaft tilt at $\theta_0 = 8°$, while the shaft torque of 4° forward tilt reaches the level of zero shaft tilt at about $\theta_0 = 12°$. Similar to the thrust predictions, the predicted results are satisfactory at moderate advance ratios ($\mu \leq 0.7$) and collective ($\theta_0 \leq 10°$). The predictions tend to underestimate the torque at higher collective and to overestimate the torque at higher advance ratio. The predictions also capture the trend of shaft torque change with different shaft tilt angles.

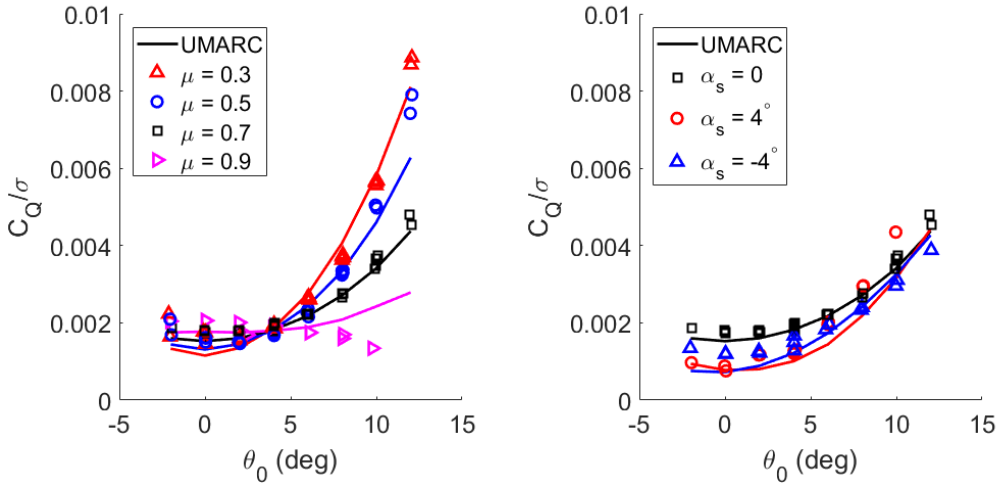

(a) Different μ at zero shaft tilt

(b) Different shaft tilts at $\mu = 0.7$

Fig. 5.6: Articulated rotor shaft torque vs. collective.

The airload distribution on in-plane tangential force $c_{in}M^2$ is evaluated to investigate the mechanism of shaft torque reduction with increasing advance ratio. The results at 900 RPM, $\theta_0 = 8°$, $\mu = 0.3$ and 0.7 are shown in Figs. 5.7(a) and 5.7(b), and the difference of $c_{in}M^2$ between them is shown in Fig. 5.7(c) (high μ minus low μ). Red on the contour plots indicates in-plane force towards the leading edge, and blue indicates in-plane force toward the trailing edge. At $\mu = 0.3$, the in-plane force is in the direction of the trailing edge, resulting in net drag on the rotor. At $\mu = 0.7$, the most significant change is that the in-plane force on the inboard section of the retreating side changes direction because of the reverse flow region. This effect is the primary contributor of the reduced shaft torque. With increasing advance ratio, the airflow with respect to the airfoil increases on the advancing side and decreases on the retreating side (not including the reverse flow region), causing more in-plane force towards the trailing edge on the advancing side and less on the

retreating side. In the fore and aft section of the rotor, the effect of free stream speed is relatively small, so the indicated in-plane force change is due to the cyclic angle predictions.

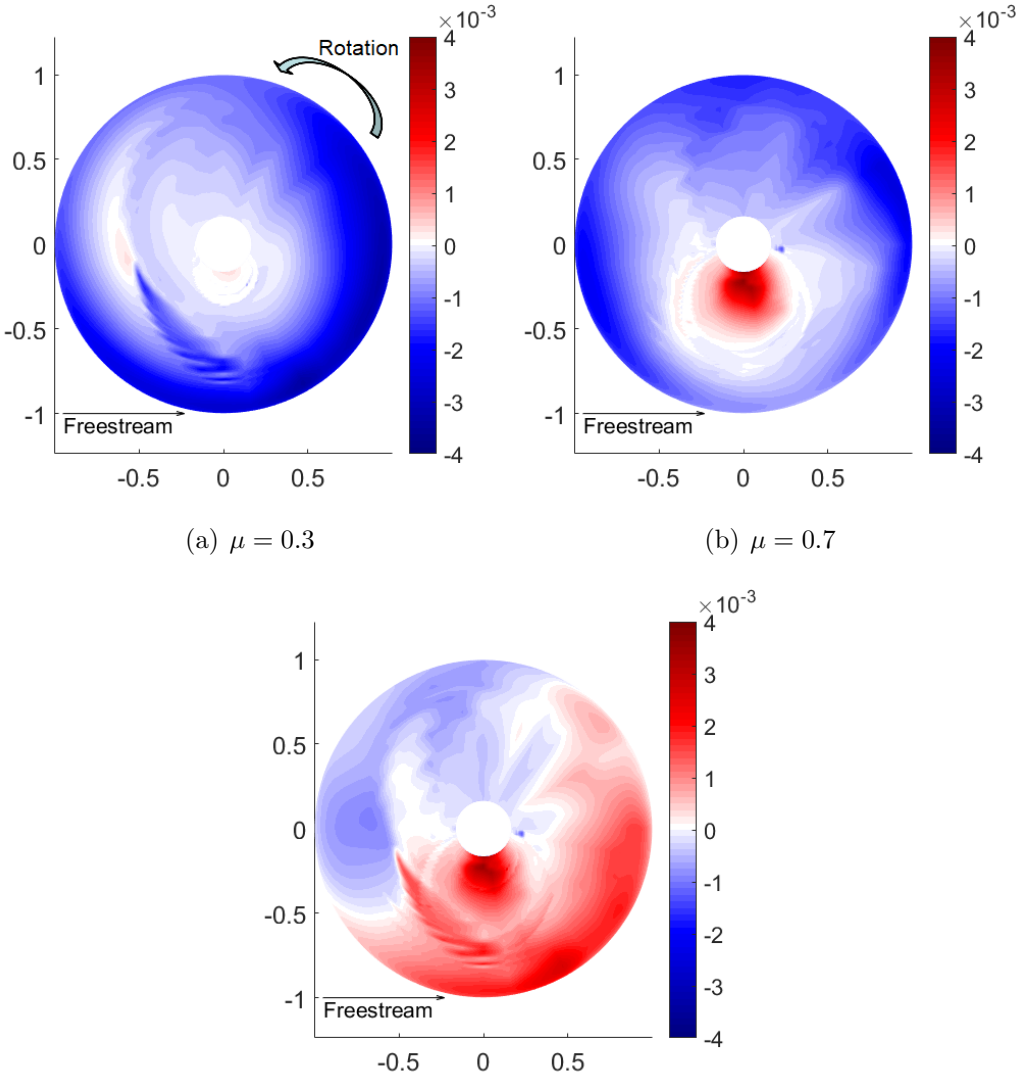

(a) $\mu = 0.3$

(b) $\mu = 0.7$

(c) $\delta c_{in} M^2$ due to higher μ

Fig. 5.7: In-plane airload distribution $c_{in} M^2$ at $\theta_0 = 8°$, zero shaft tilt.

5.1.4 *Lift-to-Drag Ratio*

A key parameter to characterize the performance of a rotor in forward flight is the effective lift-to-drag ratio L/D_e, which is defined by:

$$L/D_e = \frac{L_{rotor}}{D_{rotor} + \frac{Q_{rotor}}{R\mu}} \tag{5.4}$$

With shaft tilt angle α_s considered, the equation becomes:

$$L/D_e = \frac{T_{rotor}cos\alpha_s - H_{rotor}sin\alpha_s}{H_{rotor}cos\alpha_s + T_{rotor}sin\alpha_s + \frac{Q_{rotor}}{R\mu}} \tag{5.5}$$

The effective lift-to-drag ratio versus thrust is presented in Fig. 5.8. As shown in Fig. 5.8(a), the highest L/D_e occur at $\mu = 0.5$ and decreases rapidly with higher advance ratios at zero shaft tilt. At high advance ratios, both L/D_e and maximum thrust are limited ($L/D_e < 2$ at $\mu = 0.9$). The shaft tilt study shows that a backward tilt helps to improve both L/D_e and maximum thrust (Fig. 5.8(b)), allowing the rotor to operate more efficiently at higher advance ratios. Note that the backward shaft tilt provides a better L/D_e even at a same thrust level as for zero shaft tilt. From Figs. 5.2(b) and 5.6(b), the rotor with backward shaft tilt can generate the same thrust with lower collective to save some shaft power. The predictions of comprehensive analysis capture the overall trends at various advance ratios and shaft tilt angles, but the data correlation tends to degrade at the high thrust levels.

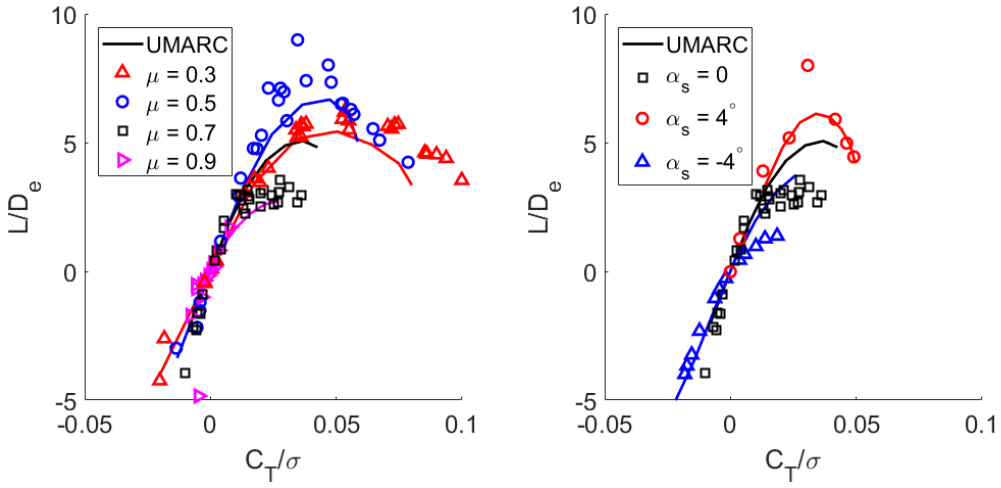

(a) Different μ at zero shaft tilt

(b) Different shaft tilts at $\mu = 0.7$

Fig. 5.8: Articulated rotor effective lift-to-drag ratio L/D_e vs thrust C_T/σ.

5.1.5 Cyclic Control Angle

Figure 5.9 shows the cyclic control angles to trim the rotor for various advance ratios at zero shaft tilt. The lateral cyclic angle θ_{1c} increases about 5° with increasing collective at all advance ratios, while negative longitudinal cyclic angle θ_{1s} is required to balance the significant lift loss in the reverse flow region with higher advance ratios. With increasing advance ratio, a larger negative longitudinal cyclic angle is required. At $\mu = 0.7$, the magnitude of longitudinal cyclic becomes greater than the collective angle (about $-13°$ at $\theta = 12°$), indicating negative local pitch on the advancing side. The predictions are satisfactory for longitudinal cyclic and discrepancies occurs for lateral cyclic, especially at lower advance ratios ($\mu \leq 0.5$). The control angle predictions are helpful for generating initial trim guesses: simulations were carried out before the wind tunnel test to gain estimation of trim control inputs, in order to speed up the trimming process during the test.

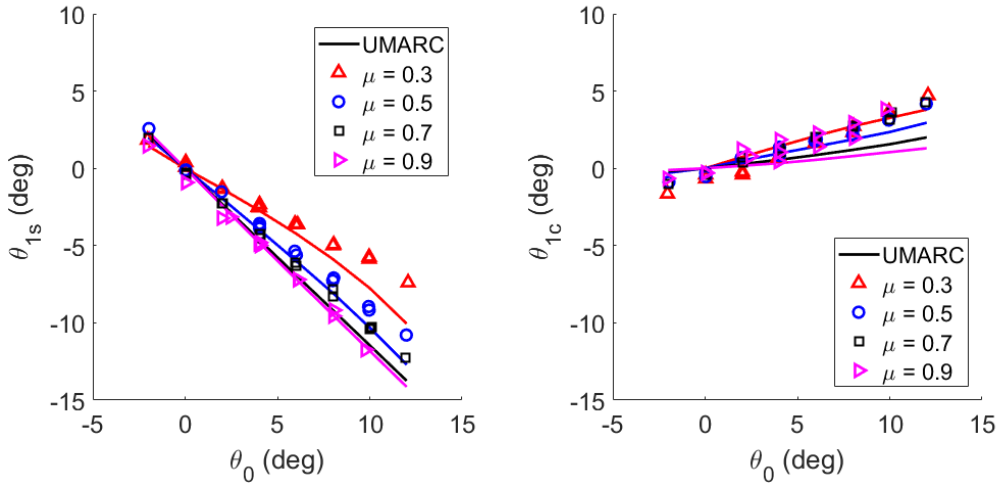

(a) θ_{1s} (b) θ_{1c}

Fig. 5.9: Articulated rotor cyclic control angles vs collective at zero shaft tilt.

5.1.6 CFD/CSD Performance Comparison

CFD/CSD coupled analysis was carried out for four cases in the second test on articulated rotor. The primary objective of the study was to generate surface pressure predictions to compare with pressure sensor data, while rotor performance and control were also predicted. The test cases are at 700 RPM, $\mu = 0.8$, $\theta_0 = 3°$ and $11°$, $\alpha_s = 0°$ and $2°$. The results are shown on Fig. 5.10 for rotor thrust, shaft torque and the two control cyclics, where hollow symbols are the test data, solid lines are the results from free wake analysis (UMARC) and solid diamond symbols are the results from CFD/CSD analysis (HAMSTR/PrasadUM). The accuracy of CFD/CSD analysis is on par with that of comprehensive analysis on rotor performance, with all major trends with backward shaft tilt captured. With CFD/CSD analysis, the data correlation quality is improved for shaft torque, especially at $\theta_0 = 11°$. The most notable discrepancy is still in the lateral cyclic prediction (Fig. 5.10(d)). Compared

to the test data, the CFD/CSD results are quite similar to the comprehensive analysis results, showing only limited improvement in data correlation. The aerodynamic effect due to the rear part of the test stand may be a contributor of the lateral cyclic discrepancy, which is not modeled in the analysis.

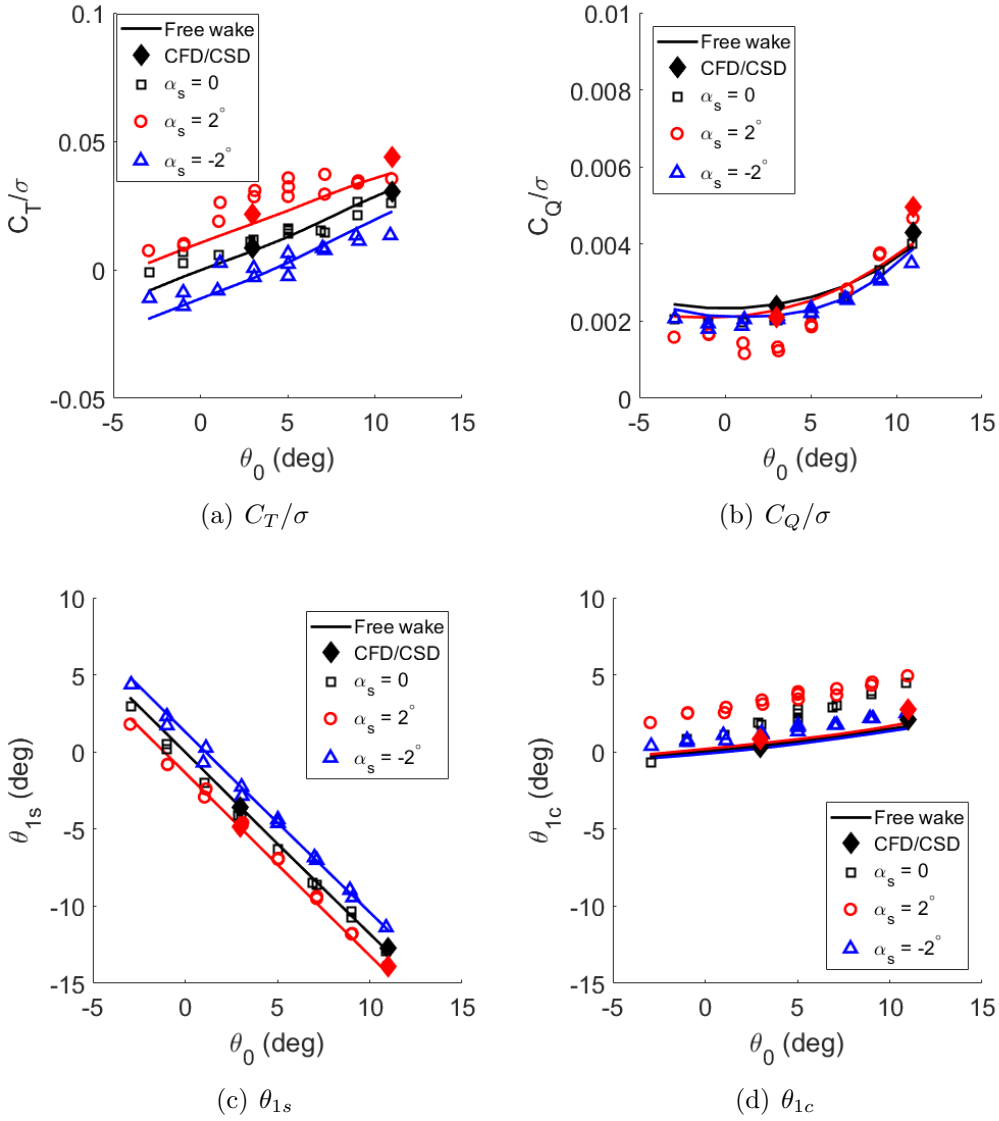

(a) C_T/σ (b) C_Q/σ

(c) θ_{1s} (d) θ_{1c}

Fig. 5.10: CFD/CSD predictions on articulated rotor performance at 700 RPM, $\mu = 0.8$.

5.2 Trim Quality Study

For a rotor with perfect balancing, tracking and trimming, all the test blades should follow an identical tip path, wherein the 1/rev flap motion is eliminated. In wind tunnel tests, two factors may degrade this condition: root pitch angle discrepancy and blade dissimilarity. With slightly different pitch angles due to swashplate and pitch link looseness, the aerodynamic force on different blades would vary. The blade dissimilarity can be due to both aerodynamic and structural aspects: differences in airfoil geometry alter the airloads on each blade, while differences in stiffness and mass distribution affect the structural response of each blade. To investigate how these terms affect the trim condition, the flap and pitch angles at blade roots were monitored with Hall sensors individually during the test. Ideally, the root pitch angle of each blade should be exactly the same (after phase shift), and the 1/rev flap angle should be completely eliminated, but discrepancies were observed in the experimental results. The azimuthal histories of root pitch and flap at 900 RPM, $\mu = 0.7$, $\theta_0 = 4^\circ$ with zero shaft tilt are shown in Fig. 5.11 as a sample dataset, where each color represents an individual blade.

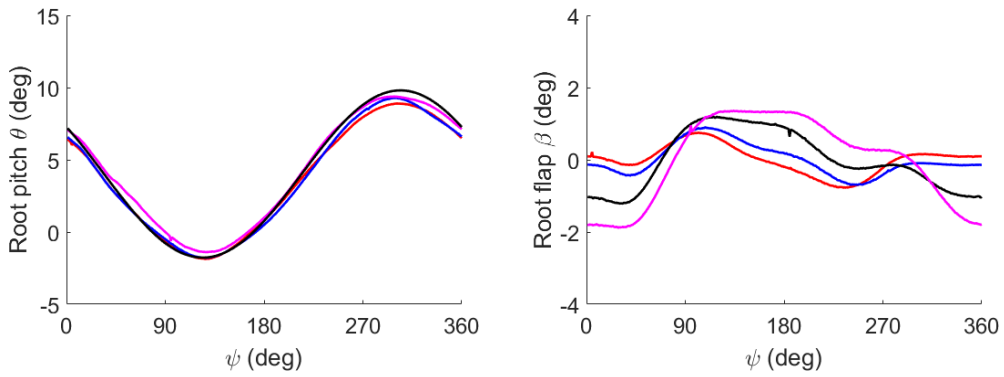

(a) Root pitch (b) Root flap

Fig. 5.11: Sample azimuthal history of root pitch and flap angle.

5.2.1 Pitch Angle

To characterize the root pitch discrepancy evident in the test data, two parameters were tracked: one is azimuthal averaged pitch angle, which is the representation of the collective angle; the other is the magnitude of the 1/rev pitch angle, which is the representation of the cyclic angles. The variations of these parameters with collective angle sweeps at 900 RPM and zero shaft tilt are presented in Fig. 5.12. The mean variation is lowest at about 4° and becomes worse in both directions. At high advance ratios and high collective settings, this variation can be greater than 1°. The 1/rev variation is lower ($< 0.2°$) at low collective, but it also increases when the collective reaches 10°. Both variations became worse at higher advance ratios for most cases. The large mean variation at high advance ratios is partially due to the pitch link adjustment during the tracking, in which case, trade root pitch consistency for tip path plane consistency. It provides evidence that the effect of dissimilarity presents in some level and becomes more significant at higher advance ratios, otherwise identical root pitch means identical tip path planes and no tradeoff

is needed. The exacerbated vibration at higher advance ratios may also contribute to these discrepancies, especially at high collectives.

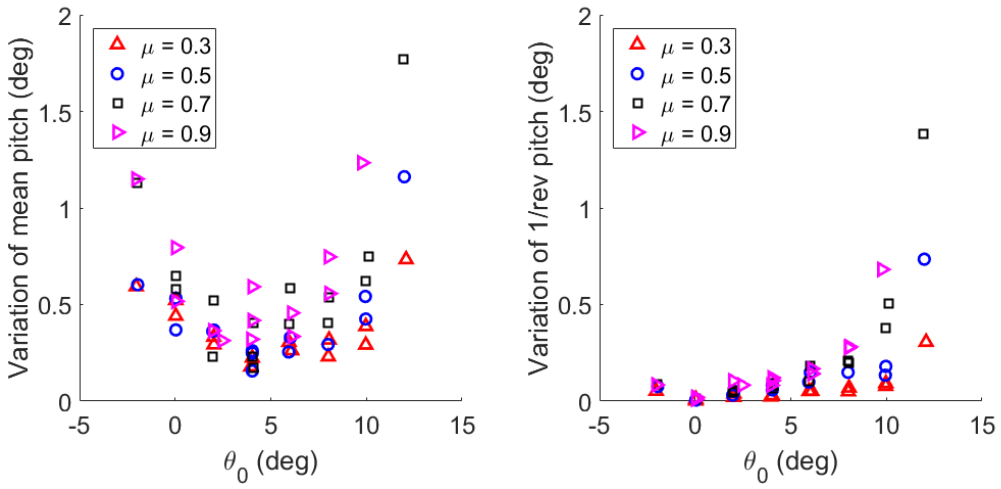

(a) Mean pitch (b) 1/rev pitch

Fig. 5.12: Variations of root pitch parameters vs collective, 900 RPM, zero shaft tilt.

5.2.2 Flap Angle

The level of trimming error can be characterized by 1/rev flap angle: the trim quality is better with lower 1/rev flap. The results at 900 RPM and zero shaft tilt for a range of collectives are shown in Fig. 5.13, in which each point represents the average of the 1/rev components for all blades for a specific test case. Similar to the trend of mean pitch variation with advance ratio, the rotor is well trimmed at about 4°, but becomes slightly worse at higher or lower collective settings. The variation deteriorates rapidly at high advance ratios. Compared with the results in the second test at $\mu = 0.7$ (which featured blade-embedded sensors), the trimming error of the current test is lower by about 0.2°, indicating that better blade similarity improve trimming.

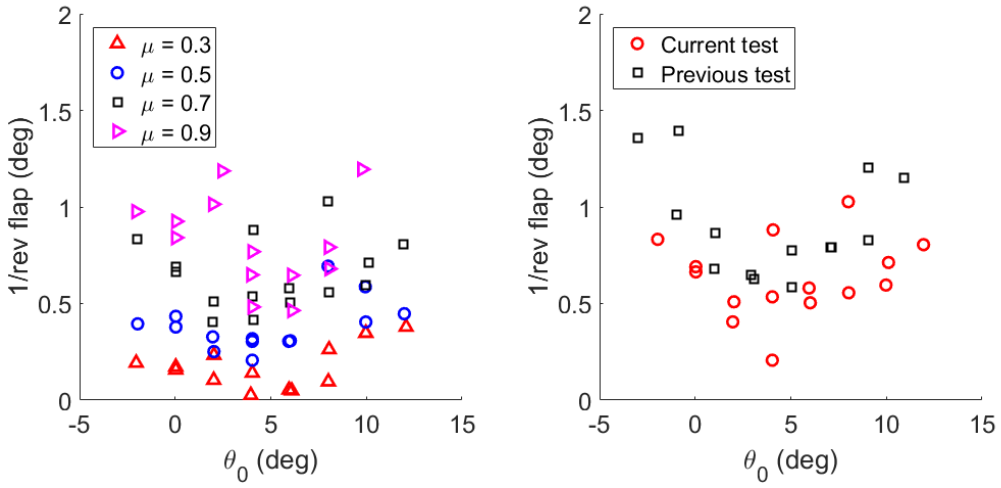

(a) At various μ

(b) Comparison with 1st articulated rotor test

Fig. 5.13: Trimming error vs collective, 900 RPM, zero shaft tilt.

5.3 Hub Load

The vibratory hub load data were initially captured by the 5-component hub balance. The raw balance data were subjected to a low-pass filter first to reject high frequency harmonics beyond 20/rev, then sorted into azimuthal domain. Next, the azimuthal data were decomposed in the harmonic domain and corrected by the transfer functions gained from the dynamic calibration, as described in chapter 3. After applying the correction function from the dynamic calibration, the in-plane components F_x and F_y are combined into F_{in} for further analysis:

$$F_{in}(\psi) = \sqrt{F_x(\psi)^2 + F_y(\psi)^2} \tag{5.6}$$

The emphasis of hub load analysis is normally in the frequency domain, in particular 4/rev. For the current 4-bladed rotor, there should be only 4n/rev hub

loads (n is an integer multiplier) if the rotor is perfectly balanced, tracked and trimmed, and the 4/rev load should be dominant. Also, the comprehensive analysis does not model blade dissimilarity, so only 4n/rev hub loads are predicted.

5.3.1 Horizontal Load

Figure 5.14 shows the 4/rev horizontal hub load at various advance ratios and shaft tilt angles at 900 RPM. The solid lines are from comprehensive analysis, while symbols represent test data. The comprehensive analysis does not include fuselage modeling, so the test results without the fuselage are presented if available (otherwise labeled in the plot legend). The in-plane hub load increases with collective at moderate advance ratios ($\mu \leq 0.7$), and the increments are larger with higher advance ratios. At $\mu = 0.9$, the data become quite scattered, indicating that the trim condition is degraded at this high advance ratio and making the hub load level less repeatable. For most cases, backward shaft tilt tends to increase in-plane hub load, while forward shaft tilt reduces the load level. The trends of 4/rev in-plane hub loads are predicted by the comprehensive analysis, but the analysis tends to underestimate the vibration level, especially at high advance ratios $\mu \geq 0.7$.

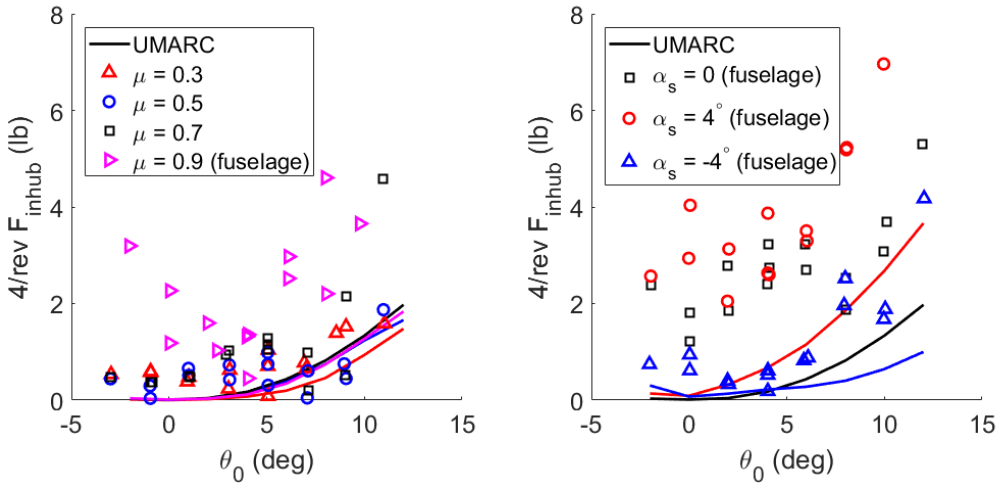

(a) Zero shaft tilt

(b) At $\mu = 0.7$ with shaft tilt

Fig. 5.14: Articulated rotor 4/rev in-plane hub vibratory load vs. collective.

5.3.2 Vertical Load

The results of 4/rev vertical hub load are presented in Fig. 5.15. The level of vertical hub load is significantly higher than in-plane: the maximum magnitude is about 20 lb compared to 5 lb for the in-plane load magnitude. At lower advance ratios ($\mu \leq 0.5$), the vertical hub load magnitudes are low and relatively insensitive to collective change, while at higher advance ratios ($\mu \geq 0.7$), the load increases rapidly with collective. Compared to the in-plane hub load, the vertical hub load is more sensitive to advance ratio and less sensitive to shaft tilt angle. The trend is also captured by the comprehensive analysis, and the results are less underestimated. The change in hub loads with advance ratio can be explained from the distribution of the airload over the azimuth. At high advance ratios, the in-plane airloads show a 1/rev component that peaks at $\psi = 270°$ (see Fig. 5.7(b)), and the vertical airloads show a 2/rev component that peaks in the fore and aft sections (see Fig. 5.3(a)).

These periodic airloads can be attributed to increased hub vibratory loads at high advance ratios.

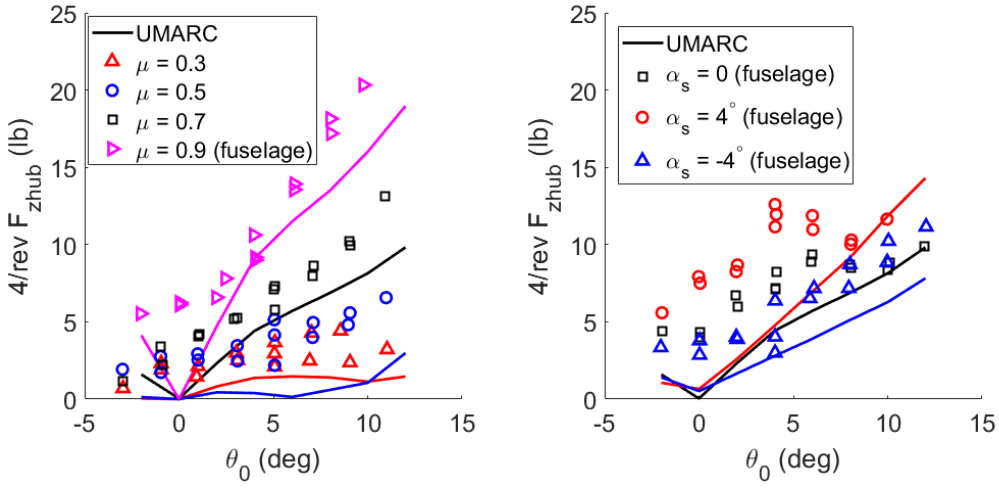

(a) Zero shaft tilt

(b) At $\mu = 0.7$ with shaft tilt

Fig. 5.15: Articulated rotor 4/rev vertical hub vibratory load vs. collective.

5.4 Pressure and Airload

In the 2nd articulated rotor test, the blades 1 and 3 were instrumented with pressure sensors at 30% radius. Similar to hub balance data, the raw pressure data were also processed with low-pass filter. Then, the phase of blade 3 data was shifted by 180° to match with the blade 1 data, and the two datasets were merged. The pressure data were compared to the CFD/CSD predictions and previous test results, and the development of the reverse flow dynamic stall was investigated. Sectional airload was obtained by integrating the pressure data at the sensor ports, and data correlation studies were performed with the predictions of comprehensive and CFD/CSD analyses.

5.4.1 Surface Pressure

With CFD/CSD analysis, the pressure data at chordwise sensor ports are compared with the predictions. The results are shown in Fig. 5.16 at 700 RPM, $\mu = 0.8$ with zero shaft tilt for two cases, respectively for $\theta_0 = 3°$ and $11°$. The thin dashed lines are 3 standard deviation error bands of the test data. At $\theta_0 = 3°$, the pressure azimuthal history is mostly smooth except behind the hub shaft (around $\psi = 0°$). The pressure fluctuations are due to the changes of angle of attack (from cyclic angles) and local flow velocity. At $\theta_0 = 11°$, the pressure fluctuation level on the advancing side ($\psi = 20°$ to $160°$) increases with negative peaks near the leading edge of the upper surface ($\psi = 50°$ to $130°$), because of the larger cyclic angles. Two strong dynamic stall peaks occur in the reverse flow region ($\psi = 210°$ to $300°$), forming on lower surface near the trailing edge and propagating toward the leading edge. When reaching the leading edge, the peaks flip to upper surface and move towards the trailing edge ($\psi = 270°$). The variability of the experimental data is low for most azimuthal sections in both cases, indicating the data are consistent and repeatable. The two exceptions are in the reverse flow region where the airflow is highly unsteady, and the section exposed to hub wake, which does not have the same period as the rotor.

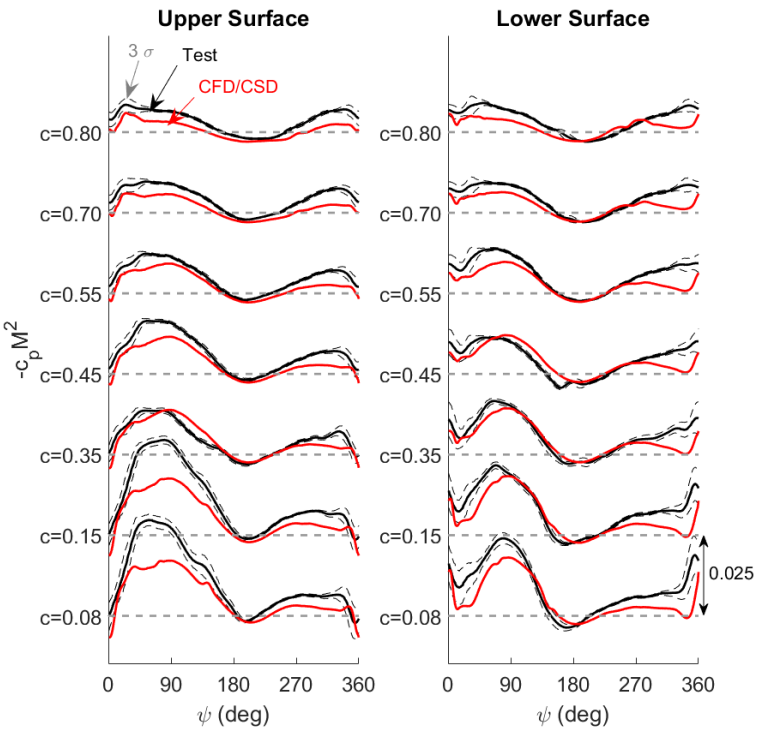

(a) $\theta_0 = 3°$

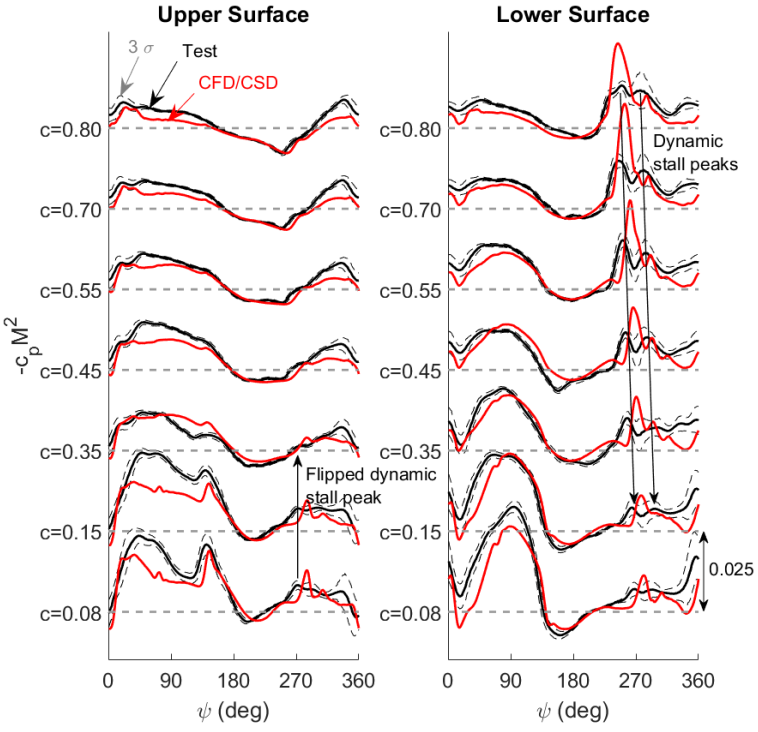

(b) $\theta_0 = 11°$

Fig. 5.16: CFD/CSD surface pressure vs. azimuth at 30% R, $\mu = 0.8, \theta_0 = 11°$ with zero shaft tilt.

Overall, the predictions from CFD/CSD analysis exhibit good correlation with the test results. The pressure fluctuations on the advancing side, the dual dynamic stall peaks on the retreating side, and the effects of hub wake on the aft section of the rotor disk are all captured by the predictions. Some discrepancies are present between the test results and the predictions. The predictions tend to underestimate the pressure on the aft section of the rotor disk, especially near the leading edge. Also, the first dynamic stall peak magnitude is overpredicted. These discrepancies may be due to the geometric imperfection of the blades, especially the tab on the trailing edge that change the airfoil shape, and the lateral cyclic mismatch between experimental results and computational predictions.

To investigate the development of the dynamic stall in the reverse flow region, the pressure distribution on the airfoil at 9 different azimuthal locations in $\psi = 220°$ to 300° are shown in Fig. 5.17, for the case of $\mu = 0.8, \theta_0 = 11°$ and zero shaft tilt. The test results at the sensor ports are represented by symbols, the predictions from the CFD/CSD analysis are represented by solid lines, and the two data series are from the blade upper and lower surfaces. Local tangential flow speed and root pitch are also indicated on the plot. The tangential flow is mostly reverse, and the local root pitch is high ($\theta_{root} > 15°$) at $\psi = 220°$, but the pressure readings are low, probably because the flow velocity and dynamic pressure is low. At $\psi = 230°$, the dynamic stall is detected by the pressure sensors at 70% and 80% chord on the lower surface, which is also predicted by the CFD/CSD analysis. At this azimuthal location, the tangential flow speed is about 30% tip speed (reversed), and the measured local pitch is 18°. For the test data, the peak reaches its maximum

in $\psi = 230°$ to $240°$, and for the CFD/CSD predictions, the maximum is in $\psi = 240°$ to $250°$. It appears that the dynamic stall proceeds slower in the CFD/CSD predictions. Then the dynamic stall peak propagates towards the leading edge and loses its strength, flipping to the upper surface when contacting the leading edge at $\psi = 270°$ (for CFD/CSD results, $\psi = 280°$). The initial peak is followed by a second weaker peak starting at $\psi = 270°$ (for CFD/CSD results, $\psi = 280°$). The second peak follows the propagating pattern of the first one, and completely fades away around $\psi = 300°$. According to the results, a strong reverse flow dynamic stall peak requires not only high local pitch and (reversal) tangential flow speed, but also a rapid increment of them. At $\psi = 270°$, the reversal tangential flow speed reaches its maximum and the local pitch is high, but the major peak already passed away.

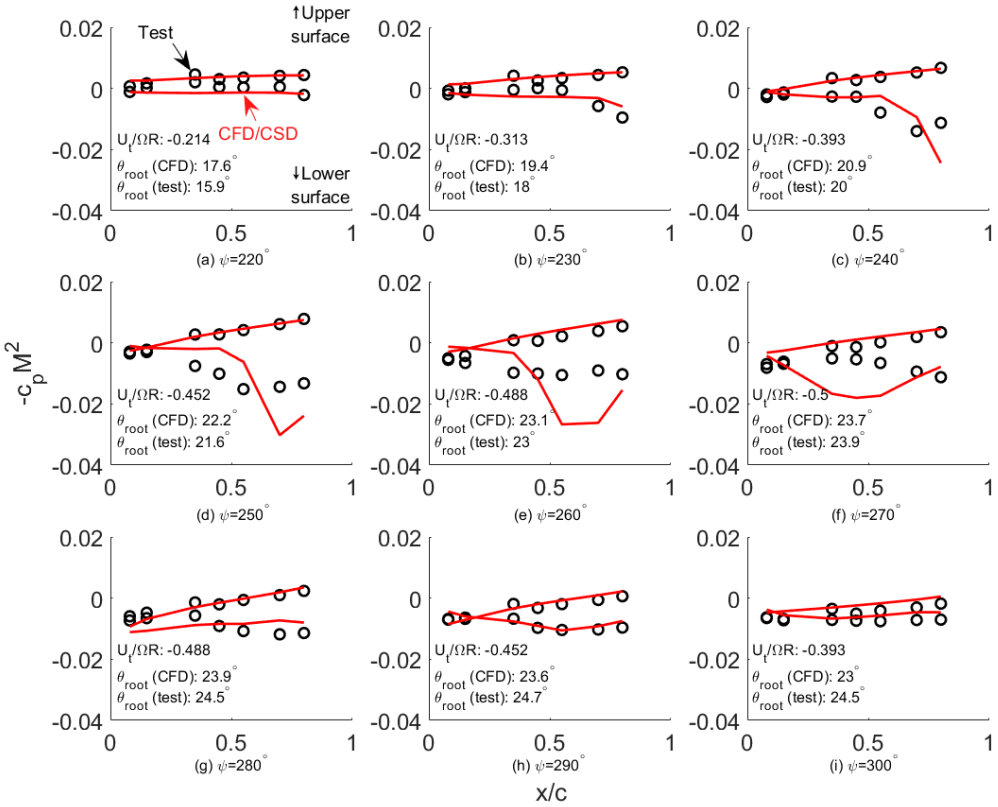

Fig. 5.17: The pressure distribution on the airfoil 9 different azimuthal locations at 30% R, $\mu = 0.8, \theta_0 = 11°$ with zero shaft tilt.

The experimental pressure data are not only validated against CFD/CSD predictions, but also previous UMD test results [1] and the UH-60A test results [9]. The case being compared is at 700 RPM, $\mu = 0.8, \theta_0 = 11°$, and two pressure sensor ports are selected: 15% chord port on the upper surface to check the pressure fluctuation on the advancing side, and 80% chord port on the lower surface to check the reverse flow dynamic stall. There is no exact same test case in the other two tests to compare with, so two most relevant cases are used: for the previous UMD test, the case is at 700 RPM, $\mu = 0.83$, $\theta_0 = 11°$, and for the UH-60A test, the case is at 103 RPM (40% nominal speed), $\mu = 0.8$, $\theta_0 = 4°$ (the collective is chosen because

the UH-60A rotor has a blade twist of $-18°$ [98], with $\theta_0 = 4°$, the local pitch at 30% radius should be about 11.2°). All of these cases are at zero shaft tilt. The chordwise sensor locations are not identical, so the closest ones are used, and 22.5% and 40% radius data are shown for UH-60A results, because sensor reading is unavailable at 30% radius. The results are presented in Fig. 5.18. Note that the mean pressure values are removed, and the data are non-dimensionalized by $1/2\rho(\Omega R)^2$. The current pressure results show exceptional similarity with the previous UMD test data (Figs. 5.18(a) and 5.18(b)), indicating the test condition is highly repeatable. Also, the pressure results agree with the UH-60A data qualitatively: the large negative peak on the advancing side, upper surface appears in both datasets, and the strength of the dynamic stall peak on the retreating side is comparable. The discrepancy can be due to airfoil difference (the UH-60A rotor featured SC1095, and the current test used NACA0012) and trim angle difference that comes from dissimilar blade twist.

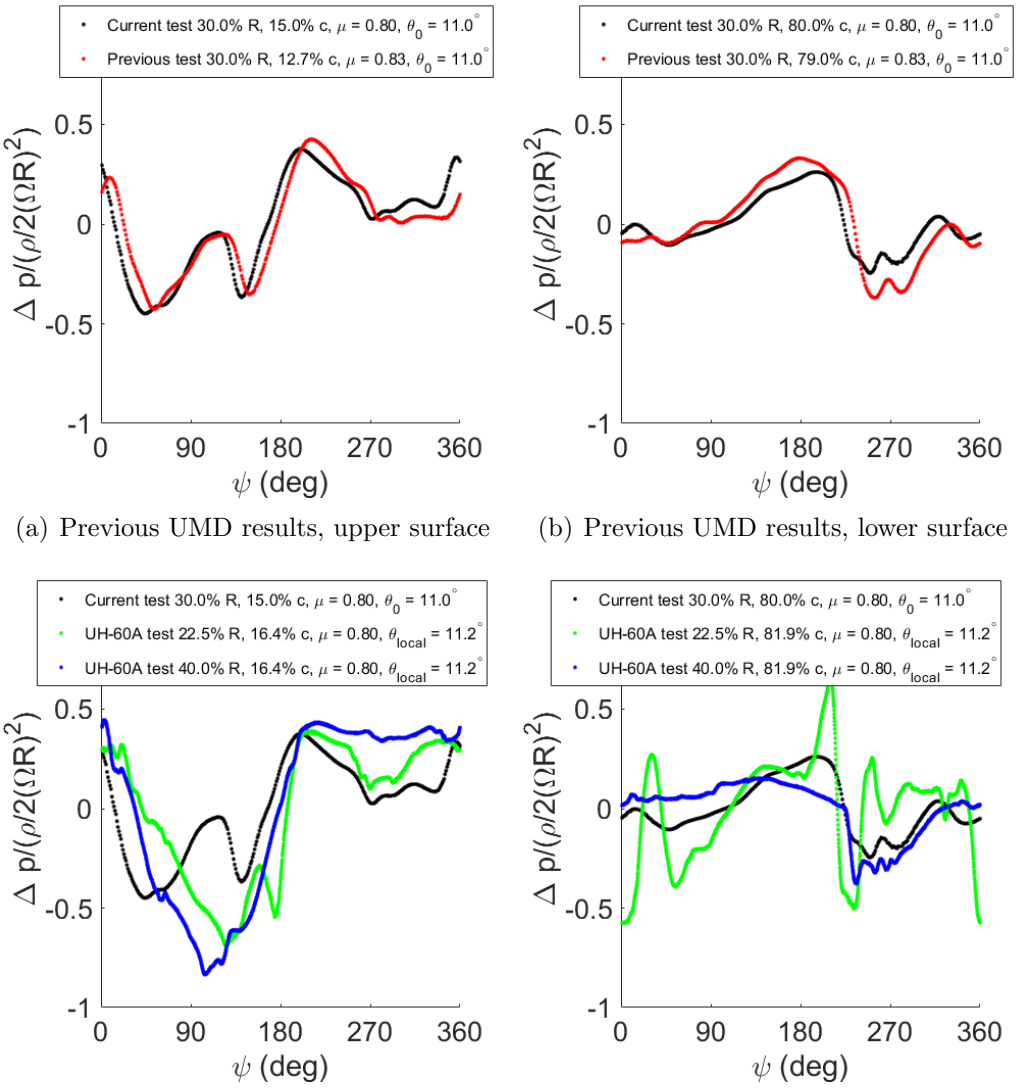

(a) Previous UMD results, upper surface

(b) Previous UMD results, lower surface

(c) UH-60A results, upper surface

(d) UH-60A results, upper surface

Fig. 5.18: Pressure data comparison with previous test and UH-60 data.

5.4.2 Airload

To gain the sectional airloads from the experimental data, the only sources are the pressure sensors on the blade surface. However, the pressure sensors are limited in number (14 in total) so that they cannot be directly integrated. The pressure data are subject to interpolation/extrapolation before surface integration. For any point

on the chord, if it is between two sensors on its surface, perform linear interpolation with the two sensors. If the point is near the leading edge or trailing edge that all the sensors on the airfoil surface are on one side, perform linear extrapolation with the two nearest sensors on its surface. Once a continuous pressure distribution along the chord are determined, surface integration can be conducted to calculate force and pitching moment at 25% chord with the following equations:

$$\vec{F} = \oint (p - p_\infty)\hat{n}ds \tag{5.7}$$

$$\vec{M_{25}} = \oint (p - p_\infty)(\vec{x} - \vec{x_{25}}) \times \hat{n}ds \tag{5.8}$$

where p is the measured surface pressure, p_∞ is the freestream pressure monitored by the wind tunnel probes, $\hat{n}$ is an unit vector perpendicular to the blade surface, s is the curve along the airfoil, and $\vec{x_{25}}$ is the location of 25% chord. Chordwise force is not calculated due to the lack of pressure sensor at the leading/trailing edge, where the pressure contribution on chordwise force are important. Then, the normal force and pitching moment are non-dimensionalized into $c_n M^2$ and $c_m M^2$. A validation study is conducted to show whether the sensor setup and the integration method are sufficient for airload calculation. First, take the full CFD/CSD dataset and only keep the pressure data at the 14 sensor ports as if they are sensor readings from a test. Next, integrate the CFD pressure data at the sensor ports to calculate the sectional airload with the same method of experimental airload integration. In Fig. 5.19, the CFD airload from the sensor ports integration and the CFD airload

from the complete surface integration are compared along with the test results. For $\theta_0 = 3°$, the results from the sensor port integration slightly underestimate the dynamic stall peak, and the overall accuracy is satisfactory. For $\theta_0 = 11°$, the two integration methods are almost identical, indicating the number of sensors and their chordwise distribution are not major sources of error for normal force. On the other hand, the sensor setup limitation causes notable error for pitching moment. To minimize the error from integration, the only solution is to implement more sensor ports, especially at the trailing edge where the dynamic stall peaks emerge.

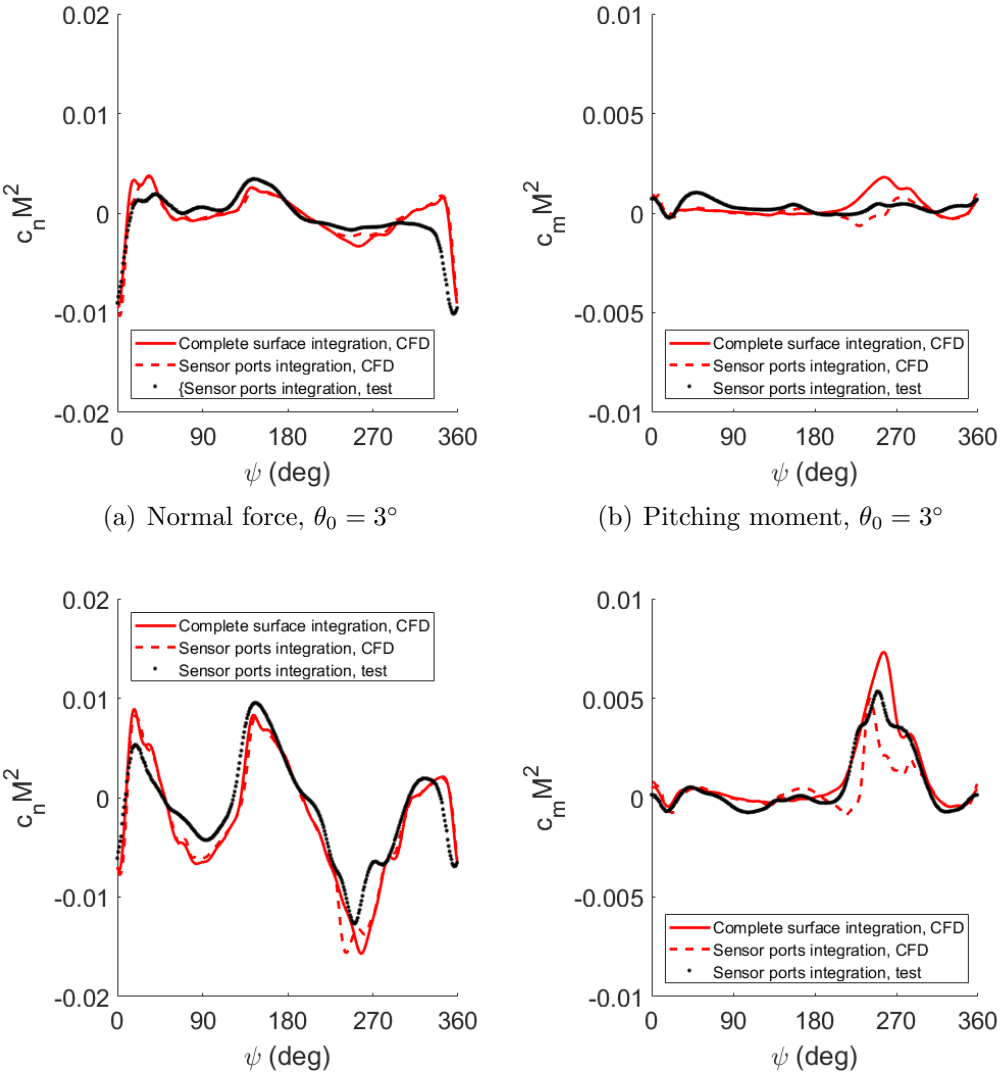

(a) Normal force, $\theta_0 = 3°$

(b) Pitching moment, $\theta_0 = 3°$

(c) Normal force, $\theta_0 = 11°$

(d) Pitching moment, $\theta_0 = 11°$

Fig. 5.19: Effects of integrating suface pressure from only sensor ports using CFD/CSD results on airloads at 30% R, $\mu = 0.8$, zero shaft tilt for two cases.

After surface integration, the sectional airloads from the wind tunnel test, the comprehensive analysis with free wake model (PrasadUM), and the CFD/CSD coupled analysis (HAMSTR/PrasadUM) are presented in Fig. 5.20. The two test cases shown are at $\mu = 0.8$, respectively for $\theta_0 = 3°$ and $11°$ with zero shaft tilt, and the spanwise location is 30% radius. The key features are the strong normal

force negative peak/nose-up pitching moment in the reverse flow region ($\psi = 210°$ to 300°) due to dynamic stall, the normal force fluctuation ($\psi = 30°$ to 150°) on the advancing side to balance the loss of thrust on the retreating side, the effect of hub wake on normal force and pitching moment ($\psi = 0°$), and the vortex interaction on the advancing side ($\psi = 70°$). According to test data, the dynamic stall effect is weak at $\theta_0 = 3°$. The stall vortex either is too weak to be reflected on pressure data or fades away before reaching the first trailing edge sensor port (at 80% chord). The magnitude of the normal force fluctuation on the advancing side is low, because the cyclic angles are moderate for this case, and the largest change on normal force is due to the hub wake. At $\theta_0 = 11°$, the normal force loss and nose-up pitching moment peaks due to dynamic stall are intense, and the normal force drop on the advancing side becomes significant (compared to the UH-60A test [9], the effect is more prominent because of the untwisted blades). The comprehensive analysis predicts most of the key features except the hub wake. However, the results are less accurate in the reverse flow area, underestimating the strength of dynamic stall and showing lagged azimuthal locations for the peaks. Also, the vortex interaction on the advancing side is represented too sharp. The predictions of CFD/CSD analysis show satisfactory data correlation for normal force. It appears that the impact of pressure underestimation on the aft section (see Fig. 5.16) is small on sectional airload because the upper and lower surface discrepancies cancel out during the integration. A conclusion can be drawn that the negative peak at about zero azimuth is due to hub wake, since the peak is missing in a previous CFD/CSD study in the absence of the modeling of the hub shaft (Ref. 25). The hub/shaft model also

contributes some details in the pitching moment prediction on the advancing side (in particular $\psi = 0°$ to $30°$), resulting in better agreement between test data and predictions.

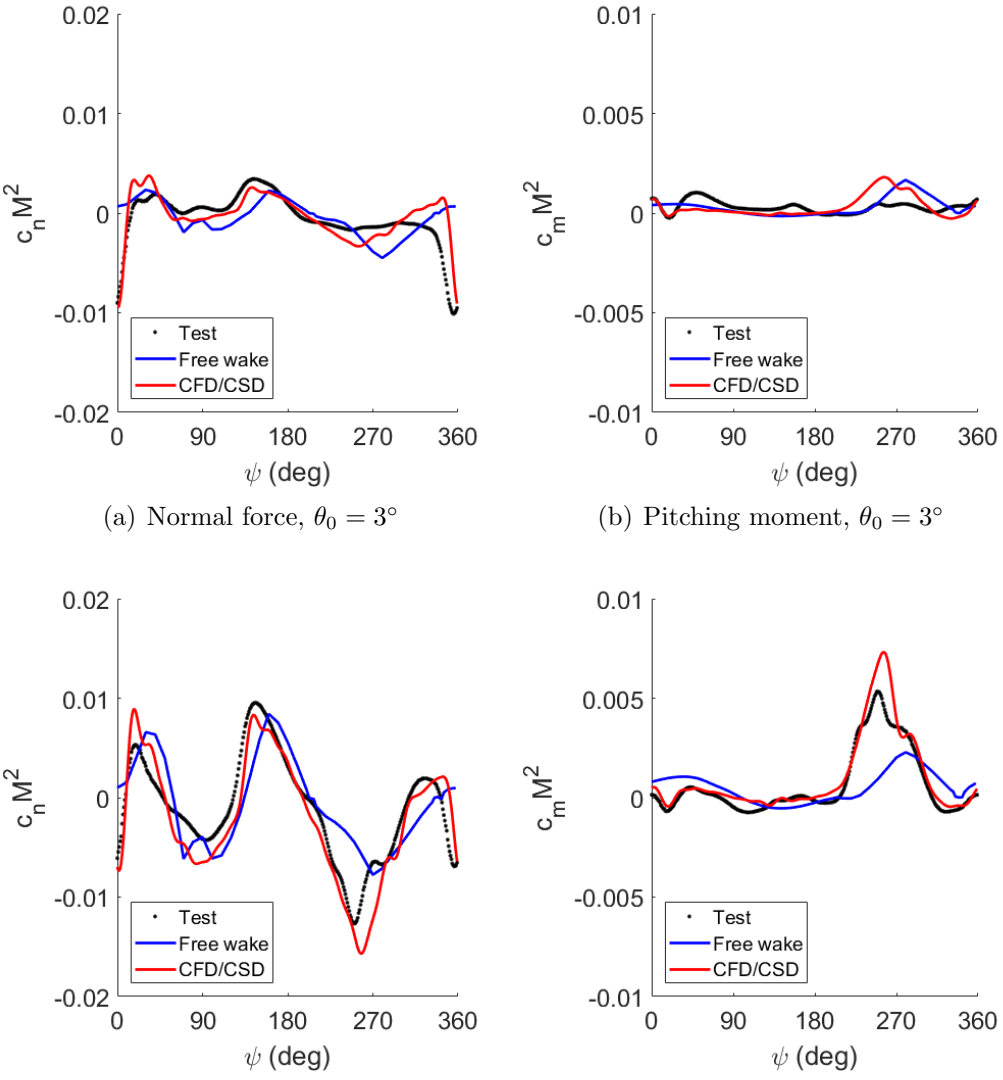

(a) Normal force, $\theta_0 = 3°$

(b) Pitching moment, $\theta_0 = 3°$

(c) Normal force, $\theta_0 = 11°$

(d) Pitching moment, $\theta_0 = 11°$

Fig. 5.20: Comparison between experimental and predicted results of airloads at 30% R, $\mu = 0.8$, zero shaft tilt for two cases.

The effect of shaft tilt on sectional airload is also an emphasis of the study, because the backward shaft tilt is observed to be more efficient in producing thrust.

CFD/CSD analysis was performed for the two cases mentioned above ($\mu = 0.8$, $\theta_0 = 3^\circ$ and 11°), at 2° backward shaft tilt in addition to zero shaft tilt. The results are shown in Fig. 5.21, in which the light-colored lines are at zero shaft tilt, and the full-colored lines are at 2° backward shaft tilt. With backward shaft tilt, the normal force fluctuation on the advancing side becomes stronger, since the additional inflow increases the thrust level on the advancing side, and the rotor is further balanced by more longitudinal cyclic to be trimmed (see Fig. 5.9(b)). Meanwhile, although the local pitch increases on the retreating side with longitudinal cyclic, the dynamic stall peaks are not more intense with backward shaft tilt. The loss of normal force in dynamic stall region is less sensitive to backward shaft tilt, while the nose-up impulsive pitching moment is slightly alleviated by backward shaft tilt. These phenomena are observed for both collective settings, and the CFD/CSD analysis predicts these trends.

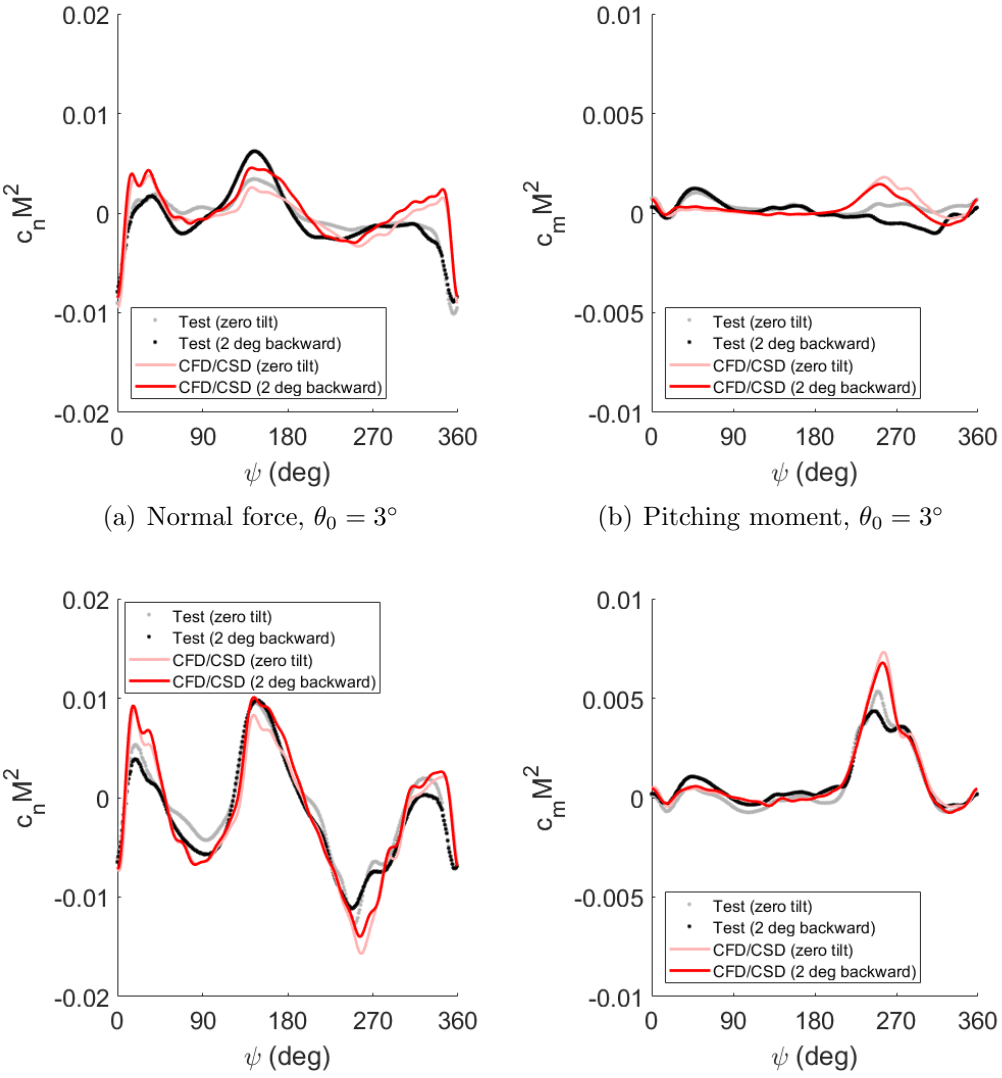

(a) Normal force, $\theta_0 = 3°$

(b) Pitching moment, $\theta_0 = 3°$

(c) Normal force, $\theta_0 = 11°$

(d) Pitching moment, $\theta_0 = 11°$

Fig. 5.21: Effects of backward shaft tilt on airloads at 30% R, $\mu = 0.8$, zero shaft tilt for two cases.

The airload data is challenging to acquire in wind tunnel tests (even at a single spanwise location), but the experimental data is crucial for validating the results of a CFD/CSD analysis. With a CFD/CSD analysis, it is possible to calculate the airload across the whole rotor disk, but the computational time cost is still high. The CFD/CSD airload results can be used to validate the predictions of a comprehensive

analysis, which is the most suitable for batch processing. Figure 5.22 compares the airload results of CFD/CSD (HAMSTR/PrasadUM) and comprehensive analysis (UMARC) across the rotor disk, and the case is 700 RPM, $\mu = 0.8, \theta_0 = 11^\circ$ with zero shaft tilt. Although the CFD/CSD results are more refined (especially for the vortex interaction representation on the advancing side), the comprehensive analysis results predict most of the key phenomena in high advance ratio flight regime. On the $C_n M^2$ plots, the normal force loss in the reverse flow region and the negative lift zone on the advancing side to trim the rotor are accurately represented. On the $C_m M^2$ plots, the nose-up impulsive moment on the retreating side is also captured, although the strength is somewhat underestimated and the pitching moment change due to cyclic angle is overpredicted. These results support the explanations on rotor performance based on UMARC-predicted airload in previous section.

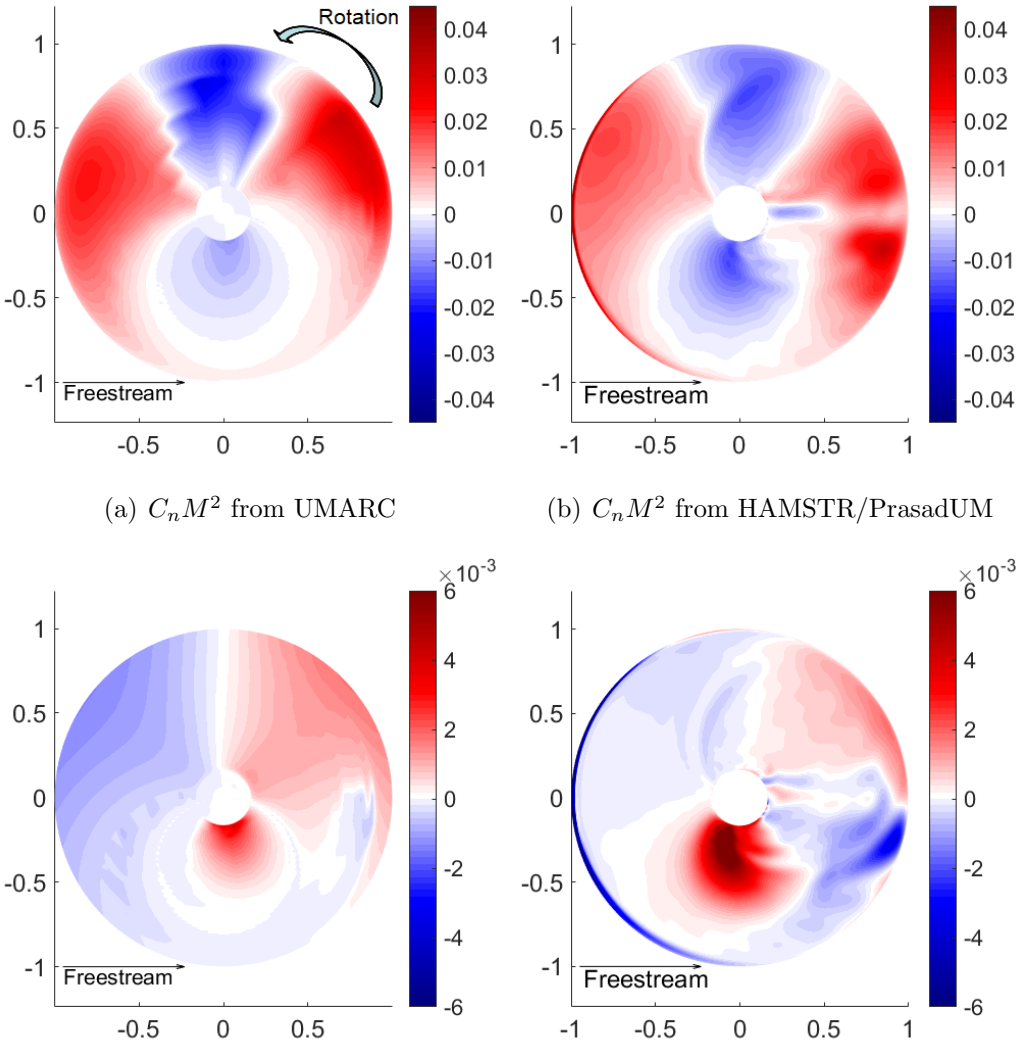

(a) C_nM^2 from UMARC

(b) C_nM^2 from HAMSTR/PrasadUM

(c) C_nM^2 from UMARC

(d) C_nM^2 from HAMSTR/PrasadUM

Fig. 5.22: Airload across the rotor disk from analyses, 700 RPM, $\mu = 0.8, \theta_0 = 11°$, $\alpha_s = 0°$

5.5 Blade Structural Load

In the 2nd articulated rotor test, the blades 2 and 4 were instrumented with flap bending and torsional strain gauges at 30% radius. The raw data were also filtered and phase-adjusted into the azimuth of blade 1. The flap bending and tor-

sional loads are selected for the study because these degrees of freedom are directly related with $c_n M^2$ and $c_m M^2$ airloads, so the trends on the structural loads can be traced back to their airload sources.

5.5.1 Flap Bending Moment

The flap bending moments azimuthal histories and harmonic decompositions, $\mu = 0.8$, respectively for $\theta_0 = 3°$ and $11°$ are presented in Fig. 5.23. The symbols represent the test data, and the two solid lines are free wake model (PrasadUM) and CFD/CSD coupled analysis (HAMSTR/PrasadUM) results. For both collectives, the predominant component of flap bending moment is 4/rev, which is affected by the adjacent 2nd flap frequency (about 3.5/rev). The peak-to-peak magnitude at $\theta_0 = 11°$ is about 30 in-lb, significantly higher than that of $\theta_0 = 3°$ (< 20 in-lb), which agrees with the airload increment with collective (see Fig. 5.20(c)). On the azimuthal history plots, two major positive peaks ($\psi = 30°$ and $110°$) and two negative peaks ($\psi = 60°$ and $160°$) are present on the advancing side, while the load is mainly positive and only one minor negative peak ($\psi = 250°$) is present on the retreating side. The measured negative peak on the retreating side appears weaker, which may be due to less abrupt airload change. For both analyses, the 4/rev moment increment with collective is captured. However, the phases of both predicted results are lagged by about $20°$ azimuth compared to the test results. Quantitively, the free wake model tends to underestimate the 4/rev load, while the CFD/CSD prediction is accurate at $\theta_0 = 3°$, but overpredicts the 4/rev load by 40% at $\theta_0 = 11°$.

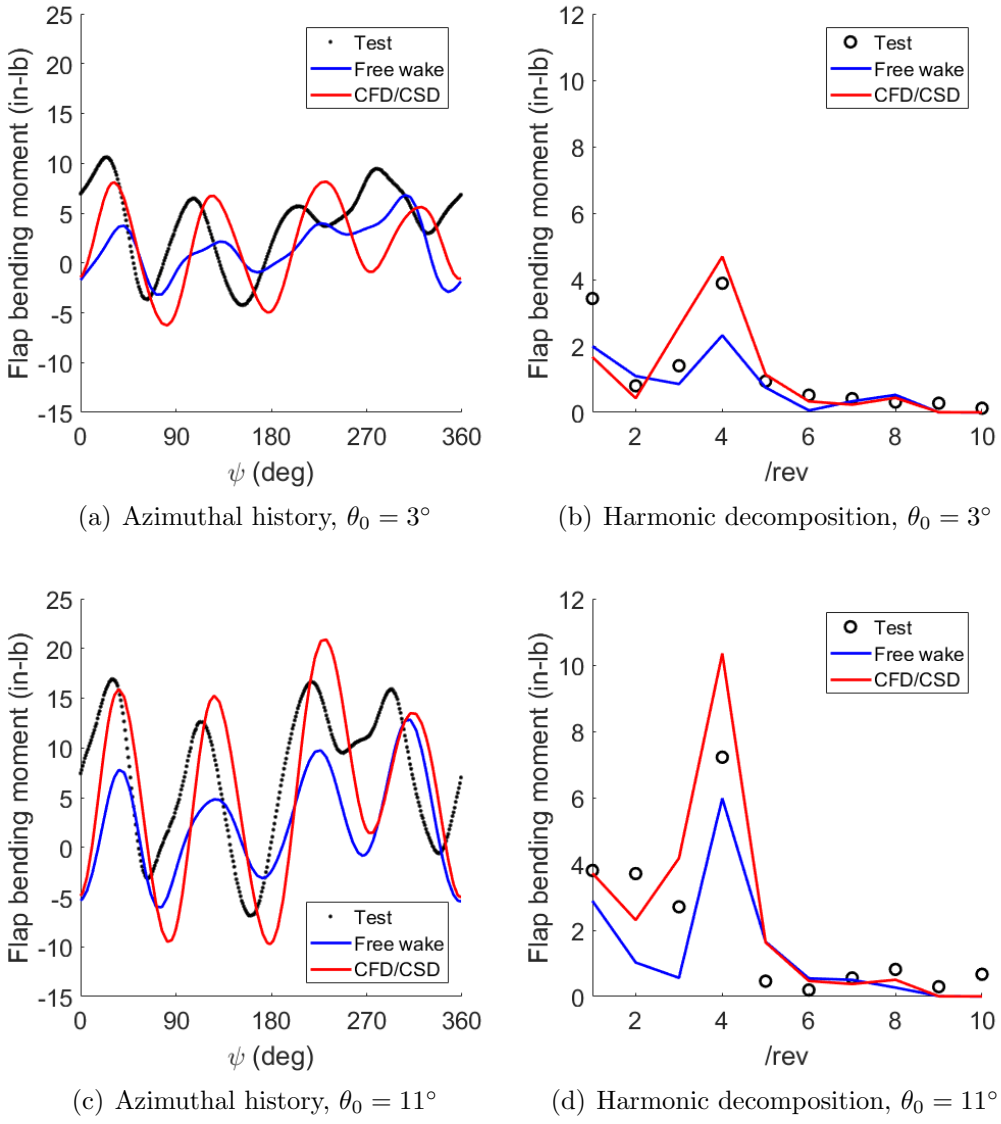

(a) Azimuthal history, $\theta_0 = 3°$

(b) Harmonic decomposition, $\theta_0 = 3°$

(c) Azimuthal history, $\theta_0 = 11°$

(d) Harmonic decomposition, $\theta_0 = 11°$

Fig. 5.23: Flap bending moment at 30% R, $\mu = 0.8$, zero shaft tilt for two cases.

5.5.2 Torsional Moment

The torsional moment results are shown in Fig. 5.24 for the same test cases and spanwise location. Unlike the flap bending moment, the torsional moment is dominated by impulsive factors due to dynamic stall instead of 4/rev harmonics. In the reverse flow region ($\psi = 210°$ to $300°$), a dynamic stall forms at the trail-

ing edge and propagates towards the leading edge, inducing an impulsive nose-up pitching moment. The pitching moment is not only present in airload results (see Fig. 5.20(d)), but also reflected on torsional structural load. The intensity of the torsional moment is positively correlated with collective setting: at $\theta_0 = 3°$, the impulse is weak (<1 in-lb), while at $\theta_0 = 11°$, the peak is about 5 in-lb. The free wake analysis underestimates the moment impulse at $\theta_0 = 11°$, and the predicted phase is somehow lagged. Predicting the $c_m M^2$ airload accurately, the CFD/CSD analysis also provides satisfactory torsional moment correlation for both azimuthal histories and harmonic decompositions, and the fluctuation on the advancing side is correctly represented.

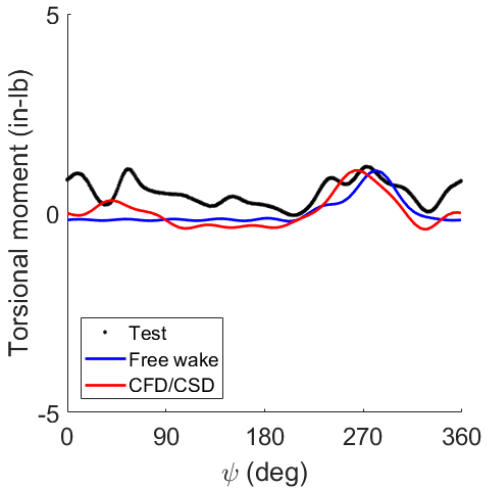

(a) Azimuthal history, $\theta_0 = 3°$

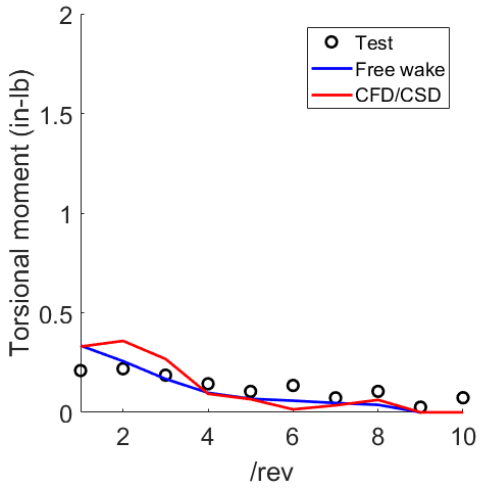

(b) Harmonic decomposition, $\theta_0 = 3°$

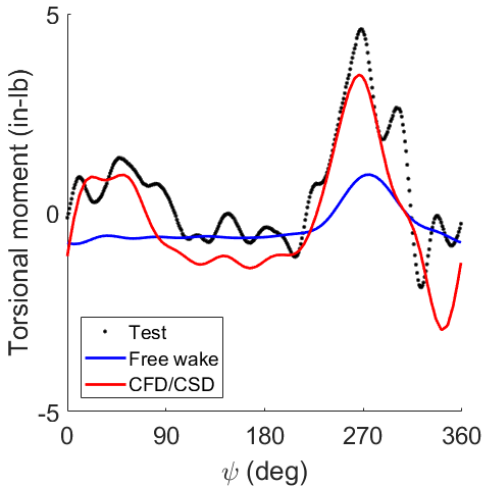

(c) Azimuthal history, $\theta_0 = 11°$

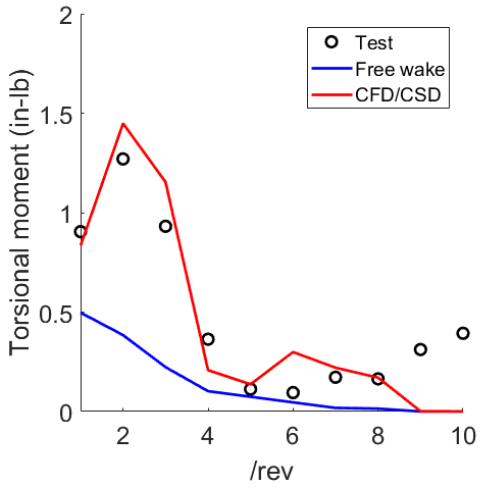

(d) Harmonic decomposition, $\theta_0 = 11°$

Fig. 5.24: Torsional moment at 30% R, $\mu = 0.8$, zero shaft tilt for two cases.

Chapter 6: Hingeless Rotor Results

In this chapter, the results of three wind tunnel tests on hingeless rotors are presented along with the predictions from UMARC plus the wing modeling from AVL. Note that most of the data presented are from the 3rd test on hingeless rotor at 700 RPM (except the sections with offset trim study and flap bending stiffness study), because the test reached the highest advance ratio of $\mu = 0.7$ with lift offset, and the dataset is the most complete. All the cases shown are at 700 RPM.

6.1 Performance and Control

The data acquisition and proceeding of a hingeless rotor performance and control were the same as those of an articulated rotor (data saving for 5 seconds at 5000 sample/s, low-pass filtering to remove > 20/rev signal). The emphasis is to examine the performance improvements on the rotor and the overall compound configuration due to the lift offset, which means more thrust on the advancing side and thereby operate more efficiently at high advance ratios. The interaction between the rotor and the wing is also a point of interest.

6.1.1 Rotor Thrust and Total Lift

The rotor thrust results versus collective are shown in Fig. 6.1, where symbols are experimental data, and solid lines are UMARC predictions. Figure 6.1(a) shows the results of a baseline rotor without a wing, and Fig. 6.1(b) shows the results of a rotor with 4° wing incidence angle, both with zero shaft tilt. The effects of shaft tilt angles and wing incidence angles on rotor thrust are shown in Figs. 6.1(c) and 6.1(d) respectively at $\mu = 0.5$. Note that only the rotor thrust is presented, and the lift on the stub wing is not included. With zero hub moment trim in Fig. 6.1(a), the trend of thrust resembles that of an articulated rotor: the thrust versus collective curve is close to linear for moderate collective, and the slope decreases with increasing advance ratio, as the rotor needs to balance the loss of lift in the reverse flow region, making it less effective in producing lift even on the advancing side. With the wing trim, the change in thrust curve slopes with advance ratio is small, while the curves shift up with increasing advance ratio. The thrust curve with a wing incidence angle of 8° shifts up by 0.02 compared to the curve without wing at $\mu = 0.5$, generating 31% more thrust at $\theta_0 = 8°$ (Fig. 6.1(d)). As observed in an articulated rotor, a backward shaft tilt improves the thrust potential of a rotor by inducing an upwash across the whole rotor disk (Fig. 6.1(c)). The phenomenon is also observed with hingeless rotors, and the benefits of backward shaft tilt and lift offset can occur simultaneously, resulting in a 49% increment of thrust at $\mu = 0.5$, $\theta_0 = 8°$ with 4° backward shaft tilt and 8° wing incidence angle (Fig. 6.1(d)). The comprehensive analysis captures the thrust curve slope reduction with increasing advance ratio,

and the thrust increments with wing trim and backward shaft tilt.

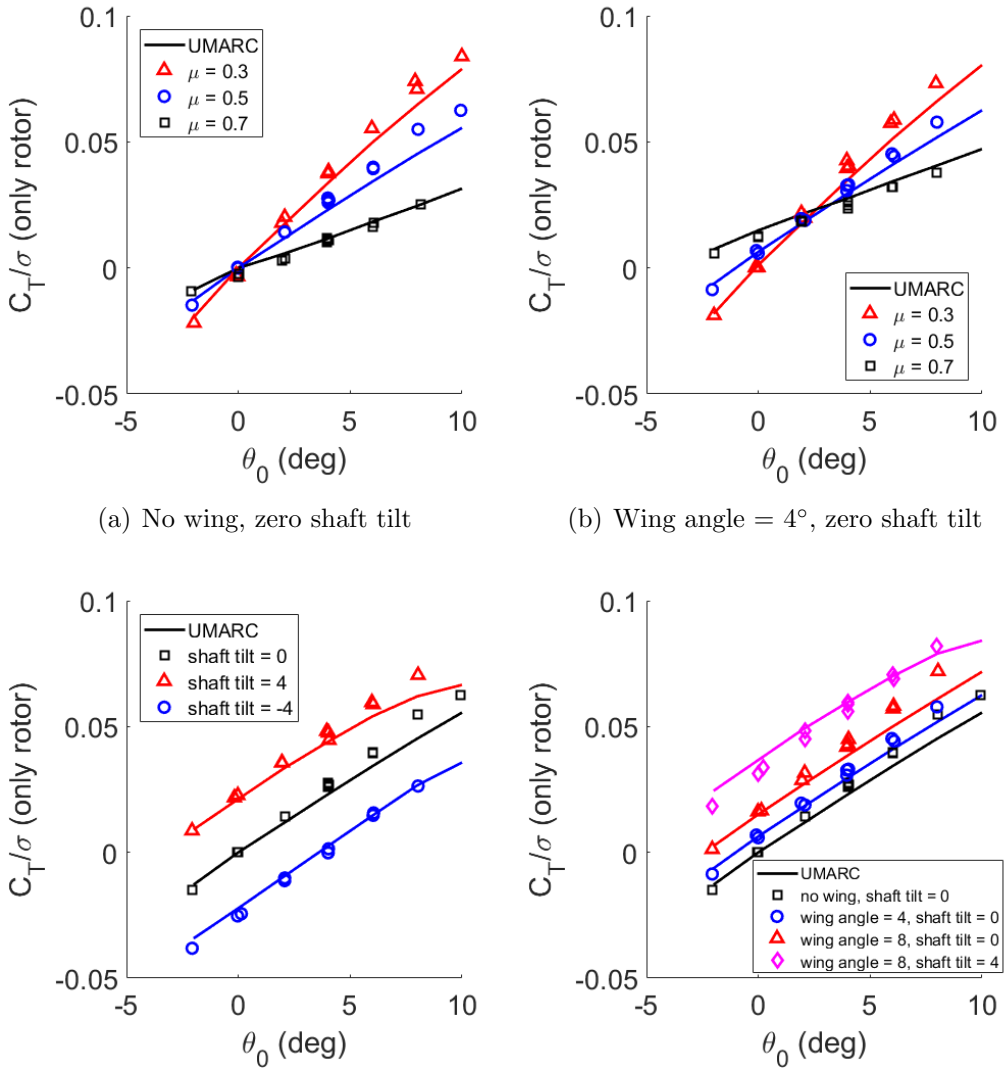

(a) No wing, zero shaft tilt

(b) Wing angle = 4°, zero shaft tilt

(c) $\mu = 0.5$ with shaft tilt, no wing

(d) $\mu = 0.5$ with wing

Fig. 6.1: Hingeless rotor thrust results vs. collective (rotor only).

The total lift results versus collective are shown in Fig. 6.2, in which the lift generated by the wing is included. Figure 6.2(a) shows the results at various advance ratios with 4° wing incidence angle and zero shaft tilt, and Fig. 6.2(b) shows results at various wing incidence angle and shaft tilt. With increasing wing incidence angle and advance ratio, the stub wing not only improves the rotor thrust by allowing

more lift offset and making the advancing side more efficient, but also generates considerable amount of lift by itself. Thus, the offset-pattern lift improvement at high advance ratios becomes more prominent. At $\mu = 0.5$ and $\theta_0 = 8°$, the total lift increases by 70% with 4° wing incidence angle alone and by 88% with 4° wing incidence angle and 4° backward shaft tilt compared with the baseline case without wing (Fig. 6.2(b)).

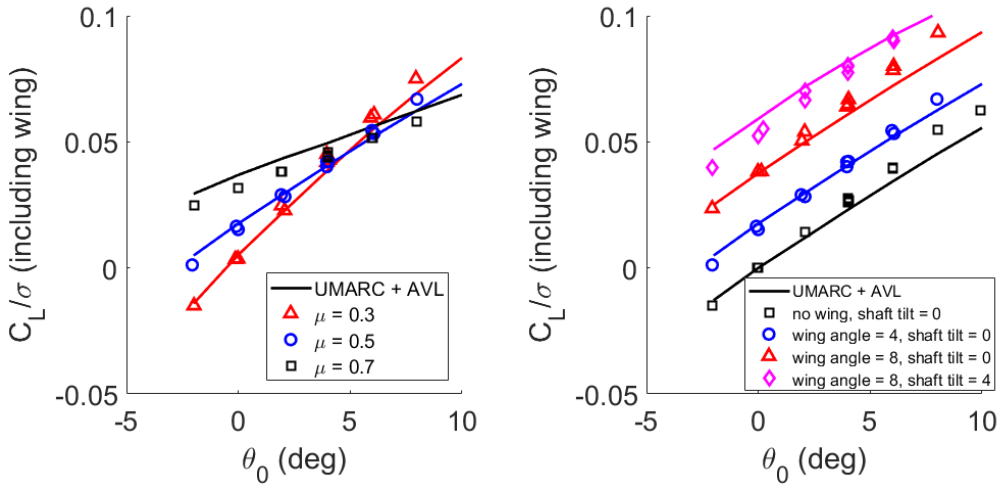

(a) Wing angle = 4°, zero shaft tilt

(b) $\mu = 0.5$ with wing

Fig. 6.2: Hingeless rotor total lift results vs. collective (rotor and wing).

Since the effects of wing trim and backward shaft tilt on rotor thrust are both insensitive to collective angle (the whole curve shifts up in an offset pattern), these improvements can be visualized by only showing the offset from the baseline dataset (same advance ratio, no wing, zero shaft tilt) in Fig. 6.3. Although the percentage improvement due to backward shaft tilt becomes more significant at high advance ratios, the absolute improvement is quite insensitive to advance ratio: 4° shaft tilt always results in about 0.018 C_T/σ increment from $\mu = 0.3$ to 0.7. In

contrast to that, the improvement from lift offset rises with advance ratio, and the benefits increase with higher wing incidence angle. Only considering the rotor thrust (Fig. 6.3(a)), the C_T/σ increment is 0.014 due to 4° wing incidence angle at $\mu = 0.7$, and 0.018 due to 8° wing incidence angle at $\mu = 0.5$, no more than the increment due to 4° shaft tilt. The C_T/σ increment from the wing can be greater than 0.03 after adding the wing lift (Fig. 6.3(b)). As shown in Fig. 6.3(a), the configuration at $\mu = 0.7$, $\theta_0 = 8°$ with a 4° wing incidence angle generate 7% more lift than a rotor with no wing at $\mu = 0.5$ and $\theta_0 = 8°$, and only 17% less lift than a rotor with no wing at $\mu = 0.3$ and $\theta_0 = 8°$. The results indicate that the wing configuration is effective in compensating the thrust loss due to high advance ratios.

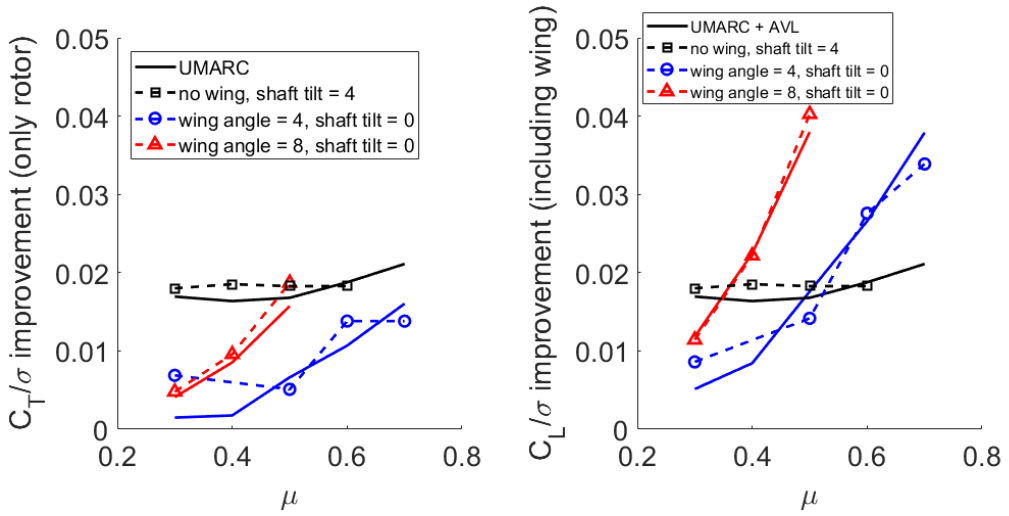

(a) Improvement in thrust (rotor only) (b) Improvement in lift (rotor and wing)

Fig. 6.3: Improvements in thrust and lift from wing effect and shaft tilt.

6.1.2 Horizontal Force and Total Drag

Figure 6.4 shows the horizontal force (only rotor) and overall drag (rotor and wing) results with collective. Figures 6.4(a) and 6.4(b) show the rotor horizontal

force at various advance ratios and the effects of wing incidence angle and shaft tilt angle at $\mu = 0.5$, and Figs. 6.4(c) and 6.4(d) include the drag force of the wing. As observed on articulated rotors, the horizontal force decreases with collective at $\mu = 0.3$ and 0.5 and increases slightly with collective at $\mu = 0.7$. At low collectives, the horizontal force does not change much with advance ratio (Fig. 6.4(a)). The horizontal force is less sensitive to wing incidence angle and shaft tilt angle than the rotor thrust: a 8° wing incidence angle reduces the horizontal force by about 0.01, and a 4° backward shaft tilt further reduces this force by 0.02 (Fig. 6.4(b)). The total drag increment with advance ratio becomes more significant with 4° wing incidence angle (Fig. 6.4(c)), because the wing drag increases with the freestream speed in a quadratic manner. At $\mu = 0.5$, the wing drag increment overcomes the horizontal force reduction on the rotor, raising the total drag slightly (Fig. 6.4(d)), and a higher drag increment is expected at higher advance ratios and higher wing angle settings.

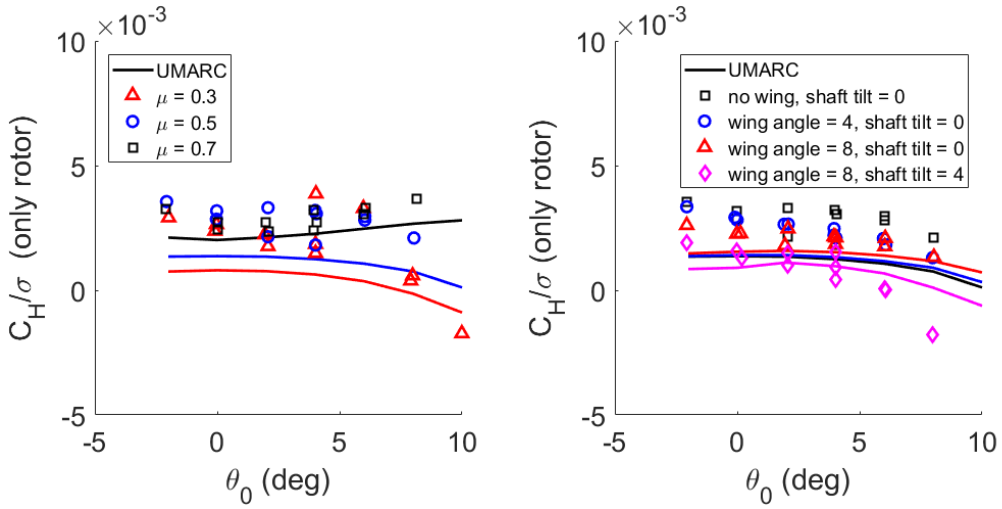

(a) Horizontal force, no wing, zero shaft tilt (b) Horizontal force at $\mu = 0.5$ with wing

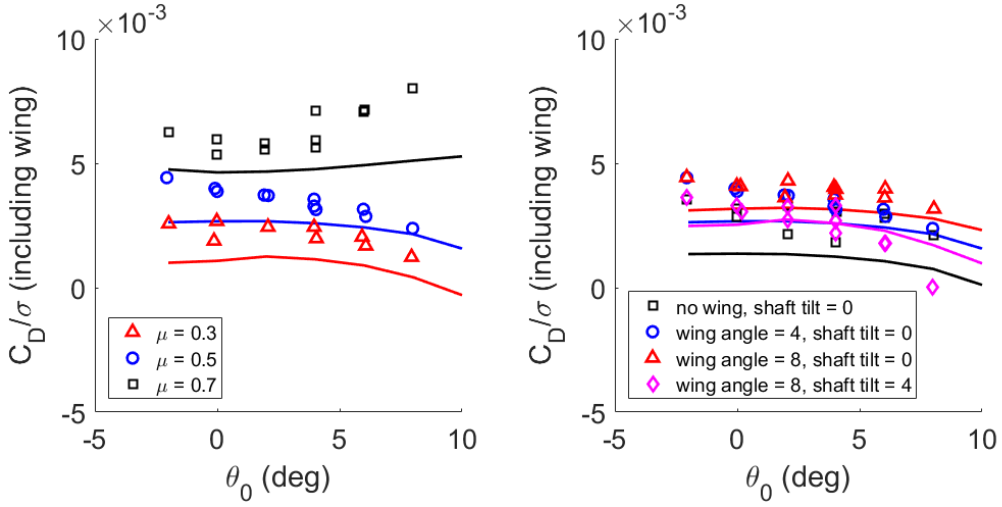

(c) Total drag, wing angle = 4°, zero shaft tilt (d) Total drag at $\mu = 0.5$ with wing

Fig. 6.4: Hingeless rotor horizontal force and total drag vs. collective.

6.1.3 *Shaft Torque*

The shaft torque versus collective results are shown in Fig. 6.5. The trend of shaft tilt resembles that of an articulated rotor with both normal trim and wing trim. The torque increases with collective in a quadratic manner, and the increment level becomes lower with higher advance ratio. At $\theta_0 = 8°$, the torque requirement is about 30% less at $\mu = 0.7$ compared to that at $\mu = 0.3$. With backward shaft tilt, the torque is significantly reduced at lower collective, but the torque with backward shaft tilt increases faster with collective and surpasses that of zero shaft tilt at about $\theta_0 = 7°$ (Fig. 6.5(b)). The torque is less sensitive to lift offset than to shaft tilt: for a rotor trimmed to the moment target set by a wing at 4° incidence angle, the shaft torque is only slightly higher than that of a rotor with normal trim. The comprehensive analysis captures the overall trend with collective and advance ratio, but the data correlation tends to degrade at high collectives.

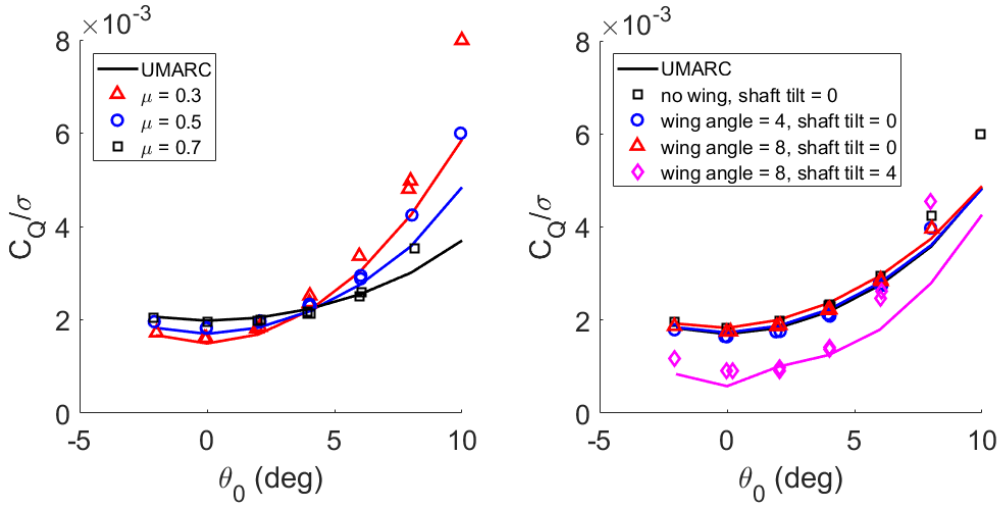

(a) No wing, zero shaft tilt

(b) $\mu = 0.5$ with wing

Fig. 6.5: Hingeless rotor shaft torque results vs. collective.

6.1.4 *Lift-to-Drag Ratio*

Effective lift-to-drag ratio is a key parameter to characterize rotor performance, for which the definition is introduced in chapter 5. Note that the thrust and drag terms are only from the rotor, and the wing forces are not considered. The L/D_e results versus thrust level C_T/σ are shown in Fig. 6.6. Without wing, the trend of L/D_e is similar to that of an articulated rotor: the maximum occurs at a moderate advance ratio, and both thrust and L/D_e are significantly reduced at higher advance ratios (Fig. 6.6(a)). Although the backward shaft tilt is beneficial for the thrust level, the improvement in L/D_e is modest and only occurs at high thrust level ($C_T/\sigma > 0.04$, see Fig. 6.6(c)), because a component of rotor thrust becomes drag with backward shaft tilt. On the other hand, the improvement from the wing trim takes effect at lower thrust level ($C_T/\sigma > 0.02$), and the increment in L/D_e is more significant than that from backward shaft tilt (Fig. 6.6(d)). Comparing with Fig. 6.1(a) and Fig. 6.5(a), the wing trim allows the rotor to operate at a certain thrust level with less shaft power. In Fig. 6.6(d), it seems that adding a backward shaft tilt on a rotor with wing trim does not further improve effective lift-to-drag ratio.

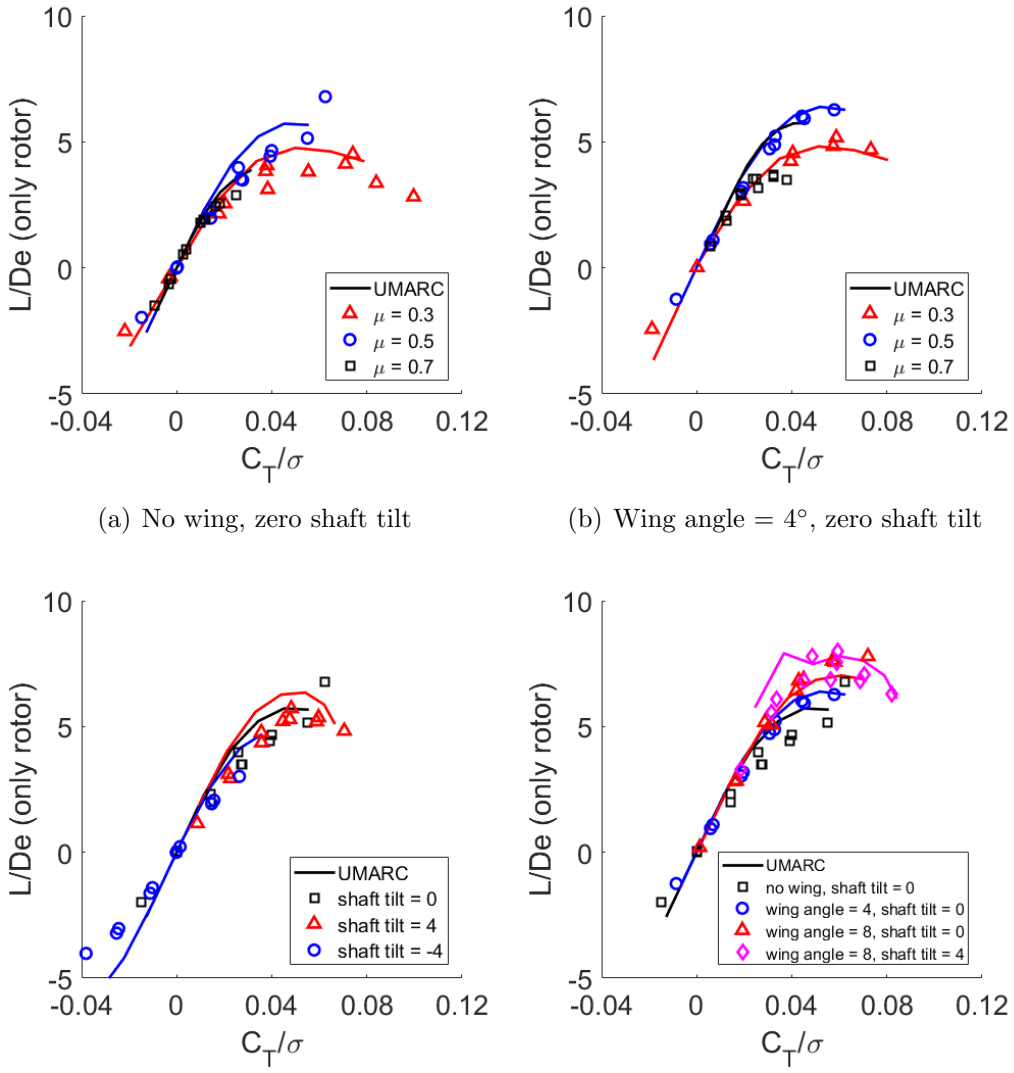

(a) No wing, zero shaft tilt

(b) Wing angle = 4°, zero shaft tilt

(c) $\mu = 0.5$ with shaft tilt, no wing

(d) $\mu = 0.5$ with wing

Fig. 6.6: Hingeless rotor effective lift-to-drag ratio L/D_e vs. rotor thrust C_T/σ (rotor only).

As a compound vehicle, not only the efficiency of the rotor should be considered, but also the wing contribution. In Fig. 6.7, the lift and drag of the wing are included, and the effective lift-to-drag ratio of the rotor becomes the overall lift-to-drag ratio:

$$L/D = \frac{L_{wing} + T_{rotor}cos\alpha_s - H_{rotor}sin\alpha_s}{D_{wing} + H_{rotor}cos\alpha_s + T_{rotor}sin\alpha_s + \frac{Q_{rotor}}{R\mu}} \tag{6.1}$$

Compared to the rotor L/D_e, the overall L/D benefits more from the wing configuration at higher advance ratios, since a wing inherently has a better lift-to-drag ratio than a rotor at higher freestream speed. With 4° wing incidence angle, the overall L/D at $\mu = 0.7$ reaches the same level as that of $\mu = 0.3$ (Fig. 6.7(a)). Compared with Fig. 6.6(d), the parametric study in Fig. 6.7(b) shows that the rotor L/D_e is on the same level as overall L/D with 4° wing incidence angle, indicating that $\mu = 0.5$ is a critical condition at which the wing and the rotor with lift offset are almost equally effective.

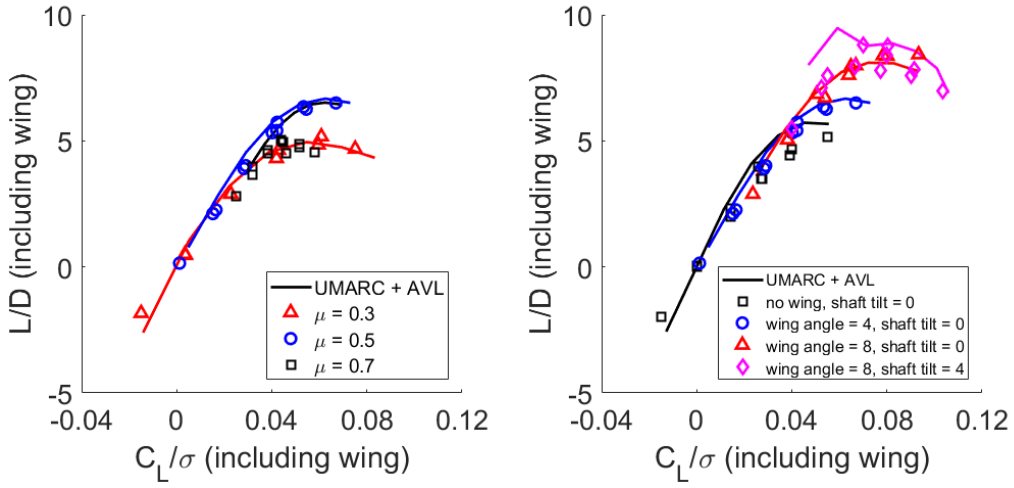

(a) Wing angle = 4°, zero shaft tilt

(b) $\mu = 0.5$, with wing

Fig. 6.7: Hingeless rotor overall lift-to-drag ratio L/D vs. total lift C_L/σ (rotor and wing).

The maximum lift-to-drag ratios at various advance ratios are shown in Fig. 6.8. Figure 6.8(a) shows the maximum L/D_e of the rotor only, and Fig. 6.8(b) shows the maximum overall L/D including the wing forces. The baseline hingeless rotor

(no wing, zero shaft tilt) reaches its maximum L/D_e of 4.5 along the μ axis at $\mu = 0.4$, which is on par with a conventional helicopter rotor. With 4° shaft tilt, the maximum L/D_e increases at moderate to high advance ratios ($\mu \geq 0.4$), and the maximum L/D_e along the μ axis is 4.8 (7% increment from the baseline), which occurs at $\mu = 0.5$. Both the rotor L/D_e and the overall L/D benefit enormously from the wing configuration: with a wing incidence angle of 4°, the compound configuration reaches its maximum rotor L/D_e of 6.3 (40% increment) and maximum overall L/D of 6.5 (44% increment) along the μ axis, both occurring at $\mu = 0.5$. Higher wing incidence angle not only makes the rotor more efficient, but also increases the lift-to-drag ratio of the wing itself, further expanding the maximum overall L/D. At $\mu = 0.5$, the maximum rotor L/D_e is 7.8 (73% increment) and the maximum overall L/D is 8.4 (87% increment) with 8° wing incidence angle. In the wind tunnel, it was not feasible to further increase advance ratio and identify the maximum lift-to-drag ratio along the μ axis, because of the extreme blade load level with the wing incidence angle. If the issue of blade structural load can be resolved, even higher maximum lift-to-drag ratio may be achieved at higher advance ratios.

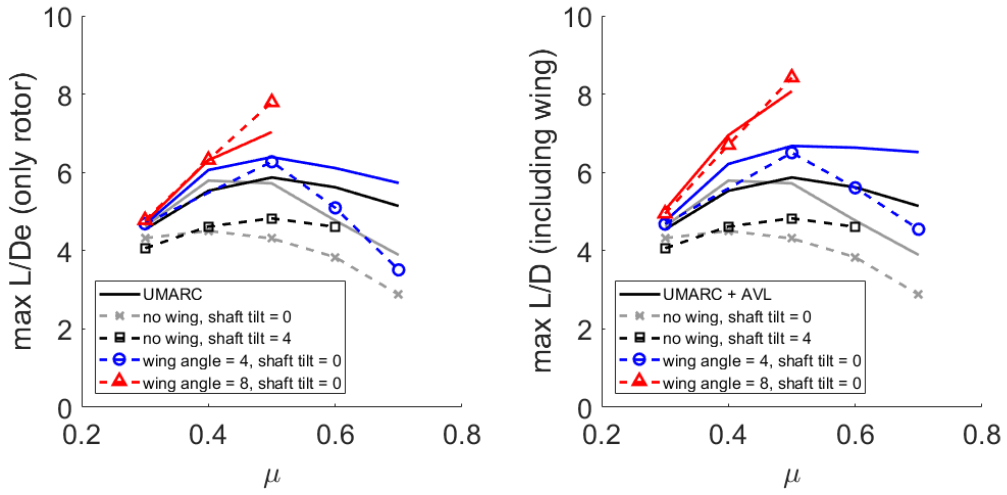

(a) Rotor only (b) Rotor and wing

Fig. 6.8: Maximum lift-to-drag ratios at various advance ratios.

6.1.5 Lift Offset and Rotor Lift Share

The concept of lift offset was previously used in coaxial rotorcraft studies [18], and the definition can be generalized for a rotor-wing compound configuration. The parameter can be defined as the lateral offset of the rotor thrust from the hub center where rolling moment becomes zero, normalized by the rotor radius:

$$LO = C_{Mx}C_T \tag{6.2}$$

Positive lift offset indicates that the equivalent center of thrust shifts more towards the advancing side. Another parameter, lift share, describes how much the rotor is unloaded at high advance ratios, which is defined by the lift generated by the rotor divided by the total lift (rotor and wing):

$$LS = \frac{C_T cos\alpha_s - C_H sin\alpha_s}{C_L} \tag{6.3}$$

The results of lift offset and lift share at $\theta_0 = 8°$ are presented in Fig. 6.9. A wing with higher incidence angle at higher advance ratio (higher freestream speed) generates more lift, resulting in higher lift offset and lower rotor lift share. At $\mu = 0.7$ and 4° wing incidence angle, the equivalent center of thrust shifts 21% radius towards the advancing side, where the flow regime is efficient in generating thrust. Meanwhile, the rotor is unloaded and only needs to produce 65% of the total lift. With 4° backward shaft tilt angle, the rotor generates more thrust, resulting in slightly lower lift offset and higher lift share. Within the lift offset level, the wing trim always improves the performance of the rotor by making the advancing side more efficient, and the rotorcraft can achieve higher overall lift-to-drag ratio with lower rotor lift share at high advance ratios, because a wing is more efficient than a rotor at high freestream speed.

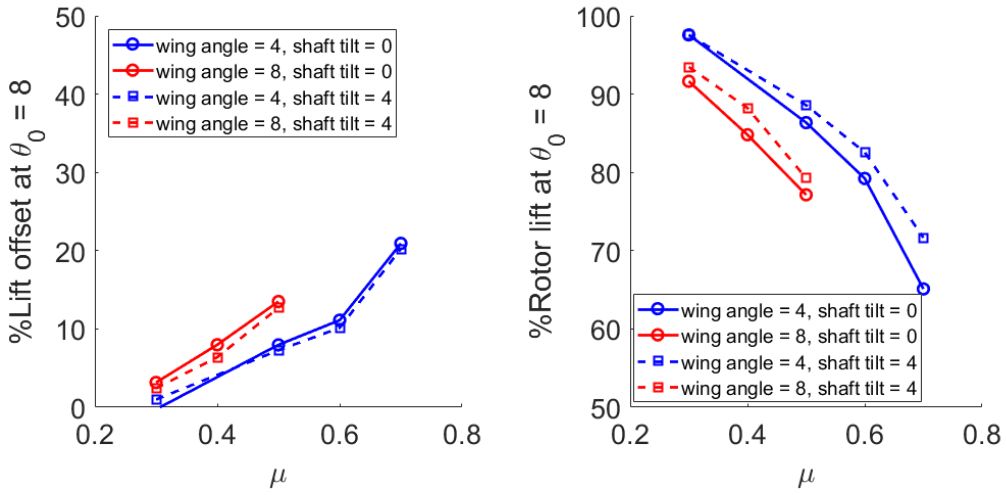

(a) Lift offset (b) Rotor lift share

Fig. 6.9: Lift offset and lift share at various advance ratios at $\theta_0 = 8°$.

6.1.6 Rotor-Wing Interaction

There are two aspects of rotor-wing interaction: the effect of the wing on the rotor, and the effect of the rotor on the wing. The effect on the rotor can be separated by inspecting the difference between wing trim and offset trim performances. The concepts of wing trim and offset trim are introduced in chapter 3: with wing trim, the rotor was trimmed to the moment target from the wing, and with offset trim, the wing was removed, and the rotor was trimmed to the prescribed moment target set by the wing in the wing trim. The comparison between wing trim and offset trim on the rotor thrust and effective lift-to-drag ratio are shown on Fig. 6.10 (similar comparison on horizontal force and shaft torque are omitted because the difference between normal trim and wing trim are limited). The thrust and L/D_e of offset trim are similar to those of wing trim (the differences are within the level of data scatter), indicating the effect of wing on rotor performance is neglectable for the

current setup at $\mu = 0.5$.

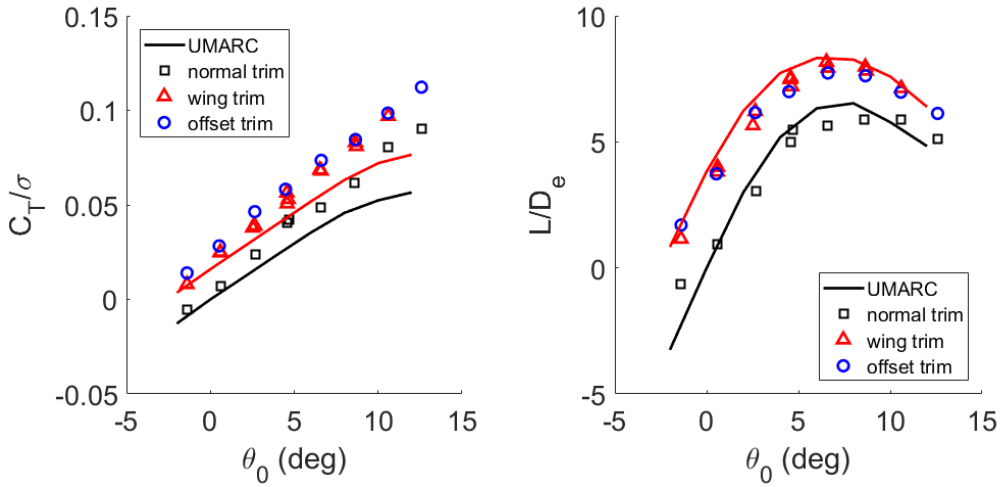

(a) Rotor thrust (b) L/D_e

Fig. 6.10: Difference between wing trim and offset trim, $\mu = 0.5$, zero shaft tilt.

The other aspect of rotor-wing interaction is on the wing. The effect can be characterized by observing the relationship between wing lift and rotor collective. As mentioned in chapter 4, the rotor affects the wing performance mainly through rotor-induced downwash. At a collective that the rotor generates zero thrust, the influence of rotor-induced downwash on the wing can be considered minimal. Thus, the wing lift at this collective can be considered as a baseline, and the effect of the rotor on the wing is the deviation from the baseline lift. The results at various advance ratios for wing angles of 4° and 8° are presented in Fig. 6.11. At $\mu = 0.3$, the wing lift reduces significantly at high collectives, especially for wing angle = 4°: the lift loss reaches 46% at $\theta_0 = 8°$. At $\mu = 0.5$, the lift loss level is much lower (about 6% at wing angle = 4° and 2% at wing angle = 8°). At $\mu = 0.7$, the rotor-induced component on the wing may be positive, because an upwash is generated

in the reverse flow region (see articulated rotor airload results).

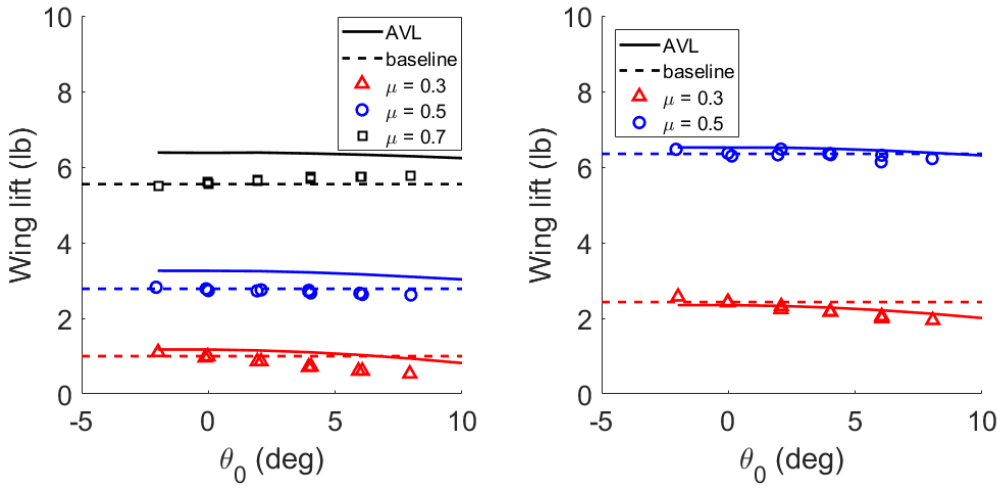

(a) Wing angle = 4°, zero shaft tilt (b) Wing angle = 8°, zero shaft tilt

Fig. 6.11: Effect of rotor collective on wing lift.

6.1.7 Cyclic Control Angle

The cyclic control angles to trim the rotor are presented in Fig. 6.12. Large negative longitudinal cyclic angle θ_{1s} (below $-10°$ at high advance ratios) is required to balance the significant lift loss in the reverse flow region (Fig. 6.12(a)), while lateral cyclic angle θ_{1c} increases in a range of less than 5° with collective (Fig. 6.12(b)), similar to what was observed in an articulated rotor. At $\mu = 0.7$, the magnitude of longitudinal cyclic is greater than the collective angle, indicating negative pitch angle on the advancing side. With backward shaft tilt, the change in inflow condition raises the angle of attack across the rotor disk, resulting in thrust increment on the rotor disk except in the reverse flow region. Consequently, the longitudinal cyclic needs to be more negative to reduce the thrust increment on the advancing side. With wing trim, the rotor is set to balance the rolling moment due to the

wing, so the rotor requires less negative longitudinal cyclic, resulting in more thrust generated on the advancing side and higher rotor thrust. At $\mu = 0.5$, the changes in longitudinal cyclic induced by 4° backward shaft tilt and wing trim almost cancel out each other (Fig. 6.12(c)). Both backward shaft tilt and wing trim appear to induce higher lateral cyclic, especially for the wing trim (Fig. 6.12(d)). The comprehensive analysis predictions are quite accurate for longitudinal cyclic and represent the effects of backward shaft tilt and lift offset correctly. However, offset pattern errors are present in the lateral cyclic prediction, in which the aerodynamic interference from the unmodeled fuselage can be a contributing factor according to a previous analytical study [99].

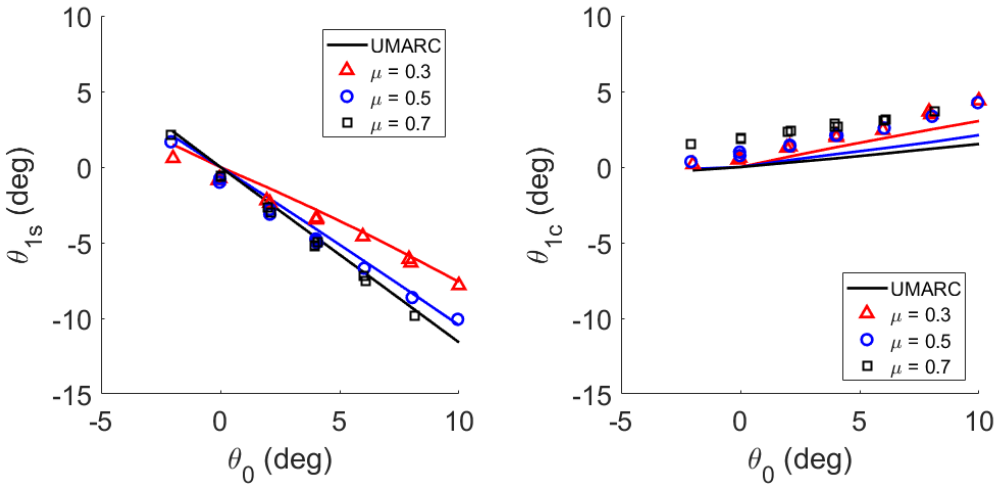

(a) θ_{1s}, no wing, zero shaft tilt

(b) θ_{1c}, no wing, zero shaft tilt

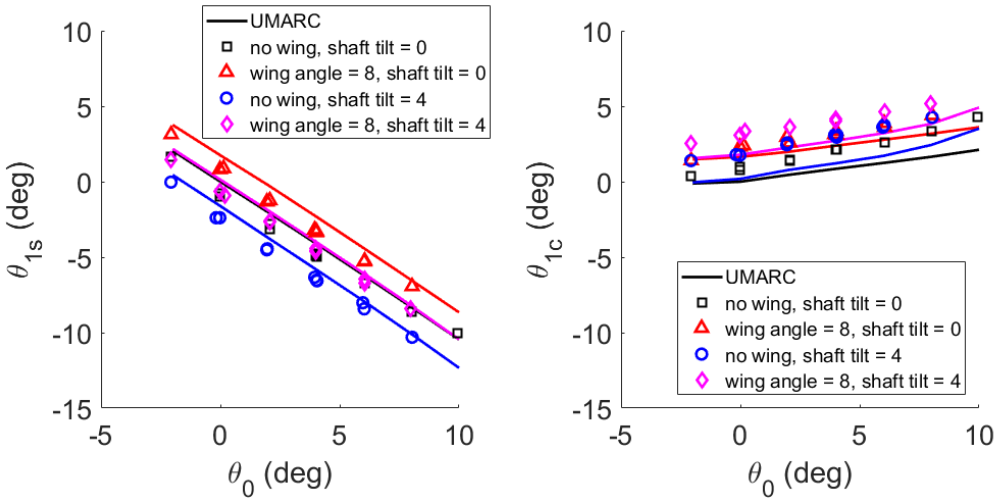

(c) θ_{1s} at $\mu = 0.5$ with wing and shaft tilt

(d) θ_{1c} at $\mu = 0.5$ with wing and shaft tilt

Fig. 6.12: Hingeless rotor cyclic control angles vs. collective.

6.2 Hub Load

Along with the rotor performance, the vibratory hub loads were measured by the 5-component hub balance. The raw azimuthal history data were decomposed in the harmonic domain and then corrected by the transfer functions gained from dynamic calibration, as described in chapter 3. After corrected using the trans-

fer functions from dynamic calibration and reconstruction into the time (azimuth) domain, the two in-plane components F_x and F_y are combined into F_{in}, following the same method for an articulated rotor. As explained in chapter 5, there should be only 4n/rev hub loads for a 4-bladed rotor (n is an integer multiplier) if it is perfectly balanced, tracked and trimmed, and the 4/rev load should be dominant. So, the emphasis of hub load analysis on the hingeless rotor is also 4/rev.

6.2.1 Horizontal Load

The results of 4/rev in-plane hub load versus collective are presented in Fig. 6.13. Figure 6.13(a) shows the in-plane load with no wing and zero shaft tilt at various advance ratios, and Figs. 6.13(b) and 6.13(c) show the effects of various shaft tilt angles and wing incidence angles on the in-plane load. In previous tests, it was observed that the in-plane hub load is lower than the vertical load for an articulated rotor. On the contrary, the in-plane hub load of the hingeless rotor is significantly higher than the vertical hub load: the maximum in-plane load is about 35 lbs at $\mu = 0.7$ compared to less than 3 pounds of vertical load. The in-plane load increases rapidly with collective, and the increment becomes steeper with higher advance ratios. A backward shaft tilt aggravates the in-plane load significantly (134% increment with 4° backward shaft tilt at $\mu = 0.5$, in Fig. 6.13(b)), and an increasing wing incidence angle tends to reduce the load (57% reduction with 8° wing incidence angle at $\mu = 0.5$, in Fig. 6.13(c)). The large 3/rev lag bending moment can be a major contributor to the large in-plane hub load, which will be discussed later in the blade structural load section. The comprehensive analysis predictions capture the

in-plane load trends with collective, advance ratio, shaft tilt and wing configuration, but the load intensity is underestimated.

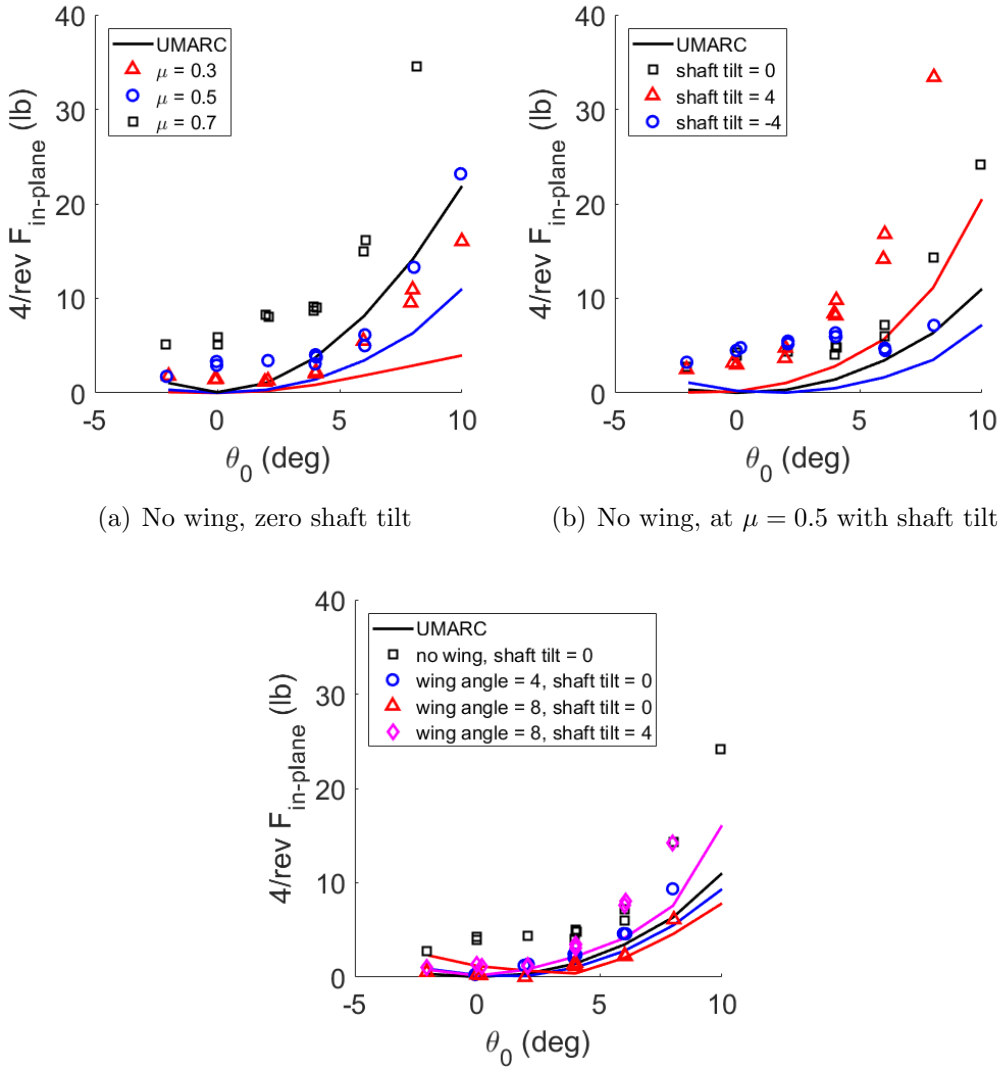

(a) No wing, zero shaft tilt

(b) No wing, at $\mu = 0.5$ with shaft tilt

(c) With wing, at $\mu = 0.5$

Fig. 6.13: Hingeless rotor 4/rev in-plane hub vibratory load vs. collective.

6.2.2 Vertical Load

Figure 6.14 shows the results of 4/rev vertical hub load versus collective, following the same plot arrangement as Fig. 6.13 for in-plane load. The overall load

level is substantially lower than that of an articulated rotor. The vertical hub load increases slightly with collective at lower advance ratios ($\mu \leq 0.5$), and the load level significantly increases near $\theta_0 = 8°$. An abrupt load increment occurs at $\mu = 0.7$; the load level peaks at $\theta_0 = 4°$ and drops rapidly at higher collectives (Fig. 6.14(a)). The comprehensive analysis predicts the load increment at $\mu = 0.7$, but the trend with collective is not correctly represented. The effects of shaft tilt angle and wing configurations on the vertical hub load are insignificant at $\mu = 0.5$ compared to its level of data scatter (Figs. 6.14(b) and 6.14(c)). No conclusive observation can be drawn on vertical hub load due to its limited magnitude and data scatter.

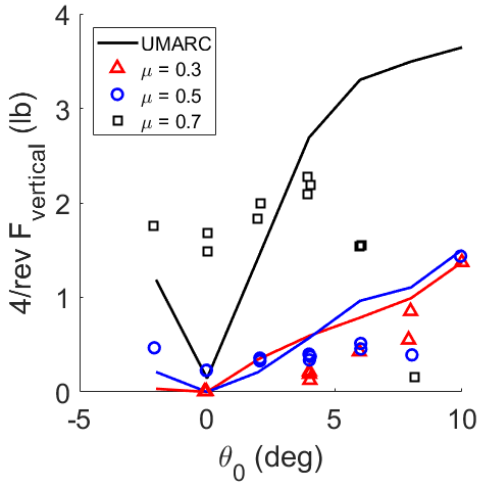

(a) No wing, zero shaft tilt

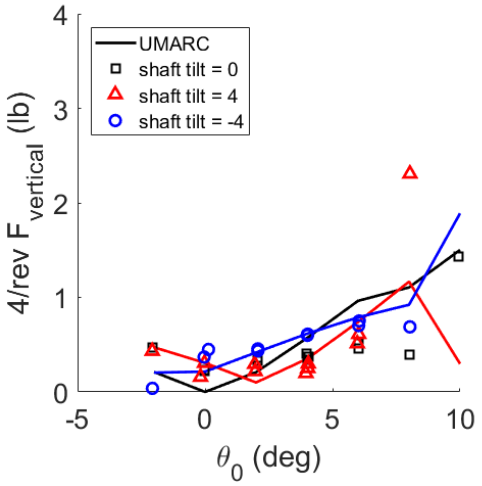

(b) No wing, at $\mu = 0.5$ with shaft tilt

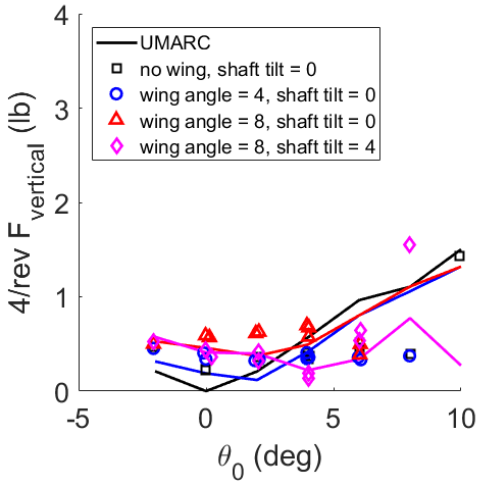

(c) With wing, at $\mu = 0.5$

Fig. 6.14: Hingeless rotor 4/rev vertical hub vibratory load vs. collective.

6.3 Blade Structural Load

Another emphasis of the hingeless rotor tests is to determine the structural load level at the blade root. Flap and lag bending moments are released at the root hinges for an articulated rotor, which is not the case with a hingeless rotor, imposing a major design constraint. The structural loads were obtained through the surface-

bond strain gauges at 25% radius. The results are first presented as phase-averaged azimuthal history to identify the physical mechanism, then harmonic decomposition is conducted to analyze the components quantitatively.

6.3.1 Flap Bending Moment

The azimuthal history and harmonic results of flap bending load are presented in Fig. 6.15, in which Figs. 6.15(a) and 6.15(b) show the effect of advance ratio at various collective angles with no wing and zero shaft tilt, Figs. 6.15(c) and 6.15(d) show the effect of shaft tilt at $\mu = 0.5$ with no wing, and Figs. 6.15(e) and 6.15(f) show the effect of wing incidence angle at $\mu = 0.5$ and zero shaft tilt. From the azimuthal history plots, it is observed that the predominant mode is 2/rev for a rotor with no wing (peaking at around $\psi = 90°$ and 270° in Figs. 6.15(a) and 6.15(c)), and 1/rev for a rotor with wing trim (peaking at $\psi = 90°$ in Fig. 6.15(e)). It has been shown in previous studies that at high advance ratios, the positive normal force on a rotor concentrates on the fore and aft section of the rotor disk, and the advancing side and retreating side are usually dominated by negative normal force due to the reverse flow region and zero hub moment trim (see the $c_n M^2$ contour plots in chapter 5). On the other hand, the lift offset due to wing trim benefits the rotor thrust mostly on the advancing side. So, it appears that the 1/rev flap bending load is almost in phase with the driving airload due to the lift offset, and the 2/rev structural load lags by about 180°. The phenomenon can be explained by the phase lag equation for a simplified forced oscillatory system with damping [100]:

$$\delta = \begin{cases} arctan(\frac{2\zeta\omega_n\omega_d}{\omega_n^2-\omega_d^2}), & \text{for } \omega_d \leq \omega_n \\ \pi + arctan(\frac{2\zeta\omega_n\omega_d}{\omega_n^2-\omega_d^2}), & \text{for } \omega_d > \omega_n \end{cases} \tag{6.4}$$

where δ is the phase angle, ζ is the damping constant, ω_n is the flap natural frequency ($\omega_n = 1.52/rev$ at 700 RPM for the third test), and ω_d is the driving frequency. With a low damping (the blade grip was replaced by a steel block without elastomer damper), the phase for 1/rev can be near zero while the phase for 2/rev is close to 180°.

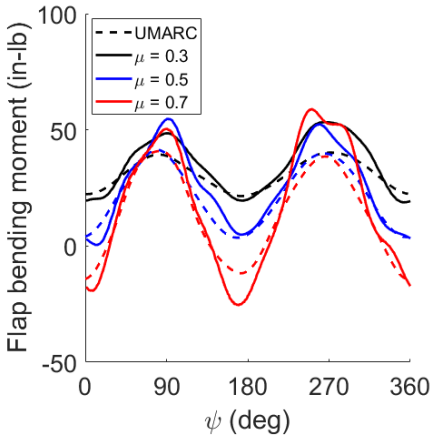

(a) No wing, zero shaft tilt

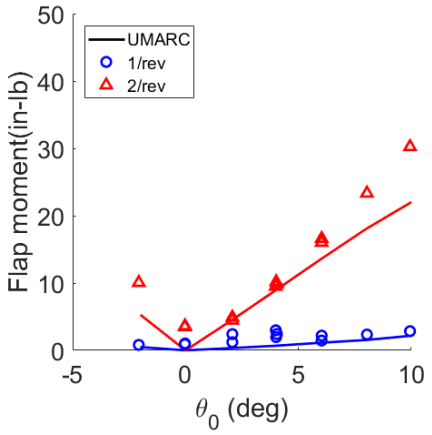

(b) No wing, zero shaft tilt, $\mu = 0.5$

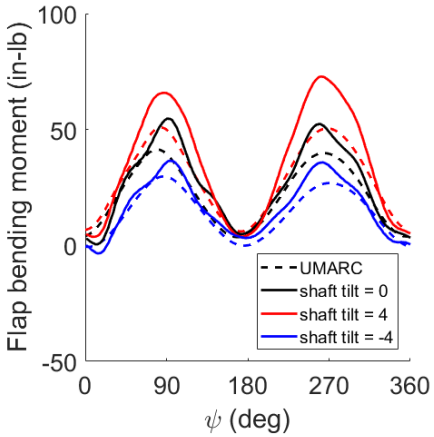

(c) No wing, $\mu = 0.5$

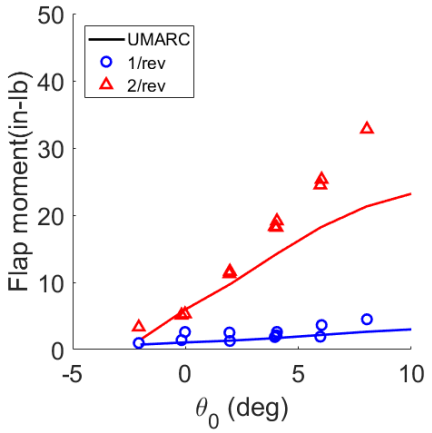

(d) No wing, 4° shaft tilt, $\mu = 0.5$

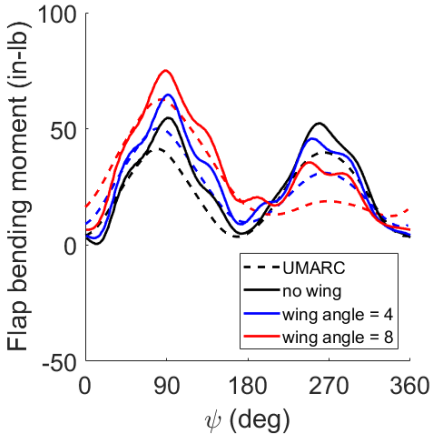

(e) With wing, zero shaft tilt, $\mu = 0.5$

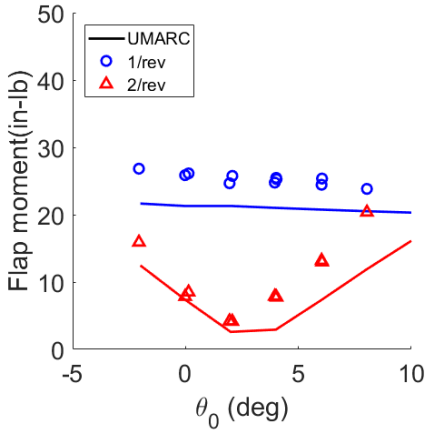

(f) 8° wing angle, zero shaft tilt, $\mu = 0.5$

Fig. 6.15: Azimuthal and harmonic results of flap bending moment at 25% radius, (hingeless rotor).

Once the aerodynamic driving forces and structural responding mechanism are understood, the behavior of flap bending load due to advance ratio, shaft tilt, and wing incidence angle changes can be inspected. With higher advance ratio, the normal force becomes more concentrated on the fore and aft sections of the rotor, making the 2/rev driving force larger. So, the 2/rev flap bending load level becomes higher (Fig. 6.15(b)), and the mean load level reduces because the rotor generates less total thrust at higher advance ratios (Fig. 6.15(a)). The backward shaft tilt induces an additional angle of attack across the rotor disk, but only the fore and aft sections benefit from it (the advancing side still needs to be balanced against the retreating side, which does not benefit substantially from shaft tilt). As a consequence, the 2/rev driving force increases and so does the flap bending load (Fig. 6.15(d)). The mean load level increases because the rotor generates more thrust (Fig. 6.15(c)). With no wing and normal trim, the 1/rev flap bending load remains low, indicating the rotor is well trimmed. Trimmed to the rolling moment target set by the wing, additional normal force is generated on the advancing side, and the 1/rev flap bending load emerges, while the 2/rev component is reduced (Fig. 6.15(f)). The effects of the wing become more pronounced with higher wing incidence angle and the overall peak-to-peak moment keeps increasing (Fig. 6.15(e)), limiting testing to advance ratio below 0.5 for 8° wing incidence angle. The predictions of the comprehensive analysis capture the trends for both azimuthal history and harmonically decomposed results but underestimate the 2/rev component to a certain extent.

6.3.2 *Parametric Study on Flap Bending Stiffness*

Since the first wind tunnel test on hingeless rotor, it was found that the 2/rev flap bending moment is the primary structural constraint on test conditions. Therefore, blades with different structural properties were fabricated and tested, and their 2/rev flap bending moment levels during the wind tunnel tests are shown in Fig. 6.16. In the second wind tunnel test, a set of blades with 16% more weight and 35% more flap bending stiffness were used. It was intended that the higher stiffness would raise the load limit and expand the test envelope on advance ratio and collective. However, the 2/rev load condition became much worse because the increased 1st flap frequency towards 2/rev (from 1.58/rev to 1.66/rev, although it was not too close to 2/rev). Compared to that in the first test, the 2/rev flap load increased by 110% in the second test at $\mu = 0.5$, $\theta = 8°$ (see Figs. 6.16(b) and 6.16(a)), making test cases at higher advance ratios infeasible. The results indicate that increasing the blade flap bending stiffness is not an effective way to expand the test envelope. The third test featured a set of heavier and softer blades to reduce the 1st flap frequency (7% more weight and 10% less flap bending stiffness than the baseline blades in the first test, the 1st flap frequency was 1.52/rev). The 2/rev flap load level was reduced by 5% at $\mu = 0.5$, $\theta = 8°$ (see Fig. 6.16(c)), allowing test cases at $\mu = 0.7$ with lift offset (however, the test envelope is not expanded compared to the baseline, because the load limit is reduced with the decreased stiffness). One may need to implement a flap damping mechanism to allow test cases with higher advance ratios/collectives.

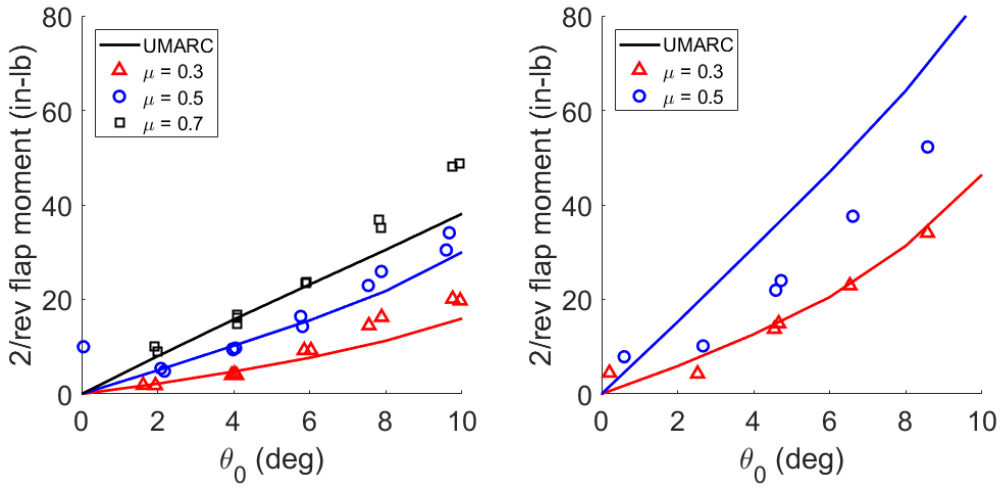

(a) Test 1 (baseline stiffness)

(b) Test 2 (more stiffness)

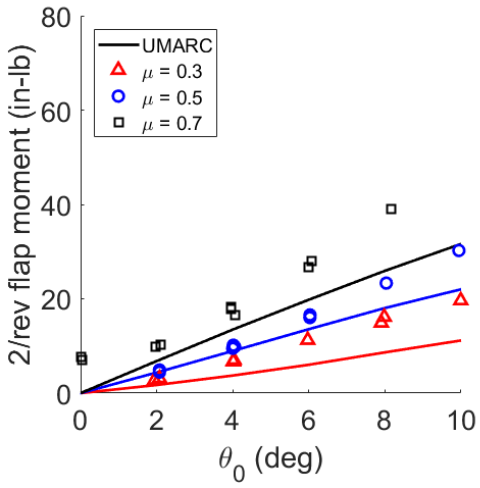

(c) Test 3 (less stiffness)

Fig. 6.16: Effect of flap bending stiffness on 2/rev flap moment (hingeless rotor).

6.3.3 Lag Bending Moment

The azimuthal history and harmonic results of lag bending load are presented in Fig. 6.17, following the same arrangement as Fig. 6.15 for flap bending moment. The lag bending load level is high: the peak-to-peak load level is more than 100% greater than that of flap bending moment with no wing, and the load level becomes

even higher with wing trim. However, the lag moment is still not a major structural constraint because the lag bending stiffness of the blades is at least 20 times higher than the flap bending stiffness. The predominant modes are 2/rev and 3/rev, especially 3/rev at high advance ratios. The large 3/rev lag moment is excited by the adjacent first lag frequency (3.1/rev at 700 RPM for the third test). The intense lag bending moment at the blade roots can be a major contributor of the large in-plane hub load, since the lag bending moment has a major in-plane component, and the trends are similar to those of in-plane hub load: the load level of lag bending moment also increases with advance ratio (Figs. 6.17(a) and 6.17(b)) and backward shaft tilt (Figs. 6.17(c) and 6.17(d)), and decreases with wing incidence angle (Figs. 6.17(e) and 6.17(f)). The comprehensive analysis predicts the 3/rev lag moment satisfactorily, but the 2/rev component is underestimated. According to the structural load results, the predominant constraint is 2/rev flap bending moment, which increases rapidly with collective and advance ratio. To alleviate the load level, one may use softer blades or implement a flap damping mechanism.

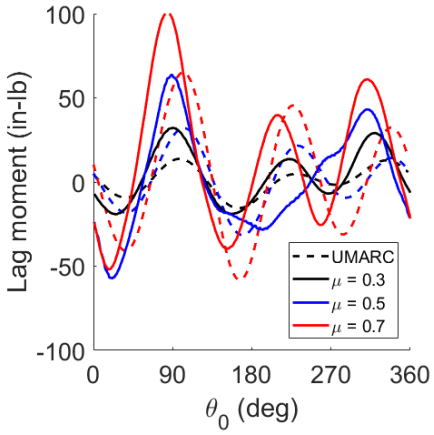

(a) No wing, zero shaft tilt

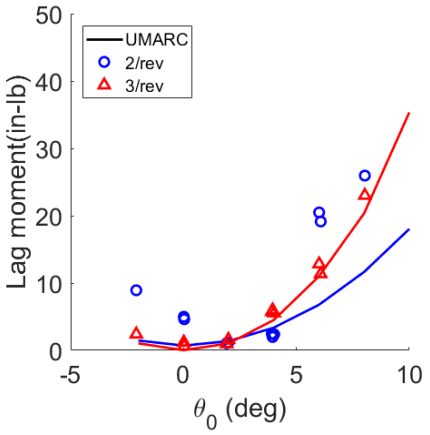

(b) No wing, zero shaft tilt, $\mu = 0.5$

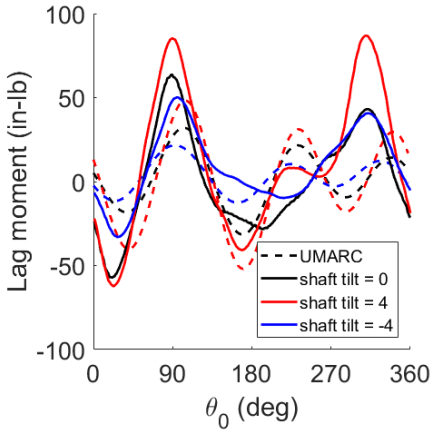

(c) No wing, $\mu = 0.5$

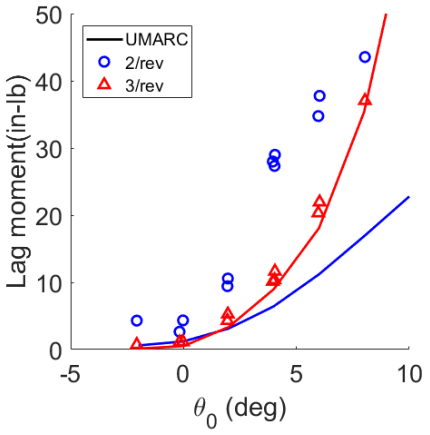

(d) No wing, 4° shaft tilt, $\mu = 0.5$

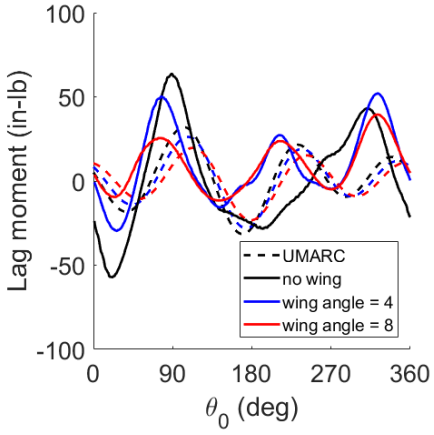

(e) With wing, zero shaft tilt, $\mu = 0.5$

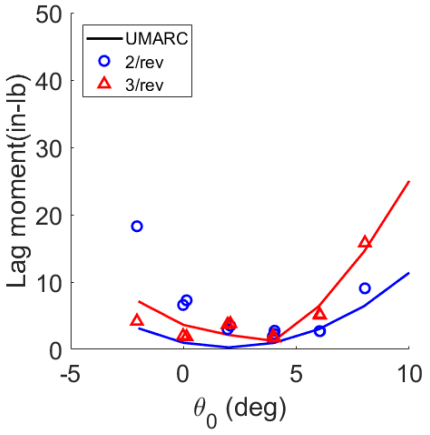

(f) 8° wing angle, zero shaft tilt, $\mu = 0.5$

Fig. 6.17: Azimuthal and harmonic results of lag bending moment at 25% radius, (hingeless rotor).

Chapter 7: Summary and Conclusions

To investigate the aerodynamic phenomena at high advance ratios and provide data for validations, six wind tunnel tests were conducted in the Glenn L. Martin Wind Tunnel with a 6-ft diameter, 4-bladed Mach-scaled rotor. Articulated rotors were used in the first three tests, and the latter three tests featured hingeless rotors. In one articulated rotor test, non-instrumented blades were used to guarantee high blade similarity. A baseline performance dataset was obtained up to an advance ratio of 0.9 at 0° and $\pm 4^\circ$ shaft tilt angles. Another test on articulated rotor featured blade-embedded pressure sensors and strain gauges with 3D-printed sensor mounts. Pressure data were acquired at 30% radius to determine the sectional airloads by surface integration. The hingeless rotors were tested with a stub wing on the retreating side. The main focus of these tests was to examine the performance improvements on the rotor and the overall compound configuration due to the lift offset.

Rotor and wing performances, swashplate control angles, hub vibratory loads, blade surface pressure, sectional airloads and structural loads were correlated with computational predictions. The experimental results were compared with previous wind tunnel test data, comprehensive analyses (UMARC and PrasadUM), CFD/CSD

coupled analysis (HAMSTR/PrasadUM), and the stub wing behavior was simulated with a vortex lattice model (AVL). Overall, the correlation results were found satisfactory, and the study provided some insights into the aerodynamic mechanisms at high advance ratio flight regime, in particular the mechanisms of shaft tilt and lift offset, and the formation of dynamic stall in the reverse flow region. Some major conclusions of the present study are listed below.

7.1 Key Conclusions

The wind tunnel tests and computational analyses can be divided into four categories: non-instrumented articulated rotor studies, articulated rotor studies with blade instruments, hingeless rotor studies with normal trim, and hingeless rotor studies with lift offset. The key observations are summarized separately.

7.1.1 Non-Instrumented Articulated Rotor

1. Wind tunnel test was conducted up to an advance ratio of 0.9 at 900 and 1200 RPM, and data correlation studies were performed with UMARC, emphasizing rotor performance and hub vibratory loads. Higher blade similarity (structural property variation was about 2.5%) was achieved with non-instrumented test blades than previous in-house tests (variation was about 5%), improving trim quality by reducing the error in 1/rev flap by 0.2°. The measured cyclic angles showed good repeatability and linearity.

2. A shaft tilt study was carried out with ±4° shaft tilt angles at various advance

ratio. The study showed that a backward tilt increases rotor thrust and reduces shaft torque at moderate collective settings. The backward shaft tilt provides a higher effective lift-to-drag ratio at the same thrust level as with zero shaft tilt, generating the same amount of thrust with lower collective setting to save shaft power. The thrust increment with backward shaft tilt is due to increased angle of attack from the inflow condition change. With backward shaft tilt, more negative longitudinal cyclic is required to balance the additional thrust on the advancing side.

3. The horizontal rotor force decreases with collective at lower advance ratios and increases with collective at higher advance ratios. This trend is due to large local pitch angle increment on the retreating side at low advance ratios, and the expanding reverse flow region on the retreating side and negative pitch induced by trim condition on the advancing side at high advance ratios.

4. The shaft torque increases with collective, and the increment drops rapidly with increasing advance ratio. The main contributor to the phenomenon is that the in-plane force towards the leading edge in the reverse flow region. With either backward or forward shaft tilt, the shaft torque is reduced compared to that of zero shaft tilt at low collective settings.

5. The hub vibratory load data showed that the 4/rev in-plane and vertical loads increase with higher advance ratios and backward shaft tilt. For an articulated rotor, the vertical hub load level is higher than the in-plane hub load. The intense 1/rev in-plane and 2/rev vertical airload components associated with

high advance ratio may be contributors of the hub vibratory load increments with advance ratio.

7.1.2 Articulated Rotor with Blade Instruments

1. Wind tunnel test was conducted up to an advance ratio of 0.8 at 700 and 900 RPM, up to an advance ratio of 0.8. High sensor survivability was achieved with 3D-printed sensor mounts, and pressure data were acquired to calculate sectional airloads at 30% radius. Data correlation studies were performed with comprehensive analyses (UMARC and PrasadUM) for all collective sweeps, and with CFD/CSD coupled analysis (HAMSTR/PrasadUM) at two collectives ($\theta = 3^\circ$ and 11°), at an advance ratio of 0.8.

2. At high advance ratios and high collectives, a strong reverse flow dynamic stall peak forms before the maximum local pitch or tangential speed, indicating that the peak requires not only high local pitch and tangential speed, but also a rapid increment of these. The peak becomes weaker and propagates toward the leading edge over the lower surface, and flips to upper surface and moves towards the trailing edge. If the stall is intense enough, another smaller dynamic stall peak forms aft the first major peak.

3. Although some discrepancies were present in pressure predictions, the data correlations between the test results and the CFD/CSD predictions were satisfactory on sectional airloads. Key features of the flight regime were captured by the analysis, including the strong dynamic stall peaks in the reverse flow

region, the normal force fluctuation on the advancing side due to rotor trim, the effect of hub wake at about zero azimuth, and the vortex interaction on the advancing side.

4. The normal force loss around zero azimuth was envisaged to be due to the wake blockage due to the rotor hub/shaft. With the hub/shaft solid body modeled in the CFD/CSD flow field, the effect of hub wake on rotor normal force was modeled with satisfactory accuracy. The hub model also improved pitching moment prediction in $\psi = 0^\circ$ to 30°.

5. At high advance ratios, the flap bending moment at 30% radius showed 4/rev pattern, with a weaker negative peak on the retreating side. The dominating 4/rev harmonic can be due to the closeness with the 2nd flap frequency. At a high collective setting, the torsional moment is impulsive on the retreating side, which corresponding to the intense nose-up pitching moment in the airload results. The predictions of CFD/CSD analysis captured the trends for both flap bending and torsional moment.

7.1.3 Hingeless Rotor with Normal Trim

1. The test stand was modified to accommodate a hingeless rotor, removing the flap and lag degrees of articulation. A wind tunnel test was conducted up to an advance ratio of 0.7 at 700 and 1200 RPM without lift offset to validate the structural integrity of the setup, and to test the trim method based on the hub balance.

2. Trimmed to zero hub moment, the performance of a baseline hingeless rotor with no wing is comparable to that of a baseline articulated rotor. The effect of wing trim on rotor horizontal force and shaft torque is limited, and the response to backward shaft tilt is similar to that of an articulated rotor.

3. The 4/rev vertical hub load of a hingeless rotor is on par with that of a previously tested articulated rotor, while the 4/rev in-plane hub load is considerably higher than the vertical load, in contrast to the articulated rotor results. Both lift offset and backward shaft tilt increase the hub vibratory load level. The substantial 3/rev lag bending moment at the blade roots can be a major contributor of the large in-plane hub load.

4. The predominant structural constraint for a hingeless rotor is 2/rev flap bending moment, which increases rapidly with collective and advance ratio, limiting the test envelope to advance ratio below 0.7. Large 3/rev lag bending moments were also observed at high advance ratio and high collective, which were not captured by the comprehensive analysis.

7.1.4 Hingeless Rotor with Lift Offset

1. A stub wing was installed on the retreating side of the rotor, and the rotor was tested at 700 RPM with lift offset. The maximum advance ratio was 0.7, and wing angles of incidence of 4° and 8° were tested. Data correlation studies were performed with UMARC.

2. Trimmed to the rolling moment target set by the wing, the advancing side of

a hingeless rotor operates in a more efficient condition at high advance ratios, resulting in a significant improvement in thrust level and lift-to-drag ratio. The wing also produces a considerable amount of lift, unloading the rotor and further increasing the overall lift-to-drag ratio. The benefits of backward shaft tilt and lift offset on rotor thrust can occur simultaneously.

3. A hingeless rotor with a wing requires less negative longitudinal cyclic to trim, while the rotor requires more negative longitudinal cyclic with backward shaft tilt. The two effects can balance out each other for many test cases.

4. At low advance ratios, the wing lift is reduced significantly by the rotor downwash, especially at high collectives. The effect becomes less prominent at high advance ratios because of the limited inflow rate and the increased freestream speed. On the other hand, the effect of wing on rotor performance is quite small even at lower advance ratios.

5. With an asymmetric wing, the mean and 1/rev components of the flap bending moment increase, the 2/rev component decreases, and the overall peak-to-peak moment keeps increasing, further worsening the flap load condition. A parametric study on flap bending stiffness showed that using stiffer or softer blades is not effective in expanding the test envelope.

In summary, reliable datesets including pressure data and section airloads were obtained in wind tunnel tests, and understandings were gained on the high advance ratio flight regime. With increasing advance ratio, the reverse flow region becomes

larger, in which strong reverse flow dynamic stall occurs, inducing normal force loss and impulsive nose-up pitching moment. Along with the zero-moment trim, the thrust and lift-to-drag ratio are limited at high advance ratios, and thrust reversal occurs around an advance ratio of 0.9. Backward shaft tilt induces an upwash and additional lift on the fore and aft sections of the rotor, improving the thrust and lift-to-drag ratio at high advance ratios. Without lift offset, the performance of a hingeless rotor is similar to that of an articulated rotor. With a lift offset, the rotor is able to generate more thrust on the advancing side and become more efficient. In addition, the rotorcraft can benefit from the asymmetric wing configuration at high speeds. However, the blade load is very high compared to an articulated rotor due to the flap natural frequency and the lack of moment release at the flap hinge.

7.2 Future Work

1. In further tests, different compound rotorcraft configurations can be investigated. To begin with, the stub wing on the retreating side can be tested at various incidence angles and X- and Z- locations with respect to the rotor. Then, a second wing can be installed on the advancing side to unload the rotor and compare the efficiency of symmetric and asymmetric trim configurations. Eventually, a rear propeller pylon with an electrical motor can be implemented to represent a whole compound helicopter, which has been designed in CAD (Fig 7.1).

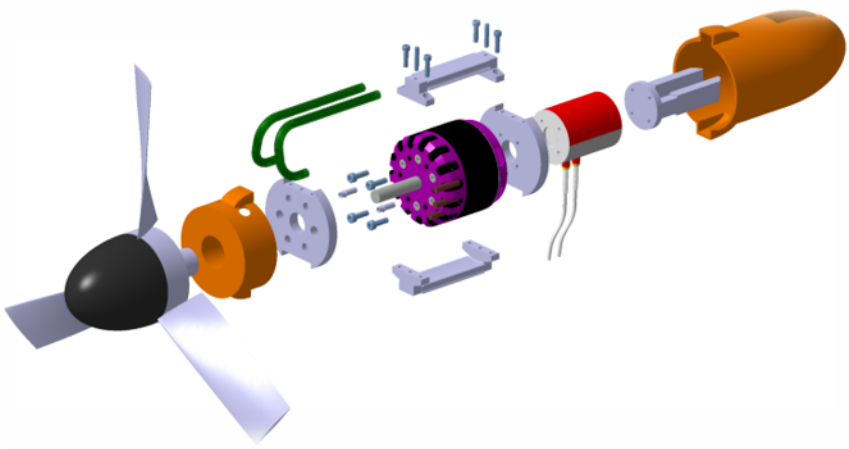

Fig. 7.1: CAD design of the rear propeller.

2. More sensors can be used to investigate the airload and flow field in further tests on hingeless rotors. Pressure sensors can be implemented in the blades and stub wings, and PIV results on the retreating side should be examined with the pressure sensors (Fig. 7.2). These measuring techniques have been applied in previous articulated rotor tests. However, it can be challenging to integrate pressure sensors into a hingeless rotor blade, because the flap load level is significantly higher than that of an articulated rotor blade, and the installation of blade sensors always undermines the blade structure. Benchtop tests and hover tests should be carried out meticulously before any wind tunnel entry to ensure the blade structural integrity.

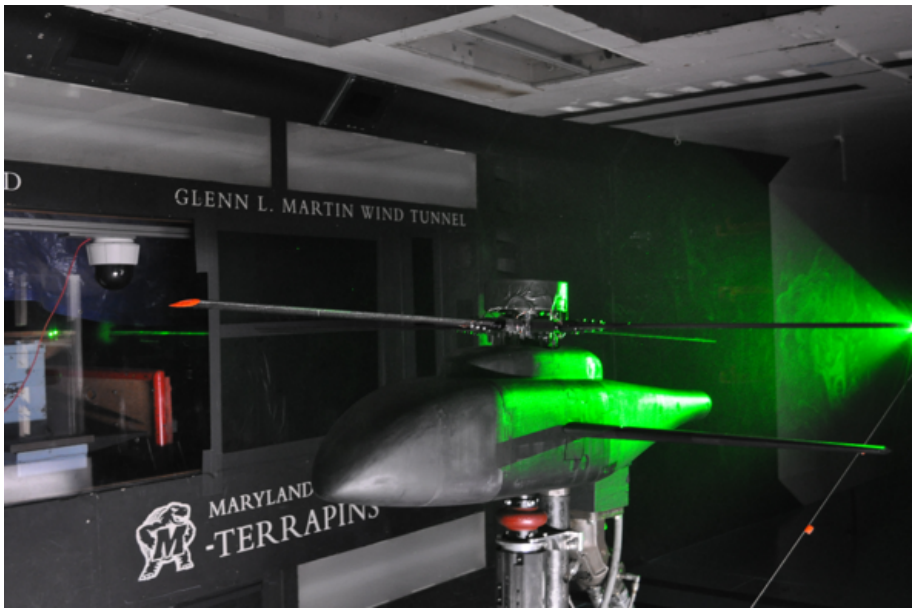

Fig. 7.2: PIV setup on the retreating side (3rd hingeless rotor test).

3. To allow test cases at higher advance ratio, collective setting or lift offset level, modification is required on the rotor structure. A parametric study on blade flap bending stiffness has shown that a stiffer rotor induces a large flap load increase because the 1st flap frequency is closer to 2/rev, and a softer rotor does not help because the load reduction is not much comparing to the load limit reduction with the decreased stiffness. A pseudo-hinge structure or flap damping mechanism may be applied at the blade root to expand the test envelope.

4. As a part of compound rotorcraft analysis, the modeling of the wing should be included in the UMARC. Currently, the stub wing performance is modeled as lift and drag forces that only depend on angle of attack, and the only input from UMARC is the averaged downwash correction. There is no periodical nor spanwise effect of these on the wing, and the effect of the wing on the

rotor is omitted except setting the rolling moment as a trim target. With the wing vortex lattice added into the UMARC main inflow-calculating iteration, the rotor-wing interaction can be represented more accurately.

5. A CFD/CSD coupled analysis has been conducted on an articulated rotor with its hub/shaft assembly, exhibiting satisfactory data correlation and having the effect of hub wake captured. With the methodology established, a similar CFD/CSD analysis should be performed with the fuselage and the wing included (and the rear propeller for further tests). The analysis can provide surface pressure predictions to compare with pressure sensor readings and visualize the interactions between the rotor, the wing, and the propeller. Also, the results will determine whether the discrepancy in lateral cyclic prediction is due to the fuselage blockage effect.

Bibliography

[1] B. Berry. Fundamental Understanding of Rotor Aeromechanics at High Advance Ratio Through Wind Tunnel Testing, 2016.

[2] A. Sridharan, B. Govindarajan, I. Chopra, and V. T. Nagaraj. Design Considerations of a Lift-Offset Single Main Rotor Compound Helicopter. San Francisco, CA, January 2016. AHS Technical Meeting on Aeromechanics Design for Vertical Lift.

[3] J. B. Wheatley and M. J. Hood. Full-Scale Wind Tunnel Tests of a PCA-2 Autogiro Rotor. Technical Report NACA-TR-515, NACA Langley Aeronautical Lab, January 1935.

[4] Jr. Meyer, J. R. and Jr. Falabella, G. An Investigation of the Experimental Aerodynamic Loading on a Model Helicopter Rotor Blade. Technical Report NACA-TN-2953, NACA, May 1953.

[5] Jr. Jenkins, J. L. Wind-Tunnel Investigation of a Lifting Rotor Operating at Tip-Speed Ratios from 0.65 to 1.45. Technical Report NASA TN D-2628, NASA Langley Research Center, February 1965.

[6] F. D. Harris. Rotor Performance at High Advance Ratio: Theory versus Test. Technical Report NASA/CR-2008-215370, NACA Ames Research Center, October 2008.

[7] J. R. Ewans and T. A. Krauss. Model Wind Tunnel Tests of a Reverse Velocity Rotor System. Technical Report HC144R1070, Fairchild Republic Division, January 1973.

[8] T. R. Quackenbush, D. A. Wachspress, Jr. McKillip, R. M., and M. J. Sibilia. Aerodynamic Studies of High Advance Ratio Rotor Systems. Virginia Beach, VA, May 2011. 67th Annual Forum of the American Helicopter Society.

[9] A. Datta, H. Yeo, and T. R. Norman. Experimental Investigation and Fundamental Understanding of a Full-Scale Slowed Rotor at High Advance Ratios. *Journal of the American Helicopter Society*, 58(2):1–17, April 2013.

[10] E. Brouwers, M. Fillman, and R. Deresz. Advanced AH-64 Compound Wind Tunnel Testing Overview. Philadelphia, PA, May 2019. 75th Annual Forum of the American Helicopter Society.

[11] H. Yeo. Investigation of Performance and Loads of a UH-60A Rotor at High Advance Ratios. Fort Worth, TX, May 2012. 68th Annual Forum of the American Helicopter Society.

[12] R. A. Ormiston. Induced Power of the Helicopter Rotor. Baltimore, MD, June 2004. 60th Annual Forum of the American Helicopter Society.

[13] G. M. Bowen-Davies. Performance and Loads of Variable Tip Speed Rotorcraft at High Advance Ratios, 2015.

[14] M. Potsdam, A. Datta, and B. Jayaraman. Computational Investigation and Fundamental Understanding of a Slowed UH-60A Rotor at High Advance Ratios. *Journal of the American Helicopter Society*, 61(2):1–17, April 2016.

[15] L. Trollinger. Refined Performance and Loads of a Mach-Scale Rotor at High Advance Ratios, 2017.

[16] A. Saxena. Primary Control of a Mach Scale Swashplateless Rotor Using Brushless DC Motor Actuated Trailing Edge Flaps, 2015.

[17] M. C. Cheney. The ABC helicopter. *Journal of the American Helicopter Society*, 14(4):10–19, October 1969.

[18] W. Johnson. Influence of Lift Offset on Rotorcraft Performance. Technical Report NASA TP-2009-215404, NASA Ames Research Center, November 2009.

[19] F. F. Felker. Performance and Loads Data from a Wind Tunnel Test of a Full-Scale, Coaxial, Hingeless Rotor Helicopter. Technical Report NASA-TM-81329, NASA Ames Research Center, October 1981.

[20] A. J. Ruddell and J. A. Macrino. Advancing Blade Concept (ABC) High Speed Development. Washington, DC, May 1980. 36th Annual Forum of the American Helicopter Society.

[21] P. R. Cumbreras and S. Sartorius. Feasibility Study of a Novel Asymmetric Rotorcraft Confi

guration: Single-Rotor Advancing Blade Concept. Los Angeles, CA, August 2013. 2013 International Powered Lift Conference.

[22] X. Wang, A. Bauknecht, S. Maurya, and I. Chopra. Slowed Hingeless Rotor Wind Tunnel Tests and Validation at High Advance Ratios. *Journal of Aircraft*, (accepted).

[23] J. L. McCloud, J. C. Biggers, and R. H. Stroub. An Investigation of Full-Scale Helicopter Rotors at High Advance Ratios and Advancing Tip Mach Numbers. Technical Report NASA TN D-4632, NASA Ames Research Center, July 1968.

[24] B. D. Charles and W. H. Tanner. Wind Tunnel Investigation of Semirigid Full-Scale Rotors Operating at High Advance Ratios. Technical Report USAAVLABS TR 69-2, US Army Aviation Material Laboratories, January 1969.

[25] G. Warwick. Groen Brothers Starts work on High-speed VTOL Heliplane for DARPA. *Flight International*, 168(5015):4, December 2005.

[26] E. Brouwers, M. Fillman, and R. Deresz. Full-Scale Wind Tunnel Test of the UH-60A Airloads Rotor. Virginia Beach, VA, May 2011. 67th Annual Forum of the American Helicopter Society.

[27] R. M. Kufeld and W. G. Bousman. UH-60A Helicopter Rotor Airloads Measured in Flight. *Aeronautical Journal*, 101(1005):217–227, May 1997.

[28] B. Berry and I. Chopra. Wind Tunnel Testing for Performance and Vibratory Loads of a Variable-speed Mach-scale Rotor. Virginia Beach, VA, May 2011. 67th Annual Forum of the American Helicopter Society.

[29] B. Berry and I. Chopra. Performance and Vibratory Load Measurements of a Slowed-Rotor at High Advance Ratios. Fort Worth, TX, May 2012. 68th Annual Forum of the American Helicopter Society.

[30] B. Berry and I. Chopra. High Advance Ratio Wind Tunnel Testing of Two Mach-Scale Rotor Geometries. Phoenix, AZ, May 2013. 69th Annual Forum of the American Helicopter Society.

[31] B. Berry and I. Chopra. High Advance Ratio Wind Tunnel Testing of a Model Rotor with Pressure Measurements. San Francisco, CA, January 2014. 5th Decennial AHS Aeromechanics Specialists Conference.

[32] B. Berry and I. Chopra. Slowed Rotor Wind Tunnel Testing of an Instrumented Rotor at High Advance Ratio. Southampton, UK, September 2014. 40th European Rotorcraft Forum.

[33] B. Berry and I. Chopra. Wind Tunnel Testing of an Instrumented Rotor at High Advance Ratio. Kissimmee, FL, January 2015. 56th AIAA Structures, Structural Dynamics, and Materials Conference.

[34] W. Johnson. Technology Drivers in the Development of CAMRAD II. San Francisco, CA, January 1994. 3rd Decennial AHS Aeromechanics Specialists Conference.

[35] H. Saberi, M. Khoshlahjeh, R. A. Ormiston, and M. J. Rutkowski. Overview of RCAS and Application to Advanced Rotorcraft Problems. San Francisco, CA, January 1994. 3rd Decennial AHS Aeromechanics Specialists Conference.

[36] D. A. Wachspress, T. R. Quackenbush, and A. H. Boschitsch. Rotorcraft Interactional Aerodynamics with Fast Vortex/Fast Panel Methods. *Journal of the American Helicopter Society*, 48(4):223–235, October 2013.

[37] P. G. Buning and R. L. Meakin. Consolidation of Time-Accurate, Moving Body Capabilities in OVERFLOW. Fort Walton Beach, FL, June 2002. 6th Overset Composite Grid and Solution Technology Symposium.

[38] M. W. Floros and W. Johnson. Performance Analysis of the Slowed-Rotor Compound Helicopter Configuration. *Journal of the American Helicopter Society*, 54(2):1–12, April 2009.

[39] Yeo. H. and W. Johnson. Optimum Design of a Compound Helicopter. *Journal of Aircraft*, 46(4):1210–1221, July 2009.

[40] S. Kottapalli. Performance and Loads Correlation of a UH-60A Slowed Rotor at High Advance Ratios. San Francisco, CA, January 2012. AHS Future Vertical Lift Aircraft Design Conference.

[41] F. D. Harris. Preliminary Study of Radial Flow Effects on Rotor Blades. *Journal of the American Helicopter Society*, 11(3):1–21, July 1966.

[42] W Johnson. A Comprehensive Analytical Model of Rotorcraft Aerodynamics and Dynamics. Technical Report USAAVRADCOM TR 80-A-5, NASA Ames Research Center and U.S. Army Aviation Research and Development Command, June 1980.

[43] R. A. Ormiston. A New Formulation for Lifting Rotor Performance Including Comparison with Full-Scale Data. Montreal, Canada, April 2008. 64th Annual Forum of the American Helicopter Society.

[44] R. A. Ormiston. Rotor Aerodynamic Characteristics at High Advance Ratio Relevant to Compound Rotorcraft. San Francisco, CA, January 2012. AHS Future Vertical Lift Aircraft Design Conference.

[45] D. A. Peters and C. J. He. Finite State Induced Flow Models Part II: Three-Dimensional Rotor Disk. *Journal of Aircraft*, 32(2):323–333, March 1995.

[46] G. Bowen-Davies and I. Chopra. Investigation of the UH-60A Slowed Rotor Wind Tunnel Tests Using UMARC. *Journal of Aircraft*, 50(2):576–589, March 2013.

[47] G. M. Bowen-Davies and I. Chopra. Performance and Loads Correlation of the UH-60 Rotor at High Advance Ratios. Southampton, UK, September 2014. 40th European Rotorcraft Forum.

[48] G. M. Bowen-Davies and I. Chopra. Investigation of the Unsteady Reverse Flow Airloads at High Advance Ratios. Munich, Germany, September 2015. 41st European Rotorcraft Forum.

[49] J. G. Leishman and T. S. Beddoes. A Semi-Empirical Model for Dynamic Stall. *Journal of the American Helicopter Society*, 34(3):3–17, July 1989.

[50] G. Bowen-Davies and I. Chopra. Validation of Rotor Performance and Loads at High Advance Ratio. San Francisco, CA, January 2014. 5th Decennial AHS Aeromechanics Specialists Conference.

[51] J. Rigsby and JVR Prasad. Stability and Control Issues Associated with Lightly-Loaded, Autorotating Rotors in High Advance Ratio Flight. Montreal, Canada, April 2008. 64th Annual Forum of the American Helicopter Society.

[52] J. Rigsby and JVR Prasad. Performance and Trim Analysis of Lightly Loaded Rotors in High Advance Ratio Autorotation. San Francisco, CA, January 2010. AHS Aeromechanics Specialists's Conference.

[53] M. Potsdam, A. Datta, and B. Jayaraman. Computational Investigation and Fundamental Understanding of a Slowed UH-60A Rotor at High Advance Ratio. Fort Worth, TX, May 2012. 68th Annual Forum of the American Helicopter Society.

[54] J. Sitaraman, M. Potsdam, B. Jayaraman, A. Datta, A. Wissink, D. Mavriplis, and H. Saberi. Rotor Loads Prediction Using Helios: A Multi-Solver Framework for Rotorcraft Aeromechanics Analysis. *Journal of Aircraft*, 50(2):478–492, March 2013.

[55] M. Potsdam, H. Yeo, and R. A. Ormiston. Performance and Loads Predictions of a Slowed UH-60A Rotor at High Advance Ratios. Moscow, Russia, September 2013. 39th European Rotorcraft Forum.

[56] J. De Montaudouin, N. Reveles, and M. J. Smith. Computational Aeroelastic Analysis of Slowed Rotors at High Advance Ratios. *The Aeronautical Journal*, 118(1201):297–313, March 2014.

[57] R. P. Marpu and L. N. Sankar. Aeromechanical Analysis of a Slowed Rotor at High Advance Ratios using a Hybrid Methodology. San Francisco, CA, January 2014. 5th Decennial AHS Aeromechanics Specialists Conference.

[58] Y. Tanabe and H. Suguwara. Aerodynamic Validation of rFlow3D Code with UH-60A Data Including High Advance Ratios. Munich, Germany, September 2015. 41st European Rotorcraft Forum.

[59] M. Sugiura, Y. Tanabe, H. Sugawara, and I. Chopra. Validation of rFlow3D Code for a Helicopter at High Advance Ratios. San Francisco, CA, January 2016. AHS Technical Meeting on Aeromechanics Design for Vertical Lift.

[60] A. Lind, L. Trollinger, F. Manar, I. Chopra, and A. Jones. Flowfield measurements of reverse flow on a high advance ratio rotor. *Experiments in Fluids*, 59(12):1–15, December 2018.

[61] L. Smith, A. Bauknecht, X. Wang, A. Lind, and A. Jones. Three-Component Reverse Flow Measurements on a Mach-Scale Rotor at High Advance Ratios. Phoenix, AZ, May 2018. 74th Annual Forum of the American Helicopter Society.

[62] A. Bauknecht, X. Wang, and I. Chopra. Wind Tunnel Test of a Rotorcraft with Lift Compounding. Warsaw, Poland, September 2019. 45th European Rotorcraft Forum.

[63] X. Wang, A. Saxena, and I. Chopra. Measurement and Validation of a Mach-Scale Rotor Performance and Loads at High Advance Ratios. West Palm Beach, FL, May 2016. 72nd Annual Forum of the American Helicopter Society.

[64] X. Wang, Y. Jung, J. Baeder, and I. Chopra. Blade Structural Load/Airload Correlation on a Slowed Mach-Scaled Rotor at High Advance Ratios. *Journal of the American Helicopter Society*, 65(2):1–12, April 2020.

[65] X. Wang, Y. Jung, J. Baeder, and I. Chopra. Correlation of Predictions with Measured Pressure Data from a Slowed Mach-Scaled Rotor at High Advance Ratios. San Francisco, CA, January 2018. Aeromechanics for Advanced Vertical Flight Technical Meeting.

[66] X. Wang, Y. Jung, J. Baeder, and I. Chopra. CFD Pressure/Airload Correlation with Experimental Data on a Slowed Mach-Scaled Rotor at High Advance Ratios. Phoenix, AZ, May 2018. 74th Annual Forum of the American Helicopter Society.

[67] X. Wang, L. Trollinger, and I. Chopra. Refined Performance Results on a Slowed Mach-Scaled Rotor at High Advance Ratios. *Journal of the American Helicopter Society*, 65(1):1–13, January 2020.

[68] L. Trollinger, X. Wang, and I. Chopra. Refined Measurement and Validation of Performance and Loads of a Mach-Scaled Rotor at High Advance Ratios. Milan, Italy, September 2017. 43rd European Rotorcraft Forum.

[69] X. Wang, A. Bauknecht, S. Maurya, and I. Chopra. Wind Tunnel Test on a Slowed Mach-Scaled Hingeless Rotor at High Advance Ratios. Philadelphia, PA, May 2019. 75th Annual Forum of the American Helicopter Society.

[70] G. Bir and I. Chopra. Status of University of Maryland Advanced Rotorcraft Code (UMARC). San Francisco, CA, January 1994. 3rd Decennial AHS Aeromechanics Specialists Conference.

[71] B. Passe, A. Sridharan, J. Baeder, and R. Singh. Identification of Rotor-Fuselage Aerodynamic interactions in a Compound Coaxial Helicopter using CFD-CSD Coupling. San Francisco, CA, January 2016. AHS Technical Meeting on Aeromechanics Design for Vertical Lift.

[72] A. Grizzle, V. Hrishikeshavan, A. Saxena, and I. Chopra. Characterization of Endevco Piezoresistive Sensors for Blade Pressure Measurements. Fort Worth, TX, May 2017. 73rd Annual Forum of the American Helicopter Society.

[73] W. C. Young and R. G. Budynas. *Roark's Formulas for Stress and Strain*. McGraw-Hill publishing, seventh edition, 2001.

[74] S. Y. Leung and Y. Y. Link. Comparison and Analysis of Strain Gauge Balance Calibration Matrix Mathematical Models. Technical Report DSTO-TR-0857, Air Operations Division Aeronautical and Maritime Research Laboratory, August 1999.

[75] C. E. Freeman and R. E. Mineck. Fuselage Surface Pressure Measurements of a Helicopter Wind-Tunnel Model with a 3.15-Meter Diameter Single Rotor. Technical Report NASA-TM-80051, NASA Langley Research Center, March 1979.

[76] J. Barlow. *Glenn L. Martin Wind Tunnel Facilities*. University of Maryland, April 2020. `https://windtunnel.umd.edu/facilities`.

[77] H. J. Sutherland and J. F. Mandell. Optimized Goodman Diagram for the Analysis of Fiberglass Composites Used in Wind Turbine Blades. Reno, NV, January 2005. 43rd AIAA Aerospace Sciences Meeting and Exhibit.

[78] S. Butterworth. On the Theory of Filter Amplifiers. *Experimental Wireless and the Wireless Engineer*, 30:536–541, October 1930.

[79] H. Glauert. The Interference on the Characteristics of an Airfoil in a Wind Tunnel of Rectangular Section. Technical Report R. & M. No. 1459, British A.R.C, 1932.

[80] H. J. Langer, .T. H. Maier, and R. L. Peterson. An Experimental Evaluation of Wind Tunnel Wall Correction Methods for Helicopter Performance. Washington, DC, June 1996. 52nd Annual Forum of the American Helicopter Society.

[81] J. B. Barlow, W. H. Rae, and A. Pope. *Low-Speed Wind Tunnel Testing*. Wiley and Sons, Inc., third edition, 1999.

[82] A. Datta. Fundamental Understanding, Prediction and Validation of Rotor Vibratory Loads in Steady Level Flight, 2004.

[83] D. H. Hodges and E. H. Dowell. Nonlinear Equations of Motion for the Elastic Bending and Torsion of Twisted Nonuniform Rotor Blades. Technical Report NASA TN D-7818, NASA Ames Research Center and U.S. Army Air Mobility R&D Laboratory, December 1974.

[84] J. H. Schmaus. Aeromechanics of a High Speed Coaxial Helicopter Rotor, 2017.

[85] C. D. Harris. Two-Dimensional Aerodynamic Characteristics of the NACA 0012 Airfoil in the Langley 8 foot Transonic Pressure Tunnel. Technical Report NASA-TM-81927, NASA Langley Research Center, April 1981.

[86] A. Bagai and J. G. Leishman. Rotor Free-Wake Modeling Using a Pseudo-Implicit Technique Including Comparisons with Experimental Data. *Journal of the American Helicopter Society*, 40(3):29–41, July 1995.

[87] J. Weissinger. The Lift Distribution of Swept-Back Wings. Technical Report NACA-TM-1120, National Advisory Committee for Aeronautics, Langley Aeronautical Lab, March 1947.

[88] J. G. Leishman. Validation of Approximate Indicial Aerodynamic Functions for Two-Dimensional Subsonic Flow. *Journal of Aircraft*, 25(10):914–922, October 1988.

[89] J. Sitaraman, A. Datta, J. Baeder, and I. Chopra. Fundamental Understanding and Prediction of Rotor Vibratory Loads in High-Speed Forward Flight. Friedrichshafen, Germany, September 2003. 29th European Rotorcraft Forum.

[90] A. Datta, J. Sitaraman, I Chopra., and J. Baeder. Analysis Refinements for Prediction of Rotor Vibratory Loads in High-Speed Forward Flight. Baltimore, MD, June 2004. 60th Annual Forum of the American Helicopter Society.

[91] A. Sridharan. Simulation Modeling of Flight Dynamics, Control and Trajectory Optimization of Rotorcraft Towing Submerged Loads, 2014.

[92] Jr. Anderson, J. D. *Fundamentals of Aerodynamics*. McGraw-Hill publishing, fifth edition, 2011.

[93] Y. Jung, B. Govindarajan, and J. Baeder. Turbulent and Unsteady Flows on Unstructured Line-Based Hamiltonian Paths and Strands Grids. *AIAA Journal*, 55(6):1986–2001, April 2017.

[94] A. Datta, J. Sitaraman, J. Baeder, and I. Chopra. CFD/CSD Prediction of Rotor Vibratory Loads in High-Speed Flight. *Journal of Aircraft*, 43(6):1698–1709, November 2016.

[95] N. Chanderjian. Navier-Stokes Simulation of UH-60A Rotor/Wake Interaction Using Adaptive Mesh Refinement. Fort Worth, TX, May 2017. 73rd Annual Forum of the American Helicopter Society.

[96] Y. Jung, D. Jude, B. Govindarajan, and J. Baeder. Line-Based Unstructured/Structured Heterogeneous CPU/GPU Framework for Complex Aerodynamic Flows. Fort Worth, TX, May 2017. 73rd Annual Forum of the American Helicopter Society.

[97] M. Drela and H. Youngren. *AVL Overview*. Massachusetts Institute of Technology, Department of Aeronautics and Astronautics, February 2017. `http://web.mit.edu/drela/Public/web/avl/`.

[98] K. B. Hilbert. A mathematical model of the UH-60 helicopter. Technical Report NASA-TM-85890, NASA Ames Research Center, April 1984.

[99] B. G. van der Wall, M. Wentrup, G. Rajagopalan, S. N. Jung, and J. Yin. A Simple Analytical Model for Investigation of Fuselage-Rotor Interference. West Palm Beach, FL, May 2016. 72nd Annual Forum of the American Helicopter Society.

[100] E. Kreyszig. *Advanced Engineering Mathematics*. Wiley and Sons, Inc., tenth edition, 2011.